STUDY OF RARE DECAYS & EXOTIC STATES IN QUARKONIUM AT BELLE

SOURAV PATRA

A thesis submitted for the partial fulfillment of

the degree of Doctor of Philosophy

Department of Physical Sciences

Indian Institute of Science Education and Research Mohali

Knowledge city, Sector 81, SAS Nagar, Manauli PO, Mohali 140306, Punjab, India.

October 2022

I dedicate this thesis to my parents and wife.

Declaration

The work presented in this thesis has been carried out by me under the guidance of Dr. Vishal Bhardwaj and Dr. Ambresh Shivaji at the Indian Institute of Science Education and Research Mohali. This work has not been submitted in part or in full for a degree, a diploma, or a fellowship to any other university or institute. Whenever contributions of others are involved, every effort is made to indicate this clearly, with due acknowledgement of collaborative research and discussions. This thesis is a bona fide record of original work done by me and all sources listed within have been detailed in the bibliography.

Sourav Patra
Registration No. PH16035
Department of Physical Sciences

In our capacity as the supervisor of the candidate's thesis work, We certify that the above statements by the candidate are true to the best of our knowledge.

Dr. Vishal Bhardwaj
Department of Physical Sciences,
Indian Institute of Science Education
and Research Mohali

Dr. Ambresh Shivaji
Department of Physical Sciences,
Indian Institute of Science Education
and Research Mohali

Acknowledgements

It is my pleasure to acknowledge some people who have contributed in completion of this thesis in many scenarios.

First and foremost, I express my sincere gratitude to my Ph.D. supervisor, Dr. Vishal Bhardwaj, for his valuable guidance and support throughout the whole duration of my PhD. I want to thank him for providing the opportunity to work with Belle and Belle II collaborations, and for providing a friendly environment. I am forever grateful to him. Also, I would like to thank my co-supervisor Dr. Ambresh Shivaji for some important discussions and reviewing my thesis.

I extend my gratitude to Prof. Karim Trabelsi, IJCLab, France, for constantly monitoring and improving my work. I thank him for many important discussions related to the my work during my KEK visits. I am always grateful to him for providing the opportunity to work with him and arranging time from his busy schedule for checking my works.

I would like to express my special thanks to Belle internal referees: Dr. S. Sandilya, Dr. U. Tamponi, Dr. J. Li, Prof. B. Yabsley, Dr. S. Jia, and Dr. X.L. Wang for constantly reviewing my works. I thank Prof. Y. Sakai, Prof. M. Nakao, Prof. F. Bryan, Prof. J. Libby, and Prof. S. Nishida for their valuable comments and suggestions to improve my work. Also, I would like to thank Prof. G.B. Mohanty for helpful comments during Belle Analysis Workshops. I also thank the convener of bottomonium working group, Prof. R. Mussa and charmonium working group convener, Prof. Y. Junhao for many important suggestions and coordinating the analyses. I acknowledge all the Belle and Belle II collaborators for their comments and suggestions during Belle General Meetings.

I would like to thank Prof. H.K. Jassal and Dr. A. Joseph for reviewing my work progress and this thesis. I would like to acknowledge Prof. S. Uno for providing me with local financial support for my visits to KEK, Japan. I would like to thank some of my collaborators: Dr. Renu, Manish, Souvik for providing various information, for important discussion sessions related to our works, and also for many chit-chats. I will always remember Juhi, Arpith, Ravi, Anweshika, Jasleen, Sudipto, Gokul, Ranbir, and others for many happy memories of campus life.

I am always grateful to my parents for constantly supporting me throughout the whole time and for providing the luxury to take my own decisions. Finally, I would like thank my friend and better half, Kalpana, for always being with me through the ups and downs of my life.

Abstract

The number of leptons belonging to each generation is conserved in any interaction: this rule is known as the lepton flavor number conservation. In 1998, the Super-Kamiokande experiment announced convincing evidence for neutrino oscillations implying that neutrinos have certain mass. This also violates the conservation of lepton flavor. On the other hand, currently lepton flavor universality LFU violation is the most excited anomaly in the flavor physics. Although the SM gauge couplings do not discriminate between different generations of leptons, there are some new physics (NP) models such as: leptoquarks model, Z' model, which predict the enhancement of the couplings with increasing lepton mass. Also, it has been pointed out that the violation of lepton flavor universality generically implies the violation of lepton flavor. Thus, one can constrain the parameters for the NP models, describing LFU violation, by studying the charge lepton flavor violation (CLFV). Moreover, flavor changing neutral current (FCNC) interactions serve as a powerful probe of physics beyond the SM. As SM model operators can not generate FCNCs in the tree level diagram, NP operators dominate the SM loop corrections by producing FCNCs in the tree level diagram. CLFV interaction in various bottomonium ($b\bar{b}$) decays can provide the alternative access to study all those NP operators. CLEO and BaBar collaborations have already published some results on the search for CLFV in $\Upsilon(nS)[n = 1, 2, 3]$ decays. For $\Upsilon(1S)$, only $\Upsilon(1S) \to \mu^{\pm}\tau^{\mp}$ has been studied so far, and not $\Upsilon(1S) \to e^{\pm}\mu^{\mp}$ and $\Upsilon(1S) \to e^{\pm}\tau^{\mp}$ transitions. Belle has the largest $\Upsilon(2S)$ data sample corresponding to 158 million $\Upsilon(2S)$ decays and the resulting number of $\Upsilon(1S)$ produced in $\Upsilon(2S) \to \pi^{+}\pi^{-}\Upsilon(1S)$ decays is around 28 million. Four particles final state in $\Upsilon(2S) \to \pi^{+}\pi^{-}\Upsilon(1S)[\to \ell\ell']$ $[\ell, \ell' = e, \mu, \tau]$ provides a better control over background with efficient triggering. On the other hand, CLFV decays with an extra photon in the final state (RLFV), $\Upsilon(nS) \to \gamma\ell\ell'$ could allow one to access the operators which are inaccessible in two-body CLFV decays. But, there are no results available on RLFV decays. In this thesis, we search for the $\Upsilon(1S) \to \ell^{\pm}\ell'^{\mp}$ and $\Upsilon(1S) \to \gamma\ell^{\pm}\ell'^{\mp}$ decays using $\Upsilon(1S)$ with di-pion tagging. We use $\Upsilon(1S) \to \ell^{\pm}\ell^{\mp}$ $[\ell = e, \mu]$ decays as the calibration modes. To validate the signal extraction procedure, we measure the branching fractions for $\Upsilon(1S) \to e^{+}e^{-}$ and $\Upsilon(1S) \to \mu^{+}\mu^{-}$ modes. The obtained results on the branching fraction measurements, $\mathcal{B}[\Upsilon(1S) \to e^{+}e^{-}] = (2.40 \pm 0.01(\text{stat}) \pm 0.12(\text{syst})) \times 10^{-2}$ and $\mathcal{B}[\Upsilon(1S) \to \mu^{+}\mu^{-}] = (2.46 \pm 0.01(\text{stat}) \pm 0.11(\text{syst})) \times 10^{-2}$, agree with the world average values within corresponding uncertai- nties. In the absence of signal, we set upper limit (UL) on the branching fraction of the CLFV decays at the 90%

CL. The obtained ULs of branching fractions for $\Upsilon(1S) \to e^{\pm}\mu^{\mp}$, $\Upsilon(1S) \to \mu^{\pm}\tau^{\mp}$, $\Upsilon(1S) \to e^{\pm}\tau^{\mp}$, $\Upsilon(1S) \to \gamma e^{\pm}\mu^{\mp}$, $\Upsilon(1S) \to \gamma\mu^{\pm}\tau^{\mp}$, and $\Upsilon(1S) \to \gamma e^{\pm}\tau^{\mp}$ are 3.9×10^{-7}, 2.7×10^{-6}, 2.7×10^{-6}, 4.2×10^{-7}, 6.1×10^{-6}, and 6.5×10^{-6}, respectively. The result for the $\Upsilon(1S) \to \mu^{\pm}\tau^{\mp}$ decay is 2.3 times more stringent than the previous result from the CLEO collaboration, while the remaining modes are searched for the first time.

Couple of studies has already been done on vector quarkonia decays such as: $\Upsilon(nS) \to \ell\ell'$ and $J/\psi \to \ell\ell'$ decays. But, no experimental studies have been performed on scalar quarkonium decays. Corresponding p-wave states of $\chi_{b0}(1P)$ and χ_{c0}, those have been efficiently produced in radiative transition of $\Upsilon(2S)$ decays, can be used to search for CLFV scalar quarkonium decays. In this thesis, we search for CLFV in $\chi_{b0}(1P) \to \ell^{\pm}\ell'^{\mp}$ decays using $\Upsilon(2S)$ data, where $\ell, \ell' = e, \mu, \tau$ leptons. Along with that, we also search for $\chi_{b1}(1P) \to \ell^{\pm}\ell'^{\mp}$ and $\chi_{b2}(1P) \to \ell^{\pm}\ell'^{\mp}$ decays, which provide the result for CLFV in axial vector and tensor meson decays, respectively. To study CLFV $\chi_{bJ}(1P) \to \ell^{\pm}\ell'^{\mp}$ decays, use $\chi_{bJ}(1P) \to \gamma\Upsilon(1S)[\to \ell^+\ell^-]$ decays as the calibration modes, where $\ell = e, \mu$ leptons. Due to very less number of charged tracks with one (or two) photons in the final state, QED Bhabha events become dominating background here. We simulate the Bhabha trigger effect to estimate the effect of Bhabha veto that has already been applied on $\Upsilon(2S)$ data collected by the Belle detector. We measure the branching fractions of calibration modes. Measured branching fractions of $\Upsilon(2S) \to \gamma\gamma e^+e^-(\gamma\gamma\mu^+\mu^-)$ decays for $J = 0$, 1, and 2 are $(1.6 \pm 0.2) \times 10^{-5}$ ($(1.5 \pm 0.1) \times 10^{-5}$), $(5.37 \pm 0.06) \times 10^{-4}$ ($(6.14 \pm 0.04) \times 10^{-4}$), and $(2.96 \pm 0.05) \times 10^{-4}$ ($(3.30 \pm 0.03) \times 10^{-4}$), respectively, which agree with the corresponding world average values within uncertainties. We study the SM backgrounds and estimate the expected ULs of branching fractions using MC simulated events. Expected ULs of branching fractions for $\chi_{b[0,1,2]}(1P) \to e^{\pm}\mu^{\mp}$, $\chi_{b[0,1,2]}(1P) \to \mu^{\pm}\tau^{\mp}$, and $\chi_{b[0,1,2]}(1P) \to e^{\pm}\tau^{\mp}$ are [1.3×10^{-6}, 6.9×10^{-7}, 7.0×10^{-7}], [1.7×10^{-5}, 1.5×10^{-5}, 1.4×10^{-5}], and [3.1×10^{-5}, 1.3×10^{-5}, 1.3×10^{-5}], respectively. This study is under internal review of the Belle collaboration.

Last two decade have been very exciting for the quarkonium sector. Many new states have been found which find no place in the conventional spectroscopy and are strong contenders of the exotic quarkonium states (like tetra-quark, molecular, hybrid). $X(3872)$ has remained the poster boy of these exotic states, from the time it was first observed by the Belle Collaboration in 2003. One of the salient features of $X(3872)$ is that the mass coincides exactly with the $\overline{D}^{*0}D^0$ (or $\overline{D}^0D^{*0}$) threshold: $m_{D^0} + m_{D^{*0}} - m_{X(3872)} = (0.00\pm0.18)$ MeV/c^2, which naturally pushes the molecular

interpretations. Negative C-odd partner search of $X(3872)$ ($X(3872) \to J/\psi\eta$, $X(3872) \to \chi_{c1}\gamma$, $X(3872) \to \eta_c\omega$, $X(3872) \to \eta_c\pi\pi$) and charged partner search in $X(3872)^+ \to J/\psi\pi^+\pi^0$ suggest that $X(3872)$ is an iso-singlet state. In that scenario, its decay into its discovery mode $X(3872) \to J/\psi\pi^+\pi^-$ is expected to be isospin violating. Further, one expect the decay $X(3872) \to J/\psi\omega(\to \pi^+\pi^-\pi^0)$ to be an isospin allowed and should have larger branching fraction, something like $R_{3\pi/2\pi} \equiv \mathcal{B}(X(3872) \to J/\psi\omega)/\mathcal{B}(X(3872) \to J/\psi\pi^+\pi^-) \sim 30$. Isospin violating decays of $X(3872)$ are sensitive to the inner structures and have been investigated in different scenarios. Couple of studies also suggest that the isospin violation comes from the molecular structure of the $X(3872)$. However, the previous measurement by the Belle with 256 fb^{-1} data suggest $R_{3\pi/2\pi}$ to be 1.0 ± 0.4 (stat) ± 0.3 (syst). BaBar Collaboration using their full data set (426 fb^{-1}) measured this ratio to be 0.7 ± 0.3 (1.7 ± 1.3) for B^+ (B^0) events. Recently, BESIII has published the result on $R_{3\pi/2\pi}$ to be $1.6^{+0.4}_{-0.3}$ (stat) ± 0.2 (syst), which is on higher side. All the results bring the picture of large isospin violation, which is not truly understood so far. Belle accumulated 711 fb^{-1} data, almost twice of BaBar. More precise measurement with the full Belle data set will help to understand the nature of $X(3872)$. Also, the $X(3915)$ is the another interesting exotic charmonium state. Measurements suggest the quantum numbers for $X(3915)$ can be either 0^{++} or 2^{++}. BaBar measured the branching fraction of $X(3915) \to J/\psi\omega$ decay to be ~ 20 times of the branching fraction for $X(3872) \to J/\psi\omega$. BESIII reported the branching fraction of $X(3915) \to J/\psi\omega$ to be suppressed as compared to $X(3872) \to J/\psi\omega$ decays. In this thesis, we study the branching fractions of $X(3872) \to J/\psi\omega$ and $X(3915) \to J/\psi\omega$ using the largest $\Upsilon(4S)$ data sample collected by the Belle detector. For this study, we describe the analysis strategy, event selection criteria, background suppression using MC simulated samples. This study is under internal review of the Belle collaboration. We hope to finalize this analysis soon.

List of publications

Journals

1. S. Patra, V. Bhardwaj *et al.* (Belle Collaboration), Study of $X(3872)$ and $X(3915)$ in $B \to J/\psi\omega K$ decays at Belle, To be submitted to PRD(L).

2. S. Patra, V. Bhardwaj, K. Trabelsi *et al.* (Belle Collaboration), Search for charged lepton flavor violating decays of $\Upsilon(1S)$, JHEP 05 (2022) 095.

Conference proceedings

1. S. Patra, R.K. Maiti, and V. Bhardwaj, Study of $X(3872)$ and $X(3915)$ in $B \to J/\psi\omega K$ at Belle, Springer Proc. Phys. 261 155-159 (2021).

2. S. Patra, V. Bhardwaj, and k. Trabelsi, Search for lepton flavor violation in $\Upsilon(1S)$ decays, to be appeared in Springer Proc. Phys.

3. S. Patra, New physics searches in τ decays at Belle, PoS(EPS-HEP2021) 524 (2022).

Contents

List of Figures

List of Tables

"Physicists are made up of atoms. A physicist is an attempt by an atom to understand itself."

– Michio Kaku

Chapter 1

Theoretical Overview

In this chapter, I give a theoretical background with a brief history of particle physics. Starting from the Standard Model (SM), I show how the studies of rare decays and exotic states in quarkonium decays are crucial to understand the SM anomalies and probe the new physics scenarios beyond the SM.

1.1 Standard Model of particle physics

Philosophers were always interested about the components of matter surrounding us. Aristotle's view that matter was composed of five basic elements (earth, water, air, fire, aether) was adopted by most of the philosophers at that time and remained the dominant way of thinking over the centuries. It was the time when natural philosophy began its transition to science. In 1738, Swiss mathematician David Bernoulli explained the behavior of pressurized gas assuming that gas was made up of tiny particles. In 1808, British chemist John Dalton proposed the idea of an atom that can not be chemically broken down into simpler substances and they are identical building blocks for a particular type of matter.

In 1878, British physicist J.J. Thomson discovered a negatively charged particle called "electron" in his cathode ray tube experiment. It was the first ever piece of elementary particles. Shortly after electrons were discovered, it was assumed that an atom was a positively charged mass that contained negative electrons inside of it. In 1909, gold foil experiment by Ernest Rutherford, challenged this picture. Rutherford

concluded that the positive charge of the gold atom was concentrated in a very small part called "nucleus", and the rest of the atom was empty space. In 1905, Einstein came up with a theory of the photoelectric effect based on a concept first proposed by Max Planck that light consists of tiny packets of energy known as photons.

During the mid of 1900 century, physicists explored the foundations of quantum physics and the components of matter. By 1974, physicists had determined a set of rules and principles called the Standard Model (SM) of particle physics [1, 2, 3] — a model that includes all interactions except for gravity. The SM of particle physics provides a mathematical description of three fundamental forces namely the strong, weak, and electromagnetic forces which act among the elementary particles of the SM. This unified theory predicted the existence and properties of the $W^{\pm}$ and Z^0 bosons before their discovery in 1983. It was followed by discoveries of other missing building blocks notably, the top quark in 1995. Finally the Higgs boson was discovered in 2012 providing the missing link for producing the massive particles. During the last decades, the SM has been tested by numerous precision measurements, the overwhelming majority of which has been able to verify its accuracy. The elementary building blocks of the SM are classified as fermions, particles with half-integer values of spin, and bosons, particles having integer spin. All visible matter of the universe is composed of fermions while bosons are the force-carriers responsible for interactions between particles. Fermions are divided into two categories, quarks and leptons. Quarks are sensitive to all known interactions, whereas leptons are not sensitive to the strong interaction.

1.1.1 Elementary particles

The SM includes six types, or flavours of quarks: up (u), down (d), charm (c), strange (s), top (t), and bottom (b). Quarks can be classified into three generations: the two lightest quarks, u and d, compose the first generation, c and s quarks the second one, and finally two heaviest quarks, t and b, enter into the third generation. In each generation, there is an up-type quark with the electric charge of $+2/3$ units of elementary electric charge (u, c, t); and a down-type quark with a charge of -1/3 units (d, s, b). Quark masses range from a few MeV/c^2 for the light quarks, up to 173 GeV/c^2 for the top quark.

Quarks have non-zero color quantum number, therefore they cannot be observed directly, and almost instantly (at a timescale of about 10^{-23} s) hadronise to form

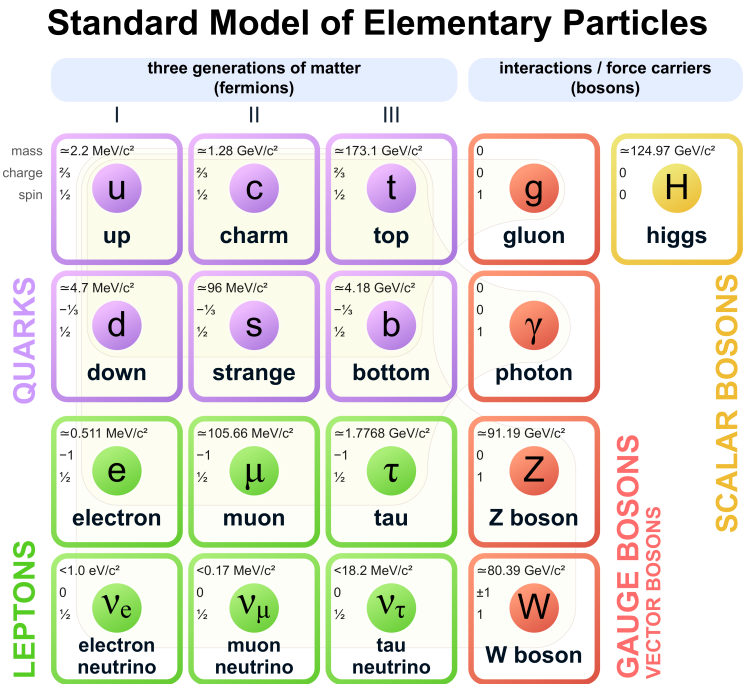

FIG. 1.1: Elementary particles in the Standard Model [4].

bound states called hadrons. Quarks are bounded inside the hadrons by the strong interaction. Possible colorless quark combinations define the classification scheme of hadrons: mesons are the states of quark content $q\bar{q}$, baryons are qqq states. There are six types of leptons, and they can also be classified in three generations. Each generation includes a charged lepton (e^-, μ^-, τ^-) carrying one unit of elementary electric charge, and its neutral partner called neutrino $(\nu_e, \nu_\mu, \nu_\tau)$ which cannot participate in electromagnetic interactions. The forces of the nature are mediated by the gauge bosons: massless gluons (g), massive weak bosons $(W^\pm, Z^0)$, and a massless photon (γ). Also, there exist a scalar massive higgs field (H) to provide the mass to the SM particles.

1.1.2 Fundamental interactions

The SM is based on symmetry principles. Specifically, the symmetry of the interactions is described by a gauge group, $SU(3)_C \otimes SU(2)_L \otimes U(1)_Y$ where C, L, and Y denote the colour, the left-handed chirality, and the weak hypercharge, respectively. The $SU(3)_C$ symmetry is associated with the strong interaction and $SU(2)_L \otimes U(1)_Y$ is associated with the electroweak interaction. However, in the energy scale below electroweak unification, weak bosons become massive through spontaneous symmetry

breaking, and the ground state of the universe respects only the $SU(3)_C \otimes U(1)_{EM}$ subgroup. The SM is predictive and determines which of the gauge symmetries are spontaneously broken. The structure of symmetries implies that the various interactions in the nature are mediated by spin-one gauge bosons: eight massless gluons for the strong interaction, two charged massive $W^{\pm}$ bosons along with a neutral massive Z^0 boson for the weak interaction, and a massless photon for the electromagnetic interaction.

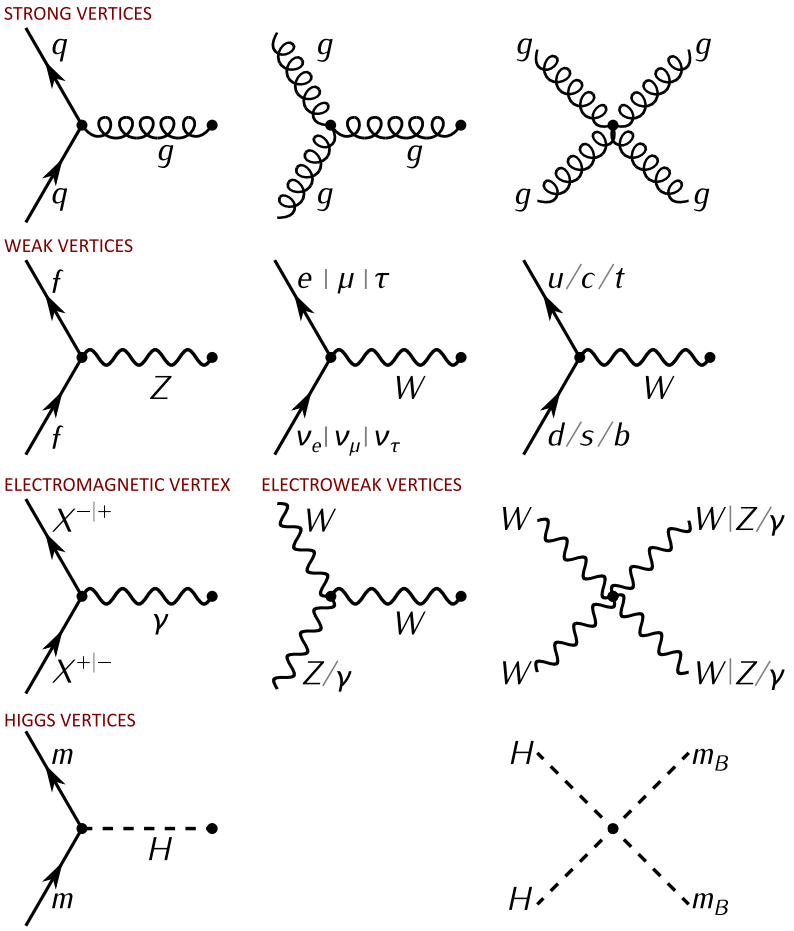

FIG. 1.2: Some possible Feynman diagram for the fundamental interactions of the Standard Model where X is any charged particle, m is any particle with mass (with the possible exception of the neutrinos), and m_B is any boson with mass [5].

The most general renormalizable Lagrangian representing the interactions of containing matter fields and the SM gauge group can be divided into three parts,

$$\mathcal{L}_{\text{SM}} = \mathcal{L}_{\text{kin}} + \mathcal{L}_{\text{Higgs}} + \mathcal{L}_{\text{Yuk}} \tag{1.1}$$

The kinetic Lagrangian $\mathcal{L}_{\text{kin}}$ includes the gauge interactions through the covariant derivative and non-Abelian field strengths which controls the fermionic interaction with gauge fields. The $\mathcal{L}_{\text{Higgs}}$ provides the Mexican hat potential. The $\mathcal{L}_{\text{Yuk}}$ represents the Yukawa interactions, the interaction of fermionic fields with the scalar Higgs field.

Quantum chromodynamics

The theory of the interaction among the quarks is the quantum chromodynamics (QCD). Since the processes dominated by the strong interaction were observed to occur on a timescale of the order of the electromagnetic ones, it is reasonable to assume that the mediator for such interaction is a massless boson. However, one single charge is not enough to explain the properties of hadrons. The charge of QCD is the so-called color charge. It can take the values commonly referred to as red, green, and blue, as well as the corresponding anti-colors. There are eight gluons which correspond to the eight generators of $SU(3)_C$. Gluons interact with quarks and other gluons via their color charges. The full QCD Lagrangian can be written as

$$\mathcal{L}_{\text{QCD}} = -\frac{1}{4} G^{a\mu\nu} G^{a}_{\mu\nu} + \sum_{f} \overline{q}_f (i\gamma^\mu D_\mu - m_f) q_f \tag{1.2}$$

Where $D_\mu = \partial_\mu - i g_s \frac{\lambda^a}{2} G^a_\mu(x)$ is the covariant derivative containing the coupling between quarks and the gauge fields with λ^a as the generators of the $SU(3)$, q_f are six massive Dirac fields representing the six quarks with mass m_f, and $G^{a\mu\nu} G^{a}_{\mu\nu}$ represents the self coupling of the gluon fields.

The strong interaction coupling constant (α_s) decreases with increasing transferred momentum this phenomenon is called as asymptotic freedom. The first evidence for this behavior was found in deep-inelastic scattering reactions in 1969 [6]. At small transferred momenta values, the value of the α_s is large and it becomes impossible to separate individual colored quarks and gluons, and this property is known as confinement. Only bound states of quarks, colorless hadrons, can be observed. The two regimes of large and small coupling values are separated by a reference scale, $\Lambda_{\text{QCD}} \sim 750$ MeV. In that scenario, u, d, s quarks are light quarks and c, b, t are treated as heavy quarks.

Electroweak theory

The detailed analysis of the energy and angular distributions in β decays, such as $\mu^- \to e^-\overline{\nu}_e\nu_\mu$ or $n \to pe^-\overline{\nu}_e$, made clear that only the left-handed (right-handed) fermion (anti-fermion) chiralities participate in the weak transitions. However, the strength of the interaction appears to be universal. In addition to this, the study of other processes like $\pi^- \to e^-\overline{\nu}_e$ or $\pi^- \to \mu^-\overline{\nu}_\mu$, which show that neutrinos have left-handed chiralities while anti-neutrinos are right-handed. To describe weak interactions with different properties of left- and right-handed fields.

Above a certain energy scale ($\sim$ 100 GeV), strength of the weak and electromagnetic interactions are identical and they become indistinguishable. The unified understanding of weak and electromagnetic interaction is known as electroweak theory. The four generators of the electroweak interactions can be represented by $SU(2)_L \bigotimes U(1)_Y$ [7, 8]. The Lagrangian of electroweak interaction can be expressed as

$$\begin{aligned}\mathcal{L}_{\rm EW} = &-\frac{1}{4}W^{a\mu\nu}W^a_{\mu\nu} - \frac{1}{4}B^{\mu\nu}B_{\mu\nu} + \overline{Q}_L i\not{D}Q_L + i\overline{u}_R\gamma^\mu D_\mu u_R \\ &+ i\overline{d}_R\gamma^\mu D_\mu d_R + i\overline{L}_L\gamma^\mu D_\mu L_L + i\overline{e}_R\gamma^\mu D_\mu e_R \end{aligned} \tag{1.3}$$

where $D_\mu = \partial_\mu - i\frac{g'}{2}YB_\mu - i\frac{g}{2}T^iW^i_\mu$ represent the covariant derivative for electroweak fields. First two terms in the Lagrangian represent the self interactions of the weak isospin and weak hypercharge, respectively and rest of the terms represent the interactions with the SM fermions. Here, Q_L, u_R, d_R, L_L, and e_R represent left-handed quark doublets, right-handed up type quark singlets, right-handed down type quark singlets, left-handed lepton doublets, and right-handed charged lepton singlets, respectively.

Below the electroweak symmetry breaking scale the electroweak symmetry breaks to QED and the actual physical fields correspond to weak and electromagnetic interactions become the linear combinations of the weak isospin (W^i_μ $[i = 1, 2, 3]$) and weak hypercharge (B_μ) bosons.

$$\begin{gathered}\text{Charge currents: } W^\pm_\mu = \tfrac{1}{\sqrt{2}}(W^1_\mu \mp W^2_\mu) \\ \text{Neutral currents: } Z_\mu = \cos\theta_W W^3_\mu - \sin\theta_W B_\mu \\ A_\mu = \sin\theta_W W^3_\mu + \cos\theta_W B_\mu\end{gathered}$$

Here θ_W is the electroweak mixing angle.

SSB and Higgs mechanism

In order describe the nature of weak interactions at $E \sim G_F^{-1/2}$ and beyond, we need massive weak vector bosons ($\sim$ 80 GeV). At the same time, the gauge symmetry prevents a mass term for the gauge vectors. In that scenario, the gauge symmetry must then be somehow broken spontaneously, in order for the gauge vectors to acquire a mass. This phenomenon is called as spontaneous symmetry breaking (SSB).

The general idea of SSB was introduced by Goldstone by introducing an complex scalar potential, ϕ.

$$\mathcal{L} = \partial_\mu \phi^\dagger \partial^\mu \phi - V(\phi), \qquad V(\phi) = \mu^2 \phi^\dagger \phi - h(\phi^\dagger \phi)^2 \tag{1.4}$$

For $\mu^2 < 0$ and $h > 0$, $|\phi| = 0$ become unstable. The minimum of the potential $V(\phi)$ is obtained at $|\phi_0| = \sqrt{\frac{-\mu^2}{2h}} \equiv \frac{v}{\sqrt{2}}$. Conserving $U(1)$ phase symmetry of the Lagrangian, there are infinite number of degenerate states of minimum energy, $\phi_0(x) = \frac{v}{\sqrt{2}} \exp(i\theta)$. By choosing a particular solution, $\theta = 0$ for example, as the ground state, the symmetry gets spontaneously broken. But, Goldstone theorem does not provide provide the complete picture of massive vector bosons. Peter W. Higgs and Tom W.B. Kibble extended the idea of Goldstone theorem by considering a doublet of complex scalar fields [9, 10]. The scalar gauged Lagrangian is written as

$$\mathcal{L}_S = (D_\mu \phi)^\dagger D^\mu \phi - \mu^2 \phi^\dagger \phi - h(\phi^\dagger \phi)^2 \tag{1.5}$$

The covariant derivative couples the scalar doublet to the electroweak gauge bosons. Thus, the bosons have acquired masses.

$$M_W = M_Z \cos\theta_W = \frac{1}{2} v g \tag{1.6}$$

Where v and g are the vacuum expectation value of the scalar Higgs field and weak coupling strength. Using the experimentally measured values of $W^\pm$ and Z masses, the weak mixing angle θ_W is determined. The determined mixing angle and $W^\pm$ boson mass are $\sin^{-1}(\sqrt{0.212})$ and 80.94 GeV/c^2, respectively. This also provide the mass of Higgs filed to be

$$M_H = \sqrt{-\mu^2} = \sqrt{2h} v \tag{1.7}$$

In 2012, the ATLAS and CMS experiments at the Large Hadron Collider discovered a particle with mass of 125.09 ± 0.24 GeV/c^2 [11, 12].

Yukawa interaction

Fermionic mass terms in Lagrangian, $-m\overline{\psi}\psi = -m(\overline{\psi}_L\psi_R + \overline{\psi}_R\psi_L)$ are not allowed in the presence of exact $SU(2)_L \bigotimes U(1)_Y$ symmetry. Thus, the SM fermions would forced to be massless. This problem get solved by the Yukawa interaction in the presence of complex doublet scalar Higgs field. The Lagrangian of Yukawa interaction can be written as

$$\mathcal{L}_{\rm Y} = -Y^d_{ij}\overline{Q}_{Li}\phi d_{Rj} - Y^u_{ij}\overline{Q}_{Li}\phi^* u_{Rj} - Y^e_{ij}\overline{L}_{Li}\phi e_{Rj} + h.c. \tag{1.8}$$

where the indices i, j run over all the three SM families. As a consequence of this family structure, each of the three Yukawa couplings is a generic 3×3 complex matrix. Once the Higgs gets a vacuum expectation value (after SSB), all the SM fermions get a mass proportional to their Yukawa couplings. As there is no signature for right handed neutrino, neutrinos are massless in the SM. However, as we do not know the coupling parameters, the values of the fermion masses are arbitrary and the Yukawa coupling parameters are fixed from the experimentally measured masses.

1.1.3 Symmetries in Standard Model

We have already discussed earlier that SM interactions can be described by imposing $SU(3)_C \bigotimes SU(2)_L \bigotimes U(1)_Y$ gauge group. Apart from the local gauge symmetry, there are also some continuous and discrete symmetries in the SM.

Global symmetries

Global symmetries in the SM are purely accidental. The global symmetries can be expressed as

$$U(1)_B \otimes U(1)_e \otimes U(1)_\mu \otimes U(1)_\tau, \tag{1.9}$$

where $U(1)_B$ is the baryon number and the other $U(1)_\ell$ ($\ell = e, \mu, \tau$) are lepton family numbers. The quarks carry baryon number, while the leptons and the bosons do

not. We usually normalize it such that the proton has $B = 1$ and thus each quark carries a third unit of baryon number. As for lepton number, in the SM each family carries its own lepton number, L_e, L_μ, and L_τ. Total lepton number is a subgroup of this more general symmetry.

Discrete symmetries

There are three important discrete symmetries in particle physics: parity transformation (P), charge conjugation (C), and time inversion (T). Parity operation inverse the spatial coordinate of wave function of a particle, and it can be defined as $P = (-1)^{L+1}$, where L implies the total orbital angular momentum of the particle state. There are two eigenvalues for the P operator: even-parity with $+1$ and odd-parity with -1. Charge conjugation inverse all the quantum numbers of a particle and transforms the particle to it's antiparticle. Only neutral flavored particle states are the eigenstate of charge conjugation and can be represented as $C = (-1)^{L+S}$, where S is the total spin quantum number of particle. Time inversion changes the timing order of an event by inverting the momentum and orbital angular momentum of a particle.

1.1.4 Flavor structure of the Standard Model

The Standard Model has ten physical flavor parameters: six quark masses, three mixing angles, and a phase. The main experimental goal of flavor physics is to measure the four parameters (mixing angles and phase) in as many ways as possible to check for consistency. Any deviation could be a sign for physics beyond the SM.

CP violation

In nature, C, P, and CP violation are closely related to flavour physics. Only left-handed fermions and right-handed antifermions couple to the $W^{\pm}$. Therefore, there is a breaking of parity and charge conjugation in the SM. The situation with CP symmetry is different. Since both C and P transform left- and right-handed fields into one another at the first glance CP is not necessarily violated. The discovery of CP violation in 1964 in the decays of neutral kaons [13] changed the whole picture, and resulted the Nobel Prize in Physics in 1980 to James Cronin and Val Fitch. The

parameters of the SM that violate CP, require a physical phase in the Lagrangian. In the SM, CP violation in quark sector arises from the complex phases of the quark Yukawa interactions.

Quark mixing

The charged-current $W^{\pm}$ interactions couple to the physical left-handed up and down quark fields is given by

$$\mathcal{L}_{Wqq} = \frac{-g}{\sqrt{2}}(\overline{u}_L, \overline{c}_L, \overline{t}_L)\gamma^{\mu} W^{+}_{\mu} V_{\mathrm{CKM}} \begin{pmatrix} d_L \\ s_L \\ b_L \end{pmatrix} + h.c. \tag{1.10}$$

Here V_{CKM} is known as the Cabibbo–Kobayashi–Maskawa (CKM) mixing matrix for quarks [14]. In the SM, this is the only source of flavour-changing quark interactions and CP violation. V_{CKM} is a 3×3 unitary matrix which can be expressed as

$$V_{\mathrm{CKM}} = \begin{pmatrix} V_{ud} & V_{us} & V_{ub} \\ V_{cd} & V_{cs} & V_{cb} \\ V_{td} & V_{ts} & V_{tb} \end{pmatrix} \tag{1.11}$$

The form of the CKM matrix is not unique. In general, it can be parametrized using three rotation angles and one phase. the standard parametrization, used by PDG [15], is given by

$$V_{\mathrm{CKM}} = \begin{pmatrix} c_{12}c_{13} & s_{12}c_{13} & s_{13}e^{-i\delta_{\mathrm{KM}}} \\ -s_{12}c_{23} - c_{12}s_{23}s_{13}e^{i\delta_{\mathrm{KM}}} & c_{12}c_{23} - s_{12}s_{23}s_{13}e^{i\delta_{\mathrm{KM}}} & s_{23}c_{13} \\ s_{12}s_{23} - c_{12}c_{23}s_{13}e^{i\delta_{\mathrm{KM}}} & -c_{12}s_{23} - s_{12}c_{23}s_{13}e^{i\delta_{\mathrm{KM}}} & c_{23}c_{13} \end{pmatrix} \tag{1.12}$$

where $c_{ij} = \cos\theta_{ij}$ and $s_{ij} = \sin\theta_{ij}$. The three θ_{ij} are the three real mixing parameters within $(0, \pi/2)$, and δ_{KM} is the Kobayashi- Maskawa phase within $(-\pi, \pi)$.

Flavor symmetries

Long before we knew that quarks are real, we had the phenomenologically identified flavor structure of what is now the SM. Including the strange quark along with the up and down quarks, flavor structure of the SM can be represented by $SU(3)_{flavor}$ group. The $SU(3)_{flavor}$ is an approximate symmetry and is partially broken by

the larger mass splitting between the strange and the lighter two quarks. One can extend $SU(3)_{flavor}$ to $SU(4)$ including the charm quark with the light quarks and to $SU(6)$ by considering all six quarks. These symmetries are too approximated by the heavy quark masses. A meson octet diagram under $SU(3)_{flavor}$ is shown in Fig 1.3.

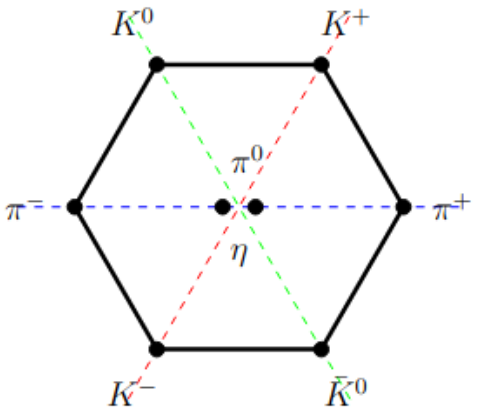

FIG. 1.3: Octet diagram of $SU(3)$ flavor symmetry [16].

Each dotted line corresponds to an $SU(2)$ is a subgroup of $SU(3)$. We can identify these $SU(2)_s$ as the familiar isospin ($u \leftrightarrow d$), v-spin ($u \leftrightarrow s$), and u-spin ($d \leftrightarrow s$) symmetries.

1.1.5 Physics beyond the Standard Model

Over the past 40 years, our understanding of the fundamental particles and forces of nature has changed beyond recognition. The SM reproduces almost all the known phenomenon up to energy of the order of electroweak scale ($\sim 10^2$ GeV). Still there remain many fundamental problems such as:

- All the three generation of quarks and leptons have very similar properties except the mass of the particles. What is the origin of flavor and why there are only three generations of quarks and leptons?
- Large difference between electron (lightest) and top (heaviest) quarks mass is a mystery. What is the origin of the mass hierarchy of the SM elementary particles?

- The fourth fundamental force of the nature, gravity, yet not incorporated in the SM.

Therefore, we need to improve our understanding, and to address the above questions. Apart from the above fundamental problems, there are some observed phenomena which are not explained by the SM.

Matter-antimatter asymmetry: In addition to quarks and leptons, which constitute matter, there are anti-quarks and anti-leptons constituting antimatter. The world surrounding us is made up of matter showing almost no signature of for antimatters. CP violation is already observed. But, the measured CP violation (so far) is not sufficient to explain the matter-antimatter asymmetry of the universe.

Dark matter: Many experimental observations such as: gravitational lensing, galaxy rotational curves, galaxy clusters, cosmic microwave background, suggest that the 27% of the universe is composed of dark matter[1]. The SM does not explain the experimental evidences for the dark matter.

Lepton flavor universality violation: In the SM, three generations of the leptons are the exact replica of each other except the mass difference for the charged leptons. The weak gauge couplings for the different generations of the leptons are also identical. Therefore, in the SM, branching fraction of leptonic decays should be independent of the generations of the leptons suggesting the value of $R_K \left(= \frac{\mathcal{B}(B^+ \to K^+ \mu^+ \mu^-)}{\mathcal{B}(B^+ \to K^+ e^+ e^-)}\right)$ to be within 1.00 ± 0.01 [17, 18]. Recently, LHCb collaboration has reported the first evidence of lepton flavor universality (LFU) violation with $R_K = 0.846^{+0.044}_{-0.041}$ in the dilepton mass-squared region, $1.1 < q^2 < 6.0$ GeV$^2/c^4$ with a significance of 3.1 standard deviations [19], which can be a signal for new physics.

1.2 Quark model and quarkonium

The quark model was introduced by Gell-Man [20] and Zweig [21] to describe the pattern of the mass spectra of the hadrons known in the middle 1960s. Hadrons

[1]Details can be found in D. Majumdar, Dark Matter: An Introduction, CRC Press, https://doi.org/10.1201/b17323 (2014).

were supposed to be composed of fundamental fermions known as quarks with fractional charge and new quantum number, the flavor. Mesons are composed of quark-antiquark pair with spin $S = 0, 1$. Total wave function of a meson can be represented as

$$\psi = \psi_{\text{space}}\psi_{\text{flavor}}\psi_{\text{spin}}\psi_{\text{color}} \tag{1.13}$$

All the hadrons are color singlet state and the color state of a meson can be expressed as

$$\psi_{\text{color}} = \sqrt{\frac{1}{3}}(r\overline{r} + b\overline{b} + g\overline{g}) \tag{1.14}$$

Total wave function of a meson is symmetric under exchange of any arbitrary pair of quarks.

1.2.1 Quantum numbers of meson

Mesons carry baryon number, $B = 0$. In addition to the baryon number and the flavor quantum numbers, mesons are characterized by the total angular momentum $J = 0, 1, 2\ .\ .\ .$, and the parity $P = \pm 1$, specifying the symmetry of the wave function under reflection through a point in space. Neutral flavorless mesons are eigenstates of the particle-antiparticle conjugation operator and thus have a defined charge conjugation parity $C = \pm 1$. Flavored mesons have one or two of the quantum numbers strangeness s, charm c, or bottomness b different from zero. All the quantum numbers mentioned above are conserved in strong interactions. Light mesons with a given J^P can be classified in multiplets according to their isospin and the strangeness s. Fig. 1.4 shows the corresponding nonets of the lightest pseudoscalar ($J^P = 0^-$) and vector ($J^P = 1^-$) mesons, respectively.

In the $L - S$ coupling scheme, the spins of the $q_i\overline{q}_j$ (i and j indicate the flavor index) pair couple to the total intrinsic spin $S = 0, 1$. The total spin J of the system is the vector sum of the total intrinsic spin S and the relative orbital angular momentum L with quantum number $|L - S| \leq J \leq (L + S)$. The meson nonets for a given J combination are obtained by combining the $SU(3)_{\text{flavor}}$ quark triplet with the antiquark triplet, resulting the nine possible combinations, transforming like an octet and a singlet in $SU(3)_{\text{flavor}}$ space: $3 \bigotimes \overline{3} = 8 \bigoplus 1$. The flavor wave functions of

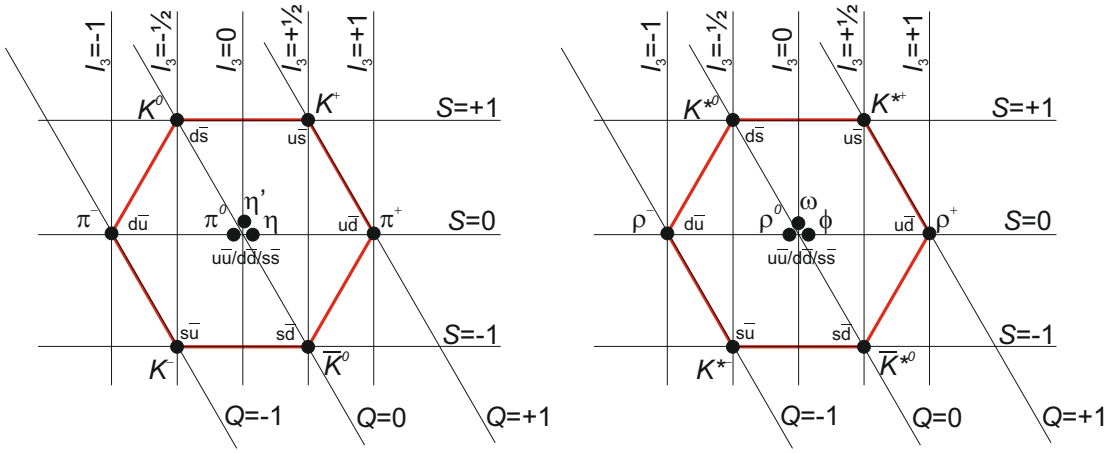

FIG. 1.4: Gruond state representation of pseudoscalar nonet (left) and vector nonet (right) [22].

the isoscalar (i.e. $I = 0$) flavor singlet and octet combinations are

$$\psi_1 = \frac{1}{\sqrt{3}}(u\bar{u} + d\bar{d} + s\bar{s}) \qquad \psi_8 = \frac{1}{\sqrt{6}}(u\bar{u} + d\bar{d} - 2s\bar{s}) \tag{1.15}$$

The flavor wave functions of the isovector (i.e. $I = 1$) triplet are

$$\left(d\bar{u}, \sqrt{\frac{1}{2}}(u\bar{u} - d\bar{d}), -u\bar{d}\right) \tag{1.16}$$

The $SU(3)_{\text{flavor}}$ singlet and octet states with $I = 0$ generally mix to produce the physical mesons A and B mesons.

$$A = \cos\theta\psi_8 - \sin\theta\psi_1 \qquad B = \sin\theta\psi_8 + \cos\theta\psi_1 \tag{1.17}$$

For pseudo-scalar (vector) ground state A and B are η (ϕ) and η' (ω), respectively with θ as the mixing angle. The mixing angle for the pseudo scalar ground state is in between -10^o and -20^o, and that for vector ground state is 36.4^o.

1.2.2 QCD and quarkonium

The quarkonium is a bound state of two heavy quarks ($q\bar{q}$ with $q = c, b$)[2]. It provides a unique environment to study the nature of quark-quark interactions. In QCD, computation of mass and decay properties of mesons belong to non-perturbative calculations. For the mesons with light quarks (u, d, s), the mass of the bound state is very high as compared to confined quark mass and those light quarks move inside the meson at highly relativistic speed. In that highly relativistic limit, one can only rely on the lattice QCD techniques. However, the speed of the charm and the bottom quarks inside their respective quarkonia is much reduced to be considered for relativistic effects ($v/c = 0.3$ for charmonium and $v/c = 0.1$ for bottomonium). The significance of relativistic effects in quarkonia can be approximated as v^2/c^2 using non-relativistic QCD (NRQCD) [23]. Quantization in NRQCD has been done based on the lattice gauge theory. To calculate the binding energy of the quarkonium states several potential models are being used. One of the popular models is the Cornell potential [24] which parametrizes the $q\bar{q}$ potential $V(r)$ as a linear combination of the Coulomb (attractive) and a repulsive potentials:

$$V(r) = -\frac{\kappa}{r} + \sigma r \tag{1.18}$$

where κ is a model parameter for the Coulomb strength and σ is the string tension which is responsible for the quark confinement. By varying the parameters in the Cornell potential, one can obtain good fits to lattice measurements of the $q\bar{q}$ static potential [25].

1.2.3 Observations of heavy quarkonium states

The quarkonium sector of particle physics was suddenly appeared in 1974 with the discovery of a narrow resonance state in e^+e^- collisions with a mass around 3.1 GeV/c^2 at the Brookhaven National Laboratory [26], and at the Stanford Linear Accelerator Center [27]. This is known as the November revolution in particle physics which led to award a Nobel Prize to Ting and Richer in 1976. The new state was identified as bound state of c-$\bar{c}$ quarks known as J/ψ. Shortly after that, in 1977, discovery of $\Upsilon(9460)$ in Fermilab [28] identified as a $b\bar{b}$ bound state put the concrete evidence of the quark model.

[2] As t decays almost instantly after getting produced, there is no signature of the topponium ($t\bar{t}$) so far.

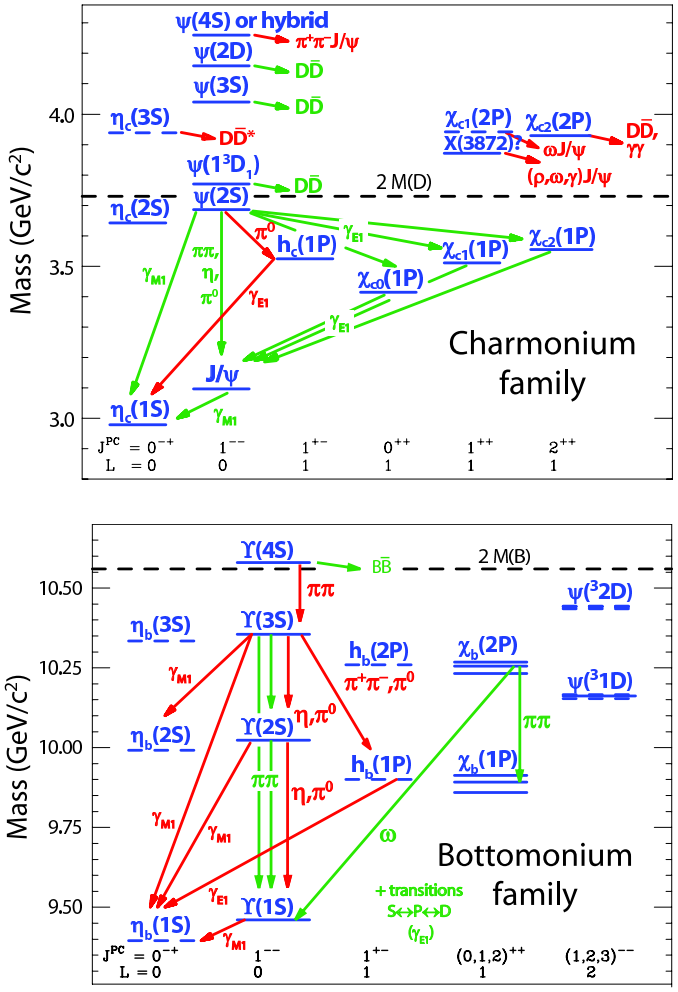

FIG. 1.5: Experimentally seen charmonium (top) and bottomonium (bottom) states with selected decay modes and transitions [29].

Four decades are passed since the discovery of J/ψ. Lot of new charmonium ($c\bar{c}$) and bottomonium ($b\bar{b}$) states have been found by different experiments. The present status of charmonium and bottomonium levels are shown in Fig. 1.5. The quarkonium states are labeled by S, P, D corresponding to relative orbital angular momentum $L = 0, 1, 2$ between quark and antiquark. No candidates for $L \geq 3$ states have been seen yet. The spin of the quark and antiquark can couple to either $S = 0$ (spin-singlet) or $S = 1$ (spin-triplet) states. The parity and charge-conjugation of a $q\bar{q}$ state is defined as $P = (-1)^{L+1}$ and $C = (-1)^{L+S}$. States are also denoted by $^{2S+1}[L]_J$, with $[L] = S, P, D$.

1.3 CLFV in bottomonium decays

The number of leptons belonging to each generation is conserved in any interaction: this rule is known as the lepton flavor number conservation. In 1998, the Super-Kamiokande experiment announced convincing evidence for neutrino oscillations [30, 31] implying that neutrinos have certain mass. This also violates the conservation of lepton flavor. On the other hand, currently LFU violation (discussed in section 1.1.5) is the most excited anomaly in the flavor physics. Although the SM gauge couplings do not discriminate between different generations of leptons, there are some new physics (NP) models such as: leptoquarks model [32], Z' model [33], which predict the enhancement of the couplings with increasing lepton mass. Also, it has been pointed out that the violation of lepton flavor universality generically implies the violation of lepton flavor [34, 35]. Thus, one can constrain the parameters for the NP models, describing LFU violation, by studying the charge lepton flavor violation (CLFV).

Moreover, flavor changing neutral current (FCNC) interactions serve as a powerful probe of physics beyond the SM. As SM operators can not generate FCNCs in the tree level diagram, NP operators dominate the SM loop corrections by producing FCNCs in the tree level diagram. In the SM, CLFV interactions, generated by massive neutrinos, are suppressed by the powers of m_ν^2/m_W^2, which makes their predictions vanishingly small, e.g. $\mathcal{B}(\mu \to e\gamma) \sim 10^{-54}$ [36, 37]. However, several new physics models such as: SUSY [38, 39], leptoquark [40], Z' [41], being inspired by grand unified theory (GUT), enhance the decay rates of the CLFV transitions. The observation of CLFV provides a clean probe for new physics. Some of the NP models predicts the CLFV τ decays such as: $\tau^\pm \to \mu^\pm\gamma$, $\tau^\pm \to \mu^+\mu^-\mu^\pm$ as the highly sensitive decay channels to search for the CLFV transitions [42, 43, 44, 45], which constrain the NP parameters for vector and dielectric operators. CLFV interaction in various bottomonium decays can provide the alternative access to study all those NP operators.

1.3.1 Theoretical description

Considering the SM as an effective theory below the scale of NP (Λ), where the heavy fields have been integrated out, one can describe the physics through an effective Lagrangian, $\mathcal{L}_{\text{eff}}$. This effective Lagrangian contains all possible terms invariant

under the SM gauge group and built with the SM fields. Besides the usual SM fields, one could introduce new light singlet fermions with renormalizable Yukawa couplings to the lepton doublets to accommodate the observed neutrino masses. Then, the effective Lagrangian at energies $E << \Lambda$ be written as [46],

$$\mathcal{L}_{\text{eff}} = \mathcal{L}^{(4)}_{\text{SM}} + \frac{1}{\Lambda}\sum_k C^{(5)}_k Q^{(5)}_k + \frac{1}{\Lambda^2}\sum_k C^{(6)}_k Q^{(6)}_k + \mathcal{O}(\frac{1}{\Lambda^3}) \tag{1.19}$$

where $\mathcal{L}^{(4)}_{\text{SM}}$ is the renormalizable SM Lagrangian containing the kinetic terms of the $U(1)$, $SU(2)$, and $SU(3)$ gauge bosons, the gauge interactions and kinetic terms of the SM fermions, Higgs, and the Yukawa couplings of the Higgs and SM fermions. The Wilson coefficients $C^{(n)}_k$ are dimensionless constants which encode NP effects due to the UV dynamics. The different higher order Lagrangians of dimension n are invariant under $SU(3) \bigotimes SU(2) \bigotimes U(1)$ group.

We are mainly interested in dimension 5 and 6 operators because many of these operators are lepton flavor violating. Thus, CLFV transitions at low energy can be expressed in terms of the SM particles such as leptons and quarks considering no new light particles exist in the low energy scale. As we are interested in the CLFV decays of bottomonium, the effective Lagrangian of new physics can be written in the form of a dipole part ($\mathcal{L}_D$), a part that involves four fermionic interaction ($\mathcal{L}_{\ell q}$) and the gluonic part ($\mathcal{L}_G$) [47]. i.e.

$$\mathcal{L}_{\text{eff}} = \mathcal{L}_D + \mathcal{L}_{\ell q} + \mathcal{L}_G + ... \tag{1.20}$$

The dipole part $\mathcal{L}_D$ which involves dimension-five dipole operators can be written as,

$$\mathcal{L}_D = -\frac{m_2}{\Lambda^2}\left[\left(C^{\ell_1\ell_2}_{DR}\ \bar{\ell}_1\sigma^{\mu\nu}P_L\ell_2 + C^{\ell_1\ell_2}_{DL}\ \bar{\ell}_1\sigma^{\mu\nu}P_R\ell_2\right)F_{\mu\nu} + h.c.\right], \tag{1.21}$$

where $P_{\text{R,L}} = (1 \pm \gamma_5)/2$ is the right (left) chiral projection operator. The Wilson coefficients would, in general, be different for different leptons ℓ_i.

The four-fermion dimension-six lepton-quark Lagrangian takes the form:

$$\begin{aligned}\mathcal{L}_{\ell q} = -\frac{1}{\Lambda^2}\sum_q \Big[&\left(C_{VR}^{q\ell_1\ell_2}\ \bar{\ell}_1\gamma^\mu P_R\ell_2 + C_{VL}^{q\ell_1\ell_2}\ \bar{\ell}_1\gamma^\mu P_L\ell_2\right)\ \bar{q}\gamma_\mu q \\ &+ \left(C_{AR}^{q\ell_1\ell_2}\ \bar{\ell}_1\gamma^\mu P_R\ell_2 + C_{AL}^{q\ell_1\ell_2}\ \bar{\ell}_1\gamma^\mu P_L\ell_2\right)\ \bar{q}\gamma_\mu\gamma_5 q \\ &+ m_2 m_q G_F\left(C_{SR}^{q\ell_1\ell_2}\ \bar{\ell}_1 P_L\ell_2 + C_{SL}^{q\ell_1\ell_2}\ \bar{\ell}_1 P_R\ell_2\right)\ \bar{q}q \\ &+ m_2 m_q G_F\left(C_{PR}^{q\ell_1\ell_2}\ \bar{\ell}_1 P_L\ell_2 + C_{PL}^{q\ell_1\ell_2}\ \bar{\ell}_1 P_R\ell_2\right)\ \bar{q}\gamma_5 q \\ &+ m_2 m_q G_F\left(C_{TR}^{q\ell_1\ell_2}\ \bar{\ell}_1\sigma^{\mu\nu} P_L\ell_2 + C_{TL}^{q\ell_1\ell_2}\ \bar{\ell}_1\sigma^{\mu\nu} P_R\ell_2\right)\ \bar{q}\sigma_{\mu\nu}q + h.c.\ \Big].\end{aligned} \tag{1.22}$$

The dimension 7 gluonic operators can be either generated by some high scale physics or by integrating out heavy quark degrees of freedom [47],

$$\begin{aligned}\mathcal{L}_G = -\frac{m_2 G_F}{\Lambda^2}\frac{\beta_L}{4\alpha_s}\Big[&\left(C_{GR}^{\ell_1\ell_2}\ \bar{\ell}_1 P_L\ell_2 + C_{GL}^{\ell_1\ell_2}\ \bar{\ell}_1 P_R\ell_2\right)G^a_{\mu\nu}G^{a\mu\nu} \\ &+ \left(C_{\tilde{G}R}^{\ell_1\ell_2}\ \bar{\ell}_1 P_L\ell_2 + C_{\tilde{G}L}^{\ell_1\ell_2}\ \bar{\ell}_1 P_R\ell_2\right)G^a_{\mu\nu}\widetilde{G}^{a\mu\nu} + h.c.\Big].\end{aligned} \tag{1.23}$$

Here $\beta_L = -9\alpha_s^2/(2\pi)$ is defined for the number of light active flavors, L. All Wilson coefficients should also be calculated at the same scale. G_F is the Fermi constant and $\widetilde{G}^{a\mu\nu} = (1/2)\epsilon^{\mu\nu\alpha\beta}G^a_{\alpha\beta}$ is a dual to the gluon field strength tensor. The Wilson coefficients of effective Lagrangian of the NP model can be determined by matching with the phenomena which involve charge lepton flavor violating interactions.

CLFV in vector meson decays

CLFV vector meson decays ($V \to \ell_1\ell_2$) can be used effectively to put experimental bounds on Wilson coefficients of vector and tensor operators in Eq. (1.22), as well as on those of the dipole operators of Eq. (1.21). The branching fraction of $V \to \ell_1\ell_2$ transition can be expressed in terms of the ratio of branching fraction of $V \to e^+e^-$ decay using the following relation,

$$\begin{aligned}\frac{\mathcal{B}(V \to \ell_1\bar{\ell}_2)}{\mathcal{B}(V \to e^+e^-)} = \left(\frac{m_V\,(1-y^2)}{4\pi\alpha f_V Q_q}\right)^2 \Big[&\left(\left|A_V^{\ell_1\ell_2}\right|^2 + \left|B_V^{\ell_1\ell_2}\right|^2\right) + \frac{1}{2}\left(1-2y^2\right)\left(\left|C_V^{\ell_1\ell_2}\right|^2 + \left|D_V^{\ell_1\ell_2}\right|^2\right) \\ &+ y\ \mathrm{Re}\left(A_V^{\ell_1\ell_2}C_V^{\ell_1\ell_2 *} + iB_V^{\ell_1\ell_2}D_V^{\ell_1\ell_2 *}\right)\Big].\end{aligned} \tag{1.24}$$

Here α is the fine structure constant. The mass of the lighter of the two leptons is neglected, y is approximated to be $y = m_2/m_V$. The form of the coefficients $A_V^{\ell_1\ell_2}$ to

$D_V^{\ell_1\ell_2}$ depends on the initial state meson. For example, for $V = \Upsilon(nS)$ ($b\bar{b}$ states), $\psi(nS)$ ($c\bar{c}$ states), or ϕ ($s\bar{s}$ state), the coefficients are:

$$\begin{aligned}
A_V^{\ell_1\ell_2} &= \frac{f_V m_V}{\Lambda^2}\Big[\ \sqrt{4\pi\alpha}Q_q y^2\left(C_{DL}^{\ell_1\ell_2}+C_{DR}^{\ell_1\ell_2}\right)+\kappa_V\left(C_{VL}^{q\ell_1\ell_2}+C_{VR}^{q\ell_1\ell_2}\right)\\
&\qquad +2y^2\kappa_V\frac{f_V^T}{f_V}G_F m_V m_q\left(C_{TL}^{q\ell_1\ell_2}+C_{TR}^{q\ell_1\ell_2}\right)\Big],\\
B_V^{\ell_1\ell_2} &= \frac{f_V m_V}{\Lambda^2}\Big[-\sqrt{4\pi\alpha}Q_q y^2\left(C_{DL}^{\ell_1\ell_2}-C_{DR}^{\ell_1\ell_2}\right)-\kappa_V\left(C_{VL}^{q\ell_1\ell_2}-C_{VR}^{q\ell_1\ell_2}\right)\\
&\qquad -2y^2\kappa_V\frac{f_V^T}{f_V}G_F m_V m_q\left(C_{TL}^{q\ell_1\ell_2}-C_{TR}^{q\ell_1\ell_2}\right)\Big],\\
C_V^{\ell_1\ell_2} &= \frac{f_V m_V}{\Lambda^2}y\left[\sqrt{4\pi\alpha}Q_q\left(C_{DL}^{\ell_1\ell_2}+C_{DR}^{\ell_1\ell_2}\right)+2\kappa_V\frac{f_V^T}{f_V}G_F m_V m_q\left(C_{TL}^{q\ell_1\ell_2}+C_{TR}^{q\ell_1\ell_2}\right)\right],\\
D_V^{\ell_1\ell_2} &= i\frac{f_V m_V}{\Lambda^2}y\left[-\sqrt{4\pi\alpha}Q_q\left(C_{DL}^{\ell_1\ell_2}-C_{DR}^{\ell_1\ell_2}\right)-2\kappa_V\frac{f_V^T}{f_V}G_F m_V m_q\left(C_{TL}^{q\ell_1\ell_2}-C_{TR}^{q\ell_1\ell_2}\right)\right].
\end{aligned} \tag{1.25}$$

Here $Q_q = (2/3, -1/3)$ is the charge of the quark q and $\kappa_V = 1/2$ is a constant for pure $q\bar{q}$ states. It is a good approximation to drop terms proportional to y^2 in Eq. (1.25) for the heavy quarkonium states.

Substituting the values of $A_V^{\ell_1\ell_2}$, $B_V^{\ell_1\ell_2}$, $C_V^{\ell_1\ell_2}$, and $D_V^{\ell_1\ell_2}$ in Eq. (1.24) and considering the single operator dominance, one can obtain the following relations.

$$\begin{aligned}
\left|\frac{C_{VL}^{q\ell_1\ell_2}}{\Lambda^2}\right| &= \left|\frac{C_{VR}^{q\ell_1\ell_2}}{\Lambda^2}\right| = \frac{4\pi\alpha Q_q}{m_V^2}\sqrt{\frac{\mathcal{B}(V\to\ell_1\ell_2)}{\mathcal{B}(V\to e^+e^-)}}\\
\left|\frac{C_{DL}^{q\ell_1\ell_2}}{\Lambda^2}\right| &= \left|\frac{C_{DR}^{q\ell_1\ell_2}}{\Lambda^2}\right| = \frac{\sqrt{2\pi\alpha}}{m_V m_{\ell_2}}\sqrt{\frac{\mathcal{B}(V\to\ell_1\ell_2)}{\mathcal{B}(V\to e^+e^-)}}\\
\left|\frac{C_{TL}^{q\ell_1\ell_2}}{\Lambda^2}\right| &= \left|\frac{C_{TR}^{q\ell_1\ell_2}}{\Lambda^2}\right| = \frac{\sqrt{2}\pi\alpha Q_q}{G_F\kappa_V m_V^2 m_q m_{\ell_2}}\sqrt{\frac{\mathcal{B}(V\to\ell_1\ell_2)}{\mathcal{B}(V\to e^+e^-)}}
\end{aligned} \tag{1.26}$$

Using the above equations, one can put constrains on the Wilson coefficients of NP operators. Inspecting the ratio in Eq. (1.26), one immediately infers that the best constraints could be placed on the four-fermion coefficients, $C_{VL}^{q\ell_1\ell_2}$ and $C_{VR}^{q\ell_1\ell_2}$, as no final state lepton mass suppression exists for those coefficients. Yet, constraints on the dipole coefficients, $C_{DL}^{\ell_1\ell_2}(C_{DR}^{\ell_1\ell_2})$, are also possible in this case. This would provide NP constraints that are complementary to the ones obtained in the radiative $\tau \to \mu(e)\gamma$ decays.

Also, radiative lepton flavor violation (RLFV), the CLFV decays with a photon in

the final state, allow the operators which are inaccessible in the two body decays. Considering axial vector operator dominance, the partial decay width of RLFV transition can be represented as,

$$\Gamma(V \to \gamma \ell_1 \ell_2) = \frac{1}{18} \frac{\alpha Q_q^2}{(4\pi)^2} \frac{f_V^2 m_V^3}{\Lambda^4} (C_{AL}^{q\ell_1\ell_2{}^2} + C_{AR}^{q\ell_1\ell_2{}^2}) f(y^2) \tag{1.27}$$

where, $f(y^2) = 1 - 6y^2 - 12y^4 \log(y) + 3y^4 + 2y^6$. Wilson coefficients for axial vector can be written as,

$$\left| \frac{C_{AL}^{q\ell_1\ell_2}}{\Lambda^2} \right| = \left| \frac{C_{AR}^{q\ell_1\ell_2}}{\Lambda^2} \right| = \frac{12\pi}{Q_q f_V} \sqrt{\frac{\Gamma_V \mathcal{B}(V \to \gamma \ell_1 \ell_2)}{\alpha m_V^3}} \tag{1.28}$$

where, Γ_V in the total decay rate of the meson.

where, Q_q, m_V, α, y and Λ are the quark charge, mass of the vector meson, fine structure constant, ratio of mass of higher mass lepton to the mass of the meson and NP mass scale respectively. Using RLFV results in the Eq. (1.28), one can put a constrain on the Wilson coefficiencts of the vector operator ($C_{VL}^{q\ell_1\ell_2}$, $C_{VR}^{q\ell_1\ell_2}$). Thus RLFV could provide important complementary access to the NP parameters.

CLFV in scalar meson decays

Scalar quarkonium decays would allow one to probe the Wilson coefficients of the scalar operators. Branching fraction for scalar quarkonium decays can be written as,

$$\mathcal{B}(S \to \ell_1 \bar{\ell}_2) = \frac{m_S}{8\pi\Gamma_S} \left(1 - y^2\right)^2 \left[\left| E_S^{\ell_1\ell_2} \right|^2 + \left| F_S^{\ell_1\ell_2} \right|^2 \right]. \tag{1.29}$$

Here Γ_S is the total width of the scalar state and $y = m_2/m_S$. The coefficients $E_S^{\ell_1\ell_2}$ and $F_S^{\ell_1\ell_2}$ are

$$\begin{aligned} E_S^{\ell_1\ell_2} &= y \frac{m_S G_F}{4\Lambda^2} \left[2 i f_S m_S m_q \left(C_{SL}^{ql_1l_2} + C_{SR}^{ql_1l_2} \right) + 9 a_S \left(C_{GL}^{ql_1l_2} + C_{GR}^{ql_1l_2} \right) \right], \\ F_S^{\ell_1\ell_2} &= y \frac{m_S G_F}{4\Lambda^2} \left[2 f_S m_S m_q \left(C_{SL}^{ql_1l_2} - C_{SR}^{ql_1l_2} \right) - 9 i a_S \left(C_{GL}^{ql_1l_2} - C_{GR}^{ql_1l_2} \right) \right]. \end{aligned} \tag{1.30}$$

where, E_S and F_S are the dimensionless constants which depend on the Wilson coefficients of the NP operators [47]. Considering left right symmetry of the Wilson

coefficients, the above relation for heavy scalar quarkonium decays leads to,

$$\left|\frac{C_{SL}^{q\ell_1\ell_2}}{\Lambda^2}\right| = \left|\frac{C_{SR}^{q\ell_1\ell_2}}{\Lambda^2}\right| = \frac{1}{G_F f_S m_q m_{\ell_2}}\sqrt{\frac{8\pi\Gamma_S \mathcal{B}(S \to \ell_1\ell_2)}{m_S^3}} \tag{1.31}$$

where, G_F, f_S, m_q, Γ_S, and m_S are the Fermi constant, scalar meson decay constant, mass of quark, total decay width of the scalar meson, and mass of the meson, respectively.

1.3.2 Experimental status

CLEO and BaBar collaborations have already published some results on the search for CLFV in $\Upsilon(nS)[n = 1, 2, 3]$ decays [48, 49]. They are summarized in Table 1.1. For $\Upsilon(1S)$, only $\Upsilon(1S) \to \mu^\pm\tau^\mp$ has been studied so far, and not $\Upsilon(1S) \to e^\pm\mu^\mp$ and

Search for the decay	Experiment	Upper bound
$\Upsilon(1S) \to \mu\tau$	CLEO [48]	$< 6.0 \times 10^{-6}$ (95%)
$\Upsilon(2S) \to \mu\tau$	CLEO [48]	$< 14.4 \times 10^{-6}$ (95%)
$\Upsilon(2S) \to e\tau$	BaBar[49]	$< 3.2 \times 10^{-6}$ (90%)
$\Upsilon(2S) \to \mu\tau$	BaBar[49]	$< 3.3 \times 10^{-6}$ (90%)
$\Upsilon(3S) \to \mu\tau$	CLEO[48]	$< 26.3 \times 10^{-6}$ (95%)
$\Upsilon(3S) \to e\tau$	BaBar[49]	$< 4.2 \times 10^{-6}$ (90%)
$\Upsilon(3S) \to \mu\tau$	BaBar[49]	$< 3.1 \times 10^{-6}$ (90%)

TAB. 1.1: Available results on CLFV transition in $\Upsilon(nS)$ decays.

$\Upsilon(1S) \to e^\pm\tau^\mp$ transitions. Those searches have been done using the $\Upsilon(1S)$ sates directly produced in collider at $\Upsilon(1S)$ energy where the final state with electrons are more difficult (as QED Bhabha events are dominating). We have 6 fb^{-1} $\Upsilon(1S)$ data which corresponds to 119 million of $\Upsilon(1S)$ decays. In that case, we have only two charged particles in the final state. We do not have much control on the background for those kind of low multiplicity decays. Belle also has the largest $\Upsilon(2S)$ data corresponding to 158 million $\Upsilon(2S)$ decays and the resulting number of $\Upsilon(1S)$ produced in $\Upsilon(2S) \to \pi^+\pi^-\Upsilon(1S)$ decays is around 28 million. Four particles final state in $\Upsilon(2S) \to \pi^+\pi^-\Upsilon(1S)[\to \ell_1\bar{\ell_2}]$ provides a better control over background with efficient triggering. Therefore, we search for the $\Upsilon(1S) \to \ell^\pm\ell'^\mp[\ell, \ell' = e, \mu, \tau]$ decays using $\Upsilon(1S)$ with di-pion tagging. On the other hand, there are no results available on RLFV decays. In this thesis, we report the first ever result on the RLFV $\Upsilon(1S) \to \gamma\ell^\pm\ell'^\mp$ decays.

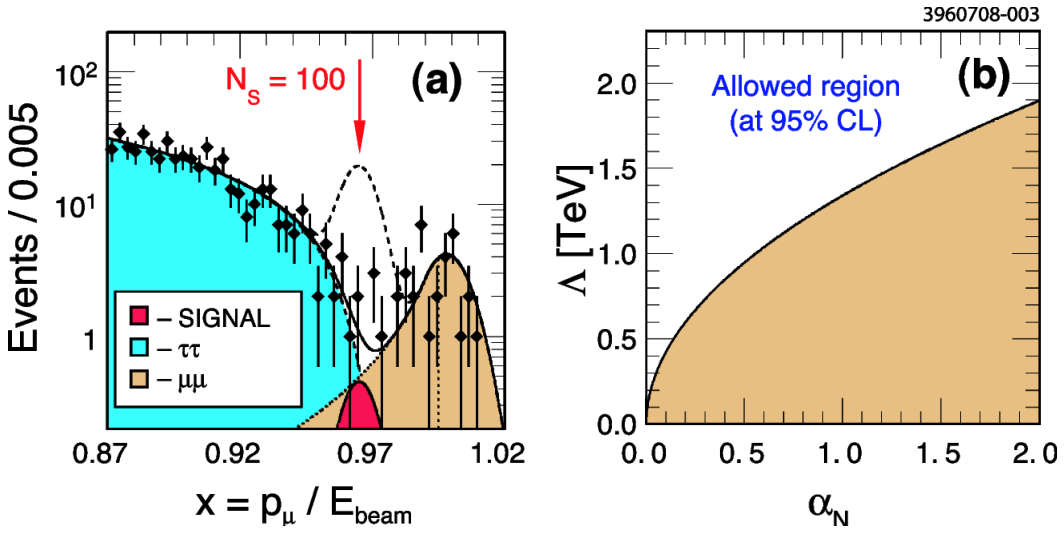

FIG. 1.6: Distributions for fitted signal events (left) and constraining new physics parameters (right) from the CLEO collaboration [48].

Couple of studies has already been done on vector quarkonia decays such as: $\Upsilon(nS) \to \ell\ell'$ and $J/\psi \to \ell\ell'$ [50, 51] decays. But, no experimental studies have been performed on scalar quarkonium decays. Corresponding p-wave states of $\chi_{b0}(1P)$ and χ_{c0}, those have been efficiently produced in gluon-gluon fusion at the LHC and in radiative transition of $\Upsilon(2,3S)$ decays, can be used to search for CLFV scalar quarkonium decays. Using $\Upsilon(2S)$ data, the rich source of corresponding $\chi_{b0}(1P)$, we search for CLFV in $\chi_{b0}(1P) \to \ell^\pm\ell'^\mp$ decays where, $\ell, \ell' = e, \mu, \tau$ leptons. Along with that, we also search for $\chi_{b1}(1P) \to \ell^\pm\ell'^\mp$ and $\chi_{b2}(1P) \to \ell^\pm\ell'^\mp$ decays which will provide the result for CLFV in axial vector and tensor meson decays, respectively.

1.4 Study of exotic charmonium states

The quark model describes mesons as the bound states of quarks and antiquarks ($q\bar{q}$). Quarkonium states are identified with well defined quantum numbers J^{PC} (as defined in section 1.2). The allowed J^{PC} quantum numbers are listed in Table 1.2.

There are several missing J^{PC} combinations: 0^{--}, 0^{+-}, 1^{-+}, and 2^{+-}. These are not allowed for convenient $q\bar{q}$ systems and are known as "exotic" quarkonium states. Also more exotic combinations such as tetraquarks ($qq\bar{q}\bar{q}$) and pentaquarks ($qqqq\bar{q}$) are allowed.

L	S	J^{PC}
0	0	0^{-+}
	1	1^{--}
1	0	1^{+-}
	1	0^{++}, 1^{++}, 2^{++}
2	0	2^{-+}
	1	1^{--}, 2^{--}, 3^{--}

TAB. 1.2: Allowed J^{PC} quantum numbers for $q\overline{q}$ mesons.

Last two decade have been very exciting for the quarkonium sector. Many new states have been found which find no place in the conventional spectroscopy and are strong contenders of the exotic quarkonium states (like tetra-quark, molecular, hybrid). $X(3872)$ has remained the poster boy of these exotic states, from the time it was first observed by the Belle Collaboration in 2003 [52]. $X(3872)$ has also been seen to decay in other final states: $X(3872) \to D^0\bar{D}^{*0}$, $X(3872) \to J/\psi\gamma$, $X(3872) \to \psi'\gamma$, $X(3872) \to J/\psi\pi^+\pi^-\pi^0$, and $X(3872) \to \pi^0\chi_{c1}(1P)$ [53, 54, 55, 56, 57, 58]. One of the salient features of $X(3872)$ is that the mass coincides exactly with the $\overline{D}^{*0}D^0$ (or $\overline{D}^0D^{*0}$) threshold: $m_{D^0} + m_{D^{*0}} - m_{X(3872)} = (0.00 \pm 0.18)$ MeV, which naturally pushes the molecular interpretations. Negative C-odd partner search of $X(3872)$ ($X(3872) \to J/\psi\eta$ [59], $X(3872) \to \chi_{c1}\gamma$, $X(3872) \to \eta_c\omega$, $X(3872) \to \eta_c\pi\pi$ [60]) and charged partner search in $X(3872)^+ \to J/\psi\pi^+\pi^0$ [61] suggest that $X(3872)$ is an iso-singlet state. In that scenario, its decay into its discovery mode $X(3872) \to J/\psi\pi^+\pi^-$ is expected to be isospin violating. Further, one expect the decay $X(3872) \to J/\psi\pi^+\pi^-\pi^0$ to be an isospin allowed and should have larger branching fraction, something like $R_{3\pi/2\pi} \equiv \mathcal{B}(X(3872) \to J/\psi\pi^+\pi^-\pi^0)/\mathcal{B}(X(3872) \to J/\psi\pi^+\pi^-) \sim 30$ [62]. Isospin violating decays of $X(3872)$ are sensitive to the inner structures and have been investigated in different scenarios. Couple of studies also suggest that the isospin violation comes from the molecular structure of the $X(3872)$ [63].

However, the previous measurement by the Belle with 256 fb^{-1} data suggest $R_{3\pi/2\pi}$ to be 1.0 ± 0.4 (stat) ± 0.3 (syst) [64]. Measurement by the BaBar Collaboration using their full data set (426 fb^{-1}) gave this number as 0.7 ± 0.3 (1.7 ± 1.3) for B^+ (B^0) events [65]. Recently, BESIII has presented their results on $R_{3\pi/2\pi}$ to be $1.6^{+0.4}_{-0.3}$ (stat)$\pm$0.2 (syst), which is on higher side [66]. All the results bring the picture of large isospin violation, which is not truly understood so far. Belle accumulated 711 fb^{-1} data, almost twice of BaBar. More precise measurement with the full Belle data set will help to understand the nature of $X(3872)$.

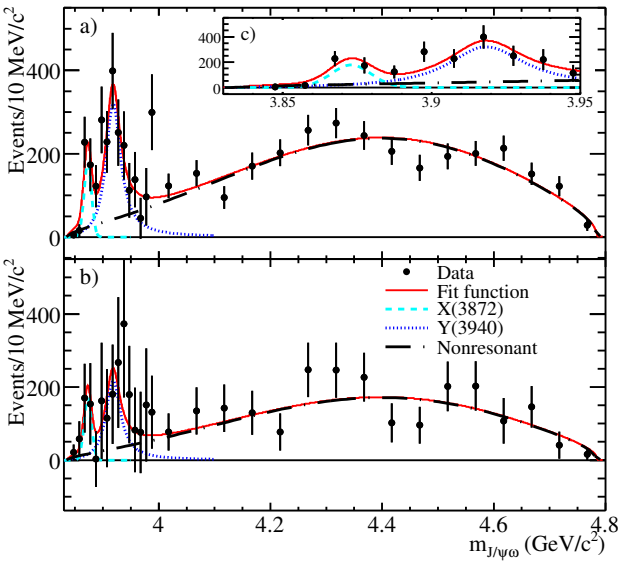

FIG. 1.7: $M_{J/\psi\omega}$ fitted distribution for charged (top) and neutral (bottom) B meson modes by the BaBar collaboration [65].

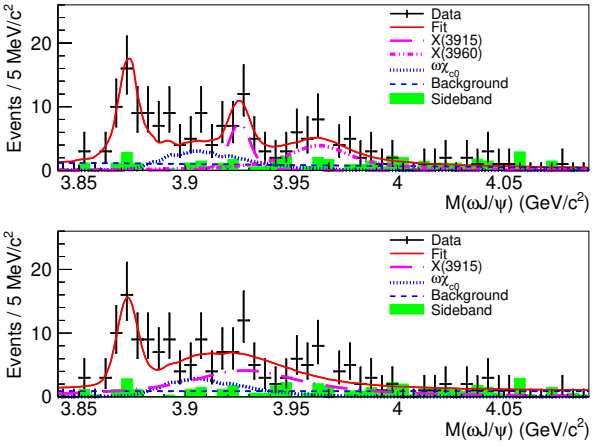

FIG. 1.8: $M_{J/\psi\omega}$ fitted distribution for charged (top) and neutral (bottom) B meson modes by the BESIII collaboration [66].

Also, the $X(3915)$ is the another interesting exotic charmonium state. Measurements suggest the quantum numbers for $X(3915)$ can be either 0^{++} or 2^{++}. BaBar measured the branching fraction of $X(3915) \to J/\psi\omega$ decay to be ~ 20 times of the branching fraction for $X(3872) \to J/\psi\omega$. As seen in charmonium, decays of B mesons to states having $J = 0$ and $J = 2$ are suppressed as compared to $J = 1$ states. In that scenario, measured branching fraction for $X(3915)$ seems to be overestimated and need to be studied more. BESIII reported the branching fraction of $X(3915) \to J/\psi\omega$ to be suppressed as compared to $X(3872) \to J/\psi\omega$ decays.

There is some disagreement between these two results. In that scenario, it is also important to update the branching fraction of $X(3915) \to J/\psi\omega$ using the high statistic data sample collected by the Belle detector.

Chapter 2

The Belle Experiment

The data used in the analyses have been collected at KEKB asymmetric e^+e^- collider using the Belle detector. The primary purpose of the Belle experiment was to precisely measure the CP-violation in B meson decays which have already been successful. The Belle experiment stopped its operation in June 2010. Now KEKB has been upgraded to SuperKEKB [67] to provide data with higher luminosity, and Belle detector has been upgraded to make the measurements more precise. As a whole, the Belle experiment has been upgraded to the Belle II experiment [68].

2.1 The KEKB accelerator

The KEKB is an asymmetric energy e^+e^- collider located at KEK (Kō Enerugi Kasokuki Kenkyū Kikō) laboratory in Tsukuba, Japan. The center-of-mass (CM) energy $\sqrt{s}$ is $\simeq$ 10.6 GeV. The detailed description of the accelerator can be found in Ref. [69]. The accelerator is composed of two side-by-side rings in which the beam is sent through a linear accelerator (LINAC). The rings are installed in a 3 km long tunnel buried 10 m below the surface. In the first stage of the linac, electrons are accelerated to an energy of 4 GeV. Positrons are then produced by hitting a thin tungsten monocrystal target with some of these electrons radiating photons. These photons create electron-positron pairs, and the positrons are collected and accelerated to 3.5 GeV. The electron beam is then accelerated further, and both beams are directly injected into the corresponding rings: the high-energy ring (HER) contains electrons at 8.0 GeV energy, and the low-energy ring (LER) contains positrons at 3.5 GeV. Fig. 2.1 shows the schematic diagram of the KEKB accelerator.

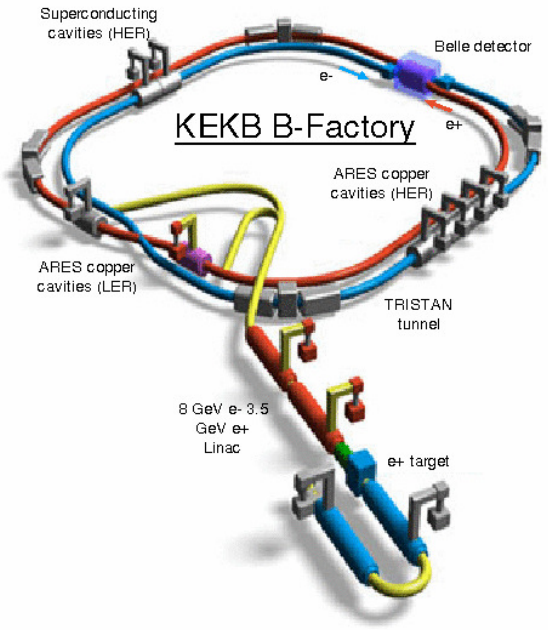

FIG. 2.1: Schematic diagram of the KEKB accelerator.

These beams are made to collide at the interaction point (IP) where the beams intersect at an angle of 22 mrad. This finite crossing-angle provides effective beam separation at the collision point, without high level of background. This also means that the electron and positron bunches do not collide head-on as would happen at zero crossing angle. This raises the effective beam cross-sectional area and causes a reduction in the specific luminosity of the collisions. To compensate for this, specialised RF cavities Crab Cavities' are installed on the beam-line in January 2007. Crab cavities give each bunch a kick to effectively rotate it to face the colliding bunch directly. The design luminosity of KEKB machine is 1×10^{34} cm^{-2}s^{-1} which corresponds to 10^8 B mesons per year. The KEKB accelerator has delivered an integrated luminosity of 1040.86 fb^{-1} data and Belle has acquired data of $\sim$ 1014 fb^{-1}. The recorded luminosities for different resonances and corresponding beam energies are summarized in Table 2.1.

2.2 The Belle Detector

The Belle detector is designed and constructed to carry out quantitative study of B mesons which are very short lived ($\sim$ 10^{-12} s) particles. The Belle detector

Resonance	Energy (GeV)			Luminosity (fb^{-1})
	HER	LER	$\sqrt{s}$	
$\Upsilon(1S)$	7.1511	3.1286	9.4603	6
$\Upsilon(2S)$	7.5750	3.3141	10.023	24
$\Upsilon(3S)$	7.8262	3.4240	10.355	3
$\Upsilon(4S)$	7.9988	3.4995	10.579	711
$\Upsilon(5S)$	8.2150	3.5941	10.860	121

TAB. 2.1: Accumulated data set at Belle at different beam energies.

actually detects these particles, namely $e^{\pm}$, $\mu^{\pm}$, $\pi^{\pm}$, $K^{\pm}$, p, $\bar{p}$, n, γ, and K^0. The Belle detector is a large assymmetric magnetic spectormeter having a large solid-angle acceptance. It consist of concentric layers of sub-detectors designed to provide momentum and position information via magnetic spectroscopy, energy measurements via electromagnetic calorimetery, and particle identification discrimination through energy loss, time-of-flight, Cherenkov radiation, and penetration depth data. Fig. 2.2 shows the animated diagram of the detector showing all sub-detectors, the solenoid which provides a 1.5 T magnetic field, and the electron and positron beam-lines.

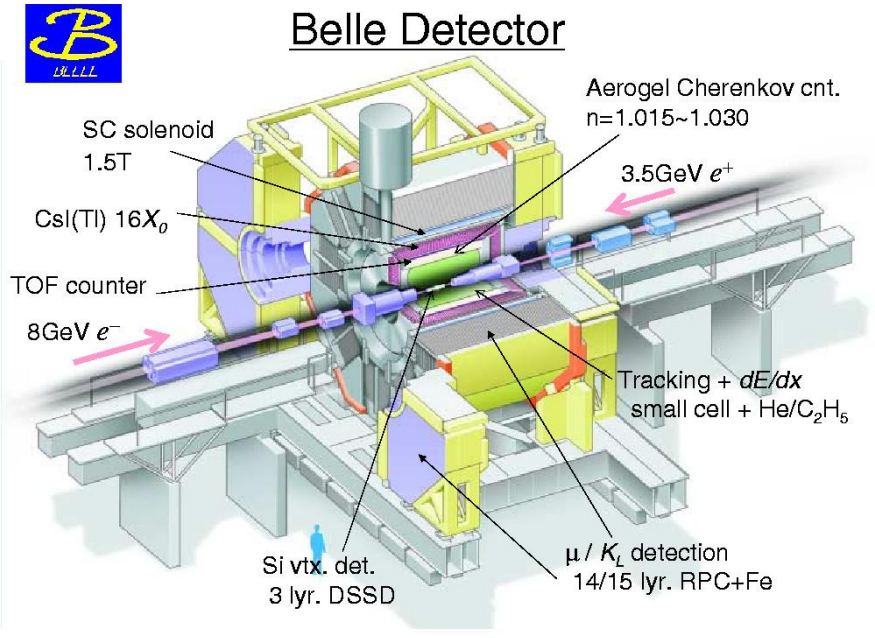

FIG. 2.2: Schematic diagram of the Belle detector.

2.2.1 Beam pipe

The beam pipe is the inner-most piece of the detector, and all the particles transverse through it before reaching the SVD. The material in the pipe must be kept to a minimum to avoid Coulomb scattering, which affects the resolution of the SVD. The thickness of the beam pipe should be such that it is capable of resisting the beam-induced heating up to several hundred watts. For this purpose double-walled beryllium cylinder is used. The two 0.5 mm thick walls are separated by a 2.5 mm gap through which helium gas is circulated as a coolant. The beryllium is covered in a 20 μm thick layer of gold foil, which absorbs X-rays from synchrotron radiation. Fig. 2.3 shows the cross-section of beam pipe at interaction point.

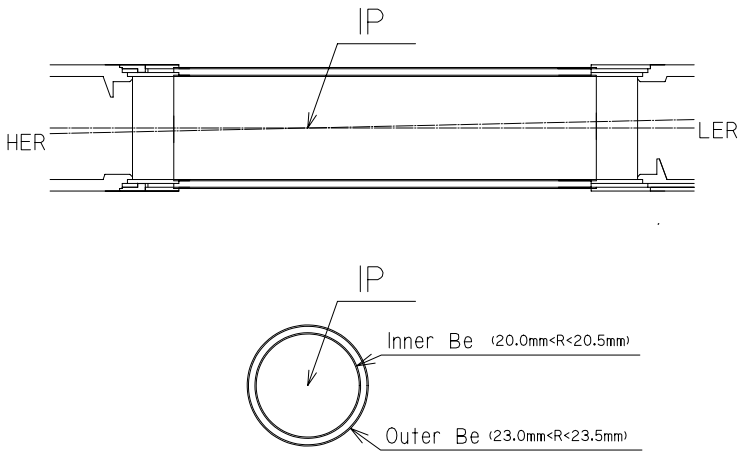

FIG. 2.3: Cross section and side-view of the Belle beam-pipe.

2.2.2 Silicon Vertex Detector (SVD)

SVD provides precise measurement of the decay vertices, which is essential to study a time-dependent CP asymmetry. The required Δz resolution is $\lesssim 200$ μm since the averaged separation of two B meson vertices is ~ 200 μm. It also helps to improve the momentum resolution of the particle. As most particles of interest in Belle have momenta less than 1 GeV/c, the vertex resolution is dominated by the multiple Coulomb scattering. It imposes strict constraints on the design of the detector. Since the vertex resolution drops with the distance of the first detection layer, the vertex detector has to be placed as close as possible to the beam pipe wall. SVD

underwent a significant modification in the middle of the data-taking period, which divides the SVD into two phases, commonly denoted as SVD I and SVD II.

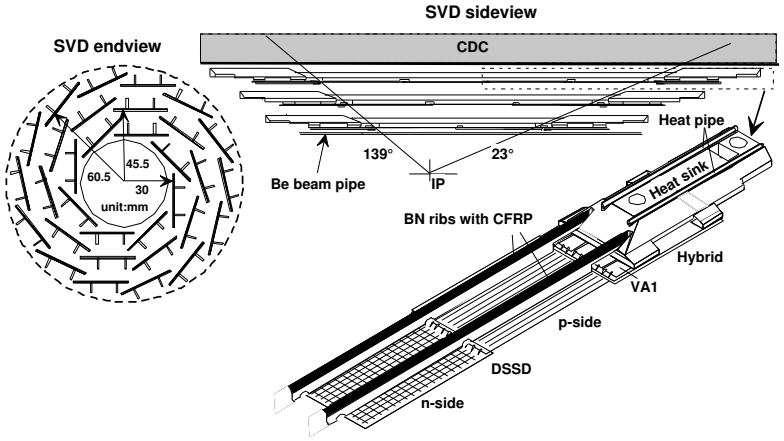

FIG. 2.4: Configuration of SVD I.

Fig. 2.4 shows the configuration of SVD I. The SVD I consists of three concentric cylindrical layers arranged in a barrel and covers a solid angle range $23^o < \theta < 139^o$. The three layers at radii of 30.0 mm, 45.5 mm, and 60.5 mm surround the beam pipe. Three layers are constructed from eight, ten, and fourteen independent ladders from inner to outer, respectively. Each ladder consists of double-sided silicon strip detectors (DSSDs) reinforced by boron-nitride support ribs. The DSSDs are reverse-biased dipole strip detectors. For the z-coordinate measurement, the n-side strips are used, and a double-metal structure running parallel to z is employed to route the signals from orthogonal z-sense strips to the ends of the detector.

The track-matching efficiency is the probability that a CDC track within the SVD acceptance associates SVD hits in at least two layers and at least one layer with both the $r-\phi$ and $r-z$ information. Tracks from K^0_S decays are excluded since these tracks do not necessarily go through the SVD. The averaged matching efficiency is better than 98.7%, although slight degradation is observed after one year of operation as a result of radiation damage [70]. The impact parameter resolution for a reconstructed track is measured as a function of the track momentum p (measured in GeV/c) and the polar angle θ to be

$$\sigma_{r\phi} = 19 \oplus \frac{50}{p\beta \sin^{3/2}\theta}\mu\text{m} \qquad \sigma_z = 36 \oplus \frac{42}{p\beta \sin^{5/2}\theta}\mu\text{m} \tag{2.1}$$

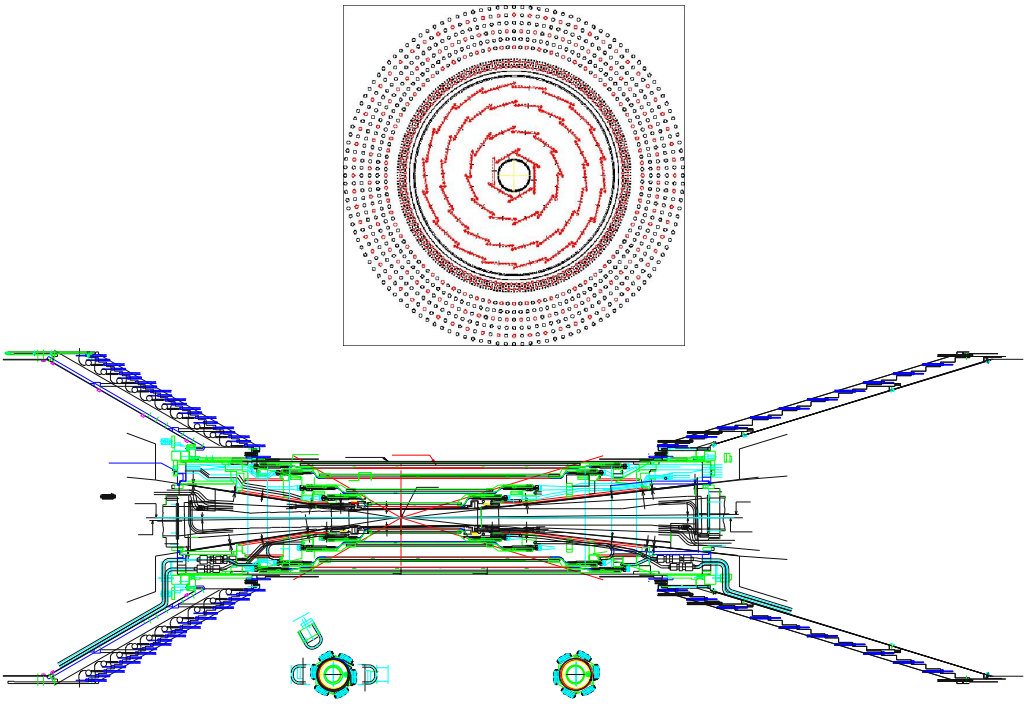

FIG. 2.5: Schematic diagram of SVDII with end-view (top) and side-view (bottom).

New SVD (SVD II) [71] was installed in the summer of 2003. There are many improvements from SVD I. The geometrical configuration of SVD II is shown in Fig. 2.5. The SVD II consists of four cylindrical layers whose radii are 20.0 mm, 43.5 mm, 70.0 mm, and 88.0 mm. The angular acceptance was from 17^o to 150^o, the same as Central Drift Chamber acceptance. The four layers include 6, 12, 18, and 18 ladders to cover all the ϕ region, and each ladder consists of 2, 3, 5, and 6 DSSDs, respectively. The n-side DSSDs are used for the measurement of the $r-\phi$ coordinate. As in SVD I, each ladder is read out by four hybrids. Each hybrid employs four VA1TA (VA1 with trigger functions) chips; each VA1TA chip amplifies the signals from 128 strips, whose pulse heights are held and sent out serially. To minimize the readout deadtime, the four chips on each hybrid are read in parallel, in contrast to SVD I where the chips were read sequentially. It represents a significant reduction in the overall deadtime of the Belle DAQ system.

2.2.3 Central Drift Chamber (CDC)

The primary role of the CDC is the determination of three-dimensional trajectories of charged particles and the precise measurement of their momenta. The 1.5 T

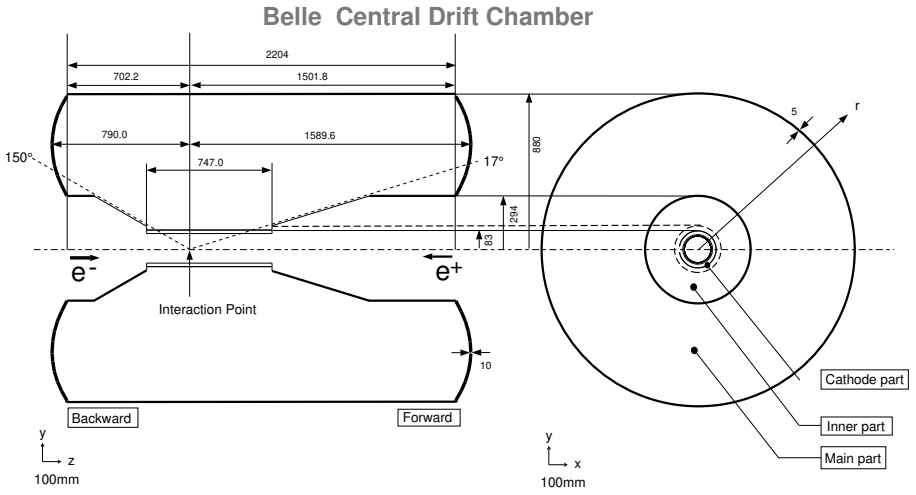

FIG. 2.6: Structure of the CDC. Lengths in Fig. are in the unit of mm.

magnetic field of superconducting solenoid bends the charged particle according to their momenta. The physics goal of the experiment requires a momentum resolution of

$$\frac{\sigma_{p_t}}{p_t} \sim \sigma_{MS} \oplus \sigma_r \sim 0.5 \oplus 0.5 p_t \ \% \tag{2.2}$$

for all charged particles with $p_t \geq 0.1$ GeV/c in the polar angle region $17^o \leq \theta \leq 150^o$. Here σ_{MS} denotes the error which comes from the multiple Coulomb scattering and shows constant contribution in above p_t region, and σ_r denotes the error proportional to p_t, which arises from the position measurement. One can calculate p_t from the radius of curvature r as

$$p_t = 0.3Br \tag{2.3}$$

Where p_t is in units of GeV/c, B is the magnetic field in Tesla, and r is in meter.

CDC provides good momentum and position resolution for charged tracks. In addition, the CDC is used to measure the energy loss (dE/dx) of charged particles, which is being used for particle identification. The amount of dE/dx depends on $\beta = v/c$ of the charged particle (Bethe-Bloch formula). Another important role of the CDC is to provide important information regarding the trigger system in the $r - \phi$ and z dimensions.

Structure of CDC is shown in Fig. 2.6. It is a cylindrical wire drift chamber having 50 layers (32 axial and 18 small angle stereo layers) of anode wires and three cathode

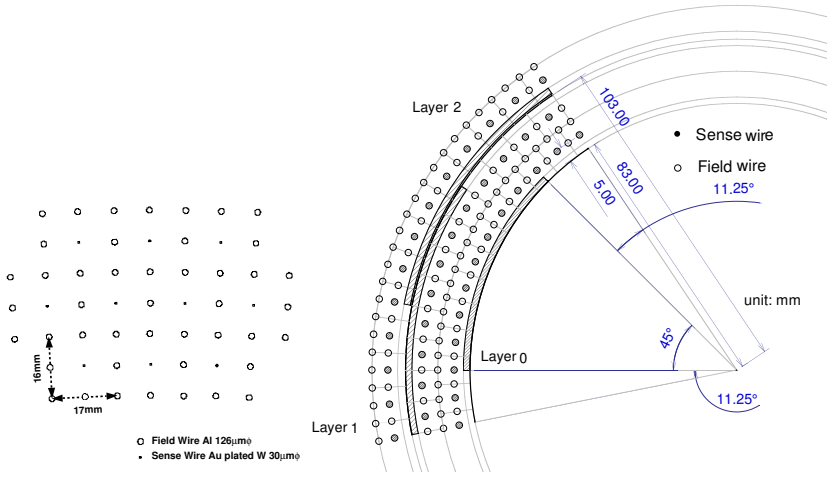

FIG. 2.7: Cell structure of the CDC. Cathode sector configuration is also shown in the right figure.

strip layers. The CDC is asymmetric in the z-direction. The axial wires are configured parallel to the z-axis while the stereo wires are slanted approximately ± 50 mrad. The stereo layers combined with axial layers provide z information of tracks. The cathode strips improve the z-measurement as well as produce a highly efficient fast z-trigger. Three z-coordinate measurements at the inner-most radii are provided by cathode strips as shown in Fig. 2.7. The cathode strip having a width of 7.4 mm, is divided into eight segments in the ϕ-direction and has an 8.2 mm pitch in the z-direction. Low-Z gas (50% helium (He) and 50% ethane) [72] is chosen to minimize multiple Coulomb scattering contributions to the momentum resolution. This mixture has a long radiation length (640 m) and a drift velocity that saturates at 4 cm/μs at a relatively low electric field.

Fig. 2.7 shows the spatial resolution as a function of the drift distance. The spatial resolution is approximately $\sigma_{r\phi} = 130$ μm. Charged particle tracking is done by Kalman filtering method [73], taking into account the effect of multiple Coulomb scattering, energy loss, and non-uniformity of the magnetic field.

The Bethe-Bloch equation gives the mean rate of energy loss (dE/dx) of a charged particle, and one can estimate β from a measurement of dE/dx using that equation. The measure of β can provide a valuable method for estimating the rest mass and thus differentiating particle species in conjunction with the momentum measurement. Track parameters are improved by combining the SVD and CDC information. The

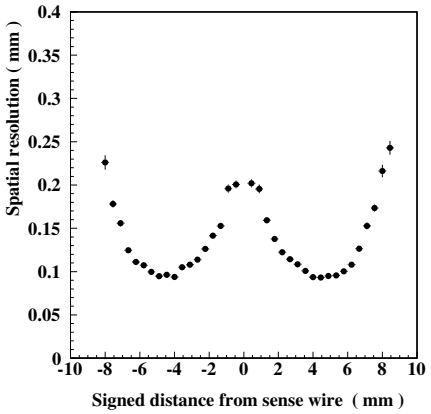

FIG. 2.8: Spatial resolution as a function of the drift distance.

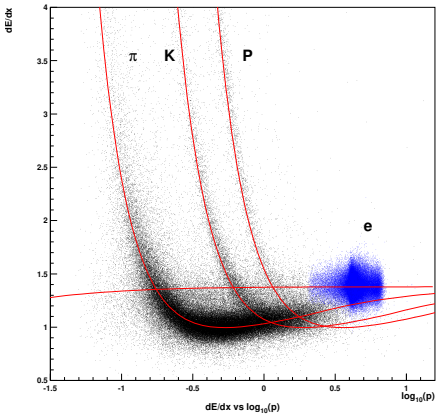

FIG. 2.9: Scatter plot for momentum vs dE/dx. Expected relation for π, K, p and e are shown by the solid curves. The momenta are given in units of GeV/c.

combined performance is

$$\sigma_{xy} = 19 \oplus \frac{50}{p\beta \sin^{3/2}\theta}\mu\mathrm{m}$$

$$\sigma_z = 36 \oplus \frac{42}{p\beta \sin^{5/2}\theta}\mu\mathrm{m} \tag{2.4}$$

$$\frac{\sigma_{pt}}{p_t} = (0.34 \oplus 0.19 p_t)\%$$

where momentum (p) and transverse momentum (p_t) are in GeV/c, β is the particle speed and θ its polar angle, and $\oplus$ represents a quadratic sum. The CDC is involved in the particle identification for the tracks with $p > 0.8$ GeV/c and $p < 2.0$ GeV/c

measuring dE/dx. Fig. 2.9 shows the scatter plot of the measured dE/dx as a function of particle momentum. Expected relation for π, K, p and e are shown by the solid curves. The dE/dx resolution is measured to be 6.9% for minimum-ionizing pions.

2.2.4 Aerogel Cherenkov Counter (ACC)

The ACC provides the K/π separation in the momentum range of $1.2 < p < 3.5$ GeV/c by detecting the Cherenkov light from particles penetrating through silica aerogel radiator. Cherenkov light is emitted if the velocity of the charged particle, β satisfies

$$\beta = \frac{p}{\sqrt{p^2 + m^2}} > 1/n \tag{2.5}$$

Where n is the refractive index of the detector material, m and p are the mass and momentum of the charged particle, respectively. Therefore, there is a momentum region where pions emit Cherenkov light while kaons do not, depending on the refractive index of the matter. For example, pions with momentum 2 GeV/c emit Cherenkov light in the matter if $n > 1.002$, while $n > 1.030$ is necessary for kaons with the same momentum.

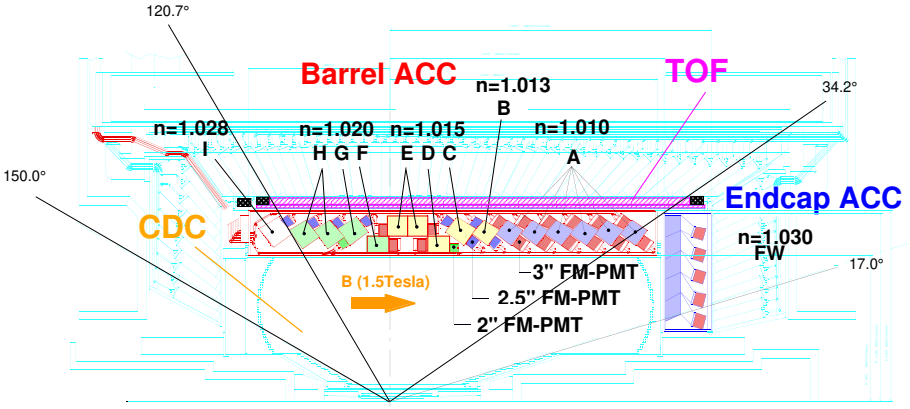

FIG. 2.10: The arrangement of ACC at the central part of Belle detector. Here n indicates the refractive index.

The configuration of ACC is shown in Fig. 2.10. The refractive indices of aerogels are selected between 1.01 and 1.028 depending on their polar angle region to obtain

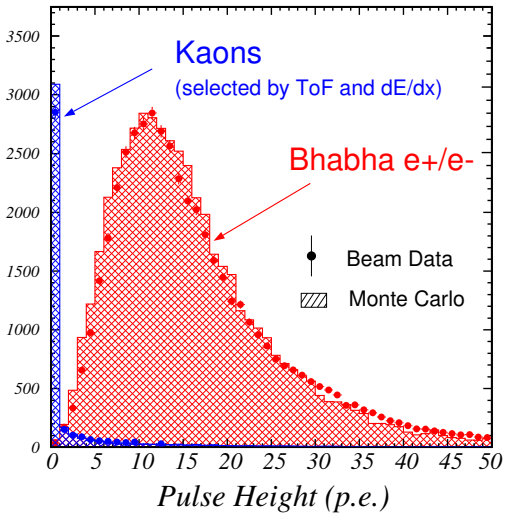

FIG. 2.11: Pulse height spectrum for electrons and kaons in units of photoelectrons (p.e.) observed by the barrel ACC. Kaon candidates are obtained by dE/dx and TOF measurements. The MC expectation are superimposed.

good K/π separation for the momentum range from 1.2 GeV/c to 3.5 GeV/c. The Cherenkov light generated in the silica aerogel is fed into one or two fine mesh photomultipliers (FMPMT) attached to the aerogel radiator modules. Fig. 2.11 shows the measured pulse height distribution for the barrel ACC for $e^{\pm}$ tracks in Bhabha events and $K^{\pm}$ candidates in hadronic events, which are selected by TOF and dE/dx measurements [74].

2.2.5 Time of Flight (TOF)

TOF detector [75] provides particle identification information for momentum below 1.2 GeV/c with time resolution 100 ps along with fast timing signals for the trigger system. The trigger modules attached to the TOF are called Trigger Scintillation Counters (TSC). The counters measure the elapsed time between a collision at the interaction point and the time when the particle hits the TOF layer. Using the measured flight time from TOF and measured flight length and momentum by CDC track fit, one can estimate the mass of each track in an event.

Fig. 2.12 shows the TOF module. One 5 mm thick TSC layer and one 4 cm thick TOF counter layer with a gap of 1.5 cm are arrayed cylindrically at the position (L) 1.2 m in radius from the IP. The scintillators are wrapped with 45 μm thick

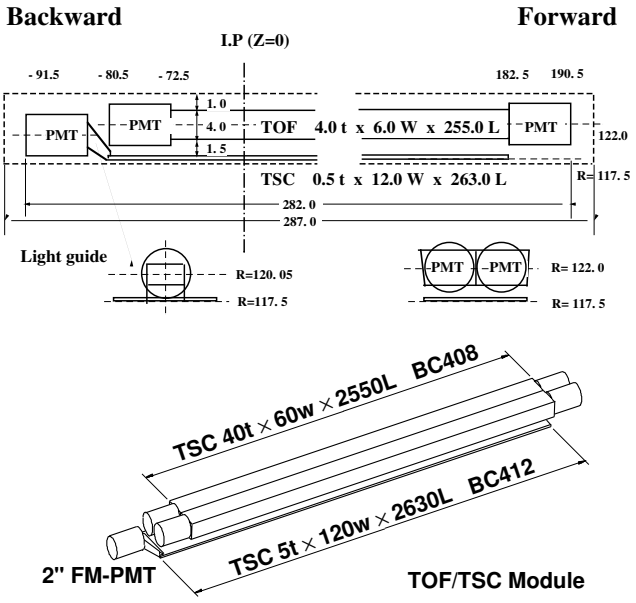

FIG. 2.12: Configuration of a TOF module made of two TOF counters and one TSC.

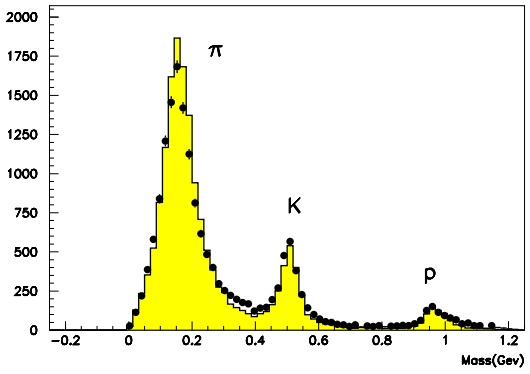

FIG. 2.13: Mass distribution from TOF measurements for particles with momentum below 1.2 GeV/c. Points and histogram show the data and MC distributions, respectively.

polyvinyl film for light tightness and surface protection. One FM-PMT is glued to each TSC at the backward end. Fig. 2.13 shows the mass distribution for each track in hadron events, and clear peaks corresponding to $\pi^{\pm}$, $K^{\pm}$ and protons (p) are seen.

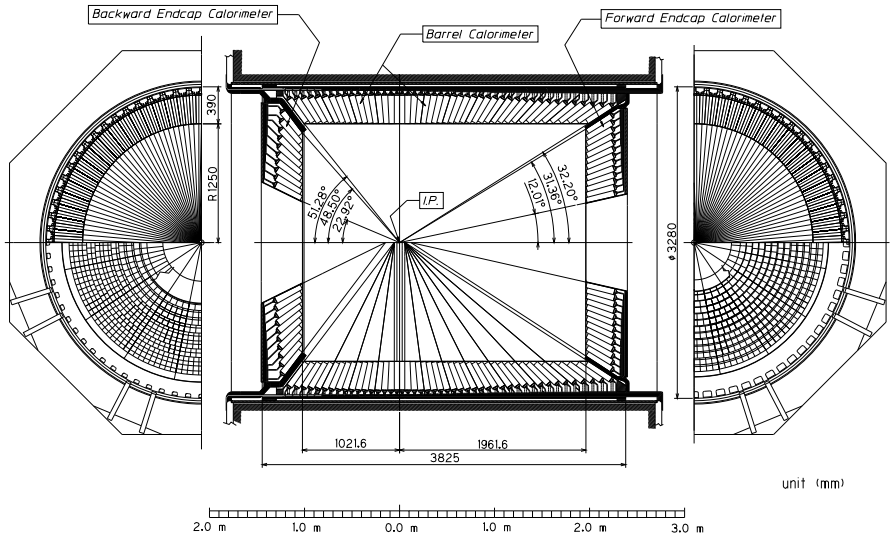

FIG. 2.14: Configuration of the ECL.

2.2.6 Electromagnetic Calorimeter (ECL)

The primary purpose of ECL [76] is the detection of photons with high efficiency and good resolutions in energy and position. It also plays a direct role in the electron identification in Belle. Most of these photons are end products of cascade decays and have relatively low energies; thus, having good performance below 500 MeV is especially important. Few decay modes also produce photon energies up to 4 GeV, so high resolution is needed to reduce the background for these modes.

The overall configuration of ECL is shown in Fig. 2.14. It consists of 8735 Thallium-doped Cesium Iodide scintillating crystal towers. Incident photons produce electron-positron pairs via interaction with crystal nuclei. The subsequent electron and positron radiate bremsstrahlung photons, which also produce e^+e^- pairs. Coulomb scattering creates a lateral shower spread. The shower proceeds to create more particles until, eventually, all the energy is in the form of ionization or excitation photons, which are read out by a pair of silicon PIN photo-diodes coupled to the rear of every crystal. The ECL barrel contains 6624 crystals in $12.4^o < \theta < 31.4^o$, and the backward end-cap 960 and covers $130.7^o < \theta < 155.1^o$. The energy resolution of ECL measured as a function of incident photon energy with 3×3 ECL matrices is given by

$$\frac{\sigma_E}{E} = \frac{0.0066(\%)}{E} \oplus \frac{1.53(\%)}{E^{1/4}} \oplus 1.18\%, \tag{2.6}$$

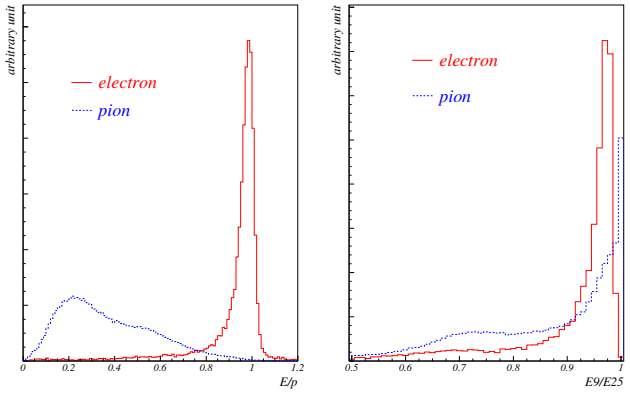

FIG. 2.15: Distributions of E/p (left) and E_9/E_{25} (right) for electrons (solid) and charged pions (dashed).

Where E is in GeV with the first term is due to the contribution of electronic noise, and the second and a part of the third term come from the shower leakage fluctuations. The third term also induces systematic effects such as the uncertainty of the calibration on crystals. The spatial resolution measured by the photon beams is given by

$$\sigma_X(mm) = 0.27 + \frac{3.4}{E^{1/2}} + \frac{1.8}{E^{1/4}} \tag{2.7}$$

where E is measured in the units of GeV.

In addition to the measurement of the energy of photons and electrons, the ECL plays a vital role in electron identification [77]. The electron identification is performed by combining the following information:

- Matching between the position of the charged track measured by the CDC and that of the energy cluster measured by the ECL.
- E/p, i.e. the ratio of energy measured by the ECL to momentum measured by the CDC.
- E_9/E_{25} at the ECL, i.e. the ratio of ECL shower energy in an array of 3×3 crystals to the energy in an array of 5×5 crystals.
- dE/dx in CDC.
- Light yield in the ACC.

Fig. 2.15 shows the data distributions for E/p and E_9/E_{25} for the electrons and charged pions. The distributions for electrons are obtained from radiative Bhabha events ($e^+e^- \to e^+e^-\gamma$) and those for pions are obtained from $K^0_S \to \pi^+\pi^-$ decays. The ECL also provides the trigger information and online luminosity information [78].

2.2.7 K_L and muon detection system (KLM)

The KLM detector [79] is designed to identify K^0_L and muons with high efficiency and low fake rate over a broad momentum range above 600 MeV/c. It is constructed from alternating 4.7 cm thick iron plates and 3.7 cm thick active KLM detector plates. The iron provides most of the 3.9 radiation lengths seen by K^0_L mesons, while the detector plates register the passage of ionizing particles. Fig. 2.16 shows the configuration of the KLM detector. The detector plates consist of two glass-electrode resistive-plate counters (RPC) sandwiched between layers of read-out strips in the θ and ϕ directions. An RPC has an active gaseous region between two highly resistive glass parallel plate electrodes. Charged particles ionize a streamer in the gas, which results in a local discharge of the resistive plates, including a signal in the read-out strips.

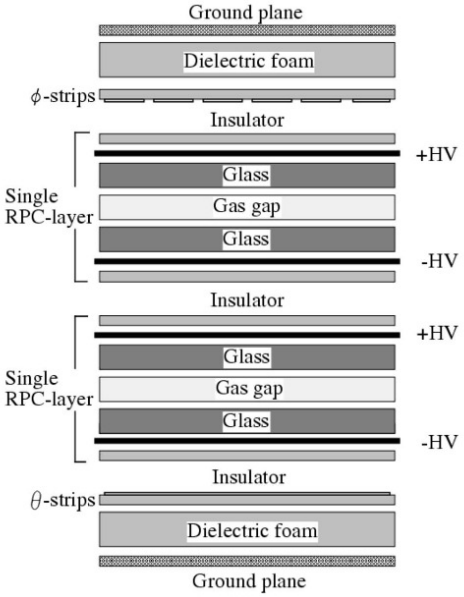

Fig. 2.16: KLM detector cross-section.

It is the only detector which is outside the solenoid magnetic field. It has two major parts: barrel KLM and endcaps (backward and forward) KLM. The barrel-shaped

region around the interaction point covers an angular range of 45^o - 125^o in the polar angle, and endcaps in the forward and backward directions extend this range to 20^o - 155^o. K_L^0 particles live long enough to travel beyond the ECL and interact primarily via the strong force. They are detected by the hadronic showers of ionizing particles. Showers initiated in the ECL will continue into the KLM. K_L^0 particles deposit most of the energy within the iron of the KLM. The detector provides position information for the K_L^0, but no helpful energy information is gained as a significant proportion of the shower will generally not be within the KLM. On the hand, muons do not interact via the strong force but have an electromagnetic cross-section. They lose most of the energy through the ionization process. They penetrate the ECL easily and will continue through most of the KLM. KLM tracks that are able to be matched with a track in the CDC are identified as muons.

2.3 Belle Trigger System

The trigger system in Belle plays an essential role in separating useful events from many unnecessary events. The Belle trigger system consists of the Level-1 hardware trigger and the Level-3 software trigger.

Belle Level-1 trigger system is composed of the sub-trigger system, and the central trigger system called the Global Decision Logic (GDL) [80]. The sub-trigger system is based on two categories, track triggers, and energy triggers. The CDC and TOF provide the trigger signals from charged particles, while the ECL trigger system provides triggers based on total energy deposit and cluster counting of crystal hits. The KLM and Extreme Forwarded Calorimeter (EFC) trigger systems provide additional trigger information, and the EFC triggers are used for tagging two-photon events and Bhabha events. The sub-triggers process event signals in parallel and provide trigger information to the GDL, where all the information is combined to distinguish physics and background events and to characterize a physics event type. Information from the SVD is not implemented in the present trigger arrangement. The Belle trigger system, including the sub-triggers, is operated in a pipelined manner, and the whole system is synchronized to the KEKB accelerator RF signal. Each multi-track, total energy, and isolated cluster counting trigger provides more than 95% efficiency for multi-hadronic data samples.

The level-3 trigger reduces the number of events to be stored on the disk for further analysis. It reduces the event rate by about 50% by selecting events with at least one track with a z impact parameter less than 5 cm and at least 3 GeV energy deposition in the ECL. It reduces the overall data rate by 50-60% retaining 99% of interesting physics events.

2.4 Data Acquisition System (DAQ)

The distributed-parallel system is devised for the Belle Data Acquisition System [81] to satisfy the requirements so that it works at 500 Hz with a deadtime fraction of less than 10%. The global scheme of the system is shown in Fig. 2.17. The entire system

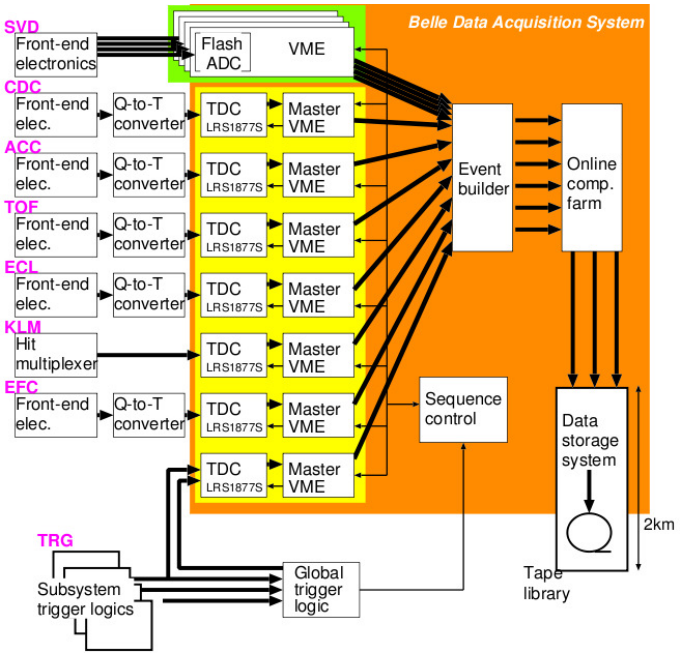

FIG. 2.17: Overview of the Belle DAQ system.

is segmented into seven subsystems running parallel, each handling the data from a sub-detector. Data from each subsystem are combined into a single event record by an event builder, which converts "detector-by-detector" parallel data streams to an "event-by-event" data driver. The event builder output is transferred to an online computer farm, where another level of event filtering is done. The data are then sent to a mass storage system at the computer center via optical fibers. The typical data size of a hadronic event by $B\bar{B}$ or $q\bar{q}$ production is measured to be about 30 kB, which corresponds to the maximum data transfer rate of 15 MB/s.

2.5 Particle identification at Belle

The particle identification is performed by combining the information from the sub-detectors. To identify the charged hadrons (pion, kaon, and proton), information of the time of flight measured by the TOF, the Cherenkov light yield measured by the ACC, and dE/dx information measured by the CDC have been used. The Belle PID [82] classification for hadrons is based on binary likelihood ratios. Likelihood functions $\mathcal{L}_x$ for different mass hypotheses are calculated from the physical quantities measured by the PID subsystems accounting for the direction and momentum of the track and then combined in the likelihood ratios

$$\mathcal{R}_{x:y} = \frac{\mathcal{L}_x^{\rm CDC}\mathcal{L}_x^{\rm ACC}\mathcal{L}_x^{\rm TOP}}{\mathcal{L}_x^{\rm CDC}\mathcal{L}_x^{\rm ACC}\mathcal{L}_x^{\rm TOP} + \mathcal{L}_y^{\rm CDC}\mathcal{L}_y^{\rm ACC}\mathcal{L}_y^{\rm TOP}} \tag{2.8}$$

where x and y are two mass assumptions. By the definition, $\mathcal{R}_{x:y} \simeq 1$ while x is the correct assumption.

For lepton identifications [77, 83], the energy deposited in the ECL (for electron) and the signal left by the track in the KLM (for muons) have been used in addition to the above sub-detector information. The likelihood ratio for leptons is defined as:

$$L_\ell = \frac{\mathcal{L}_\ell}{\mathcal{L}_\ell + \mathcal{L}_\pi + \mathcal{L}_K + \mathcal{L}_p} \tag{2.9}$$

where L_ℓ with $\ell = e, \mu$ is the combined likelihood for leptons.

Chapter 3

Study of $X(3872)$ & $X(3915)$ in B meson decays

In this chapter, we describe analysis procedure, Monte-Carlo simulations, and obtained results on the study of $X(3872) \to J/\psi\omega$ and $X(3915) \to J/\psi\omega$ decays in B meson decays. The $B\bar{B}$ mesons produced in the $\Upsilon(4S)$ decays have been used for the analysis.

3.1 Analysis strategy

We apply various kinematic selections to reduce the backgrounds and to select the $B \to J/\psi\omega K$ signal events. To extract the signal, we fit the invariant $J/\psi\omega$ mass ($M_{\mathrm{J}/\psi\omega}$). $X(3872)$ and $X(3915)$ are expected to peak on the $M_{\mathrm{J}/\psi\omega}$ distribution at their respective masses.

3.2 Monte Carlo signal generation

We generate 1 million MC signal events for each of the following decay modes:

- $B^+ \to X(3872)K^+$, $X(3872) \to J/\psi\omega$
- $B^0 \to X(3872)K^0_S$, $X(3872) \to J/\psi\omega$

- $B^+ \to X(3915)K^+$, $X(3915) \to J/\psi\omega$
- $B^0 \to X(3915)K^0_S$, $X(3915) \to J/\psi\omega$

For this purpose, we have used EvtGen generator [93] with the PHOTOS [94] to consider the initial and final state radiation. Detector response is followed by detector simulation software package, GSIM, based on Geant3.4 [95]. In Fig. 3.1, we show the schematic diagram for our decay chain of interest starting from the colliding e^+e^- beam. The VSS model (decays a vector particle into two scalars) has been used to generate the events for $\Upsilon(4S) \to B\bar{B}$. We use the PHSP model (generic phase space to n-bodies) to generate the events for $X \to J/\psi\omega$ decays. Further, $J/\psi \to \ell\ell$ and ω decays are generated with the VLL model (decay of a vector meson to a pair of charged leptons) and the OMEGA DALITZ model (the Dalitz amplitude for the $\omega \to \pi^+\pi^0\pi^-$ decay), respectively.

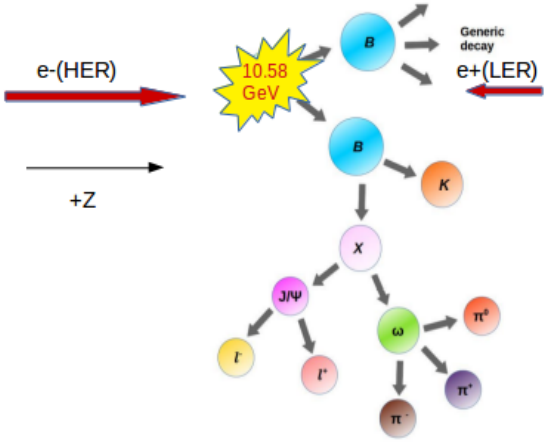

FIG. 3.1: Schematic diagram for our decay chain of interest.

3.3 Event selection

B mesons are reconstructed from its decay products. The particles used to reconstruct B mesons are $e^\pm$, $\mu^\pm$, $\pi^\pm$, $K^\pm$, and γ. These are the final particles, which are detected by the Belle detector.

K, π selection: Charged K and π selection is based on the information from ACC (number of Cherenkov photons), TOF (time of flight measurement) and CDC

(dE/dx measurement) from detectors. Kaon (pion) identification is based upon the likelihood ratio, which is defined as:

$$\mathcal{R}(K, \pi) = \frac{\mathcal{L}(K, \pi)}{\mathcal{L}(K) + \mathcal{L}(\pi)}. \tag{3.1}$$

Charged kaons (pions) are identified by requiring $\mathcal{R}_K > 0.6$ ($\mathcal{R}_\pi > 0.6$) with the identification efficiency of 94% (86%) and the misidentification rate of 7.5% (4%) for misidentifying kaon as pion (pion as kaon).

e, μ selection: Using the information of track penetration depth from the KLM system, muons are identified. Electrons are identified using E/p ratio (energy (E) from ECL and momentum (p) from CDC and SVD), and dE/dx from CDC. Likelihood ratio for lepton identification are mentioned in the section 2.5. We select the electron with electron likelihood (L_e) > 0.01, and muons with muon likelihood (L_μ) > 0.1.

γ selection: In the Belle detector, γ candidate selection is based upon their EM interactions inside the ECL (with a shower production mechanism). A loose selection is applied on the EM shower with $\frac{E_9}{E_{25}} > 0.85$, where E_9 (E_{25}) is the energy deposited in the 3x3 (5x5) crystals of the ECL.

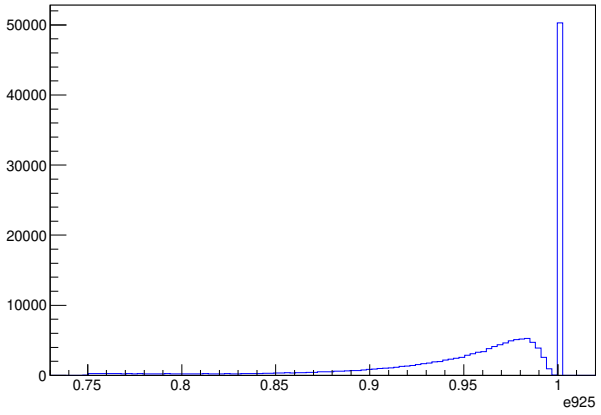

FIG. 3.2: Distribution of ratio of energy deposited to 3×3 and 5×5 ECL crystals for $B^+ \to X(3872)K^+$ decays using signal MC sample.

3.4 MC signal study

Using the identified final states, intermediate resonances and B mesons have been reconstructed.

3.4.1 π^0 reconstruction

Neutral pions are reconstructed from two photons (in $\pi^0 \to \gamma\gamma$ decays). In Fig. 3.3, we show the distributions of energy of a daughter photon (E_1) and energy asymmetry parameter $\frac{|E_1-E_2|}{(E_1+E_2)}$, where E_1 (E_2) is the energy of the first (second) photon in the laboratory frame. As one can see, mis-reconstructed photon candidates dominates below 60 MeV on E_1 distribution. To reduce combinatorial background, we select the photons with energy greater than 60 MeV, and π^0 candidates are also required to have an energy asymmetry parameter smaller than 0.8. Fig. 3.4, we compare the mass distribution of distribution of truth-matched and mis-reconstructed π^0 candidates. Candidates with 123 MeV/c^2 $< M_{\pi^0} <$ 147 MeV/c^2 (corresponding to 2σ significance) have been selected. Further, we apply pi^0 mass constrained fit to improve the resolution of reconstructed π^0 events.

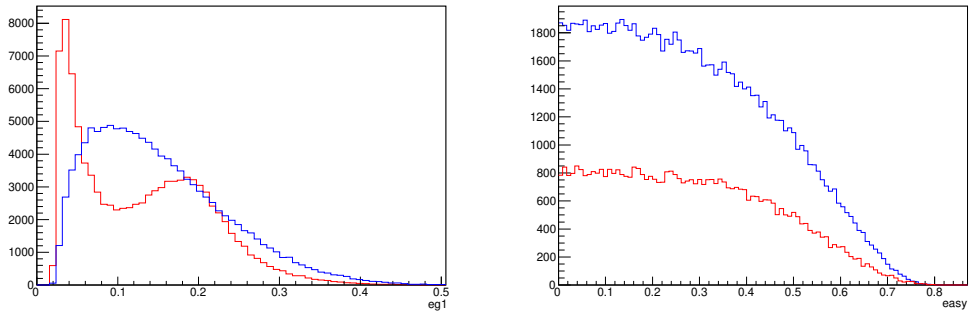

FIG. 3.3: Distribution of E_γ in GeV (left) and energy asymmetry parameter (right) of photons with truth-matched (blue) and combinatorial (red) π^0 events using signal MC sample.

3.4.2 ω reconstruction

In this study, ω is reconstructed in $\omega \to \pi^+\pi^0\pi^-$ decays. In Fig. 3.5, we show the M_ω distribution of truth-matched and mis-reconstructed events. Most of the mis-reconstructed events come from bad π^0 reconstructions. We fit the M_ω for

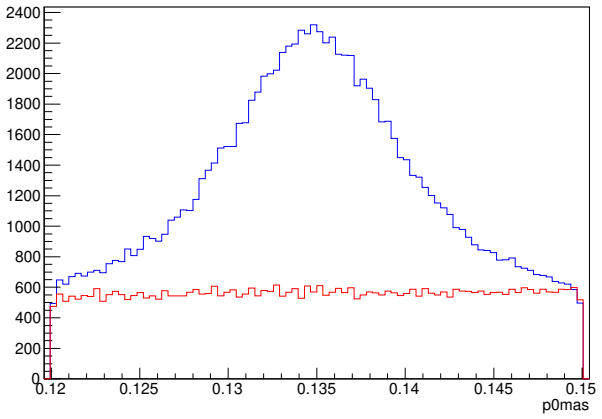

FIG. 3.4: $M_{\gamma\gamma}$ distribution (in GeV/c^2) of the truth-matched (blue) and mis-reconstructed (red) π^0 events using signal MC sample.

truth-matched events, and select the events within $\pm 2.5\sigma$ region from the mean position, 710 MeV/c^2 $< M_\omega <$ 820 MeV/c^2, for further usage.

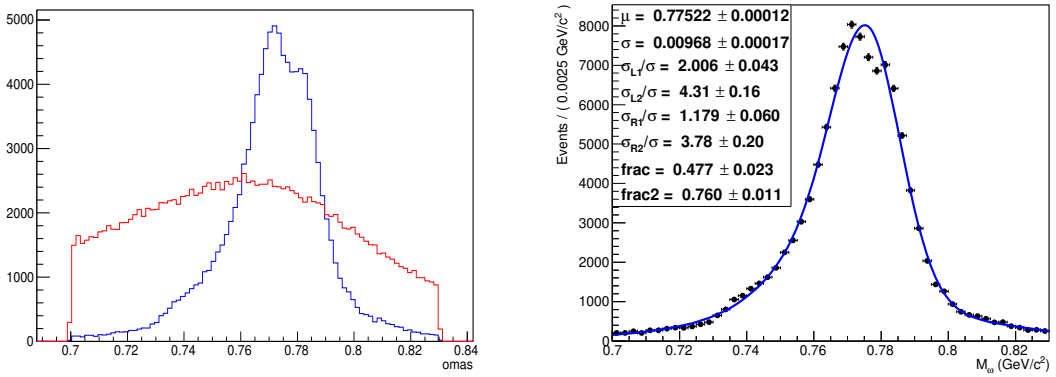

FIG. 3.5: Distribution of $M_{\pi^+\pi^-\pi^0}$ in GeV/c^2 (left) with truth-matched (blue) and mis-reconstructed (red) events for $B^+ \to J/\psi\omega K^+$ decays. UML fit to M_ω (in GeV/c^2) for truth-matched events (right) using signal MC sample.

If a particle decays into three daughters then its kinematics can be described by the Dalitz plot. For a 3-body decay, there are total 12 parameters (three 4-momentum), out of which 2 independent (10 constraint: 4 conservation of momentum, 3 masses, 3 Euler angles). These two independent parameters can be described by,

$$X = \frac{\sqrt{3}(T_{\pi^+} - T_{\pi^-})}{Q} \tag{3.2}$$

$$Y = \frac{2T_{\pi^0} - (T_{\pi^+} + T_{\pi^-})}{Q} \tag{3.3}$$

Where T_{π^0}, T_{π^+}, and T_{π^-} are kinetic energies of π^0, π^+, and π^-, respectively in the rest frame of ω. $Q = T_{\pi^0} + T_{\pi^+} + T_{\pi^-}$ is the energy released in the decay. Fig. 3.6 shows the Dalitz plots for truth-matched and mis-reconstructed ω events in the rest frame of ω.

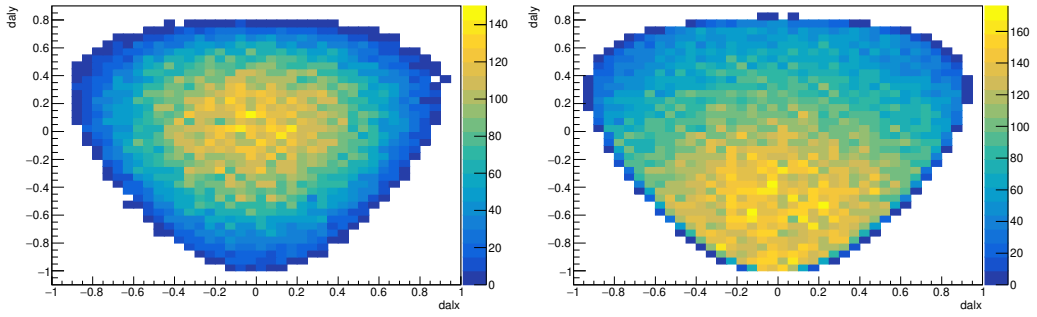

FIG. 3.6: Dalitz plot for $\omega \to \pi^+\pi^0\pi^-$ decays with X (Y) in the horizontal (vertical) direction for truth-matched ω events (left) and mis-reconstructed ω events (right) using signal MC sample.

3.4.3 Reconstruction of J/ψ

J/ψ is reconstructed using $\ell^+\ell^-$, where ℓ stands for electron or muon. Different cuts are used to select the J/ψ candidates from ee and $\mu\mu$. We find prominent peaks for J/ψ mass ($M_{J/\psi}$). We fit the $M_{J/\psi}$ from each of the reconstruction modes separately, and select the events within $\pm 3\sigma$ region from the mean position. Corresponding window for $J/\psi \to \mu^+\mu^-$ decay is 3.06 GeV/c^2 $< M_{\mu\mu} <$ 3.13 GeV/c^2. There is a loss of energy from the electron in the form of bremsstrahlung photon emissions. The 4-momentum of the photons within 50 mrad of $e^\pm$ direction are included in the invariant mass calculation. However, even after this correction, the $J/\psi \to e^+e^-$ signal shape is still skewed Fig. 3.7, which is taken into account by using an asymmetric invariant mass window 3.01 GeV/c^2 $< M_{ee\gamma} <$ 3.13 GeV/c^2 to define J/ψ candidate in the electron channel. J/ψ candidates are selected with momentum in the $\Upsilon(2S)$ rest-frame ($|\vec{p}^{\,\mathrm{CM}}_{J/\psi}|$) less than 2 GeV/$c$ to avoid J/ψ coming directly from B meson decays. In order to improve the resolution, we perform a mass constrained fit to the reconstructed J/ψ candidates to make the J/ψ mass more close to its nominal mass.

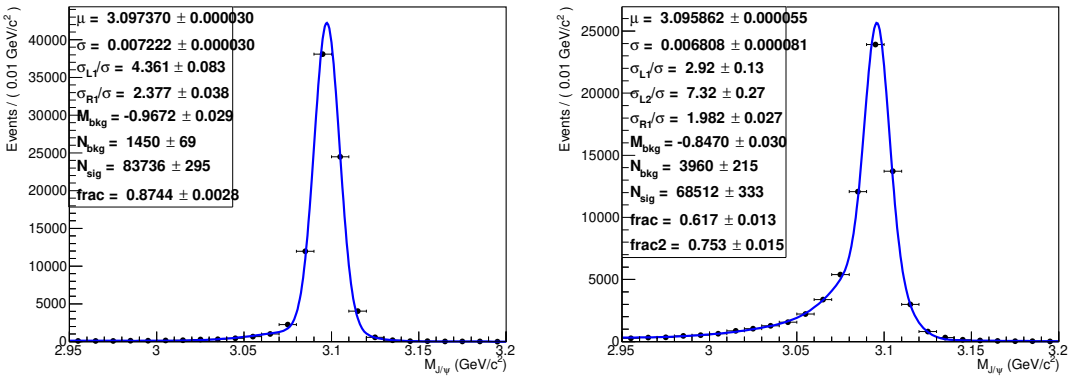

FIG. 3.7: UML fit to $M_{\ell\ell}$ (in GeV/c^2) for $J/\psi \to \mu^+\mu^-$ decays (left) and $J/\psi \to e^+e^-/e^+e^-\gamma$ decays (right) using signal MC sample.

3.4.4 Reconstruction of K^0_S

In this analysis neutral K^0 has been identified in K^0_S decays. Further K^0_S has been reconstructed in $K^0_S \to \pi^+\pi^-$ decays. Fig. 3.8 shows the fitted distribution of K^0_S mass ($M_{\mathrm{K^0_S}}$). Due to very less background contamination from K^0_S reconstruction, we select an 5σ region, $0.485 < M_{\mathrm{K^0_S}} < 0.511$ GeV/c^2, from the mean position.

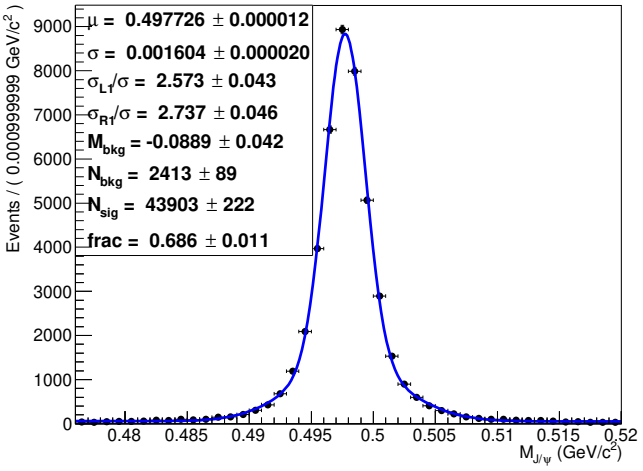

FIG. 3.8: UML fit to K^0_S mass (in GeV/c^2) using signal MC sample.

3.4.5 Kinematical variables

To identify the B meson, two kinematical variables are used: beam constrained mass and energy difference. Beam constrained mass (M_{bc}) and energy difference (ΔE)

are defined as

$$M_{\rm bc} = \sqrt{E^2_{\rm beam} - \sum_i p_i^2} \qquad \Delta E = E_{\rm beam} - \sum_i E_{\rm i} \tag{3.4}$$

Where $E_{\rm beam}$ is the beam energy in the $\Upsilon(4S)$ rest-frame, and p_i ($E_{\rm i}$) is the momentum (energy) of the i-th particle in the $\Upsilon(4S)$ rest-frame. Summation is over all of the final states used for reconstruction. Distributions of ΔE and $M_{\rm bc}$ are shown in Fig. 3.9. B meson candidates within -50 MeV $< \Delta E <$ 50 MeV and $M_{\rm bc} > 5.27$ GeV/c^2 are taken for further analysis.

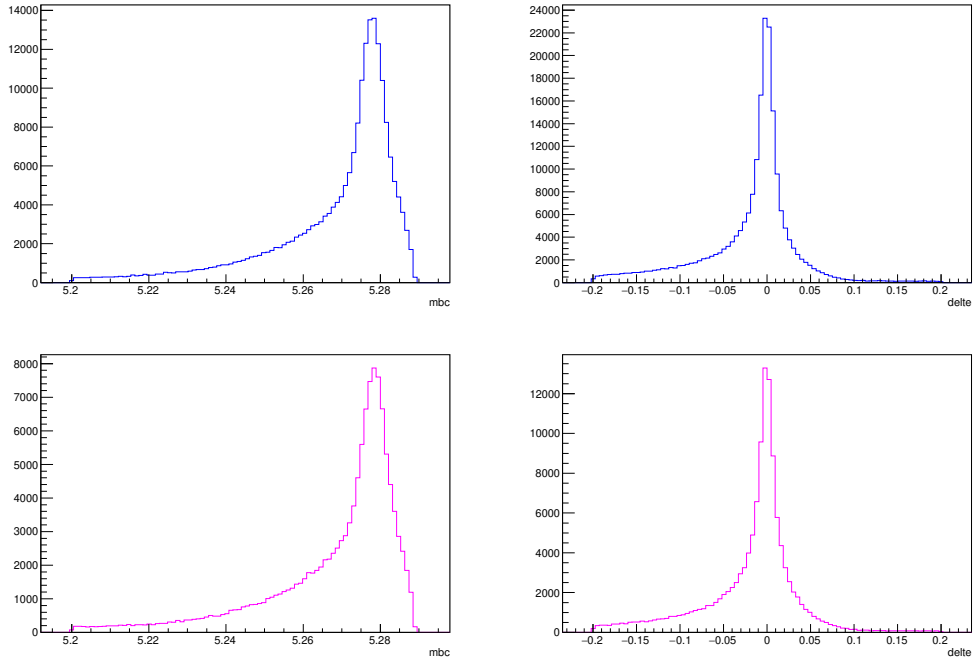

FIG. 3.9: Distributions of $M_{\rm bc}$ in GeV/c^2 (left) and ΔE in GeV (right) for charged B meson decays (top) and neutral B meson decays (bottom) using signal MC samples.

3.4.6 Best candidate selection

One expects at most one B candidate of interest in each event. Due to wrong combinations and mis-reconstructed particles, we get multiple B candidates for some of the events. In Fig. 3.10, we show the distributions of multiplicity of reconstructed B candidates for charged and neutral modes. Inside the signal search

window (discussed later), fraction of multiple candidates for $B^+ \to X(3872)K^+$ and $B^0 \to X(3872)K^0_S$ are 28% and 30%, respectively.

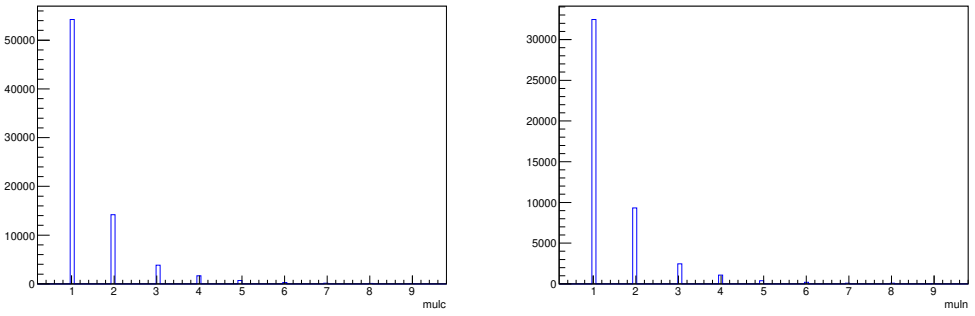

FIG. 3.10: Distributions of multiple candidates for $B^+ \to X(3872)K^+$ decays (left) and $B^0 \to X(3872)K^0_S$ decays (right).

The best candidate selection (BCS) among the multiple candidates is based on a least χ^2 method. Here χ^2 for BCS is defined as,

$$\chi^2_{\text{BCS}} = \chi^2_V + \left(\frac{\Delta E}{\sigma_{\Delta E}}\right)^2 \tag{3.5}$$

Where χ^2_V is obtained by fitting the vertex of all the charged tracks, and width of the ΔE ($\sigma_{\Delta E}$) is obtained by fitting ΔE for truth-matched events. Among the multiple B candidates, the candidate with least value is selected. Here BCS efficiency is defined as:

$$\text{BCS efficiency} = \frac{\text{Number of true signal events selected in BCS with multiplicity} > 1}{\text{Number of true signal events having multiplicity} > 1} \tag{3.6}$$

We estimate the BCS efficiencies inside the signal window. Tab. 3.1 shows the BCS efficiencies for different modes. For neutral mode, K^0_S is reconstructed in $K^0_S \to \pi^+\pi^-$ decays. Due to increase in the charged track multiplicity for neutral mode, multiplicity of the reconstructed events increases and BCS efficiency decreases as compared to the charged mode.

χ^2_{BCS}	BCS efficiency (%)	
	$B^+ \to X(3872)K^+$	$B^0 \to X(3872)K^0_S$
χ^2_{BCS}	72	67

TAB. 3.1: Best candidate selection efficiencies for different modes.

3.5 Background Study

For background study, we use 100 times $B \to J/\psi X$ inclusive sample, a sample that contains all the B meson decays with a J/ψ in the final state having a statistics of 100 times of Belle data. This sample is generated with wrong mass and width of the $X(3915)$. Instead of the $X(3915)$ there are $Y(3940)$ decays. In order to study the possible sources of background, we replace the $Y(3940)$ decays with $X(3915)$ decays (at 1:1 ratio) in the reconstructed inclusive $B \to J/\psi X$ sample from the generated signal events. We plan to extract the signal yields from an UML fit to $M_{\mathrm{J}/\psi\omega}$ below 4.15 GeV/c^2. Therefore, distributions with $M_{\mathrm{J}/\psi\omega} < 4.15$ GeV/c^2 have been shown in this section.

3.5.1 Continuum suppression

To suppress the background coming from the $e^+e^- \to q\bar{q}$ $[q = u, d, s, c]$ backgrounds, the ratio of second to zeroth Fox-Wolfram moments is used [100].

$$R_2 = \frac{H_2}{H_0} \tag{3.7}$$

$$H_k = \sum_{i,j} \mid p_i \mid p_j \mid P_k(\cos\theta_{ij}) \tag{3.8}$$

Here p_i is the there momentum of i-th track, and $\cos\theta_{ij}$ is the angle between i-th and j-th tracks. P_k is the Legendre polynomial. The B mesons are produced at rest and their decay axis are un-correlated. So, $B\bar{B}$ events are spherical in shape, and can be distinguished from jet-like $e^+e^- \to q\bar{q}$ events of $u\bar{u}$, $d\bar{d}$, $s\bar{s}$, $c\bar{c}$. R_2 is zero for the spherical events. Fig. 3.11 shows the distribution of R_2 for signal and background events. Here and in the future plots X_{sd} is the $s\bar{d}$ fragmentation. Distribution of signal and backgrounds are very much similar to each other. We select the events with loose R_2 cut, $R_2 < 0.5$. Charged tracks are required to have a distance of closest approach to interaction point (IP) in the beam direction (z) of less than 3.5 cm, and less than 1.0 cm in the transverse plane (xy-plane).

Backgrounds come from $e^+e^- \to q\bar{q}$ $(q = u, d, s, c)$ are called $e^+e^- \to q\bar{q}$ events. In the $\Upsilon(4S)$ rest-frame, those events are produced in a jet-like shape where $B\bar{B}$ events are spherical. Requiring two high momentum lepton track within a narrow J/ψ mass window rejects most of the contribution from $e^+e^- \to q\bar{q}$ background.

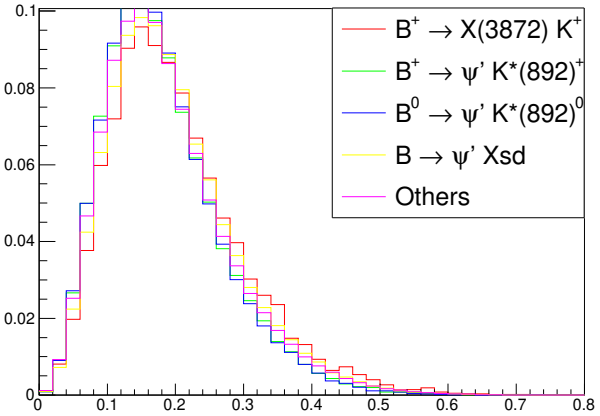

FIG. 3.11: Distribution of Fox-Wolfarm moments (R_2) (normalized to unity) for signal and background events using $B \to J/\psi X$ inclusive sample.

Further, we already use $R_2 < 0.5$ and $|\vec{p}^{\,\mathrm{CM}}_{J/\psi}| < 2.0$ GeV/c, which rejects the possible $e^+e^- \to q\bar{q}$ background. To find the contribution of $q\bar{q}$ background events, we check the distributions of M_{bc} and ΔE for $q\bar{q}$ MC sample generated at $\Upsilon(4S)$ energy. As one can see in Fig. 3.12, M_{bc} and ΔE distributions are flat around the expected signal region.

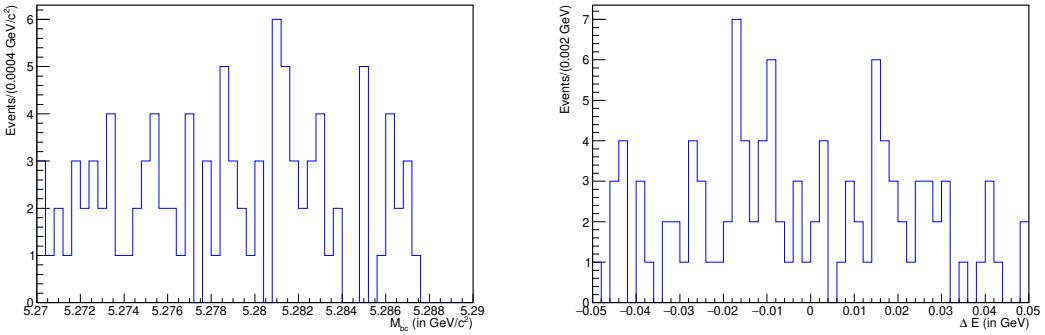

FIG. 3.12: Distributions of M_{bc} (in GeV/c^2) and ΔE (in GeV) for charged mode using $q\bar{q}$ MC sample at $\Upsilon(4S)$ energy.

3.5.2 Optimization of ω events

As one can see in Fig. 3.13, the concentration of signal events at the central region of the omega Dalitz plot is higher, while the background events are more likely to concentrate over the lower part. We optimize both of Y and $R = \sqrt{X^2 + Y^2}$ using

figure of merit ($F_{\rm OM}$).

$$F_{\rm OM} = \frac{N_{\rm sig}}{\sqrt{N_{\rm sig} + N_{\rm bkg}}} \tag{3.9}$$

Where $N_{\rm sig}$ is the number of signal event and $N_{\rm bkg}$ represents the number of background estimated from $B \to J/\psi X$ inclusive sample. We show $F_{\rm OM}$ distributions for Y and R optimizations in Fig. 3.14. We find no optimized selection for R, but find an optimization for Y. We select the events with $Y > -0.67$ which reduces 8% of signal events (with 3% truth-matched events), and rejects 13% of background events.

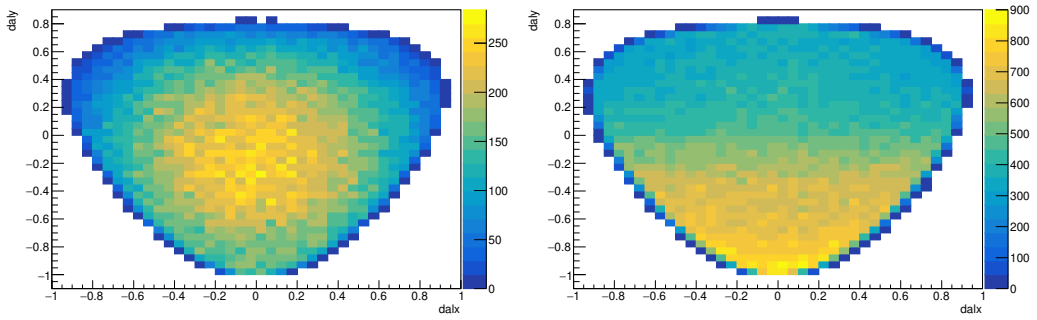

FIG. 3.13: Dalitz plots for $\omega \to \pi^+\pi^0\pi^-$ decays for signal events (left) and for background events (right) using $B \to J/\psi X$ inclusive MC sample.

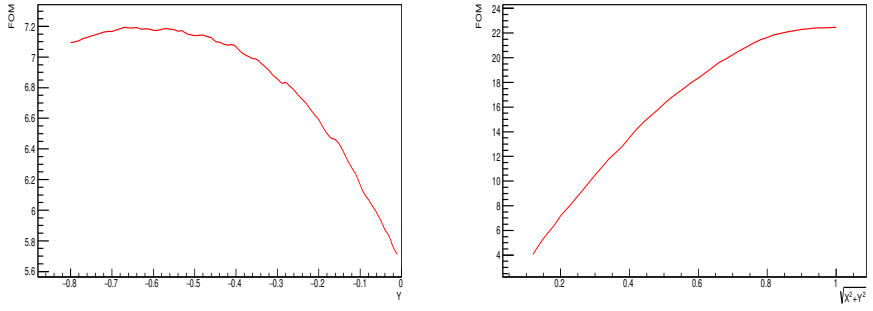

FIG. 3.14: Figure of merit for Y optimization (left) and for R optimization (right).

As most of the backgrounds come from ω reconstructions, we further optimize the omega mass window using figure of merit. Distributions of signal and backgrounds on $M_{\pi^+\pi^-\pi^0}$ distributions are shown in Fig. 3.15. Lower (upper) bound of $M_{\pi^+\pi^-\pi^0}$ mostly effects the $X(3872)$ ($X(3915)$) signal events. Therefore, lower and upper bounds of $M_{\pi^+\pi^-\pi^0}$ window are optimized using $X(3872) \to J/\psi\omega$ and $X(3915) \to J/\psi\omega$ events, respectively (Fig. 3.16). We select the events with 740 MeV/c^2 $< M_{\pi^+\pi^-\pi^0} <$ 810 MeV/c^2, which further rejects 23% signal events (with 7% of truth-matched events) for $X(3872) \to J/\psi\omega$ decays and 19% of signal events (with 5% of

truth-matched events) for $X(3915) \to J/\psi\omega$ decays, respectively with 37% reduction of background events.

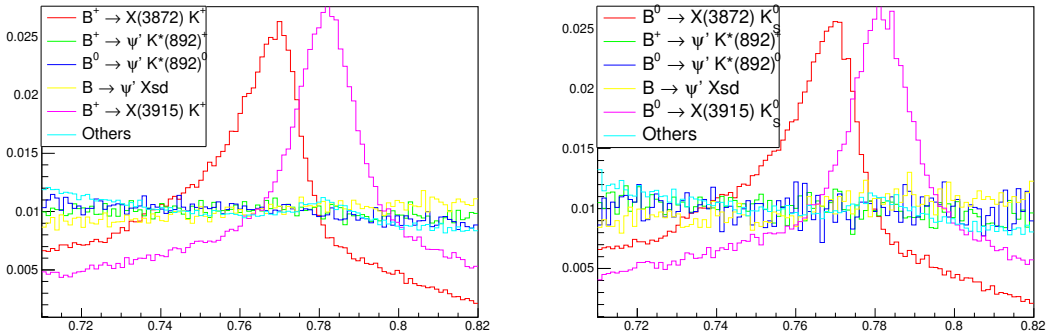

FIG. 3.15: Distributions of $M_{\pi^+\pi^-\pi^0}$ in GeV/c^2 for charged B meson decays (left) and for neutral B meson decays (right) using $B \to J/\psi X$ inclusive MC sample.

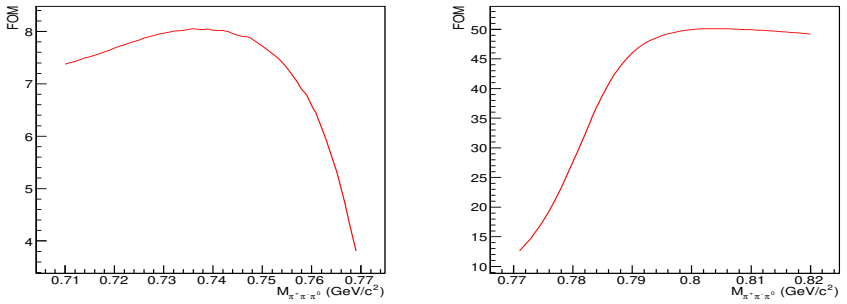

FIG. 3.16: Figure of merit for $M_{\pi^+\pi^-\pi^0}$ optimization.

3.5.3 $M_{\rm bc}$ and ΔE selection

To reduce the peaking background on $M_{J/\psi\omega}$, we select events with a tight $M_{\rm bc}$ selection. In Fig. 3.17, $M_{\rm bc}$ distribution for signal and dominating backgrounds are shown on the same canvas. We optimize the $M_{\rm bc}$ window using figure of merit in a similar approach to omega optimizations using Eq. (3.9). One expects signal events to be peaking at the nominal B meson mass. To find the lower bound of $M_{\rm bc}$ window, upper bound is fixed at 5.29 GeV/c^2, and lower bound is varied from 5.27 to 5.28 GeV/c^2. Similarly, to find the upper bound of $M_{\rm bc}$ window, we vary the upper bound from 5.28 to 5.29 GeV/c^2 keeping the lower bound fixed at the optimized point. Figure of merit for lower and upper bound of $M_{\rm bc}$ optimizations are shown in

Fig. 3.18. We select the events within 5.274 GeV/c^2 $< M_{\rm bc} <$ 5.286 GeV/c^2, which rejects 18% of signal events (with 8% of truth-matched events) and reduces 32% of background events.

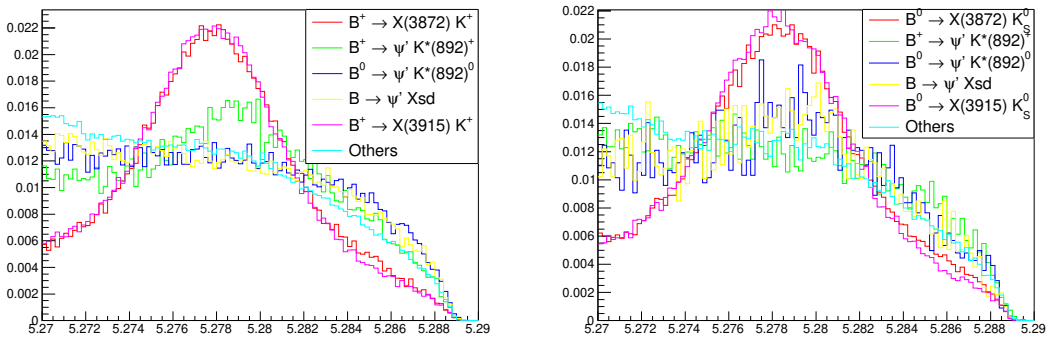

FIG. 3.17: $M_{\rm bc}$ (in GeV/c^2) distributions for signal events and dominating background components for charged B meson decays (left) and for neutral B meson decays (right) using $B \to J/\psi X$ inclusive MC sample.

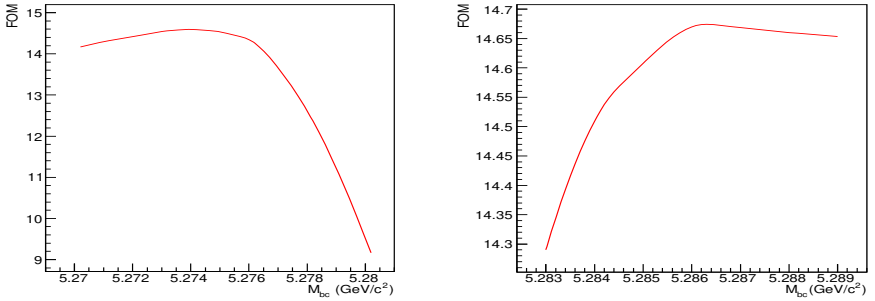

FIG. 3.18: Figure of merit for $M_{\rm bc}$ optimization.

Inside the optimize $M_{\rm bc}$ window, distributions of ΔE are shown in Fig. 3.19. In order to remove maximum background with less signal loss, we optimize the ΔE window within $M_{\rm bc}$ window using Eq. (3.9). One expect signal events to be peaking over ΔE with a mean values close to zero. Therefore, the lower bound of the ΔE selection window should be a negative and upper bound should be a positive value. To find the lower bound, positive boundary is fixed at $\Delta E = 0.05$ GeV, and a negative value varied from -0.05 to 0 GeV. Similarly, to find the positive bound of the ΔE, we vary the positive boundary from 0 to 0.05 GeV keeping the negative boundary fixed at the optimized lower bound of ΔE. Figure of merit for ΔE optimizations are shown in Fig. 3.20. We select the region from -20 MeV to 20 MeV as ΔE signal window for both charged and neutral B meson decays. ΔE selection further rejects 19%

of signal events (with 5% of truth-matched events) and reduces 45% of background events.

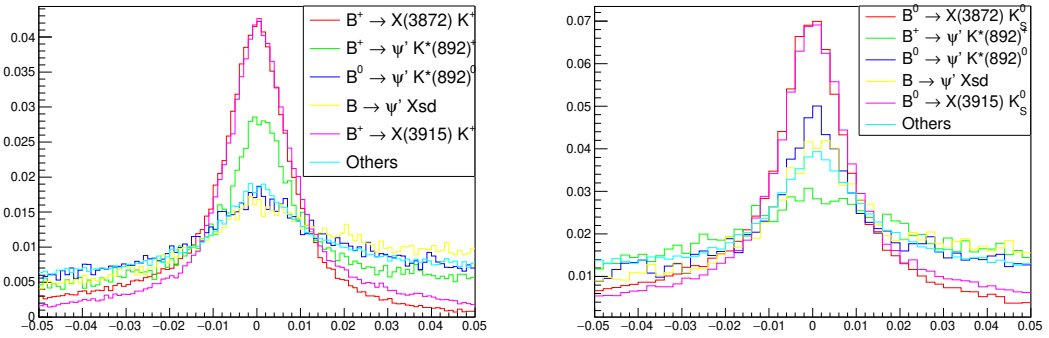

FIG. 3.19: ΔE (in GeV) distributions for signal events and dominating background components for charged B meson decays (left) and for neutral B meson decays (right).

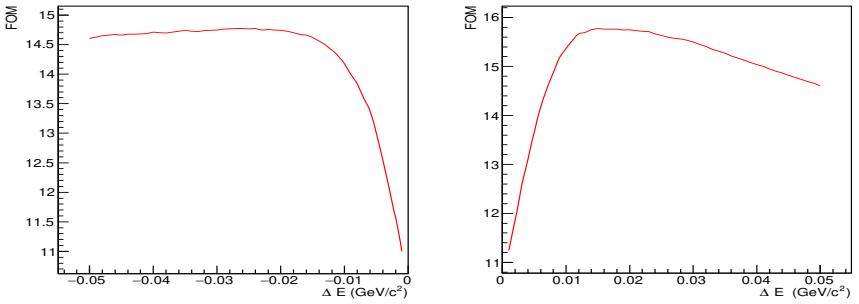

FIG. 3.20: Figure of merit for ΔE optimization.

3.5.4 $\psi(2S)$ background rejection

We find some peaking backgrounds coming from $B^+ \to \psi(2S)K^{*+}$ and $B^0 \to \psi(2S)K^{*0}$ decays for both charged and neutral modes. Also, some other background (like $B \to \psi(2S)X_{sd}$) linked with $\psi(2S)$ decays are expected to be peaking in the signal region. Here, $J/\psi\pi^+\pi^-$ from $\psi(2S)$ decays get combined with π^0 (from K^{*0} or any other decays) give broad structure in $M_{J/\psi\omega}$ distribution, and mimic the $J/\psi\omega$ signal events. In Fig. 3.21, one can see a clear peaking structure around $\psi(2S)$ mass on $M_{J/\psi\pi^+\pi^-}$ distribution. To remove such background, we remove the events within 3.67 GeV/c^2 $< M_{J/\psi\pi^+\pi^-} <$ 3.705 GeV/c^2. As a result, we loose 11% more signal events (with 7% of truth-matched events) for $X(3872) \to J/\psi\omega$ decays and 19% of

signal events (with 11% truth-matched events) for $X(3915) \to J/\psi\omega$ decays with 41% reduction of $\psi(2S)$ backgrounds.

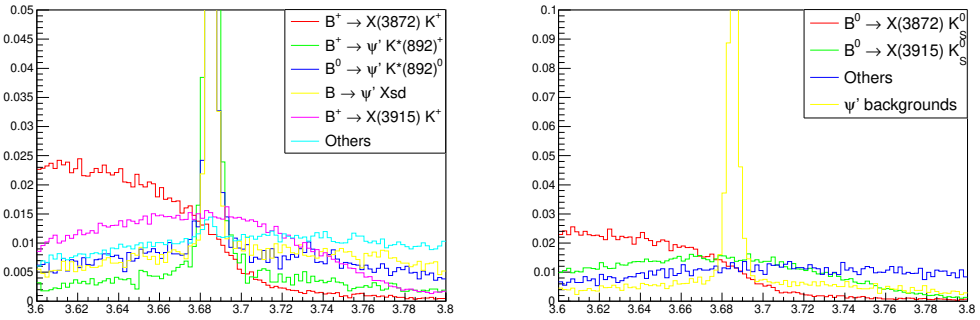

FIG. 3.21: Distributions of $M_{J/\psi\pi^+\pi^-}$ (in GeV/c^2) for charged B meson decays (left) and for neutral B meson decays (right) $B \to J/\psi X$ inclusive MC sample.

3.5.5 $M_{\omega K}$ selection

Huge background comes from $B^+ \to J/\psi K_1(1270)^+$ decays, where omega and kaon from $K_1(1270)$ have been misidentified as signal events. Those background events mostly contribute on $M_{J/\psi\omega}$ distribution above 4.15 GeV/c^2. In Fig. 3.22, we show the distribution of $M_{\omega K}$ for tagged MC events with $M_{J/\psi\omega} < 4.15$ GeV/c^2. Background events with higher $M_{\omega K}$ mostly contribute on the signal region. To reduce such backgrounds, we select the events with $M_{\omega K} < 1.97$ MeV/c^2. We estimate the efficiency of $M_{\omega K}$ selection with $\pm 4\sigma$ region for $X(3872)$ and $X(3915)$ events separately. It rejects 0.2% signal events with 7% of background events for $X(3872)$ decays, and rejects 14% of signal events and 15% background events for $X(3915) \to J/\psi\omega$ decays. As $M_{\omega K}$ selection improves the $X(3872) \to J/\psi\omega$ measurements, we apply this selection for further study.

3.5.6 Resolution improvement with ΔE constraining

In the ideal scenario, ΔE should be zero for perfect reconstruction. As we have π^0 in the final state, where π^0 is reconstructed in $\pi^0 \to \gamma\gamma$ decays. Rest of the final state particles are the charged tracks, where the precision of energy measurements are comparatively better. We assume that the resolution of ΔE is worse due to the poorly reconstructed π^0 candidates. In that scenario, we scale the π^0 momentum

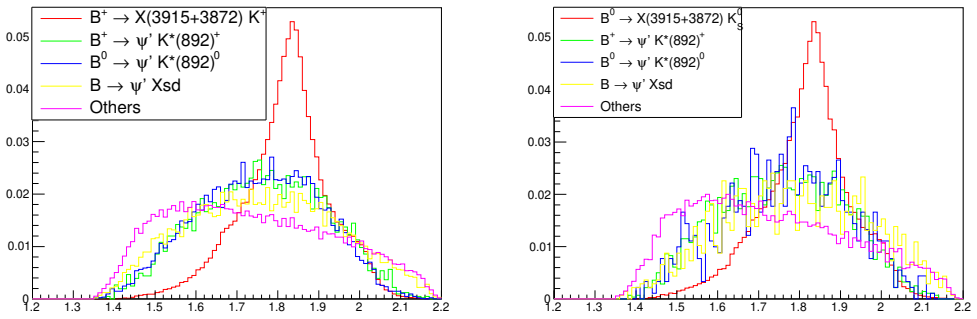

FIG. 3.22: $M_{\omega \mathrm{K}}$ (in GeV/c^2) distributions for signal events and dominating background components for charged B meson decays (left) and for neutral B meson decays (right) using $B \to J/\psi X$ inclusive MC sample.

and energy to force the ΔE to be 0, when mass of the π^0 remains unchanged. Energy scale factor (s) and momentum scale factor (α) can be expressed as,

$$s = \frac{E_{\mathrm{beam}} - (E_{\mathrm{J}/\psi} + E_{\pi^+} + E_{\pi^-} + E_{\mathrm{K}})}{E_{\pi^0}} \tag{3.10}$$

$$\alpha = \sqrt{1 - (1 - s^2)\frac{E_{\pi^0}^2}{|\vec{p}_{\pi^0}|^2}} \tag{3.11}$$

Where E_{x} represents the energy of a reconstructed particle (x). For any event, if α^2 is negative, we keep the π^0 unmodified. In Fig. 3.23, we compare $M_{\mathrm{J}/\psi\omega}$ distributions for charged and neutral modes, before and after the ΔE constraining. After ΔE constraining, one can notice a clear improvement for $M_{\mathrm{J}/\psi\omega}$ for the signal modes without sculpting the background shape. Also, we compare the distribution of M_{bc} before and after ΔE constraining in Fig. 3.24.

3.5.7 $M_{\mathrm{J}/\psi\omega}$ distribution

Finally, after applying all the selections, we plot the distribution of $M_{\mathrm{J}/\psi\omega}$ inside the signal window for both charged and neutral B reconstruction modes in Fig. 3.25. As one can see from the tagged $M_{\mathrm{J}/\psi\omega}$ distributions, there is no peaking background in the signal region. Also, the $X(3872)$ and $X(3915)$ signal distributions are nicely separated from each other.

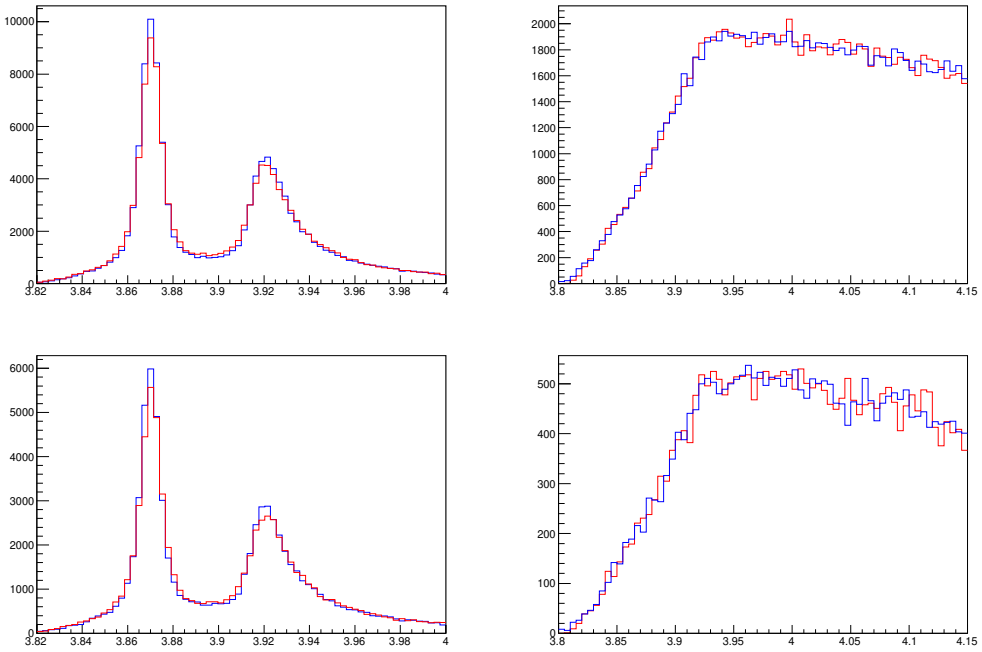

FIG. 3.23: Comparison of $M_{J/\psi\omega}$ (in GeV/c^2) resolutions before (red) and after (blue) ΔE constraining for signal events (left) and background events (right) using charged B meson decays (top) and using neutral B meson decays (bottom).

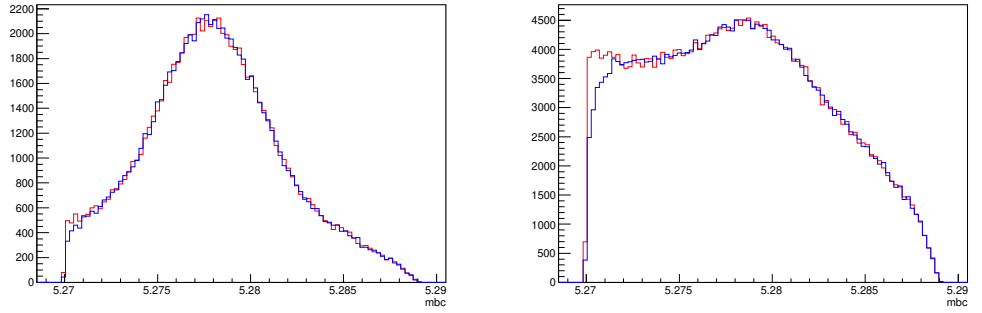

FIG. 3.24: Comparison of $M_{\rm bc}$ (in GeV/c^2) resolutions before (red) and after (blue) ΔE constraining for $B^+ \to J/\psi\omega K^+$ decays.

3.6 Signal Extraction

We use one dimensional unbinned maximum likelihood (UML) fit to extract the signal yields. We fit the $M_{J/\psi\omega}$ of signal and background components separately. Then, we combine the signal and background PDFs to get the final fits.

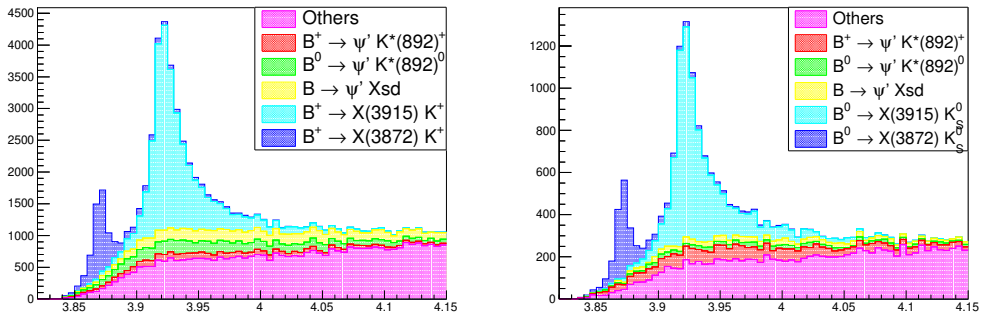

FIG. 3.25: $M_{J/\psi\omega}$ (in GeV/c^2) distributions for charged B meson decays (left) and for neutral B meson decays (right) using $B \to J/\psi X$ inclusive MC sample (with 100 times data).

3.6.1 Signal MC fits

We fit $M_{J/\psi\omega}$ distribution within 3.82 to 4.15 GeV/c^2 to get the efficiencies and resolutions of the signal modes. We use a sum of two Gaussian and a bifurcated Gaussians sharing a common mean for parameterization of each of the $X(3872)$ signal modes, and we use a sum of a Gaussian and two bifurcated Gaussians sharing a common to model the signal events for each of the $X(3915)$ modes. Signal fits for charged and neutral modes are shown in Fig. 3.26 and Fig. 3.27, respectively. Efficiency of a MC signal can be expressed in terms of the following relation.

$$\text{Signal efficiency } (\epsilon) = \frac{\text{Yield of fitted events}}{\text{Total number generated events}} \tag{3.12}$$

Estimated efficiencies for different signal modes are summarized in Tab. 3.2.

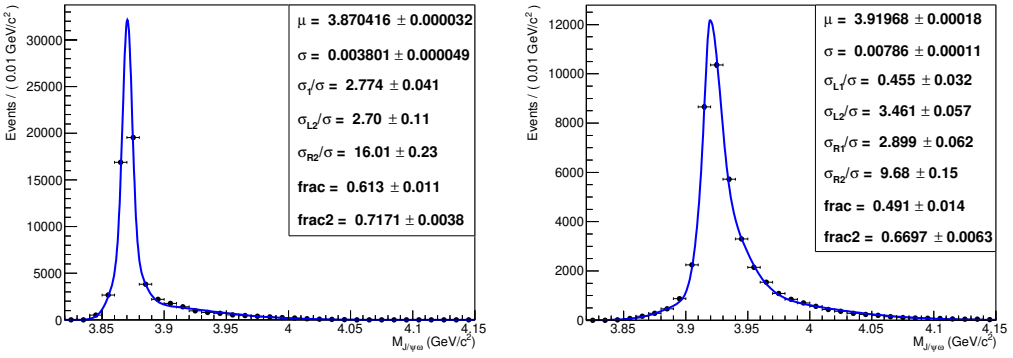

FIG. 3.26: UML fits to $M_{J/\psi\omega}$ (in GeV/c^2) for $B^+ \to J/\psi\omega K^+$ decays with $X(3872)$ (left) and $X(3915)$ (right) resonances using signal MC sample.

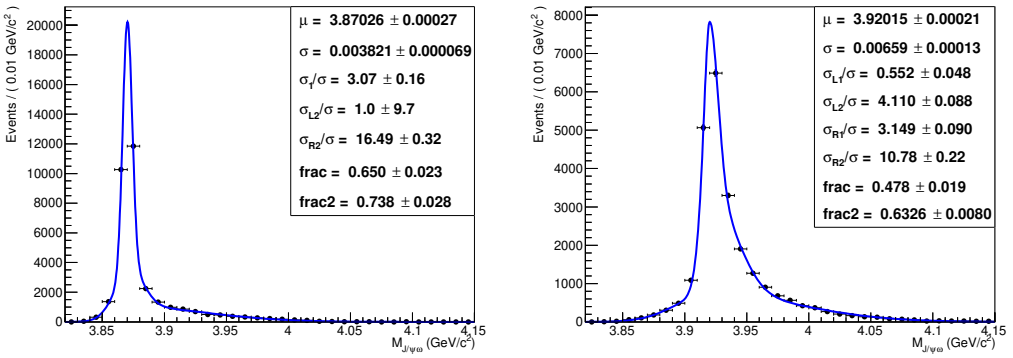

FIG. 3.27: UML fits to $M_{J/\psi\omega}$ (in GeV/c^2) for $B^0 \to J/\psi\omega K^0_S$ decays with $X(3872)$ (left) and $X(3915)$ (right) resonances using signal MC sample.

Decay mode	Resonance	ϵ (%)
$B^+ \to J/\psi\omega K^+$	$X(3872)$	5.37 ± 0.02
	$X(3915)$	4.06 ± 0.02
$B^0 \to J/\psi\omega K^0$	$X(3872)$	3.26 ± 0.01
	$X(3915)$	2.42 ± 0.01

TAB. 3.2: Estimated efficiencies for different signal modes.

3.6.2 Background fit

As one see from Fig. 3.25, the background distribution for both of the charged and neutral modes are not peaking in the signal region. We parameterize the background PDFs using a threshold polynomial likelihood function starting somewhere near 3.8 GeV/c^2. We tried a set of threshold polynomials. Finally, we choose the following likelihood function to extract the backgrounds for both charged and neutral modes.

$$\mathcal{L}(x; A, B, M_{th}) = \frac{e^{-N}}{N!} \prod_{i=1}^{N} (x - M_{th})^3 \exp\left[A(x - M_{th}) + B(x - M_{th})^2\right] \qquad (3.13)$$

Where A and B are the dimensionless shape parameters, and M_{th} is the threshold value of $M_{J/\psi\omega}$ variable. In Fig. 3.28, we show the fitted background distributions for signal and background.

3.6.3 Final fit to $B \to J/\psi X$ sample

We combine the signal and background PDFs to get the final fits to $M_{J/\psi\omega}$ distributions. We fixed the resolutions of the $X(3872)$ and $X(3915)$ PDFs from the signal MC

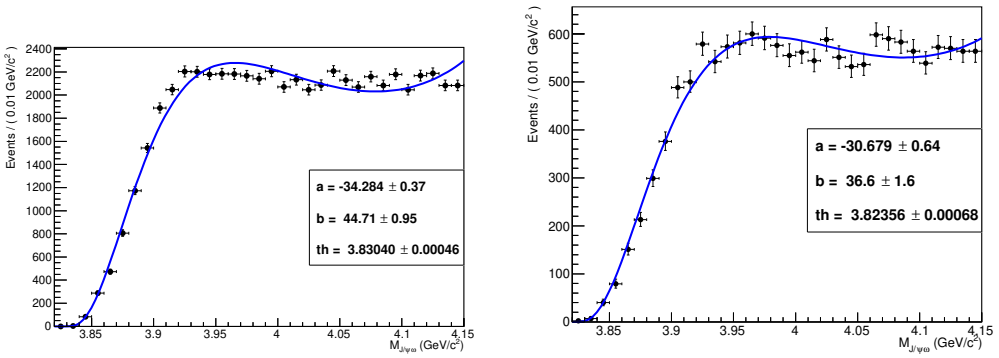

FIG. 3.28: UML fits to $M_{\mathrm{J}/\psi\omega}$ (in GeV/c^2) for $B^+ \to J/\psi\omega K^+$ decays (left) and for $B^0 \to J/\psi\omega K^0_S$ decays (right) using $B \to J/\psi X$ inclusive MC sample.

fits, and mean positions are floated to measure the masses of $X(3872)$ and $X(3915)$ resonances. For background, we fix the threshold points M_{th}, and the shape parameters A and B are allowed to float to normalize systematic effect in the data. Final $M_{\mathrm{J}/\psi\omega}$ fits for the charged and neutral B modes are shown in Fig. 3.29.

3.7 Validation of input branching fractions

We determine the branching fraction for $\mathcal{B}(B \to XK) \times \mathcal{B}(X \to J/\psi\omega)$ to check the validation of our MC fits, where X implies to $X(3872)$ or $X(3915)$ resonances. The branching fractions can be measured using the following relation.

$$\mathcal{B}[B \to X(J/\psi\omega)K] = \frac{N_{\mathrm{sig}}}{N_{\mathrm{B\bar{B}}} \times \epsilon \times \mathcal{B}_{secondary} \times \mathrm{f}_K} \tag{3.14}$$

Where N_{sig} is the signal yield for a particular resonance, $N_{\mathrm{B\bar{B}}}$ $(=(772 \pm 11) \times 10^6)$ is the estimated number of $B\bar{B}$ events in $\Upsilon(4S)$ data, and ϵ is the estimated signal efficiency. Here $\mathcal{B}_{secondary}$ $(=0.1052 \pm 0.0012)$ is the product of all the secondary branching fractions involved in the measurement process: $\mathcal{B}[J/\psi \to \ell\ell]$ (0.1193 ± 0.0010), $\mathcal{B}[\omega \to \pi^+\pi^0\pi^-]$ (0.892 ± 0.007), and $\mathcal{B}[\pi^0 \to \gamma\gamma]$ (0.9882 ± 0.0003). As we identify $K^\pm$ directly in the Belle detector, and we reconstruct K^0 in K^0_S decays, f_K coefficient is introduced to incorporate the kaon reconstructions. Here f_K has been considered to be 1.0 and 0.5 for charged and neutral modes, respectively. The uncertainties in real data is expected to increase by $\sim$ 10 times, as compared to uncertainties for $B \to J/\psi X$ sample. In Tab. 3.3, we summarize the measured branching fractions for different signal modes using the fits to $B \to J/\psi X$ sample.

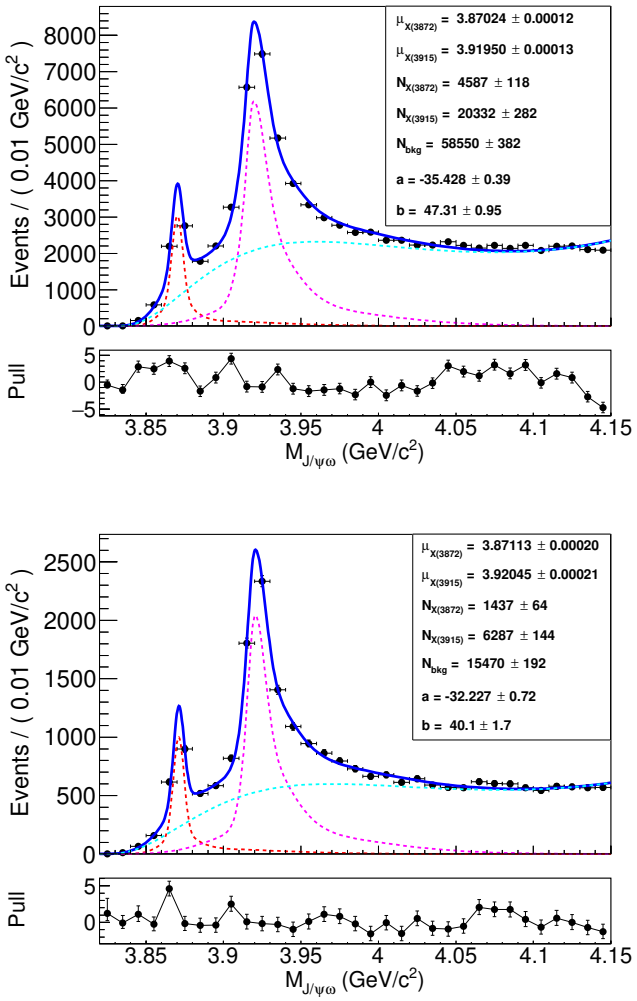

FIG. 3.29: UML fits to $M_{J/\psi\omega}$ (in GeV/c^2) for $B^+ \to J/\psi\omega K^+$ decays (left) and for $B^0 \to J/\psi\omega K^0_S$ decays (right) with $X(3872)$ (red), $X(3915)$ (magenta), and background (cyan) components using $B \to J/\psi X$ inclusive MC sample.

As one can see, obtained values of branching fractions agree with the input values within uncertainties.

Mode	Resonance	ϵ (%)	$N_{\rm sig}$	Measured BF	Input BF/Yield
K^+	$X(3872)$	5.37	45.9 ± 1.2	$(10.51 \pm 0.27) \times 10^{-6}$	10.30×10^{-6}
	$X(3915)$	4.06	203.3 ± 2.8	$(6.17 \pm 0.09) \times 10^{-5}$	203.5
K^0_S	$X(3872)$	3.26	14.4 ± 0.6	$(10.85 \pm 0.48) \times 10^{-6}$	10.30×10^{-6}
	$X(3915)$	2.42	62.9 ± 1.4	$(6.41 \pm 0.15) \times 10^{-5}$	62.5

TAB. 3.3: Measured input branching fractions for different decays.

3.8 Fit bias study

3.8.1 Pseudo experiment study

We generate 500 data samples using final signal and background PDFs for $M_{J/\psi\omega}$ distribution. For $B^+ \to J/\psi\omega K^+$ decay, after scaling to luminosity of $\Upsilon(4S)$ data, we find around 46, 203, and 586 yield for $X(3872)$, $X(3915)$, and background PDFs, respectively (Fig. 3.29). We generate the events accordingly using the PDFs fixing the shape from the MC fits. We perform UML fits for the generated toy samples in order to extract the signal yields for each toy data sets. To estimate the bias in our fitting model, we fit the distribution of fitted signal yield ($N_{\rm fit}$) and pull ($P_{\rm fit}$) using a Gaussian function. Here $P_{\rm fit}$ is defined as $\frac{N_{\rm fit}-N_{\rm gen}}{\delta N_{\rm fit}}$, where $\delta N_{\rm fit}$ and $N_{\rm gen}$ are the uncertainty in the fitted signal yield and corresponding generated signal yield, respectively. Distribution of the signal yield and pull are shown in Fig. 3.30. As one can see, the mean value (μ_1) of fitted signal yields for both $X(3872)$ and $X(3915)$ are close to the corresponding generated one. Also for pull distributions, mean values (μ_2) are close to 0 and sigma values (σ_2) are close to 1.

Similarly, we generate 500 data sets for neutral modes with 14, 63, and 155 events for $X(3872)$, $X(3915)$, and background events using pseudo experiments. In Fig. 3.31, we show the distribution fitted mean and pull, which agree well with the expected values. The fitted values for μ_1 are slightly deviated from the expected values. For charged (neutral) mode, we found a 0.8% (3.5%) bias for $X(3872)$ and 0.3% (3.3%) bias for $X(3915)$. These biases are included in the systematic uncertainty.

3.8.2 GSIM study

As a second test for fit bias study, we divide the $B^{\pm}$ events inside signal window for $B \to J/\psi X$ sample to 100 data sets by picking the events randomly. We fit each of the data sets using the final fitting model. Similar to pseudo experiment study, we fit the distribution of fitted signal yield and pull using a Gaussian function. Fitted distributions mean and pull for charged and neutral modes are shown in Fig. 3.32 and Fig. 3.33, respectively. As one can see from the respective figures for charged and neutral modes, for both $X(3872)$ and $X(3915)$ resonances the mean of the fitted signal yield (μ_1), mean of the pull (μ_2), and sigma of the pull (σ_2) agree to the expected values within uncertainties. For charged (neutral) mode, we found a

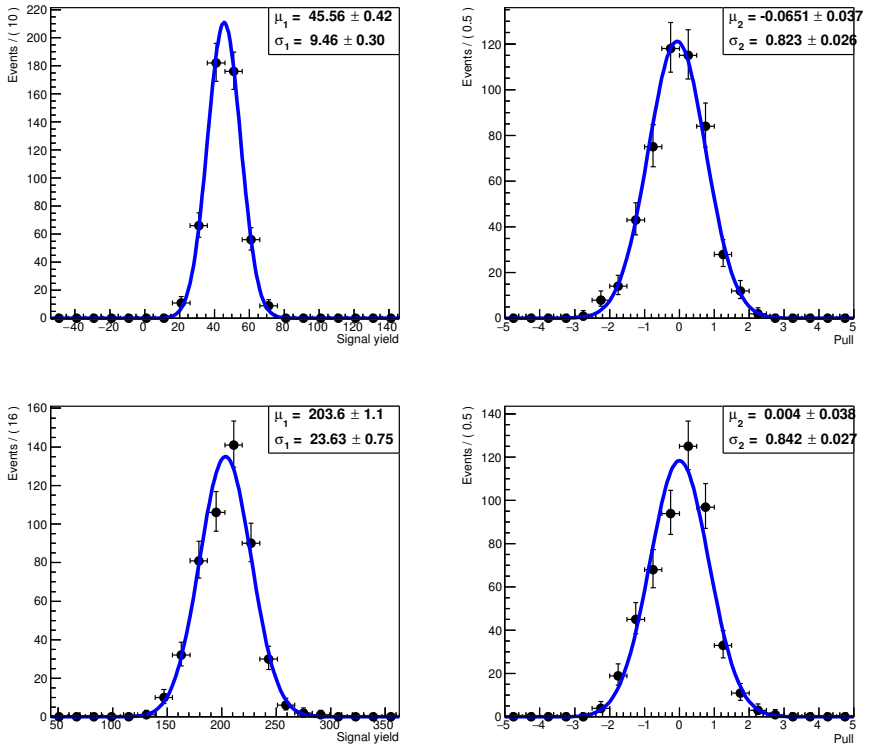

FIG. 3.30: UML fits to the distributions of fitted signal yield (left) and pull (right) for $B^+ \to J/\psi\omega K^+$ decays with $X(3872)$ (top) and $X(3915)$ (bottom) resonances.

2.6% (6.9%) bias for $X(3872)$ and 1.4% (3.7%) bias for $X(3915)$. These biases are included in the systematic uncertainty.

3.8.3 Linearity test

To check the stability of our fitting model, we perform a fit bias study over a range of signal yields. For charged mode, we choose the range of signal yield from 20 to 80 for $X(3872)$, and that for $X(3915)$ is from 50 to 400. We generate data sets for 2000 pseudo experiments varying the signal yields of $X(3872)$ and $X(3915)$ resonances with some interval. For each of input signal yields, we fit the distributions of output signal yield and pull using a Gaussian function. In Fig. 3.34, we show distributions of output signal yield and sigma of pull as a function of input yield. Similarly, for neutral mode, we check the stability of our fit with a signal yield from 10 to 50 for $X(3872)$, and from 20 to 140 for $X(3915)$ (in Fig. 3.35). Each of the distributions of $X(3872)$ and $X(3915)$ fitted well with a straight line (fit parameters are mentioned

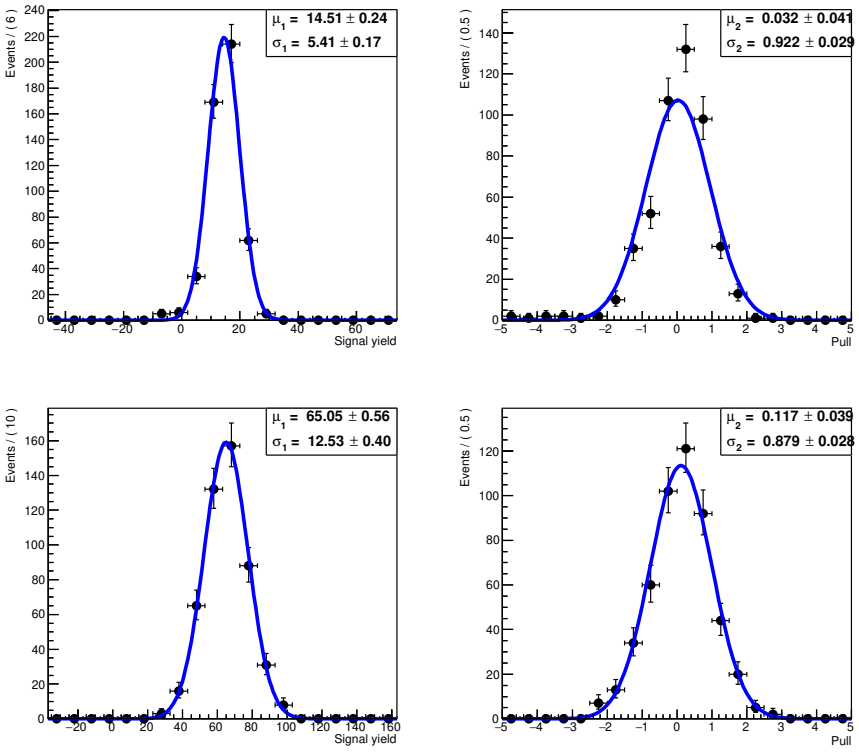

FIG. 3.31: UML fits to the distributions of fitted signal yield (left) and pull (right) for $B^0 \to J/\psi\omega K^0_S$ decays with $X(3872)$ (top) and $X(3915)$ (bottom) resonances using.

on the fits), which indicates that our fitting model is stable over an wide range of signal yield.

3.9 Systematic uncertainty

Estimating uncertainties coming from measurement techniques is crucial for all the physics analysis. We calculate those uncertainty from various sources, which have been discussed in this section.

3.9.1 Systematic from the number of $B\bar{B}$

In order to estimate the systematic uncertainty from the number of $B\bar{B}$, we use a previous Belle measurement. The expected number of $B\bar{B}$ events ($N_{\mathrm{B\bar{B}}}$) in 711 fb^{-1}

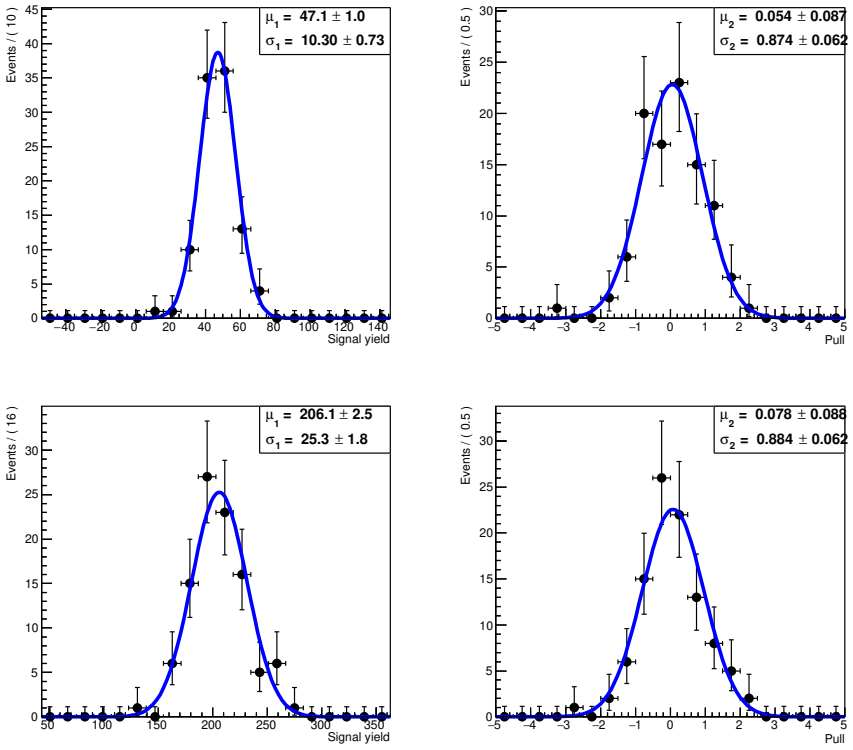

FIG. 3.32: UML fits to the distributions of fitted signal yield (left) and pull (right) for $B^+ \to J/\psi\omega K^+$ decays with $X(3872)$ (top) and $X(3915)$ (bottom) resonances using divided $B \to J/\psi X$ inclusive MC sample.

data on $\Upsilon(4S)$ resonance is estimated to be 772 ± 11 million. This result indicates the uncertainty from $N_{\mathrm{B\bar{B}}}$ is 1.42%.

3.9.2 Secondary branching fraction

We use some previously measured branching fractions to draw the final results. These fractions have some uncertainties. The uncertainties in the PDG values [15] can be taken as a source of systematic. The uncertainty coming from secondary branching fraction is estimated to be 1.14% for both of the charged and neutral $B \to J/\psi\omega K$ modes.

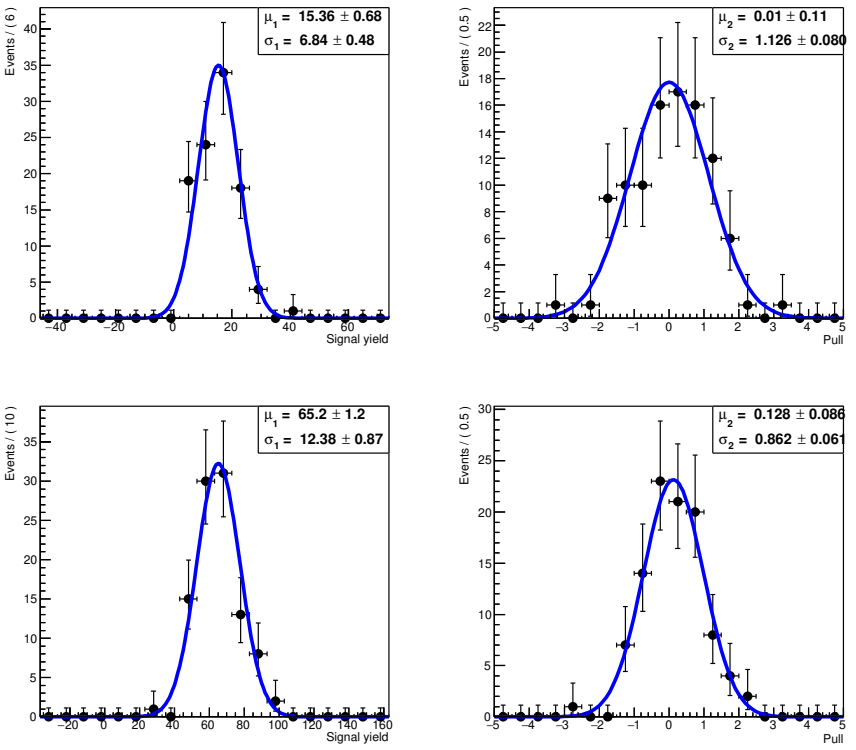

FIG. 3.33: UML fits to the distributions of fitted signal yield (left) and pull (right) for $B^0 \to J/\psi\omega K^0_S$ decays with $X(3872)$ (top) and $X(3915)$ (bottom) resonances using divided $B \to J/\psi X$ inclusive MC sample.

3.9.3 Track reconstruction

Systematic of charged particle tracks are studied using partially reconstructed $D^{*+} \to D^0(K^0_S\pi^+\pi^-)\pi^+$ decays with $p^T > 200$ MeV/c [87]. Systematic uncertainty associated with each charged track is estimated to be 0.35%. Due to correlation, these errors are added linearly. The number of charged tracks used for charged and neutral mode reconstructions are 5 and 6, respectively. Therefore, the systematic uncertainty from the track reconstruction efficiency for charged and neutral modes are estimated to be 1.75% and 2.10%, respectively.

3.9.4 Lepton identification

For lepton identification, systematic uncertainties are calculated from the comparison between data and MC for $2\gamma \to ee/\mu\mu$ decays. We are using $L_e > 0.01$ for electron identification, and $L_\mu > 0.1$ for muon identification. The muon identification cut

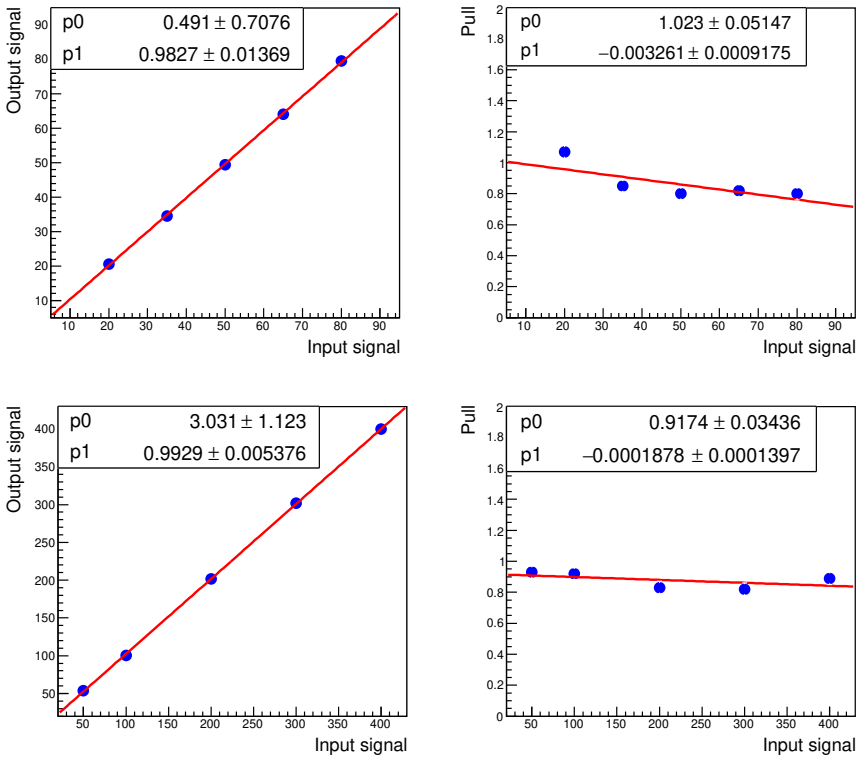

FIG. 3.34: For $B^+ \to J/\psi\omega K^+$ decays, output signal yield as a function of input signal yield (left), and pull distribution as a function of input signal yield (right) for $X(3872)$ (top) and $X(3915)$ (bottom) resonances.

(>0.1) is already studied at the Belle, and the electron identification cut (>0.01) is studied only for the Exp. 31 and above (after upgrading the SVD). Therefore, the systematic uncertainties associated with the L_e cut for the experiments below Exp. 31 is taken from an another Belle measurement [101]. The systematic uncertainties from lepton identification is summarized in Tab. 3.4. Efficiency correction factors for e^+e^- and $\mu^+\mu^-$ are the products of the individual correction factors. Uncertainties in the correction factors are considered as systematic errors. Due to the correlation, systematic from the individual leptons are added linearly to get the systematic errors for e^+e^- and $\mu^+\mu^-$ pairs. The results from experiments with SVD1 and SVD2 are normalized according to the corresponding luminosities. Combined values of e^+e^- and $\mu^+\mu^-$ modes (listed as $\ell^+\ell^-$) are calculated by normalizing them according to their reconstruction efficiencies and branching fractions.

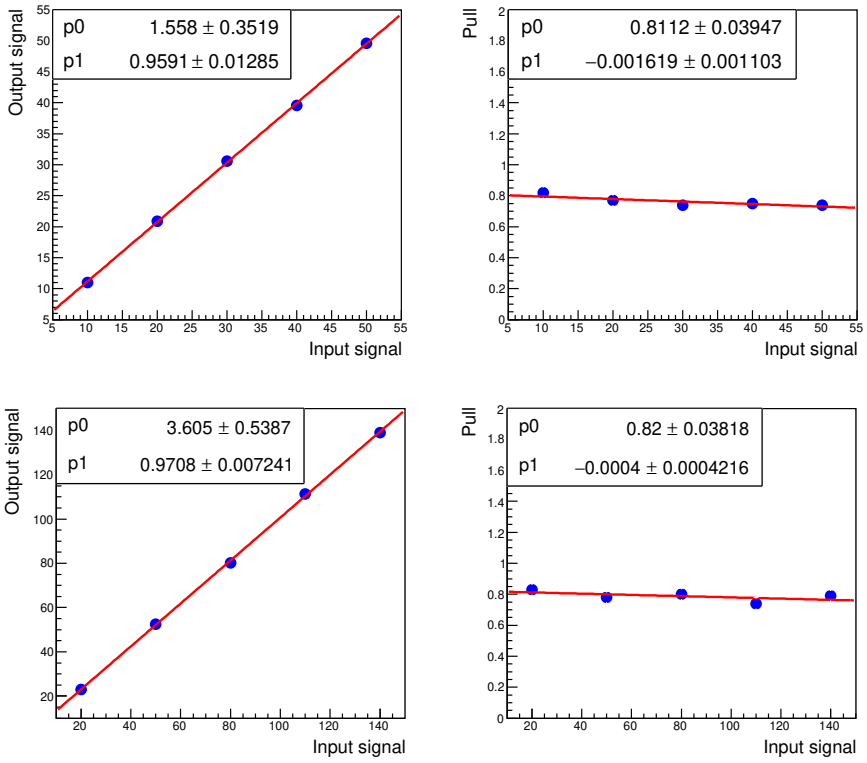

FIG. 3.35: For $B^0 \to J/\psi\omega K^0_S$ decays, output signal yield as a function of input signal yield (left), and pull distribution as a function of input signal yield (right) for $X(3872)$ (top) and $X(3915)$ (bottom) resonances.

		J/ψ mode	Efficiency correction factor				Systematic (%)			
			SVD1	SVD2	All Exp.	$\ell^+\ell^-$	SVD1	SVD2	All Exp.	$\ell^+\ell^-$
$X(3872)$	$K^\pm$	e^+e^-	0.9918	0.9659	0.9711	0.9623	1.10	2.06	1.87	2.22
		$\mu^+\mu^-$	0.9530	0.9554	0.9549		3.25	2.33	2.51	
	K^0_S	e^+e^-	0.9918	0.9659	0.9711	0.9622	1.10	2.06	1.87	2.22
		$\mu^+\mu^-$	0.9526	0.9554	0.9548		3.25	2.33	2.51	
$X(3915)$	$K^\pm$	e^+e^-	0.9918	0.9661	0.9712	0.9626	1.10	2.05	1.86	2.22
		$\mu^+\mu^-$	0.9512	0.9563	0.9553		3.26	2.34	2.52	
	K^0_S	e^+e^-	0.9918	0.9659	0.9711	0.9626	1.10	2.05	1.86	2.21
		$\mu^+\mu^-$	0.9525	0.9563	0.9555		3.21	2.34	2.51	

TAB. 3.4: Systematic uncertainties from lepton identifications.

3.9.5 Charged pion identification

To estimate the systematic uncertainty from pion identifications, we use standard results by the Belle particle identification group based on the $D^{*+} \to D^0(K^+\pi^-)\pi^+_{\rm slow}$ decay [88]. In that study, a correction for the difference in efficiency between data

and signal MC is obtained. This correction is used to correct the efficiency, and its error is added as systematic uncertainty associated with pion identification. The efficiency correction factors and systematic uncertainties associated with pion identifications are summarized in Tab. 3.5.

		Particle	Efficiency correction factor				Systematic (%)			
			SVD1	SVD2	All Exp.	$\pi^+\pi^-$	SVD1	SVD2	All Exp.	$\pi^+\pi^-$
$X(3872)$	$K^\pm$	π^+	1.0009	0.9998	1.0000	0.9999	0.78	1.33	1.22	2.44
		π^-	1.0005	0.9998	0.9999		0.77	1.33	1.22	
	K^0_S	π^+	1.0009	0.9998	1.0000	1.0000	0.79	1.34	1.23	2.45
		π^-	1.0007	0.9998	1.0000		0.78	1.33	1.22	
$X(3915)$	$K^\pm$	π^+	1.0002	0.9998	0.9999	0.9999	0.77	1.34	1.23	2.46
		π^-	1.0007	0.9999	1.0000		0.79	1.34	1.23	
	K^0_S	π^+	1.0005	0.9998	0.9999	0.9998	0.78	1.33	1.22	2.45
		π^-	1.0003	0.9998	0.9999		0.77	1.34	1.23	

TAB. 3.5: Systematic uncertainties from $\pi^\pm$ identifications.

3.9.6 π^0 reconstruction

There may be some difference for pion reconstruction efficiencies in data and MC. We use a previous Belle measurement to estimate the same [102]. For the π^0 with momentum 0 to 500 MeV/c, that study obtained the efficiency correction factor to be 1.009, and systematic uncertainty to be 2.28%. Most of the π^0 candidates used by this analysis belong to the same momentum range. Therefore, we use the above mentioned results in this study.

3.9.7 Charged kaon identification

To estimate data/MC correction factors associated with $K^\pm$, we use a study by the Belle particle identification group based on the decay $D^{*+} \to D^0(K^+\pi^-)\pi^+_{\rm slow}$ [88]. This correction is used to correct the efficiency, and its error is added as systematic uncertainty coming from kaon reconstruction. Fig. 3.6 summarizes the efficiency correction factors and systematic uncertainties for kaon identification.

Decay Mode	Resonance	Efficiency correction factor			Systematic (%)		
		SVD1	SVD2	All Exp.	SVD1	SVD2	All Exp.
$B^+ \to J/\psi\omega K^+$	$X(3872)$	1.0033	1.0071	1.0063	0.83	1.13	1.07
	$X(3915)$	1.0026	1.0073	1.0064	0.83	1.17	1.10

TAB. 3.6: Systematic uncertainties from $K^{\pm}$ identifications.

3.9.8 K^0_S reconstruction

K^0_S is reconstructed in $K^0_S \to \pi^+\pi^-$ decay, we use a previous Belle study to estimate the data/MC correction associated with K^0_S reconstruction [103]. According to the mentioned study, reconstructed K^0_S events belong to three momentum bins: (0.5-1.0) GeV/c, (1.0-1.5) GeV/c, and (1.5-2.0) GeV/c. We draw the effective correction factor according to the selected number of K^0_S events in different momentum bins. The final correction factors for $B^0 \to X(3872)K^0_S$ and $B^0 \to X(3915)K^0_S$ are 0.9907 ± 0.0077 and 0.9910 ± 0.0076, respectively. Therefore, the efficiency correction factor and the systematic uncertainty associated with $X(3872)$ ($X(3915)$) resonance are taken as 0.9907 (0.9910) and 0.78% (0.77%), respectively.

3.9.9 Uncertainty in signal efficiency

Due to limited size of generated signal events, we have certain fluctuation in the fitted signal events. As a result, there is some uncertainty in the obtained signal efficiency (ϵ), which can act as a source of systematic. We take the ratio of uncertainty of fitted events to the yield of fitted events ($\frac{\delta\epsilon}{\epsilon}$) for MC signal as the systematic uncertainty from signal efficiency (summarized in Tab. 4.10).

Decay mode	Resonance	Systematic uncertainty (%)
$B^+ \to J/\psi\omega K^+$	$X(3872)$	0.44
	$X(3915)$	0.50
$B^0 \to J/\psi\omega K^0_S$	$X(3872)$	0.57
	$X(3915)$	0.64

TAB. 3.7: Systematic uncertainties from fitted signal efficiencies.

3.9.10 Fitting model

Signal yield is extracted by fitting the experimental data. To fit the data, we fix some parameters of the signal PDF from the signal MC. Those parameters have some uncertainty which may affect the signal yield. We estimate those systematics by estimating the difference in the fitted yield in varying all the fixed parameters by $\pm 1\sigma$ from the central values. To include the data MC resolution difference, we consider a fudge factor 1.14 ± 0.03 [104]. We estimate the systematic uncertainty from the fudge factor varying the fudge factor by $\pm 1\sigma$ from the central value. The systematic uncertainties from the fitting model are listed in the Tab. 3.8. Also, we include the average values systematic uncertainties from pseudo experiment study and GSIM study to consider the uncertainties from fitting bias. We summarize the systematic uncertainties from fit biases in Tab. 3.9.

Mode	Resonance	Systematic (%)			
		Signal PDF	Background PDF	Fudge factor	Overall
K^+	$X(3872)$	$^{+1.11}_{-0.98}$	± 0.00	$^{+0.62}_{-1.21}$	$^{+1.27}_{-1.56}$
	$X(3915)$	$^{+2.21}_{-2.24}$	$^{+0.89}_{-0.74}$	$^{+1.63}_{-2.86}$	$^{+2.88}_{-3.71}$
K^0_S	$X(3872)$	$^{+0.82}_{-0.63}$	± 0.00	$^{+0.59}_{-0.64}$	$^{+1.01}_{-0.90}$
	$X(3915)$	$^{+2.02}_{-1.89}$	$^{+0.83}_{-1.24}$	$^{+1.58}_{-1.22}$	$^{+2.69}_{-2.57}$

TAB. 3.8: Systematic uncertainties from the fitting models.

3.9.11 Total systematic

Efficiency correction factors from the individual sources such as $N_{B\bar{B}}$, secondary branching fractions, track reconstruction, particle identification, signal efficiency, fitting model are multiplied to get the effective correction factors for different modes. Also, the systematic uncertainties for the individual sources are added in a quadrature to find the effective systematic errors. Effective correction factors and effective systematic uncertainties for different decay modes are summarized in Tab. 3.9.

3.10 Summary

We study the possible sources of background using $B \to J/\psi X$ inclusive MC sample. We estimate the efficiencies for different signal modes. Obtained results from MC

Source	Efficiency correction factor				Systematic (%)			
	$X(3872)$		$X(3915)$		$X(3872)$		$X(3915)$	
	K^+	K^0_S	K^+	K^0_S	K^+	K^0_S	K^+	K^0_S
Number of $B\bar{B}$	-	-	-	-	1.42	1.42	1.42	1.42
Secondary B.F.	-	-	-	-	1.14	1.14	1.14	1.14
Track reconstruction	-	-	-	-	1.75	2.10	1.75	2.10
$\ell^+\ell^-$ reconstruction	0.9623	0.9622	0.9626	0.9626	2.22	2.22	2.22	2.21
$\pi^+\pi^-$ reconstruction	0.9999	1.0000	0.9999	0.9998	2.44	2.45	2.46	2.45
π^0 reconstruction	1.0090	1.0090	1.0090	1.0090	2.28	2.28	2.28	2.28
K^+/K^0_S reconstruction	1.0063	0.9907	1.0064	0.9910	1.07	0.78	1.10	0.77
Signal efficiency	-	-	-	-	0.44	0.57	0.50	0.64
Fitting parameters	-	-	-	-	$^{+1.27}_{-1.56}$	$^{+1.01}_{-0.90}$	$^{+2.88}_{-3.71}$	$^{+2.69}_{-2.57}$
Fitting bias	-	-	-	-	1.72	5.24	0.91	3.45
Effective	0.9776	0.9618	0.9774	0.9623	$^{+5.33}_{-5.40}$	$^{+7.30}_{-7.28}$	$^{+5.76}_{-6.21}$	$^{+6.63}_{-6.58}$

TAB. 3.9: Effective efficiency correction factors and systematic uncertainties for different decay modes.

fitted events are validated with with good agreement. Most of the systematic uncertainties are estimated. We are waiting for the permission to study with real data.

Chapter 4

Search for CLFV decays of Υ(1S)

In this chapter, we describe analysis procedure, Monte-Carlo simulations, and obtained results on the search for charged lepton flavor violation (CLFV) in $\Upsilon(1S)$ decays. We choose $\Upsilon(2S) \to \pi^+\pi^-\Upsilon(1S)$ decays and further $\Upsilon(1S) \to \ell^\pm\ell'^\mp/\gamma\ell\ell'$ decays to search for the two- and three-body CLFV transition in $\Upsilon(1S)$ decays, where $\ell, \ell' = e, \mu, \tau$.

4.1 Signal Monte Carlo generation

We have generated 0.25 million signal events for each of the samples. In order to validate the signal extraction procedure, we study the $\Upsilon(1S) \to e^+e^-/\mu\mu$ as control modes. For $\Upsilon(2S) \to \pi^+\pi^-\Upsilon(1S)$ decays, we use the VVPIPI model (EvtGen model to generate a vector particle with a charged pion pair from a vector particle), and we use the VLL model (EvtGen model to generate two charged leptons from a vector particle) to generate the events for 2-body leptonic decays of $\Upsilon(1S)$. Further, we generate τ decays using the TAUOLA package [96] of PYTHIA package [97]. In absence of a suitable model, we use the PHSP model with PHOTOS to generate the events for $\Upsilon(1S) \to \gamma\ell^\pm\ell'^\mp$ events. In Fig. 4.1, we show the distribution of gamma energy in $\Upsilon(1S)$ of the generated events, which moderately agrees with the theoretical interpretation [47].

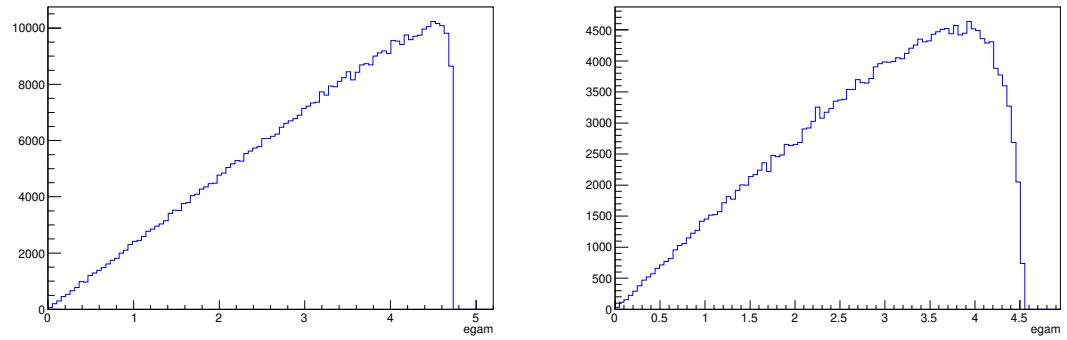

FIG. 4.1: E_γ distributions (in GeV) in the rest frame of $\Upsilon(1S)$ for generated $\Upsilon(1S) \to \gamma e^\pm \mu^\mp$ decays (left) and $\Upsilon(1S) \to \gamma \mu^\pm \tau^\mp$ decays (right).

4.2 Study of $\Upsilon(1S) \to e^\pm \mu^\mp$ decay

A schematic diagram of our decay of interest, $\Upsilon(2S) \to \pi^+\pi^-\Upsilon(1S)$, is presented in Fig. 4.2. As we are interested in $\Upsilon(1S)$ decays, we look at the $e\mu$ invariant mass which should peak around $\Upsilon(1S)$ mass ($M_{\Upsilon(1S)}$). We apply a cut on $M_{e\mu}$ in order to reduce background from low energetic lepton tracks. In order to extract the signal yield, we plot the mass difference of the reconstructed $\Upsilon(2S)$ and $\Upsilon(1S)$ mesons, $\Delta M = M_{\pi\pi\ell\ell} - M_{\ell\ell}$.

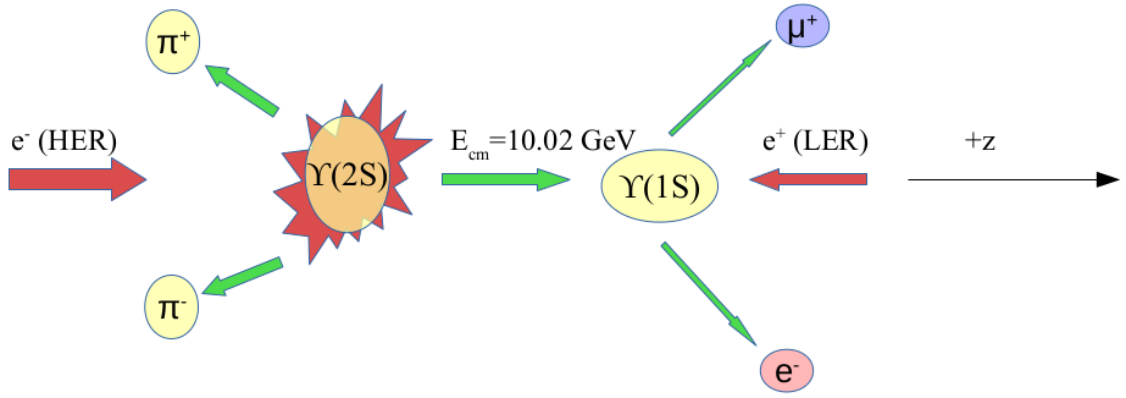

FIG. 4.2: Schematic diagram for $\Upsilon(2S) \to \pi^+\pi^-\Upsilon(1S)[\to e^\pm\mu^\mp]$ decay.

4.2.1 Event selection

As we have $\pi^+\pi^-\ell^+\ell^-$ in the final state, we use the following selections to identify the charged particle states.

- The distance of closest approach from the interaction point (IP) is less than 1 cm in vertical direction ($|dr|$) and is less than 3.5 cm in horizontal direction ($|dz|$).
- Pion vs kaon likelihood, $\mathcal{L}_\pi/(\mathcal{L}_\pi + \mathcal{L}_K)$ is greater than 0.6 to select pion candidates.
- $L_e > 0.1$ and $L_\mu > 0.1$ are used for basic reconstruction. Those are optimized later.

Along with the above selection, we select $\Upsilon(1S)$ having mass from 8.5 to 9.8 GeV/c^2. Photons within 50 mrad of each of $e^\pm$ original direction are considered as bremsstrahlung photons to get the correct four-momentum of $\Upsilon(1S)$ candidates. As there are four charged tracks with no neutral particle, number of events with multiple candidates is only 3%. The χ^2 of charged track vertex has been used to select the best candidate.

4.2.2 Background study

The background study has been performed using 158 million $\Upsilon(2S)$ generic MC sample and 80 fb^{-1} $\Upsilon(4S)$ off-resonance data.

Lepton identification: Backgrounds are found to come from $\Upsilon(1S) \to e^+e^-$ and $\Upsilon(1S) \to \mu^+\mu^-$ modes, when $e(\mu)$ is misidentified as $\mu(e)$. It is difficult to completely remove such backgrounds. We use a figure of merit (FOM) to optimize the L_e and L_μ cuts (Fig. 4.3). FOM is drawn using small-signal approach:

$$\text{FOM} = \frac{\epsilon}{a/2 + \sqrt{B}} \tag{4.1}$$

where ϵ, a, B are estimated efficiency, significance to be taken and number of the background events in generic MC sample. We take the a equals to 3, i.e. expected significance of 3σ. Optimized lepton identification cuts, $L_e > 0.6$ and $L_\mu > 0.95$, are used to suppress the background from lepton misidentification.

$M_{\Upsilon(1S)}$ **cut:** To decide the $\Upsilon(1S)$ signal region, we fit the $M_{\Upsilon(1S)}$ distribution to estimate the resolution. Then we select the 3σ region from the mean position (Fig. 4.4). The selected $M_{\Upsilon(1S)}$ signal window is 9.09 to 9.65 GeV/c^2, which rejects the 8% of signal and 21% of background events.

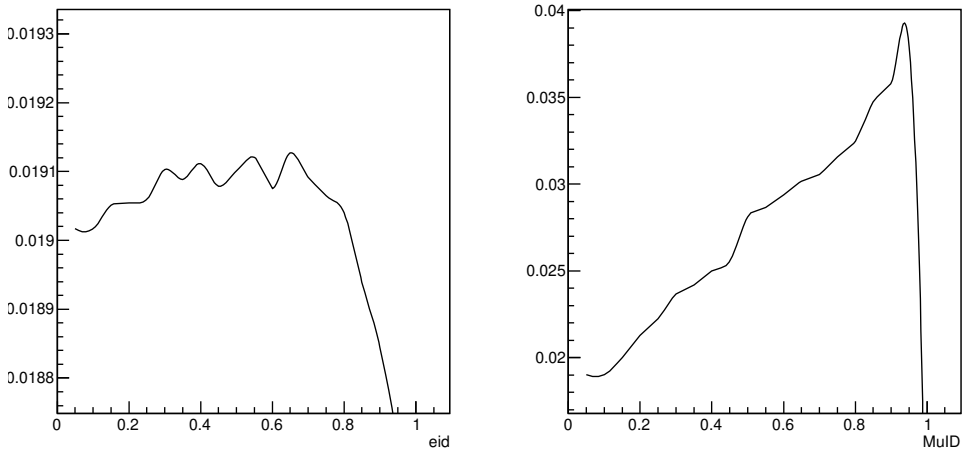

FIG. 4.3: Figure of merit for L_e optimization (left) and L_μ optimization (right).

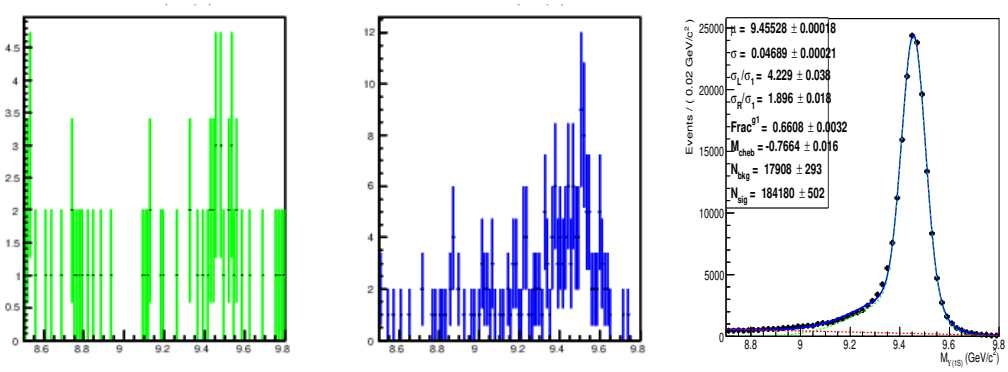

FIG. 4.4: $M_{\Upsilon(1S)}$ (in GeV/c^2) distributions for $\Upsilon(1S) \to e^\pm\mu^\mp$ decays using generic MC sample (left), $\Upsilon(4S)$ off-resonance data (middle), and UML fit to $M_{\Upsilon(1S)}$ (in GeV/c^2) using signal MC sample (right).

$|\vec{p}_{\Upsilon(1S)}|$ cut: For $e^+e^- \to q\bar{q}$ background study, $\Upsilon(4S)$ off-resonance data sample collected at 10.52 GeV is used. We scale yield of those events by a factor of $\frac{\mathcal{L}_{on}E_{off}^2}{\mathcal{L}_{off}E_{on}^2}$ (=0.3). Further, we select $\Upsilon(1S)$ with momentum in lab frame (Fig. 4.5) less than 4.4 GeV/c, which rejects 30% $e^+e^- \to q\bar{q}$ background with only 1% signal loss.

$N_{\rm e}$ and N_μ cut: We count the number of prompt (>1 GeV) electron ($N_{\rm e}$) and prompt muon (N_μ) for each event. As there are only one prompt electron and one prompt muon in the signal mode, one can see a delta function like distribution for signal mode (Fig. 4.6). Due to presence of electrons from converted photons, misidentified pions, distribution for backgrounds are deviated (Fig. 4.6). In order

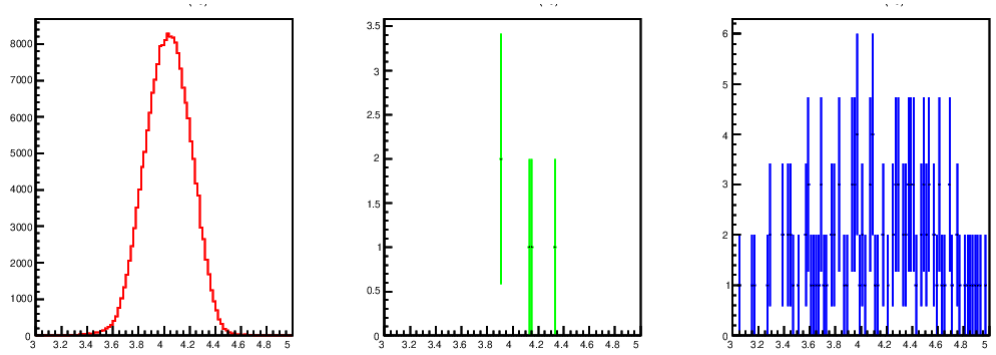

FIG. 4.5: $|\vec{p}_{\Upsilon(1S)}|$ (in GeV/c) distributions for $\Upsilon(1S) \to e^{\pm}\mu^{\mp}$ decays using signal MC sample (left), generic MC sample (middle), and $\Upsilon(4S)$ off-resonance data (right).

to remove those backgrounds, we select the events with $N_{\rm e} = 1$ and $N_{\mu} = 1$, which further rejects 0.6% of signal and 13% of background events.

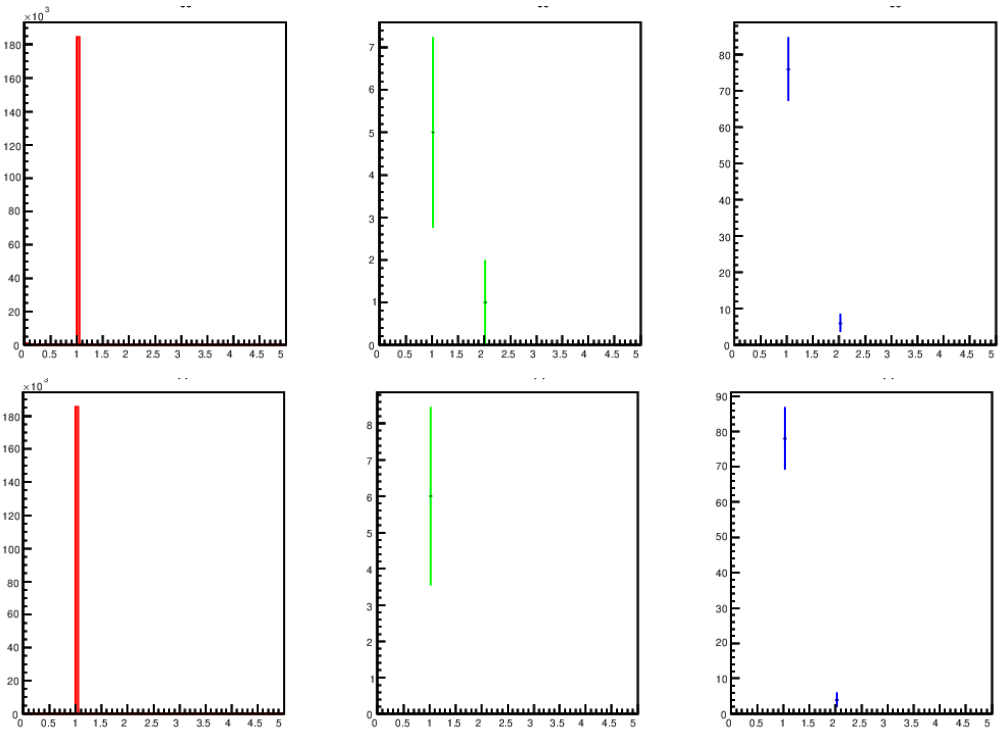

FIG. 4.6: $N_{\rm e}$ (top) and N_{μ} (bottom) distributions for $\Upsilon(1S) \to e^{\pm}\mu^{\mp}$ decays using signal MC sample (left), generic MC sample (middle), and $\Upsilon(4S)$ off-resonance data (right).

ΔM inside the signal window: Within signal window, we get 5 background events (including 2 events from $\Upsilon(1S) \to e^+e^-$ mode, 1 from $\Upsilon(1S) \to \mu^+\mu^-$ mode, and 2 from the hadronic decays of $\Upsilon(1S)$) in generic MC sample, and 72 events as $e^+e^- \to q\bar{q}$ background (Fig. 4.7).

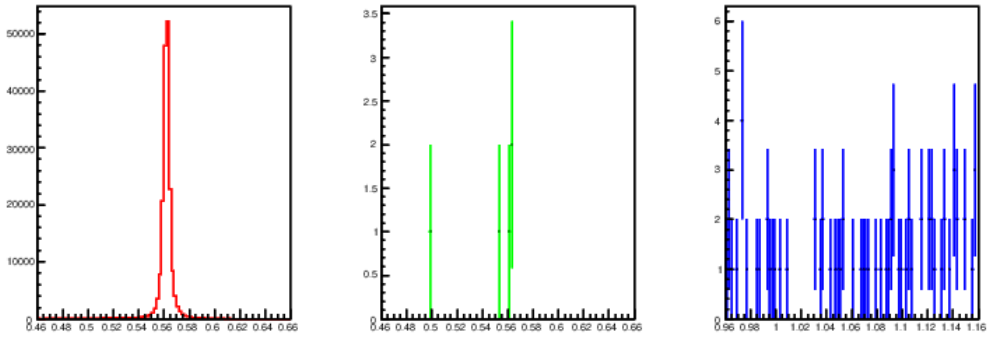

FIG. 4.7: ΔM (in MeV/c^2) distributions for $\Upsilon(1S) \to e^{\pm}\mu^{\mp}$ decays using signal MC sample (left), generic MC sample (middle), and $\Upsilon(4S)$ off-resonance data (right).

4.2.3 Signal extraction

We perform 1D unbinned likelihood (UML) fit with ΔM to extract the signal yield.

Signal MC fit: 1D UML fit with two Gaussians is performed on ΔM (Fig. 4.8) to get the resolution and efficiency of the signal events. The expected efficiency for $\Upsilon(1S) \to e^{\pm}\mu^{\mp}$ signal is 32.7%.

Peaking background estimation: Background events from electron vs muon misidentification have a prominent peak at the signal position. Therefore, we need to estimate the yield of lepton misidentification background precisely. We study them by generating a 40 million $\Upsilon(1S) \to \ell^{\pm}\ell^{\mp}$ $[\ell = e, \mu, \tau]$ MC sample. We fit those misidentification background events fixing all the parameters of the signal PDF (Fig. 4.9). For $\Upsilon(1S) \to e^+e^-$ decays, we find only 4 events (by counting the misidentified events), and expected misidentification yield to be negligible. After considering that 4 events, our $e \to \mu$ misidentification efficiency is expected to be $\sim 10^{-7}$. This can contribute a maximum up to 0.2 peaking background yield. For $\Upsilon(1S) \to \mu^+\mu^-$ background, estimated peaking background yield in MC is 3.5 ± 0.4.

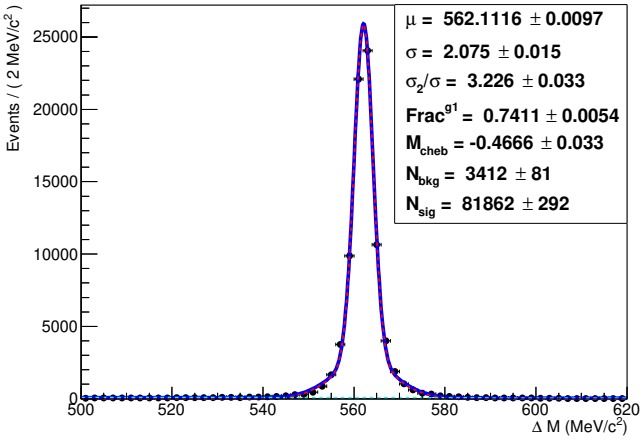

FIG. 4.8: UML fit to ΔM (in MeV/c^2) for $\Upsilon(1S) \to e^{\pm}\mu^{\mp}$ decays using signal MC sample.

$\Upsilon(2S)$ data is taken in experiment 67 and 71. As shown in appendix B.3, relative L_μ efficiency for Exp 51-73 is consistent with Exp 67 and Exp 71. Considering the muon misidentification correction factor to be 2.5 ± 0.5 (for Exp 51-73), misidentification yield in data is estimated to be 8.8 ± 2.0. Estimation of misidentification yield is summarized in Tab. 4.1.

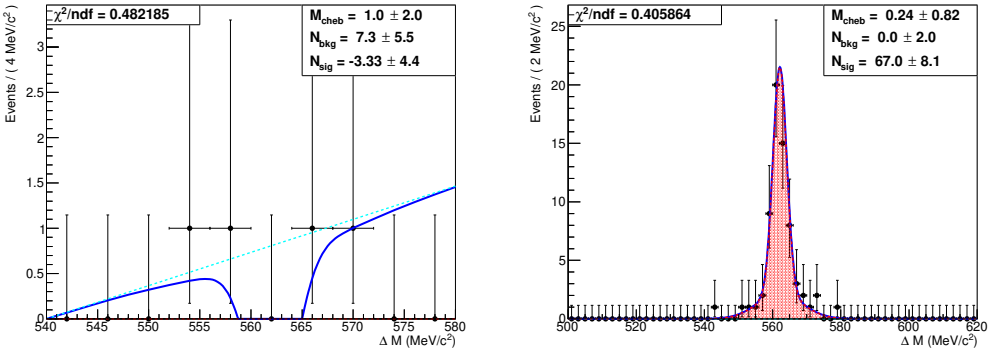

FIG. 4.9: UML fits to ΔM (in MeV/c^2) for $\Upsilon(1S) \to e^+e^-$ decays (left) and for $\Upsilon(1S) \to \mu^+\mu^-$ decays (right) for lepton misidentification backgrounds using 40 million $\Upsilon(1S) \to \ell^{\pm}\ell^{\mp}$ MC sample.

Background	Generated events in		Peaking misidentification yield		
	$\Upsilon(1S) \to \ell^{\pm}\ell^{\mp}$	$\Upsilon(2S)$ data	$\Upsilon(1S) \to \ell^{\pm}\ell^{\mp}$	Generic MC	$\Upsilon(2S)$ data
$\Upsilon(1S) \to e^+e^-$	12.8 million	0.67 million	-3.3 ± 4.4	< 0.2	–
$\Upsilon(1S) \to \mu^+\mu^-$	13.3 million	0.70 million	67.0 ± 8.1	3.5 ± 0.4	8.8 ± 2.0

TAB. 4.1: Estimation of electron and muon misidentification yield.

Flat background fit: Rest of the generic background is combined with the scaled $\Upsilon(4S)$ off-resonance data. Considering the energy difference between $\Upsilon(4S)$ off-resonance data and $\Upsilon(2S)$ on-resonance data, the signal search window for $e^+e^- \to q\bar{q}$ data is shifted by 500 MeV/c^2 with respect to the $\Upsilon(2S)$ signal window. We fit the rest of the background events fixing the shape of the signal PDF (Fig. 4.10). Estimated yield of those background is 0.0 ± 1.2. Hence, it is expected to be flat in data.

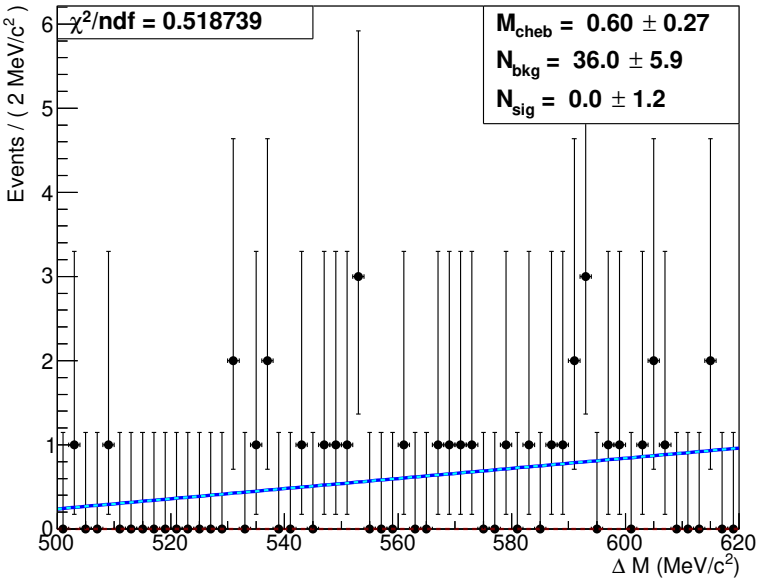

FIG. 4.10: UML fit to ΔM (in MeV/c^2) for backgrounds other than lepton misidentifications for $\Upsilon(1S) \to e^\pm\mu^\mp$ decays using generic MC sample with scaled $\Upsilon(4S)$ off-resonance data.

4.2.4 UL estimation with MC background

Once we study the $\Upsilon(2S)$ data, we will calculate the proper branching fraction. Before that we estimate the sensitivity of $\Upsilon(1S) \to e^\pm\mu^\mp$ transition using a frequentist method. We fix the shape of signal and background PDFs according to the generic MC fit. We generate a set 500 of samples having 30 background events. For each of these 500 samples, 10 signal samples have been generated with varying yields from 2 to 20. 1D UML fit is performed for each of these 5000 samples. Expecting 5.8 signal events at 90% confidence level (CL), we estimate the UL of branching fraction using

following relation.

$$\mathcal{B}^{UL}[\Upsilon(1S) \to \ell\ell'] < \frac{N_{\rm sig}^{\rm UL}}{N_{\Upsilon(2S)} \times \mathcal{B}[\Upsilon(2S) \to \pi^+\pi^-\Upsilon(1S)] \times \epsilon} \tag{4.2}$$

Where $N_{\rm sig}^{\rm UL}$ and ϵ are the signal yield at 90% CL and the efficiency of the signal, respectively. Using Eq. (5.8), the expected upper limit of the branching fraction for $\Upsilon(1S) \to e^{\pm}\mu^{\mp}$ with 90% CL is $\sim 10^{-7}$.

4.3 Study of $\Upsilon(1S) \to \mu^{\pm}\tau^{\mp}$ decay

Here τ is reconstructed from three decays: $\tau^- \to e^-\bar{\nu}_e\nu_\tau$, $\tau^- \to \pi^-\nu_\tau$, and $\tau^- \to \pi^-\pi^+\pi^-\nu_\tau$. To avoid the large background from $\Upsilon(1S) \to \mu^+\mu^-$ decays, we do not reconstruct the τ in $\tau^- \to \mu^-\bar{\nu}_\mu\nu_\tau$ decays.

4.3.1 Analysis strategy

We look at the recoil mass of two pions from $\Upsilon(2S)$ ($M_{\pi\pi}^{\rm recoil}$) which should peak at the $\Upsilon(1S)$ mass. One can evaluate the $M_{\pi\pi}^{\rm recoil}$ using the following relation:

$$M_{\pi\pi}^{\rm recoil} = \sqrt{(E_{\rm CM} - E_{\pi\pi}^*)^2 - |\vec{p}_{\pi\pi}|^2} \tag{4.3}$$

We select the optimized $M_{\pi\pi}^{\rm recoil}$ window which rejects most of the background coming from the $\Upsilon(2S)$ decays. We extract the signal with recoil mass of $\pi\pi\mu$ ($M_{\pi\pi\mu}^{\rm recoil}$) which should peak at the tau mass (1.775 GeV/c^2).

4.3.2 Event selection

Basic criteria for the identification of charged particles are same with the $\Upsilon(1S) \to e^{\pm}\mu^{\mp}$ study (section 4.2.1). In order to avoid huge hadronic background from $\Upsilon(1S)$ decays, events with number of pions less than 8 (5) have been used for $\tau^- \to \pi^-\pi^+\pi^-\nu_\tau$ ($\tau^- \to \pi^-\nu_\tau$) reconstruction. Further we select the candidate with three pion invariant ($M_{\pi\pi\pi}$) less than 1.8 GeV/c^2, and energy ($\rm E_{\pi\pi\pi}$) greater than 2.6 GeV for $\tau^- \to \pi^-\pi^+\pi^-\nu_\tau$ reconstruction to reject the hadronic background (Fig. 4.11).

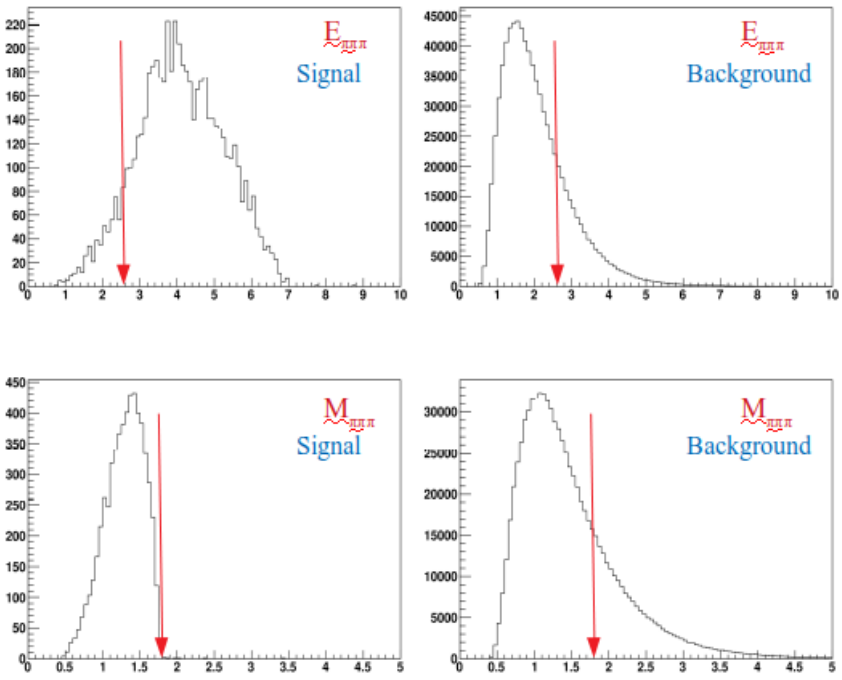

FIG. 4.11: $E_{\pi\pi\pi}$ (in GeV) distributions (top) and $M_{\pi\pi\pi}$ (in GeV/c^2) distributions (bottom) for $\tau^- \to \pi^-\pi^+\pi^-\nu_\tau$ decays using truth-matched signal events (left) and generic MC background events (right).

Vertex χ^2 has been used to choose the best candidate for the events with multiple $\Upsilon(2S)$ candidates.

4.3.3 Background study

We use 24.7 fb^{-1} $\Upsilon(2S)$ generic MC sample and 80 fb^{-1} $\Upsilon(4S)$ off-resonance data to study the background. We take the optimized L_μ cut, $L_\mu > 0.95$, from the $\Upsilon(1S) \to e^\pm\mu^\mp$ study.

$M_{\pi\pi}^{\rm recoil}$ window selection: $M_{\pi\pi}^{\rm recoil}$ distribution for signal MC and generic MC are shown in Fig. 4.12. For $\Upsilon(2S) \to \pi^+\pi^-\Upsilon(1S)$ decay, $M_{\pi\pi}^{\rm recoil}$ peaks at the $\Upsilon(1S)$ mass, and rest of the backgrounds remain flat. We optimize the $M_{\pi\pi}^{\rm recoil}$ window (Fig. 4.13) and select the events within 9.450 to 9.466 GeV/c^2, which rejects 9% of signal and 63% of background events.

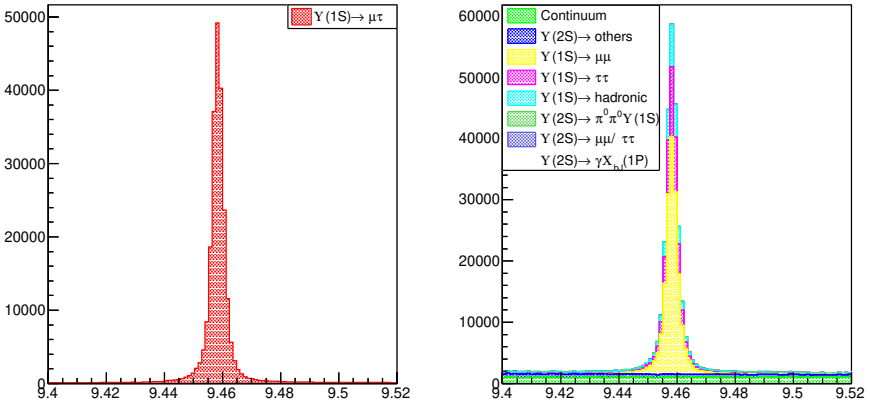

FIG. 4.12: $M_{\pi\pi}^{\text{recoil}}$ (in GeV/c^2) distributions for $\Upsilon(1S) \to \mu^{\pm}\tau^{\mp}$ decays using signal MC sample (left) and generic MC sample with scaled $\Upsilon(4S)$ off-resonance data (right).

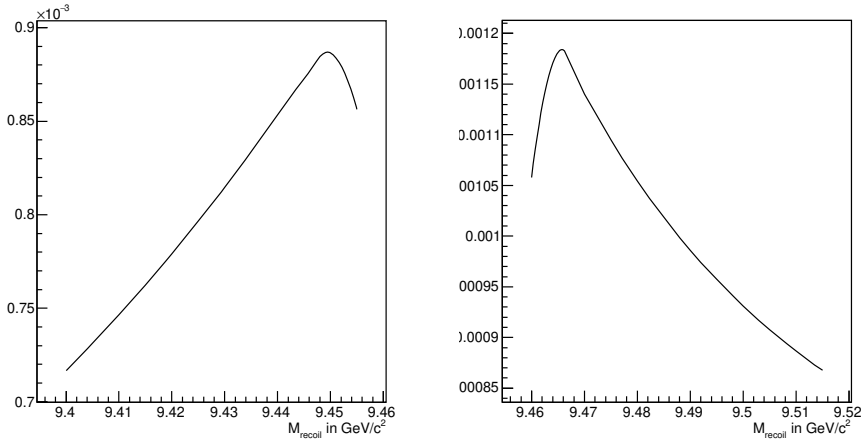

FIG. 4.13: Figure of merit for $M_{\pi\pi}^{\text{recoil}}$ optimization for $\Upsilon(1S) \to \mu^{\pm}\tau^{\mp}$ decays.

Prompt track counting: There is only one muon in our signal. As it is coming from the $\Upsilon(1S)$ decay, it should be high energetic. We count the number of prompt (with energy $>$ 1 GeV) muons (N_μ) and prompt electrons in each event ($N_{\rm e}$). Background coming from $\Upsilon(1S) \to \mu^+\mu^-$ decays have two prompt muons (Fig. 4.14). Therefore, events with N_μ equals to 1 have been selected. Further, we have selected the events from $\tau^- \to e^-\bar{\nu}_e\nu_\tau$ decays with $N_{\rm e} \leq 1$, and that for $\tau^- \to \pi^-\pi^+\pi^-\nu_\tau$ and $\tau^- \to \pi^-\nu_\tau$ with $N_{\rm e}$ equals to 0. These prompt track selections further reject 1% signal and 58% of the background events.

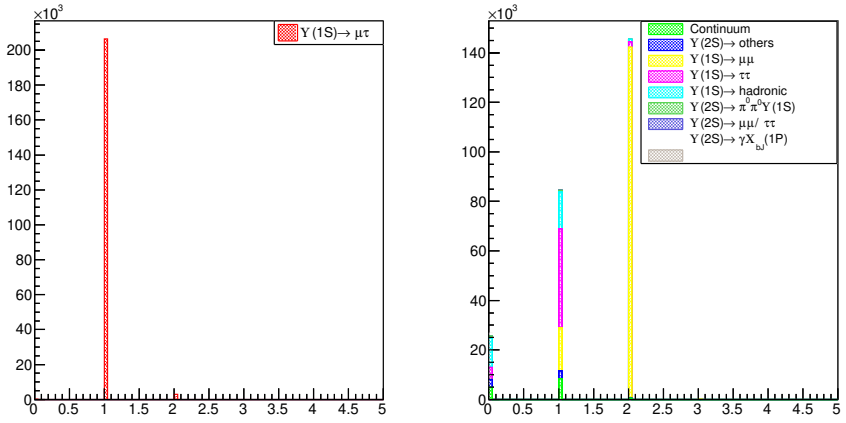

FIG. 4.14: N_μ distributions for $\Upsilon(1S) \to \mu^\pm\tau^\mp$ decays using signal MC sample (left) and generic MC sample with scaled $\Upsilon(4S)$ off-resonance data (right).

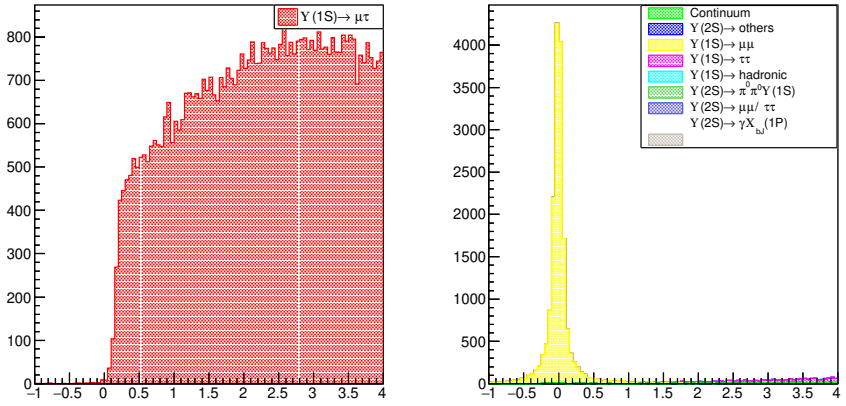

FIG. 4.15: δM (in GeV/c^2) distributions for $\Upsilon(1S) \to \mu^\pm\tau^\mp$ decays using signal MC sample (left) and generic MC sample with scaled $\Upsilon(4S)$ off-resonance data (right).

δM cut for $\tau^- \to \pi^-\nu_\tau$ mode: After applying $M_{\pi\pi}^{\text{recoil}}$ and prompt track selections, dominating background come through $\tau^- \to \pi^-\nu_\tau$ mode reconstruction. It seems that most of the backgrounds come from the $\Upsilon(1S) \to \mu^+\mu^-$ decays, where one muon misidentified as pion. Angular distribution of those pions shows two peaks at the junctions of the barrel and endcaps of KLM where muons remain undetected [more details in appendix B.1]. We tried to veto the misidentification peaks, but, it was not so helpful as the fake pions are distributed over the whole angular region. We look at the difference between recoil mass of two pions ($M_{\pi\pi}^{\text{recoil}}$) and the invariant mass of two leptons ($M_{\mu\tau}$), δM (Fig. 4.15). As τ decays with neutrino in the final

state, which do not interact with our detector, $M_{\mu\tau}$ get shifted from its real value, and δM also get shifted from 0. But for the $\Upsilon(1S) \to \mu^+\mu^-$ decays, as there is no missing neutrino δM peaks at 0. We select the region with $\delta M > 1$ GeV/c^2, which causes 8.5% loss in signal events and 70% reduction of background events.

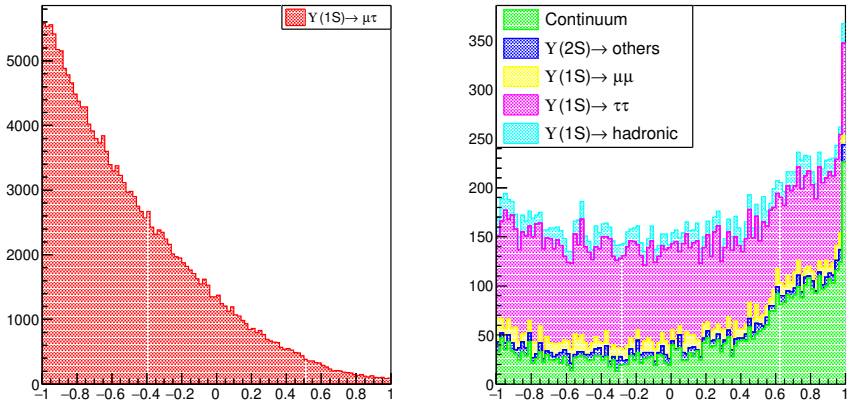

FIG. 4.16: $\cos(\theta_{\pi\pi})$ distributions for $\Upsilon(1S) \to \mu^{\pm}\tau^{\mp}$ decays using signal MC sample (left) and generic MC sample with scaled $\Upsilon(4S)$ off-resonance data (right).

$\cos(\theta_{\pi\pi})$ **window selection:** Pions from $\Upsilon(2S)$ decays can have momentum less than 250 MeV/c. In that energy region, a converted photon from $e^+e^-\gamma$ and $\mu^+\mu^-\gamma$ background can be identified as pions. Distribution of cosine angle between two pions from $\Upsilon(2S)$ ($\cos(\theta_{\pi\pi})$) in CM frame shows a clear increase in the $e^+e^- \to q\bar{q}$ background after $\cos(\theta_{\pi\pi}) > 0.5$ (Fig. 4.16). We select the events with $\cos(\theta_{\pi\pi}) < 0.5$ to remove such background, which further reject 2% of signal and 34% of background events.

$p^{\tau}_{\rm vis}$ **window selection:** Here τ has been reconstructed from $\tau^- \to e^-\bar{\nu}_e\nu_\tau$, $\tau^- \to \pi^-\nu_\tau$, $\tau^- \to \pi^-\pi^+\pi^-\nu_\tau$ decays. Fraction of tau momentum shared by the visible daughter particles can have a wide range. Fig. 4.17 compares the visible momentum distribution of τ for signal and background events. Background coming from the low energetic electrons dominates near the low $p^{\tau}_{\rm vis}$ region. Events with $p^{\tau}_{\rm vis} > 0.3$MeV/c have been selected to remove such evens, which further rejects 19% of background with a signal loss of 4%.

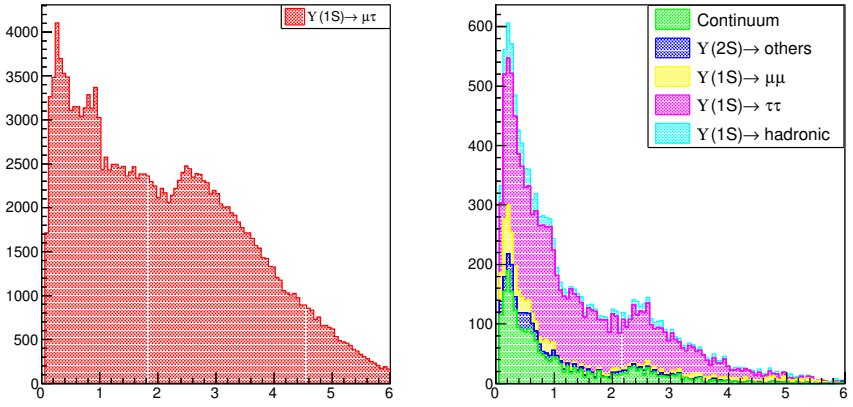

FIG. 4.17: $p^{\tau}_{\rm vis}$ (in GeV/c) distributions for $\Upsilon(1S) \to \mu^{\pm}\tau^{\mp}$ decays using signal MC sample (left) and generic MC sample with scaled $\Upsilon(4S)$ off-resonance data (right).

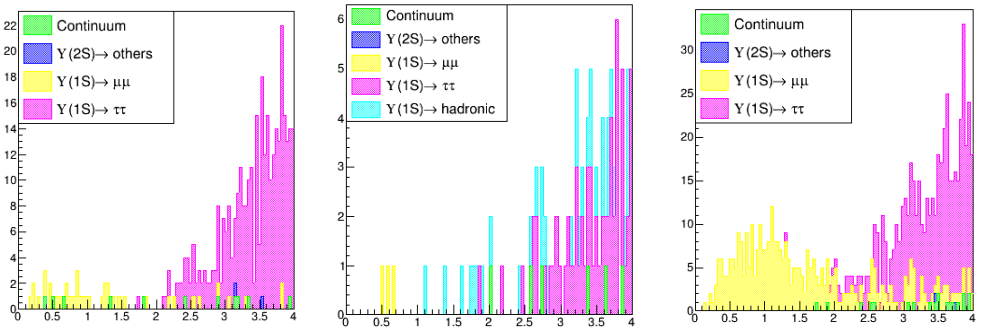

FIG. 4.18: $M^{\rm recoil}_{\pi\pi}$ (in GeV/c^2) distributions for background evens for $\tau^- \to e^-\bar{\nu}_e\nu_\tau$ mode (left), $\tau^- \to \pi^-\pi^+\pi^-\nu_\tau$ mode (middle), and $\tau^- \to \pi^-\nu_\tau$ mode (right) using generic MC sample with scaled $\Upsilon(4S)$ off-resonance data.

Distribution of $M^{\rm recoil}_{\pi\pi\mu}$: We plot the $M^{\rm recoil}_{\pi\pi\mu}$ inside the signal window. Out of the three tau modes, most of the background near signal region is coming from the $\tau^- \to \pi^-\nu_\tau$ mode (Figure 4.18). As seen from the figure, low background from the two tau modes will provide better sensitivity.

4.3.4 Signal extraction

As one can see from Fig. 4.18, most of the backgrounds come from the $\tau^- \to \pi^-\nu_\tau$ mode. We estimate the upper limit for two cases: with and without $\tau^- \to \pi^-\nu_\tau$ mode. Signal yield and UL are estimated using combined and simultaneous fit for

both of the cases. We find that the combined fit with two modes is a bit better than others. Here we provide all the fits corresponding to two combined τ modes (excluding $\tau^- \to \pi^-\nu_\tau$).

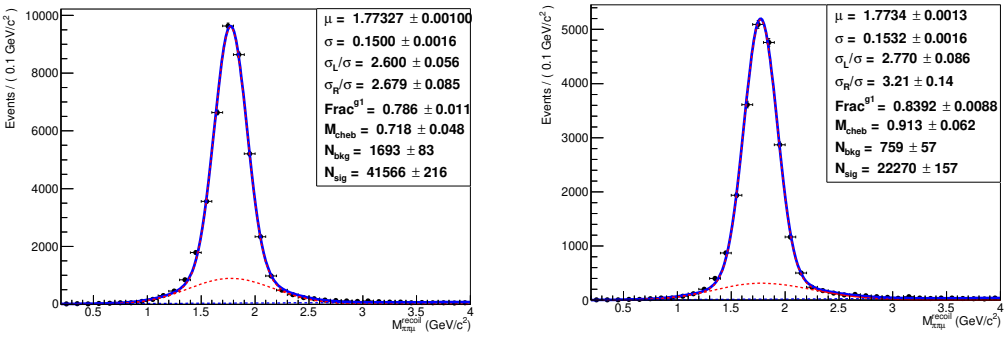

FIG. 4.19: UML fits to $M^{\text{recoil}}_{\pi\pi\mu}$ (in GeV/c^2) for $\Upsilon(1S) \to \mu^\pm\tau^\mp$ decays with $\tau^- \to e^-\bar{\nu}_e\nu_\tau$ reconstruction mode (left) and with $\tau^- \to \pi^-\pi^+\pi^-\nu_\tau$ reconstruction mode (right) using signal MC sample.

Decay $\Upsilon(1S) \to \mu^\pm\tau^\mp$	Effective efficiency (%)
$\tau^- \to e^-\bar{\nu}_e\nu_\tau$	8.3
$\tau^- \to \pi^-\pi^+\pi^-\nu_\tau$	0.8
Combined efficiency	9.1

TAB. 4.2: Effective signal efficiencies for $\Upsilon(1S) \to \mu^\pm\tau^\mp$ decays using different τ modes.

Signal MC fit: Inside the signal window, we perform 1D UML fit on $M^{\text{recoil}}_{\pi\pi\mu}$ with one Gaussian and one bifurcated Gaussian. We fit each of the two tau decay modes separately to get the individual efficiency (Fig. 4.19). Fitted efficiency for $\tau^- \to e^-\bar{\nu}_e\nu_\tau$ mode has been estimated using a MC sample with 0.5 million $\Upsilon(1S) \to \mu^\pm\tau^\mp$ decays, where τ decays generically. As $\tau^- \to \pi^-\pi^+\pi^-\nu_\tau$ decays are not included in the generic tau decays at Belle, we use 0.25 million of $\Upsilon(1S) \to \mu^\pm\tau^\mp$ to estimate the efficiency for $\tau^- \to \pi^-\pi^+\pi^-\nu_\tau$, where tau decays to 3-pion final state. Fitted efficiencies are listed in Tab. 4.2. Effective efficiency with $\tau^- \to \pi^-\pi^+\pi^-\nu_\tau$ decays is calculated by multiplying the corresponding tau decay branching fraction with fitted efficiency.

Background fit: $\Upsilon(1S) \to \tau^+\tau^-$ and $\Upsilon(1S) \to \mu^+\mu^-$ decays are the dominant sources of background here. Size of generic MC sample is not good enough. Therefore,

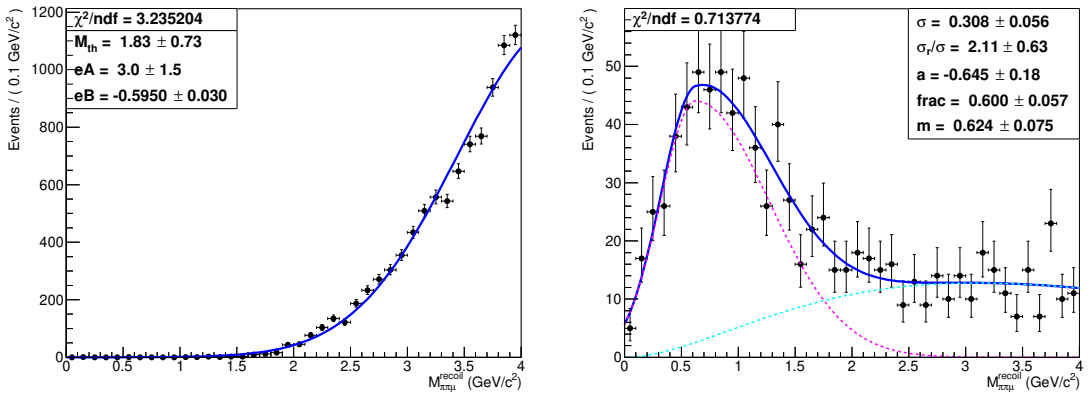

FIG. 4.20: UML fits to $M^{\text{recoil}}_{\pi\pi\mu}$ (in GeV/c^2) for $\Upsilon(1S) \to \tau^+\tau^-$ backgrounds (left) and for $\Upsilon(1S) \to \mu^+\mu^-$ background (right) using 40 million $\Upsilon(1S) \to \ell^\pm\ell^\mp$ MC sample.

we use 40 million $\Upsilon(1S) \to \ell^\pm\ell^\mp$ MC sample to get the shape of the $\tau\tau$ and $\mu\mu$ background. We define the following likelihood function to model the $\tau\tau$ background.

$$\mathcal{L}(x; A, B, M_{th}) = \frac{e^{-N}}{N!} \prod_{i=1}^{N} \exp^{A(x-M_{th})+B(x-M_{th})^2} \tag{4.4}$$

We use the sum of a bifurcated Gaussian and a threshold function (starting from 0) to model $\mu\mu$ background. Fig. 4.20 summarizes the fits for $\Upsilon(1S) \to \tau^+\tau^-$ and $\Upsilon(1S) \to \mu^+\mu^-$ background fits using 40 million $\Upsilon(1S) \to \ell^\pm\ell^\mp$ MC sample.

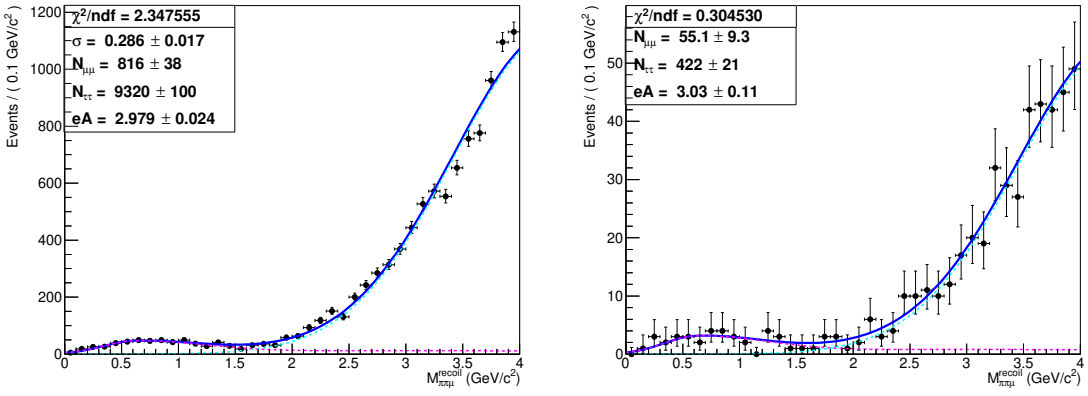

FIG. 4.21: UML fits to $M^{\text{recoil}}_{\pi\pi\mu}$ (in GeV/c^2) for backgrounds using 40 million $\Upsilon(1S) \to \ell^\pm\ell^\mp$ MC sample (left) and using generic MC sample (right).

We combine both of the background components to get the shape of the effective background. One shape parameter of the $\tau\tau$ PDF (A) and resolution (σ) of $\mu\mu$

background have been floated and rest of the parameters are fixed from the individual background fits (Fig. 4.21).

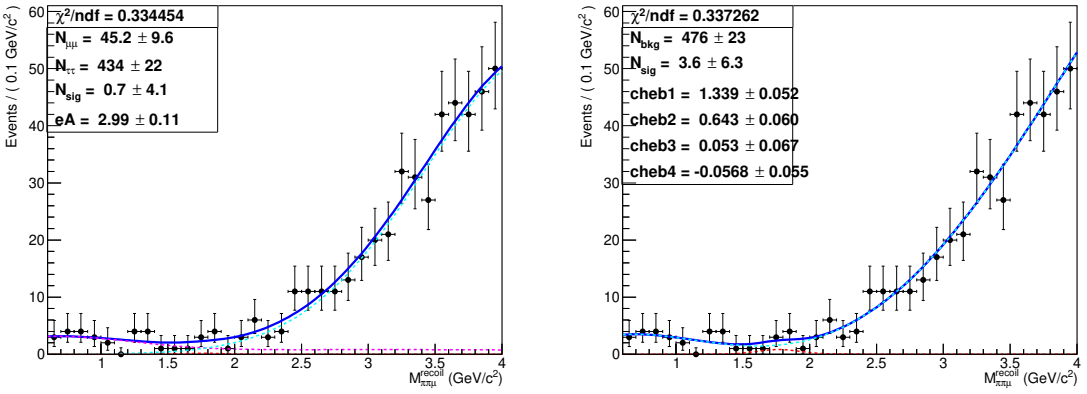

FIG. 4.22: UML fits to $M^{\text{recoil}}_{\pi\pi\mu}$ (in GeV/c^2) for combined signal and backgrounds with nominal background PDF (left) and with polynomial background PDF (right) using generic MC sample with scaled $\Upsilon(4S)$ off-resonance data.

Generic MC fit: We fit the generic background fixing the resolution of the $\mu\mu$ background from the combined background fit. To estimate the peaking background yield, we fit generic background with a combined (signal and background) PDF within 0.6 to 4.0 GeV/c^2. Parameters of the signal PDF are fixed using the generated signal MC. Expected yield of peaking background is estimated to be 0.7 ± 4.1. Also, as an alternative approach, we fit generic MC events considering the background as a 4th order Chebychev polynomial. In this case, total yield of the peaking background is estimated to be 3.6 ± 6.3. Both of the generic MC fits are shown in Fig. 4.22. Peaking background yields from both of the fits are consistent with 0 within the uncertainties.

4.3.5 Fit bias study

We study the stability of the signal extraction PDF for the nominal background using an ensemble of 2000 pseudo experiments. We generate data sets with constant 478 background events fixing all the parameters of the final PDF, and fit each of those data sets. We fit the distribution of signal yields and uncertainties with Gaussian PDFs (Fig. 4.23). We find good agreement for the mean of the signal yield and uncertainty distributions with the fit using nominal background PDF.

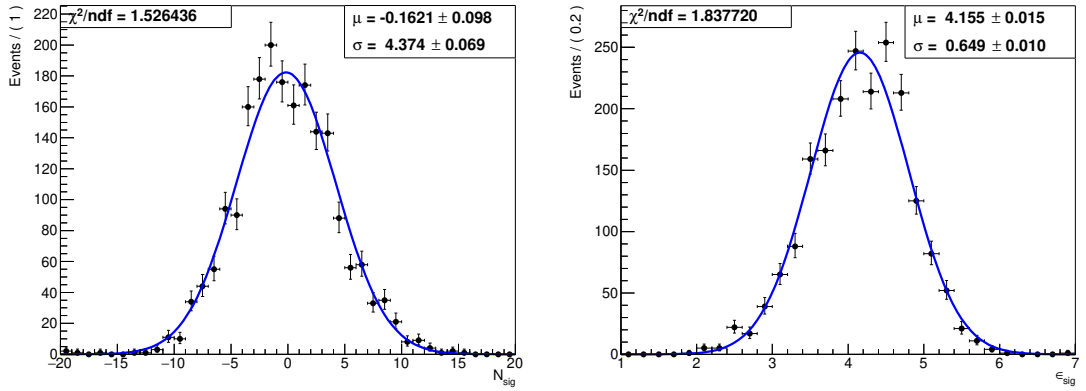

FIG. 4.23: UML fits to the fitted mean of signal yields of the pseudo experiments (left) and fitted uncertainty of signal yields of the pseudo experiments (right).

4.3.6 Data-MC resolution difference

To fix the width of $\Upsilon(1S) \to \mu^{\pm}\tau^{\mp}$ signal in data, we check the data-MC resolution difference for $M^{\text{recoil}}_{\pi\pi\mu}$ variable using $\Upsilon(1S) \to \mu^+\mu^-$ events. We fit the MC events with sum of a Gaussian and a bifurcated Gaussian. $\Upsilon(1S) \to \mu^+\mu^-$ events from data are fitted with the same PDF fixing the shape of the tail parameters. $M^{\text{recoil}}_{\pi\pi\mu}$ fits to MC and data events are shown in Fig. 4.24. We obtain a resolution difference between MC and data to be 6.5%.

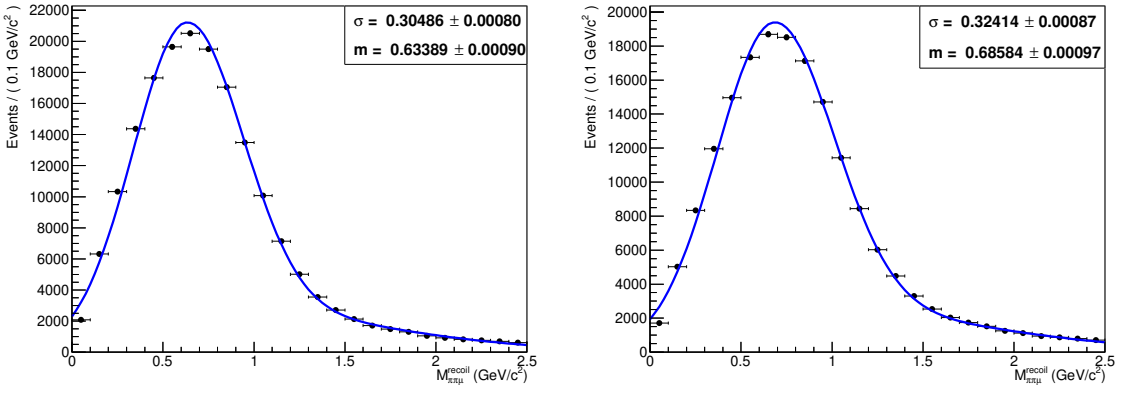

FIG. 4.24: UML fits to $M^{\text{recoil}}_{\pi\pi\mu}$ (in GeV/c^2) for $\Upsilon(1S) \to \mu^+\mu^-$ events using generic MC sample (left) and $\Upsilon(2S)$ data (right).

4.3.7 UL estimation with MC background

We estimate the sensitivity of $\Upsilon(1S) \to \mu^{\pm}\tau^{\mp}$ transition using a frequentist method. From the fits to the generic MC sample, signal and background PDF shapes are used to generate the toy MC data. To the generated toy data, background yield is generated as per our fit to the generic MC (Fig. 4.22) varying the signal yield from 2 to 20 (in 10 steps). In order to mimic the statistical fluctuation, we allow Poisson fluctuation in the generated yield. We perform 1D UML fit for each of these samples and estimate the possible CL. One can expect the UL of the signal yield to be 7.8 at 90% CL. One can calculate the UL of branching fraction using relation (5.8). The expected upper limit of the branching fraction for $\Upsilon(1S) \to \mu^{\pm}\tau^{\mp}$ with 90% CL is $\sim 10^{-6}$.

4.4 Study of $\Upsilon(1S) \to e^{\pm}\tau^{\mp}$ decay

Here τ has been reconstructed from three decays: $\tau^- \to \mu^-\bar{\nu}_\mu\nu_\tau$, $\tau^- \to \pi^-\nu_\tau$, and $\tau^- \to \pi^-\pi^+\pi^-\nu_\tau$. In order to avoid the huge background from the $\Upsilon(1S) \to e^+e^-$ decays, we do not reconstruct the τ in $\tau^- \to e^-\bar{\nu}_e\nu_\tau$ decays.

4.4.1 Analysis strategy

We look at the recoil mass of two pions from $\Upsilon(2S)$ ($M^{\rm recoil}_{\pi\pi}$) which should peak at the nominal $\Upsilon(1S)$ mass. One can evaluate the $M^{\rm recoil}_{\pi\pi}$ using Eq. (4.3). We extract the signal with recoil mass of $\pi\pi e$ ($M^{\rm recoil}_{\pi\pi{\rm e}}$), which should peak at the tau mass (1.775 GeV/c^2).

4.4.2 Event selection

Event selection criteria for $\Upsilon(1S) \to e^{\pm}\tau^{\mp}$ decay is similar to $\Upsilon(1S) \to \mu^{\pm}\tau^{\mp}$ decay (as described in section 4.3.2). Photons within 50 mrad of each of $e^{\pm}$ direction are considered as bremsstrahlung photons to get the correct four-momentum of electrons.

4.4.3 Background study

We use the optimized L_e selection from $\Upsilon(1S) \to e^{\pm}\mu^{\mp}$ study, $L_e > 0.6$.

$M_{\pi\pi}^{\rm recoil}$ **selection:** $M_{\pi\pi}^{\rm recoil}$ distribution for signal MC and generic MC are given in Fig. 4.25. For $\Upsilon(2S) \to \pi^+\pi^-\Upsilon(1S)$ decay, $M_{\pi\pi}^{\rm recoil}$ peaks at the $\Upsilon(1S)$ mass and rest of the $\Upsilon(2S)$ and $e^+e^- \to q\bar{q}$ background remain flat. We select the events within 9.450 to 9.466 GeV/c^2 (taken from $\Upsilon(1S) \to \mu^{\pm}\tau^{\mp}$ study), which rejects 9% of signal and 42% of background events.

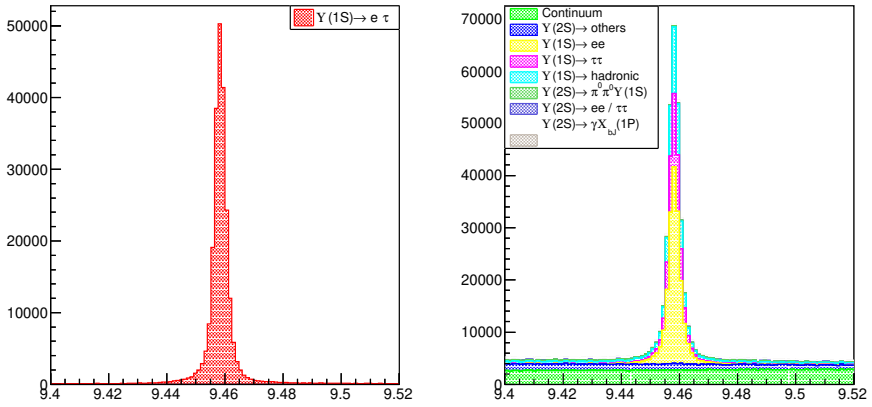

FIG. 4.25: $M_{\pi\pi}^{\rm recoil}$ (in GeV/c^2) distributions for $\Upsilon(1S) \to e^{\pm}\tau^{\mp}$ decays using signal MC sample (left) and using generic MC sample with scaled $\Upsilon(4S)$ off-resonance data (right).

Prompt lepton counting: There is only one electron in our signal mode, and it should be high energetic. We count the number of prompt (with energy > 1 GeV) electrons ($N_{\rm e}$) and prompt muons (N_μ) in each event. Background coming from $\Upsilon(1S) \to e^+e^-$ decays have two prompt electrons (Fig. 4.26). Therefore events with $N_{\rm e} = 1$ have been selected. Further, we have selected the events from $\tau^- \to \mu^-\bar{\nu}_\mu\nu_\tau$ decays with $N_\mu \leq 1$, and from $\tau^- \to \pi^-\pi^+\pi^-\nu_\tau$ and $\tau^- \to \pi^-\nu_\tau$ decays with $N_\mu = 0$. These prompt track selections further reject only 1% of signal and 62% of background events.

δM **selection for** $\tau^- \to \pi^-\nu_\tau$ **mode:** After applying $M_{\pi\pi}^{\rm recoil}$ and $N_{\rm e}$ selection, most of the background events come through $\tau^- \to \pi^-\nu_\tau$ mode reconstruction. It

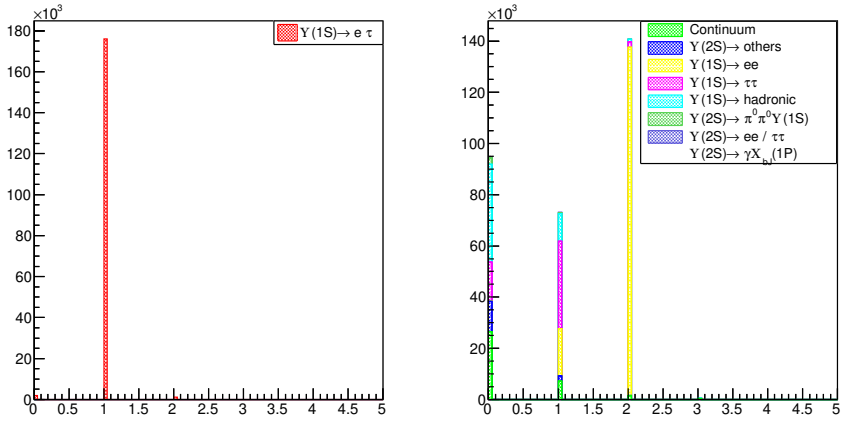

FIG. 4.26: $N_{\rm e}$ distributions for $\Upsilon(1S) \to e^{\pm}\tau^{\mp}$ decays using signal MC sample (left) and using generic MC sample with scaled $\Upsilon(4S)$ off-resonance data (right).

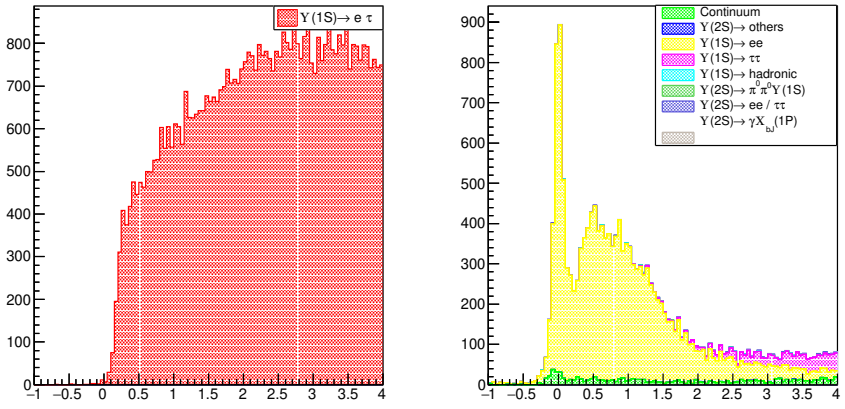

FIG. 4.27: δM (in GeV/c^2) distributions for $\Upsilon(1S) \to e^{\pm}\tau^{\mp}$ decays using signal MC sample (left) and using generic MC sample with scaled $\Upsilon(4S)$ off-resonance data (right).

seems that most of the backgrounds come from the $\Upsilon(1S) \to e^+e^-$ decays, where one electron is misidentified as pion. Angular distribution of those pions shows two peaks the junctions of the barrel and endcaps of ECL where electron remain undetected (more details in appendix B.1). We look at the difference between $M_{\pi\pi}^{\rm recoil}$ and the invariant mass of two leptons ($M_{e\tau}$), δM (Fig. 4.27). As explained earlier, δM get shifted from 0 for most of the signal events. But the δM distribution for $\Upsilon(1S) \to e^+e^-$ decays peaks at 0. Due to the bremsstrahlung energy loss δM plot for generic MC has a bump like structure (not likely to be for $\Upsilon(1S) \to \mu^{\pm}\tau^{\mp}$ case). We select the region with $\delta M > 2$ GeV/c^2 which rejects 21% of signal events and

55% of background events.

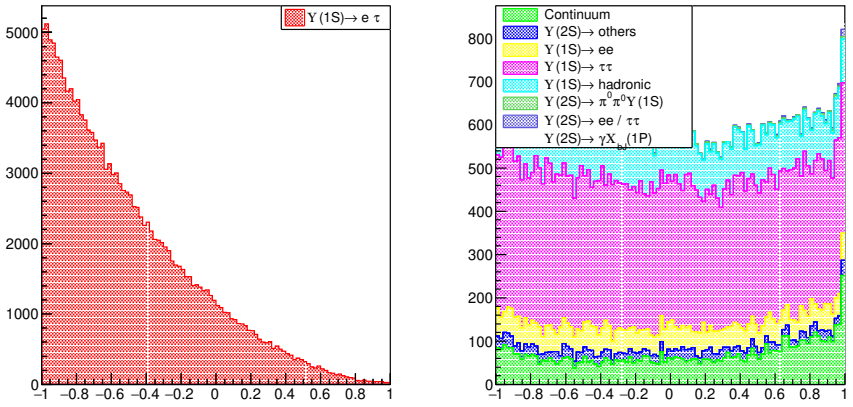

FIG. 4.28: $\cos(\theta_{\pi\pi})$ distributions for $\Upsilon(1S) \to e^{\pm}\tau^{\mp}$ decays using signal MC sample (left) and using generic MC sample with scaled $\Upsilon(4S)$ off-resonance data (right).

$\cos(\theta_{\pi\pi})$ **selection:** As one can see in Fig. 4.28, we find some peaking structure near $\cos(\theta_{\pi\pi}) = 1$ for $\Upsilon(1S) \to e^{\pm}\tau^{\mp}$ decays. That peaking structure is expected to come from converted photons, as discussed in $\Upsilon(1S) \to \mu^{\pm}\tau^{\mp}$ study. We select the events with $\cos(\theta_{\pi\pi}) < 0.5$ to reduce such background, which further reject 2% of signal and 26% of background.

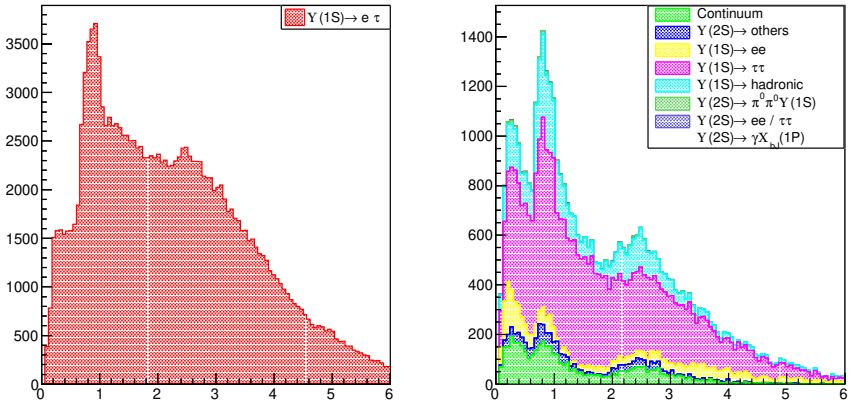

FIG. 4.29: p^{τ}_{vis} (in GeV/c) distribution for $\Upsilon(1S) \to e^{\pm}\tau^{\mp}$ decays using signal MC sample (left) and generic MC sample (right).

Decay $\Upsilon(1S) \to e^{\pm}\tau^{\mp}$	Effective efficiency (%)
$\tau^- \to \mu^-\bar{\nu}_\mu\nu_\tau$ (a)	6.5
$\tau^- \to \pi^-\pi^+\pi^-\nu_\tau$ (b)	0.7
Combined efficiency	7.2

TAB. 4.3: Effective signal efficiencies for $\Upsilon(1S) \to e^{\pm}\tau^{\mp}$ decays for different τ reconstruction modes.

$p^{\tau}_{\rm vis}$ selection: Here τ has been reconstructed from $\tau^- \to \mu^-\bar{\nu}_\mu\nu_\tau$, $\tau^- \to \pi^-\nu_\tau$, $\tau^- \to \pi^-\pi^+\pi^-\nu_\tau$ decays. Fig. 4.29 compares the visible momentum distribution of τ for signal and background events. Background from low energetic electrons dominates near the low $p^{\tau}_{\rm vis}$ region. Events with $p^{\tau}_{\rm vis} > 0.3$ MeV/c have been selected to remove such backgrounds, which rejects 18% of background with 3% signal loss.

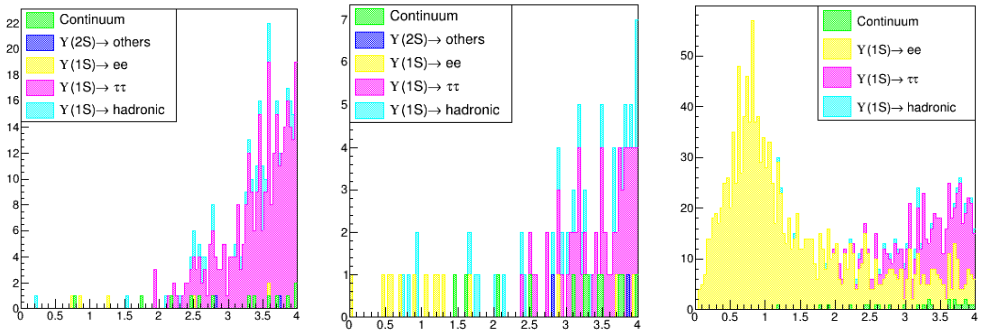

FIG. 4.30: $M^{\rm recoil}_{\pi\pi e}$ (in GeV/c^2) distributions for backgrounds with $\tau^- \to \mu^-\bar{\nu}_\mu\nu_\tau$ (left), $\tau^- \to \pi^-\pi^+\pi^-\nu_\tau$ (middle), and $\tau^- \to \pi^-\nu_\tau$ reconstruction modes (right) using generic MC sample with scaled $\Upsilon(4S)$ off-resonance data.

Distribution of $M^{\rm recoil}_{\pi\pi e}$: We plot the $M^{\rm recoil}_{\pi\pi e}$ inside the signal window. Most of the background near signal region is coming from the $\tau^- \to \pi^-\nu_\tau$ mode as like as $\Upsilon(1S) \to \mu^{\pm}\tau^{\mp}$ study. Fig. 4.30 compares the background coming from different τ reconstruction modes.

4.4.4 Signal extraction

Estimated UL for $\Upsilon(1S) \to e^{\pm}\tau^{\mp}$ decay excluding $\tau^- \to \pi^-\nu_\tau$ mode gives better sensitivity as compared to three combined tau modes. Therefore, we estimate the UL for $\Upsilon(1S) \to e^{\pm}\tau^{\mp}$ decay corresponding to two tau modes (excluding $\tau^- \to \pi^-\nu_\tau$).

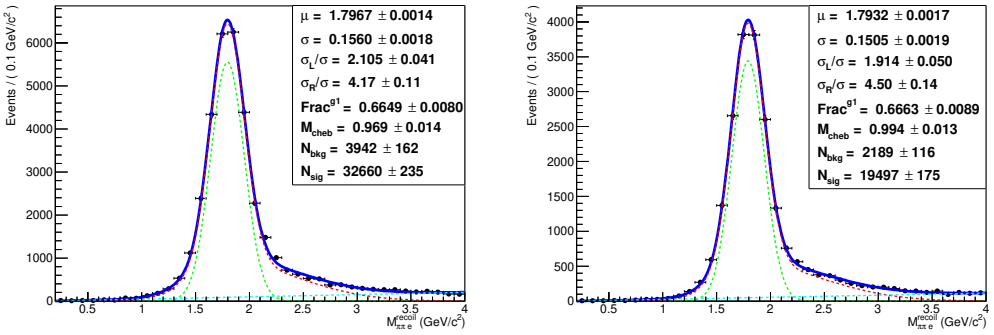

FIG. 4.31: UML fits to $M^{\text{recoil}}_{\pi\pi\text{e}}$ (in GeV/c^2) for $\Upsilon(1S) \to e^{\pm}\tau^{\mp}$ decays for $\tau^- \to \mu^-\bar{\nu}_\mu\nu_\tau$ reconstruction mode (left) and for $\tau^- \to \pi^-\pi^+\pi^-\nu_\tau$ reconstruction mode (right) using signal MC sample.

Signal MC fit: Inside the signal window, we perform 1D UML fit on $M^{\text{recoil}}_{\pi\pi\text{e}}$ with sum of a Gaussian and a bifurcated Gaussian. We fit each of the two tau decay modes separately to get the individual efficiency (Fig. 4.31). Fitted efficiency for $\tau^- \to \mu^-\bar{\nu}_\mu\nu_\tau$ mode has been estimated using a MC sample with 0.5 million $\Upsilon(1S) \to e^{\pm}\tau^{\mp}$ decays, where τ decays generically. As $\tau^- \to \pi^-\pi^+\pi^-\nu_\tau$ decays are not included in the generic tau decays at Belle, we use 0.25 million of $\Upsilon(1S) \to e^{\pm}\tau^{\mp}$ to estimate the efficiency for $\tau^- \to \pi^-\pi^+\pi^-\nu_\tau$, where tau decays to 3-pion final state. Fitted efficiencies are listed in Tab. 4.3.

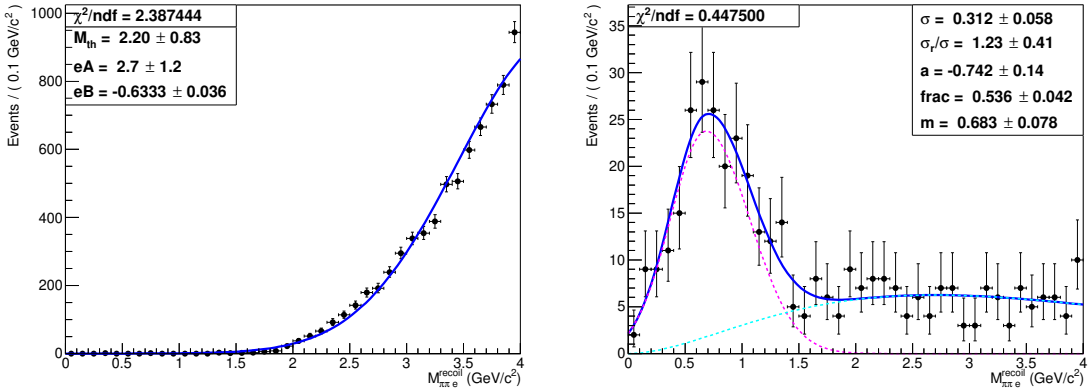

FIG. 4.32: UML fits to $M^{\text{recoil}}_{\pi\pi\text{e}}$ (in GeV/c^2) for $\Upsilon(1S) \to \tau^+\tau^-$ backgrounds (left) and for $\Upsilon(1S) \to e^+e^-$ backgrounds (right) using 40 million $\Upsilon(1S) \to \ell^{\pm}\ell^{\mp}$ MC sample.

Background fit: $\Upsilon(1S) \to \tau^+\tau^-$ and $\Upsilon(1S) \to e^+e^-$ decays are the dominant sources of background here. We use 40 million $\Upsilon(1S) \to \ell^{\pm}\ell^{\mp}$ MC sample to get

the shape of the $\tau\tau$ and ee background. As in $\Upsilon(1S) \to \mu^{\pm}\tau^{\mp}$ decay, we model the $\tau\tau$ background using the likelihood function in Eq. (4.4). For the ee background, we use the sum of a bifurcated Gaussian and a threshold function starting from 0. Fig. 4.32 summarizes the fits for $\Upsilon(1S) \to \tau^+\tau^-$ and $\Upsilon(1S) \to e^+e^-$ background corresponding to 40 million $\Upsilon(1S) \to \ell^{\pm}\ell^{\mp}$ MC sample.

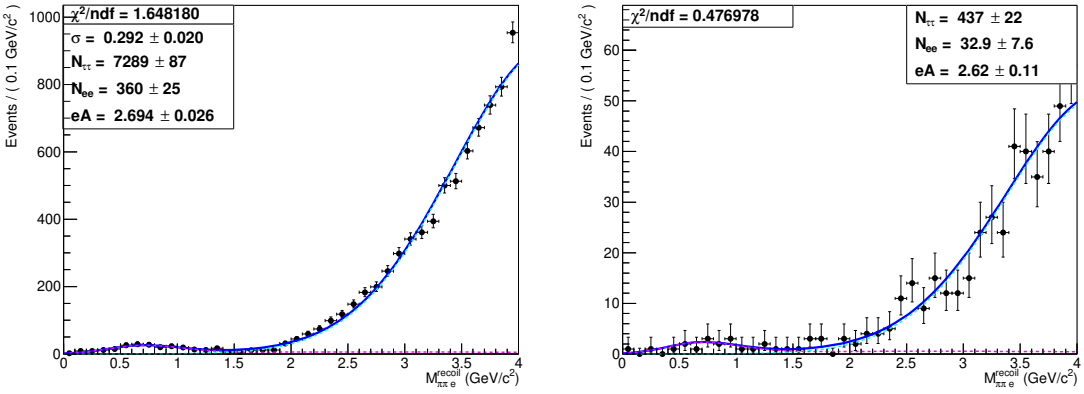

FIG. 4.33: UML fits to $M^{\text{recoil}}_{\pi\pi\text{e}}$ (in GeV/c^2) for all backgrounds using 40 million $\Upsilon(1S) \to \ell^{\pm}\ell^{\mp}$ sample (left) and using generic MC sample (right).

To get the combined background PDF, we fix all the parameters of $\tau\tau$ and ee background PDFs except the shape parameter of the $\tau\tau$ PDF (A), and resolution (σ) of ee background (Fig. 4.33).

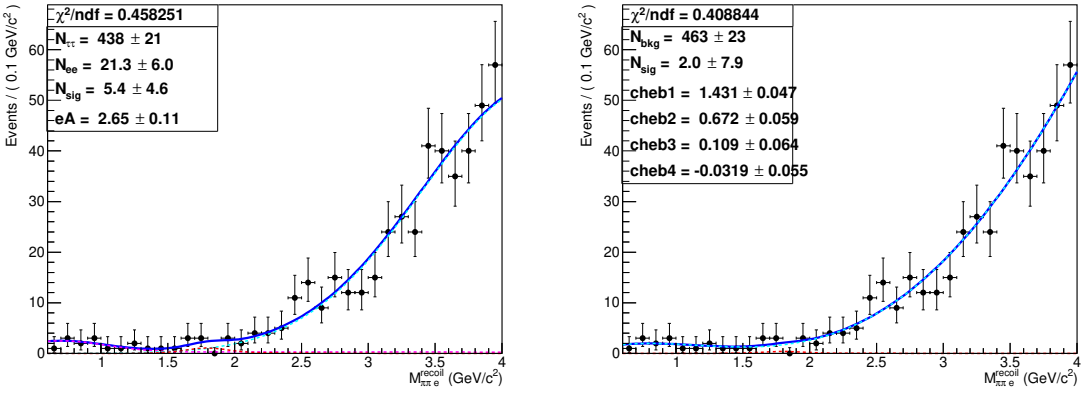

FIG. 4.34: UML fits to $M^{\text{recoil}}_{\pi\pi\text{e}}$ (in GeV/c^2) for combined signal and backgrounds with nominal background PDF (left) and with polynomial background PDF (right) using generic MC sample with scaled $\Upsilon(4S)$ off-resonance data.

Generic MC fit: To estimate the peaking background yield, we fit generic background with a combined signal and background PDF within 0.6 to 4.0 GeV/c^2. Parameters

of the signal PDF are fixed from the MC signal. Expected yield of peaking background is estimated to be $\mathbf{5.4 \pm 4.6}$. Also, as an alternative option, we fit the signal considering the background as a 4th order Chebychev polynomial. In this case, total yield of the peaking background is estimated to be $\mathbf{2.0 \pm 7.9}$. Both of the generic fits are shown in Fig. 4.34.

4.4.5 Fit bias study

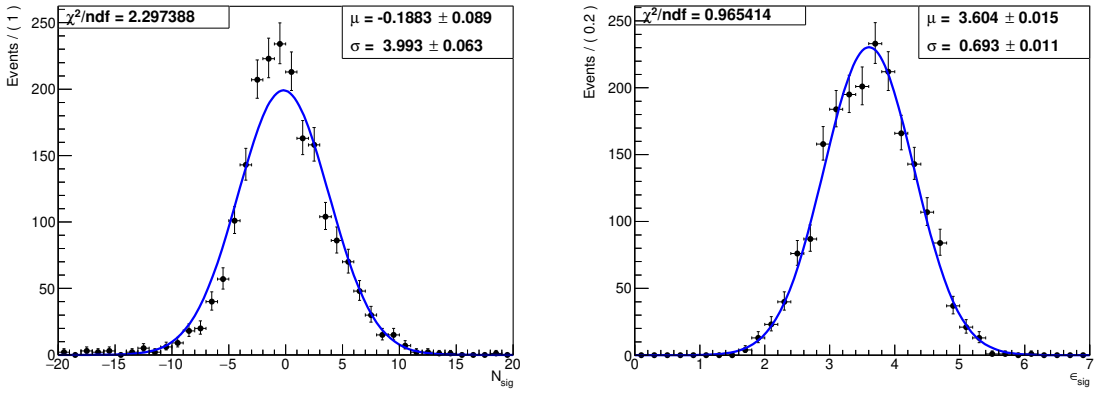

FIG. 4.35: UML fits to the fitted mean of signal yields of the pseudo experiments (left) and fitted uncertainty of signal yields of the pseudo experiments (right).

We study the stability of the signal extraction PDF for the nominal background using an ensemble of two thousand pseudo experiments. We generate data sets with constant 460 background events fixing all the parameters of the final PDF, and fit each of those data sets. We fit the distribution of signal yields and uncertainties with Gaussian PDFs (Fig. 4.35). We find better agreement for the mean of the signal yield and uncertainty distributions for the fit with the nominal background.

4.4.6 Data-MC resolution difference

To fix the width of $\Upsilon(1S) \to e^{\pm}\tau^{\mp}$ signal in data, we check the data-MC resolution difference for $M^{\text{recoil}}_{\pi\pi\text{e}}$ variable using $\Upsilon(1S) \to e^+e^-$ events. We fit the MC events with sum of a Gaussian and a bifurcated Gaussian. $M^{\text{recoil}}_{\pi\pi\text{e}}$ fits to MC and data events are shown in Fig. 4.36. We obtain a resolution difference between MC and data (in the right side from the mean position) to be 26.6%.

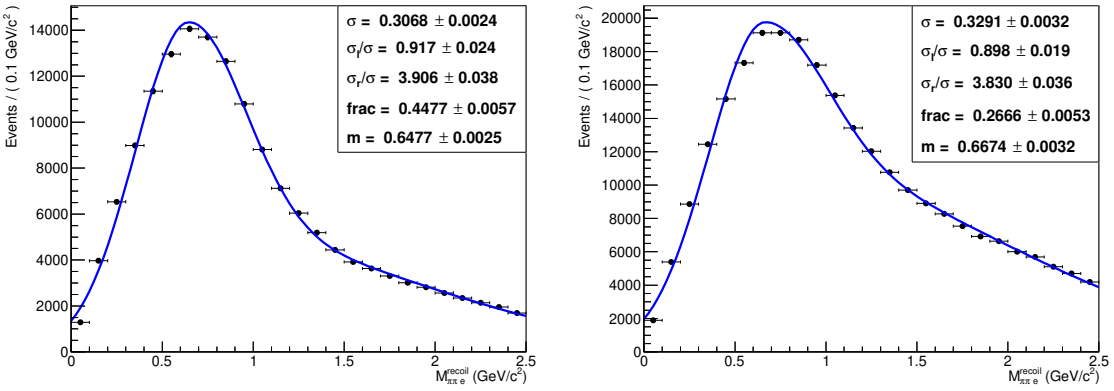

FIG. 4.36: UML fits to $M^{\text{recoil}}_{\pi\pi\text{e}}$ (in GeV/c^2) for $\Upsilon(1S) \to e^+e^-$ events using generic MC sample (left) and using $\Upsilon(2S)$ data (right).

4.4.7 UL estimation with MC background

We estimate the sensitivity of $\Upsilon(1S) \to e^{\pm}\tau^{\mp}$ transition using a frequentist method in a similar approach to $\Upsilon(1S) \to \mu^{\pm}\tau^{\mp}$ study. We generate the 500 toy data sample fixing the shape of the PDFs. Background yield for the toy samples is fixed at 438, and we vary yield of the signal PDF from 2 till 20. To estimate the CL, we use the central value of the signal to be as zero. Expecting 11.0 signal yield at 90% CL, one can calculate the UL of branching fraction using relation (5.8). The expected upper limit of the branching fraction for $\Upsilon(1S) \to e^{\pm}\tau^{\mp}$ at 90% CL is $\sim 10^{-6}$.

4.5 Calibration modes study

We need to validate the recoil $\Upsilon(1S)$ sample as well as the lepton identification in the high momentum region at the Belle. For that purpose, we choose the $\Upsilon(1S) \to e^+e^-$ and $\Upsilon(1S) \to \mu^+\mu^-$ decays as the calibration modes. Also, signal extraction procedure and MC efficiency can be verified by measuring the branching fractions of $\Upsilon(1S) \to \ell^{\pm}\ell^{\mp}$ $[\ell = e, \mu]$ decays.

4.5.1 Analysis strategy and event selection

Analysis strategy and event selection criteria is very similar to $\Upsilon(1S) \to e^{\pm}\mu^{\mp}$ study (section 4.2.1). We look at the $\ell\ell$ invariant mass ($M_{\ell\ell}$), which should peak at $\Upsilon(1S)$

$\Upsilon(2S) \to \pi^+\pi^-\Upsilon(1S)$	Efficiency (in %)
$\Upsilon(1S) \to e^+e^-$	28.3
$\Upsilon(1S) \to \mu^+\mu^-$	35.9

TAB. 4.4: Estimated signal efficiencies of calibration modes.

mass. We apply a cut on $M_{\ell\ell}$ to remove background coming from low energetic lepton pairs. In order to extract the signal, we plot the mass difference between $\Upsilon(2S)$ and $\Upsilon(1S)$, ΔM.

4.5.2 Background study

We include all the selection from the $\Upsilon(1S) \to e^\pm\mu^\mp$ study (section 4.2.2). For both of the lepton tracks of $\Upsilon(1S) \to e^+e^-$ and $\Upsilon(1S) \to \mu^+\mu^-$ events, we apply $L_e > 0.6$ for and $L_\mu > 0.95$, respectively. Events having $M_{\Upsilon(1S)}$ from 9.09 to 9.65 GeV/c^2 are selected both for $\Upsilon(1S) \to e^+e^-$ and $\Upsilon(1S) \to \mu^+\mu^-$ case. In order to suppress the $e^+e^- \to q\bar{q}$ background $|\vec{p}_{\Upsilon(1S)}| < 4.4$ GeV/c is also applied.

4.5.3 Signal extraction

Signal MC fits: 1D UML fit is performed with two Gaussian sharing common mean on ΔM to get the resolution and efficiency (Fig. 4.37). The estimated signal efficiency for ee and $\mu\mu$ are given in Tab. 4.4.

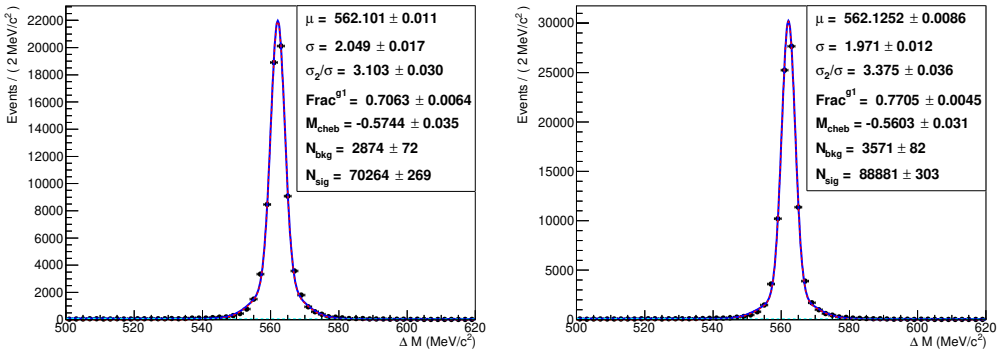

FIG. 4.37: UML fits to ΔM (in MeV/c^2) for $\Upsilon(1S) \to e^+e^-$ decays (left) and for $\Upsilon(1S) \to \mu^+\mu^-$ decays (right) using signal MC sample.

Generic MC fit: Number of background is small, and there are no peaking backgrounds. We combine the scaled $\Upsilon(4S)$ off-resonance data with generic MC data. We fit the background with a 1st order Chebyshev polynomial. To fit the generic MC events, all the tail parameters of the signal PDFs are fixed from signal MC fits. Generic MC fits are shown in Fig. 4.38.

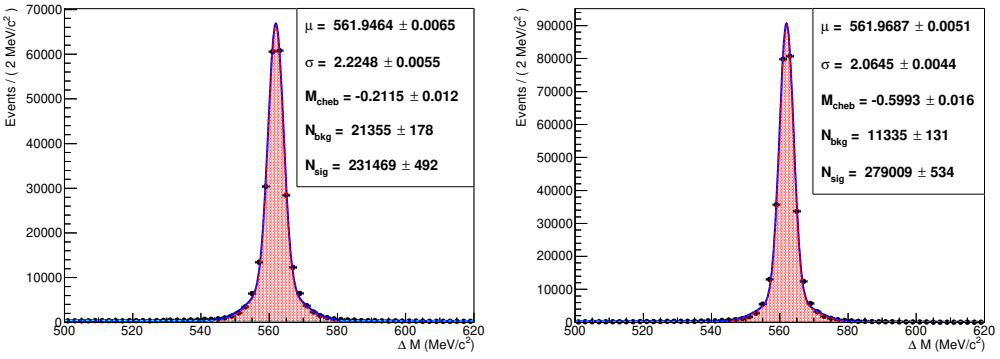

FIG. 4.38: UML fits to ΔM (in MeV/c^2) for $\Upsilon(1S) \to e^+e^-$ decays (left) and for $\Upsilon(1S) \to \mu^+\mu^-$ decays (right) using generic MC sample with scaled $\Upsilon(4S)$ off-resonance data.

$\Upsilon(2S)$ on resonance data fit: To fit the $\Upsilon(2S)$ on-resonance data we use exactly same PDFs, which have been used to fit generic MC events. As one can see Fig. 4.39, there is a difference between the yields for on resonance data and generic MC for both $\Upsilon(1S) \to e^+e^-$ and $\Upsilon(1S) \to \mu^+\mu^-$ modes. We think that is due to use of different branching fraction for generating the MC.

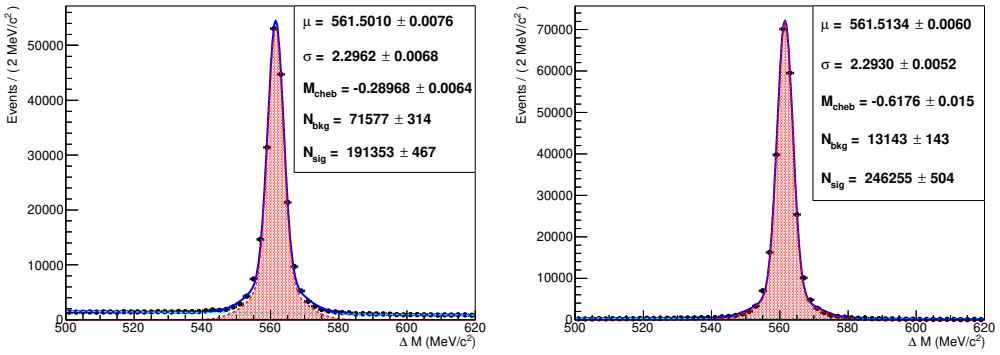

FIG. 4.39: UML fits to ΔM (in MeV/c^2) for $\Upsilon(1S) \to e^+e^-$ decays (left) and for $\Upsilon(1S) \to \mu^+\mu^-$ decays (right) using $\Upsilon(2S)$ on resonance data.

Branching fraction	Generic MC		$\Upsilon(2S)$ data (10^{-2})	
	Input value	Fit result	PDG value	Fit result
$\mathcal{B}[\Upsilon(1S) \to e^+e^-]$	2.56	2.77 $\pm$0.01	2.38 $\pm$0.11	$2.40 \pm 0.01 \pm 0.12$
$\mathcal{B}[\Upsilon(1S) \to \mu^+\mu^-]$	2.56	2.64 $\pm$0.01	2.48 $\pm$0.05	$2.46 \pm 0.01 \pm 0.11$

TAB. 4.5: Calculated branching fraction for control samples. In the data results, first (second) uncertainty implies the statistical (systematic) uncertainty.

4.5.4 Validation of control samples

One can calculate the branching fractions by substituting the constant value for the branching fraction of $\Upsilon(2S) \to \pi^+\pi^-\Upsilon(1S)$ decay and corresponding signal efficiency (ϵ_ℓ) in the following relation.

$$\mathcal{B}[\Upsilon(1S) \to \ell^\pm\ell^\mp] = \frac{N_{\rm sig}}{N_{\Upsilon(2S)} \times \mathcal{B}[\Upsilon(2S) \to \pi^+\pi^-\Upsilon(1S)] \times \epsilon_\ell} \tag{4.5}$$

Calculated values of branching fractions including systematic uncertainty are summarized in Tab. 4.5. As one can see obtained results agree very well with PDG values.

4.6 Side-band study

MC signal study for CLFV modes looks promising. Also, the control modes have been validated with $\Upsilon(2S)$ data, and results agree with the world average values within $\pm 1\sigma$. Now we are ready to study the CLFV in $\Upsilon(2S)$ data. Before unblinding the data, we look the data and MC distributions in the side-band region. As one can see in the following distributions, the agreement between data and MC for $e\mu$ (Fig. 4.40), $\mu\tau$ (Fig. 4.41), and $e\tau$ (Fig. 4.42) decays are good enough to unblind the data in the signal regions.

4.7 CLFV study with data

Fits to $\Upsilon(2S)$ data: We perform the 1D UML fit with $\Upsilon(2S)$ on resonance data for each of the CLFV modes. $\Upsilon(1S) \to e^\pm\mu^\mp$ signal resolution in data is fixed from the signal MC according to the average of data and MC difference on ΔM for $\Upsilon(1S) \to e^+e^-$ and $\Upsilon(1S) \to \mu^+\mu^-$ events. For $\Upsilon(1S) \to e^\pm\mu^\mp$ decays, we add a

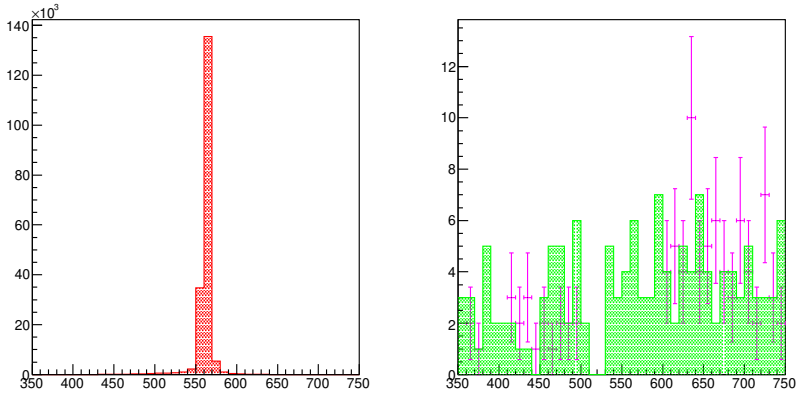

FIG. 4.40: ΔM (in MeV/c^2) distributions for $\Upsilon(1S) \to e^{\pm}\mu^{\mp}$ decays using signal MC sample (red), MC backgrounds (green), and $\Upsilon(2S)$ data side band (magenta).

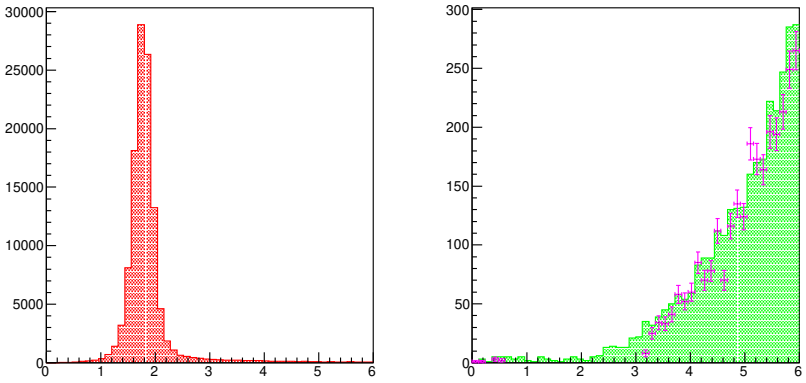

FIG. 4.41: $M^{\text{recoil}}_{\pi\pi\mu}$ (in GeV/c^2) distributions for $\Upsilon(1S) \to \mu^{\pm}\tau^{\mp}$ decays using signal MC sample (red), MC backgrounds (green), and $\Upsilon(2S)$ data side band (magenta).

fixed PDF of 8.8 misidentification background, where resolution of misidentification events is fixed according to the data-MC difference for the dimuon sample. For $\Upsilon(1S) \to \ell\tau$ fits, signal resolutions in data are fixed from the signal MC corrected by the data and MC difference on $M^{\text{recoil}}_{\pi\pi\ell}$ obtained by studying $\Upsilon(1S) \to \ell\ell$ events. Fits for the $e\mu$, $\mu\tau$, $e\tau$ are given in Fig. 4.43, Fig. 4.44, Fig. 4.45, respectively. For $\Upsilon(1S) \to e^{\pm}\mu^{\mp}$, $\Upsilon(1S) \to \mu^{\pm}\tau^{\mp}$, and $\Upsilon(1S) \to e^{\pm}\tau^{\mp}$ decays obtained signal yields are -1.3 ± 3.7, -1.5 ± 4.3, and -3.5 ± 2.7, respectively. Hence, all the signal yields are considered to be 0 within uncertainties.

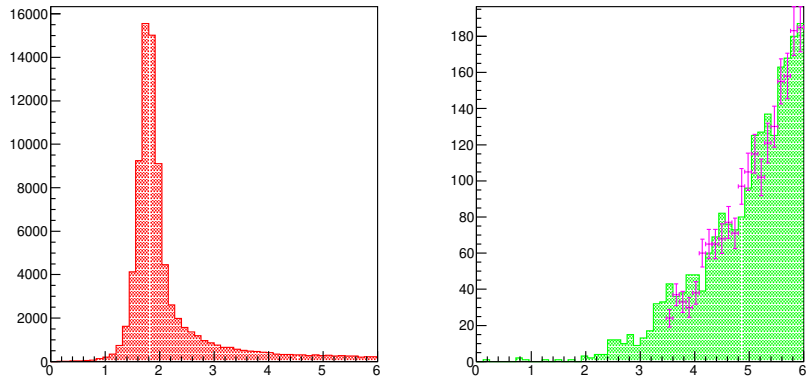

FIG. 4.42: $M_{\pi\pi e}^{\text{recoil}}$ (in GeV/c^2) distributions for $\Upsilon(1S) \to e^{\pm}\tau^{\mp}$ decays using signal MC sample (red), MC backgrounds (green), and $\Upsilon(2S)$ data side band (magenta).

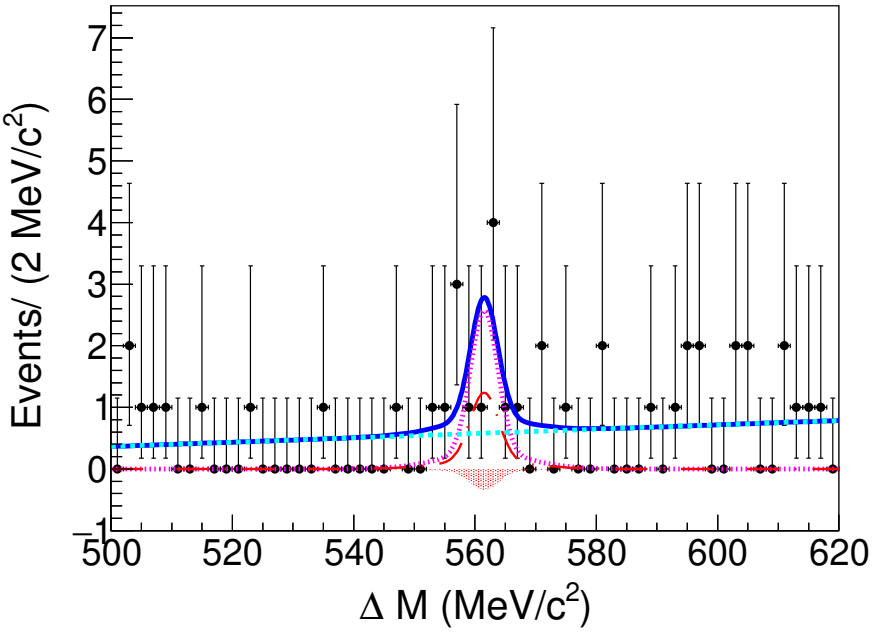

FIG. 4.43: ΔM fit with $\Upsilon(2S)$ data for $\Upsilon(1S) \to e^{\pm}\mu^{\mp}$ decay. The fitted signal PDF is represented by the filled red region, the dashed cyan line represents the flat background, and the dotted magenta curve is the peaking background from lepton misidentification. The long-dashed red curve represents the signal PDF corresponding to 5 hypothetical signal events.

Result for CLFV: One can calculate the branching fractions using the following relation,

$$\mathcal{B}[\Upsilon(1S) \to \ell\ell'] < \frac{N_{\text{sig}}}{N_{\Upsilon(2S)} \times \mathcal{B}[\Upsilon(2S) \to \pi^+\pi^-\Upsilon(1S)] \times \epsilon_{\text{cor}}} \tag{4.6}$$

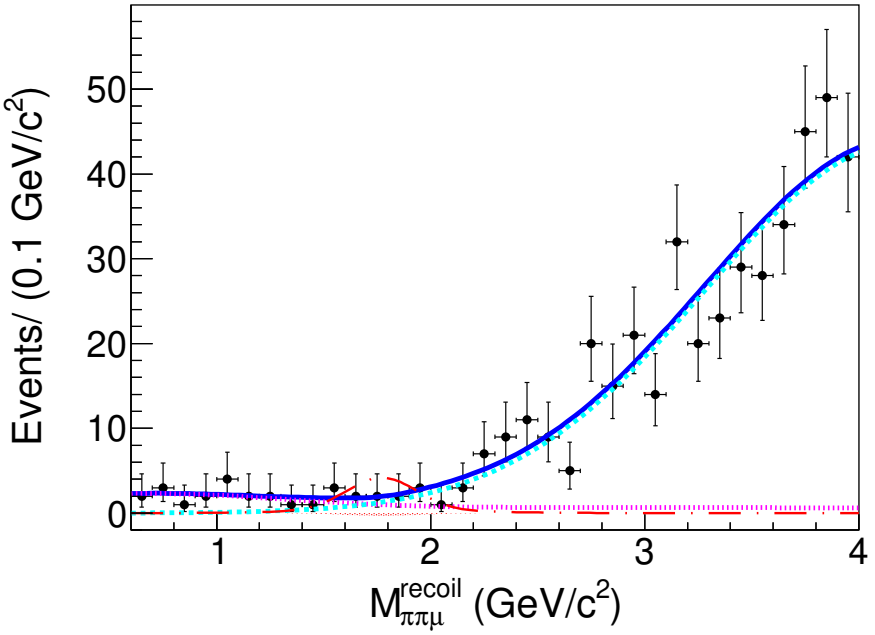

FIG. 4.44: $M^{\text{recoil}}_{\pi\pi\mu}$ fit with $\Upsilon(2S)$ data for $\Upsilon(1S) \to \mu^{\pm}\tau^{\mp}$ decay. The dotted magenta line represents the contribution from $\mu\mu$ background and the dashed cyan line represents the $\tau\tau$ background. The long-dashed red curve represent the signal PDFs corresponding to 20 hypothetical signal events.

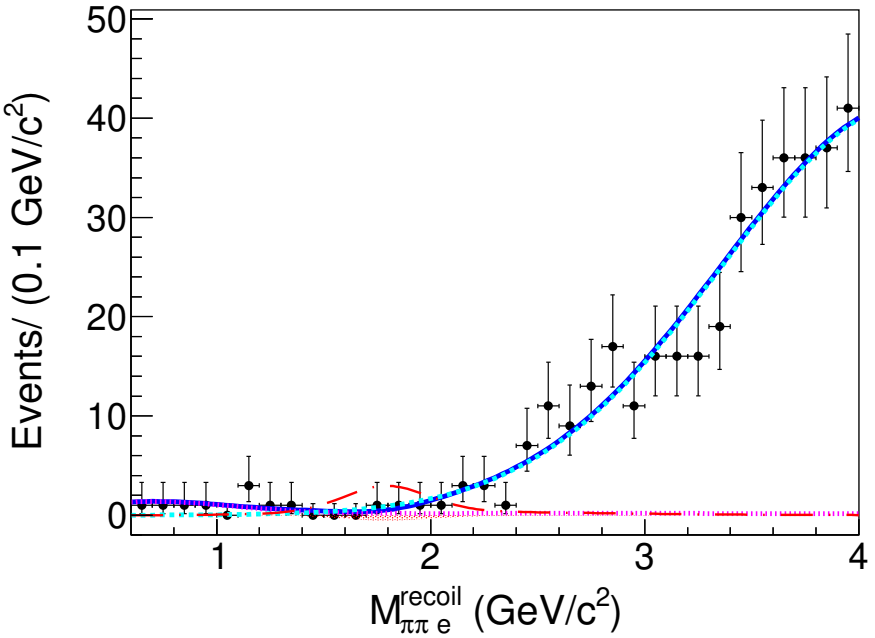

FIG. 4.45: $M^{\text{recoil}}_{\pi\pi\text{e}}$ fit with $\Upsilon(2S)$ data for $\Upsilon(1S) \to e^{\pm}\tau^{\mp}$ decay. The dotted magenta line represents the contribution from ee background and the dashed cyan line represents the $\tau\tau$ background.

where, $N_{\rm sig}$ and $\epsilon_{\rm cor}$ are the signal yield and the corrected efficiency of the signal, respectively. All the calculated branching fractions of CLFV modes are statistically dominated. In absence of significant signal, we calculate ULs of branching with a frequentist method using an ensemble of 500 pseudo experiments. We calculate the CL as the percentage of pseudo experiments with fitted yield greater than expected signal yield in data. Systematic of different CLFV modes have been included by smearing the yield of the pseudo experiments within the fluctuations. In Fig. 4.46, we show the CL distribution as a function of input signal yield for different CLFV modes.

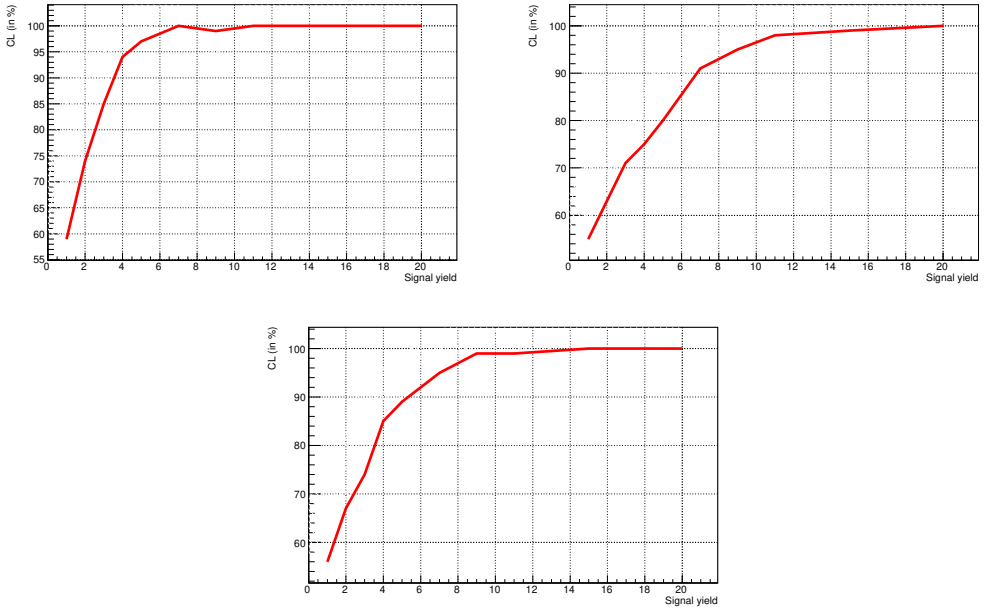

FIG. 4.46: Confidence level distributions for $\Upsilon(1S) \to e^{\pm}\mu^{\mp}$ (top left), $\Upsilon(1S) \to \mu^{\pm}\tau^{\mp}$ (top right), and $\Upsilon(1S) \to e^{\pm}\tau^{\mp}$ (bottom) decays.

Decay	ϵ_{cor} (%)	N^{UL} (90% CL)	UL @ 90% CL
$\Upsilon(1S) \to e^{\pm}\mu^{\mp}$	32.5	3.6	3.9×10^{-7}
$\Upsilon(1S) \to \mu^{\pm}\tau^{\mp}$	8.8	6.8	2.7×10^{-6}
$\Upsilon(1S) \to e^{\pm}\tau^{\mp}$	7.1	5.3	2.7×10^{-6}

TAB. 4.6: Results of CLFV searches in $\Upsilon(1S) \to \ell^{\pm}\ell'^{\mp}$ decays.

Considering number of $\Upsilon(2S)$ as 157.8 million [86], and $\mathcal{B}[\Upsilon(2S) \to \pi^+\pi^-\Upsilon(1S)]$ as 0.1785, we estimate ULs of branching fractions using Eq. (4.6). We summarize those upper limits in Tab. 4.6. Calculated ULs for $\Upsilon(1S) \to e^{\pm}\mu^{\mp}$, $\Upsilon(1S) \to \mu^{\pm}\tau^{\mp}$, and $\Upsilon(1S) \to e^{\pm}\tau^{\mp}$ at 90% CL are 3.9×10^{-7}, 2.7×10^{-6}, and 2.7×10^{-6}, respectively.

4.8 Study of $\Upsilon(1S) \to \gamma e^{\pm}\mu^{\mp}$ decays

Analysis strategy and event selection are similar to the $\Upsilon(1S) \to e^{\pm}\mu^{\mp}$ study (section 4.2). In addition to that selections, photon candidates with energy (E_γ) greater than 200 MeV have been selected to reconstruct $\Upsilon(1S)$ to remove beam backgrounds.

4.8.1 Background study

Here also, background was studied using $\Upsilon(2S)$ generic MC sample along with $\Upsilon(4S)$ off-resonance data. As $\Upsilon(1S)$ decays to 3-body final state, photon from $\Upsilon(1S)$ has a wide energy range (0-7 GeV). Fig. 4.47 shows the distributions of E_γ in the lab frame using the predefined signal window [(a) $9.09 < M_{\Upsilon(1S)} < 9.65$ GeV/c^2, (b) $|\vec{p}_{\Upsilon(1S)}| < 4.4$ GeV/c, (c) $N_\mu = 1$ and $N_e = 1$]. We tried to optimize the E_γ. But, due to the less number of background events, no proper optimization is found. Distribution of ΔM inside the signal window is shown in Fig. 4.48. Most of the backgrounds come from the $e^+e^- \to q\bar{q}$ events. Inside the signal window, we get two background events from radiative hadronic decays of $\Upsilon(1S)$.

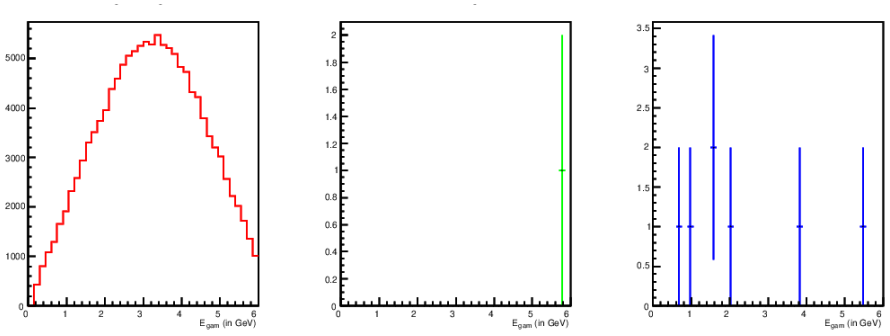

FIG. 4.47: E_γ (in GeV) distributions for $\Upsilon(1S) \to \gamma e^{\pm}\mu^{\mp}$ decays using signal MC sample (left), generic MC sample (middle), and scaled $\Upsilon(4S)$ off-resonance data (right).

4.8.2 Signal extraction

Signal MC fit: A 1D UML fit with two Gaussians has been performed on ΔM (Fig. 4.49), to estimate the resolution and efficiency of the signal events. Expected efficiency for $\Upsilon(1S) \to \gamma e^{\pm}\mu^{\mp}$ signal is 25.8%.

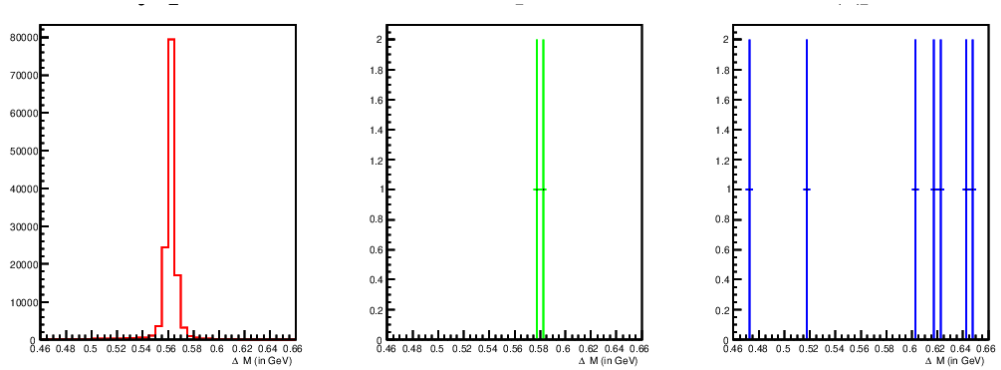

FIG. 4.48: ΔM (in GeV/c^2) distributions for $\Upsilon(1S) \to \gamma e^{\pm}\mu^{\mp}$ decays using signal MC sample (left), generic MC sample (middle), and scaled $\Upsilon(4S)$ off-resonance data (right).

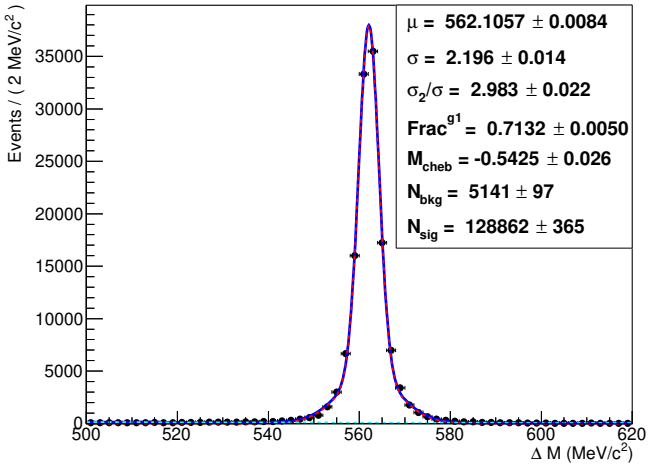

FIG. 4.49: UML fit to ΔM (in MeV/c^2) for $\Upsilon(1S) \to \gamma e^{\pm}\mu^{\mp}$ decays using signal MC sample.

Background estimation: In order to estimate the peaking background from leptonic decays of $\Upsilon(1S)$, 40 million $\Upsilon(1S) \to \ell^{\pm}\ell^{\mp}$ sample has been used. We find 1, 2, and 16 background events from $\Upsilon(1S) \to \mu^+\mu^-$, $\Upsilon(1S) \to e^+e^-$, and $\Upsilon(1S) \to \tau^+\tau^-$ decays, respectively. We perform a ΔM fit to $\Upsilon(1S) \to \tau^+\tau^-$ background fixing the shape of the signal PDF (Fig. 4.50). Fitted $\Upsilon(1S) \to \tau^+\tau^-$ background in high statistic MC is estimated to be 1.8 ± 1.9. After scaling according to the $\Upsilon(2S)$ data, expected peaking background is estimated to be 0.1 ± 0.1. As the contribution from $\Upsilon(1S) \to \ell^{\pm}\ell^{\mp}$ background is very less we will consider them in the systematic. We fit the scaled $\Upsilon(4S)$ off-resonance data to estimate the expected signal yield in $e^+e^- \to q\bar{q}$ background. Expected yield of signal in $e^+e^- \to q\bar{q}$ data is estimate to be 0 (Fig. 4.50).

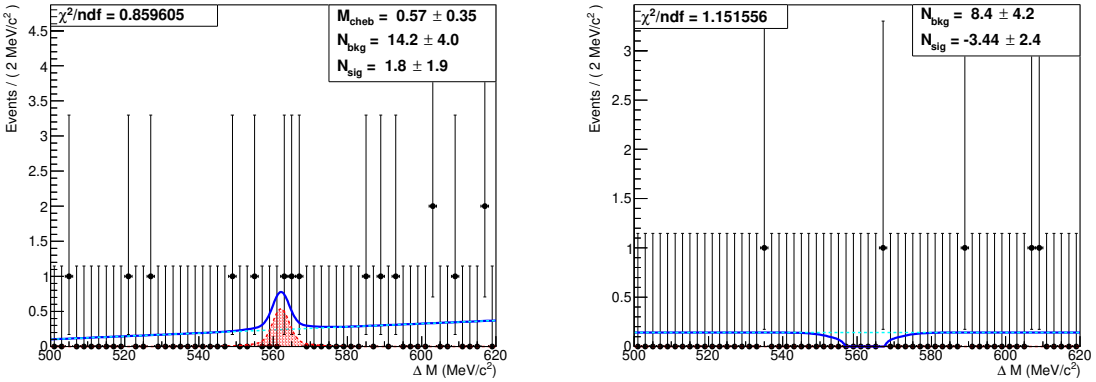

FIG. 4.50: UML fits to ΔM (in MeV/c^2) for $\Upsilon(1S) \to \tau^+\tau^-$ backgrounds using 40 million $\Upsilon(1S) \to \ell^\pm\ell^\mp$ MC sample (left) and for $q\bar{q}$ backgrounds using scaled $\Upsilon(4S)$ off-resonance data (right).

4.8.3 UL estimation with MC background

We test the sensitivity of $\Upsilon(1S) \to \gamma e^\pm \mu^\mp$ transition using a frequentist method in a similar approach as $\Upsilon(1S) \to e^\pm\mu^\mp$ study. We plot the confidence level, percentage of the samples having signal yield greater than 0.1, as a function of input yield. One can then estimate the UL of branching fraction using following relation.

$$\mathcal{B}^{UL}[\Upsilon(1S) \to \gamma\ell^\pm\ell'^\mp] < \frac{N_{\rm sig}^{\rm UL}}{N_{\Upsilon(2S)} \times \mathcal{B}[\Upsilon(2S) \to \pi^+\pi^-\Upsilon(1S)] \times \epsilon} \tag{4.7}$$

Where $N_{\rm sig}^{\rm UL}$ and ϵ are the signal yield and the efficiency of the signal, respectively. Using Eq. (4.7), the expected UL of the branching fraction for $\Upsilon(1S) \to \gamma e^\pm\mu^\mp$ at 90% CL is estimated to be 4.0×10^{-7}.

4.8.4 Study of $\Upsilon(1S) \to \gamma\mu^\pm\tau^\mp$ decays

For $\Upsilon(1S) \to \gamma\mu^\pm\tau^\mp$ study, τ has been reconstructed from two decays: $\tau^- \to e^-\bar{\nu}_e\nu_\tau$ and $\tau^- \to \pi^-\pi^+\pi^-\nu_\tau$. Analysis strategy and event selection are as in previous $\Upsilon(1S) \to \mu^\pm\tau^\mp$ study (section 4.3). We extract the signal through recoil mass of $\pi\pi\mu\gamma$ ($M^{\rm recoil}_{\pi\pi\mu\gamma}$) which should peak at the τ mass. Photons with energy (E_γ) greater than 200 MeV have been selected to reconstruct $\Upsilon(1S)$ to reduce the beam background.

4.8.5 Background study

We include all the selections which have been imposed on leptons and pion-pair systems for $\Upsilon(1S) \to \mu^{\pm}\tau^{\mp}$ study. The energy of the photon is expected to have wide distribution due to three body decay. In Fig. 4.51, we compare the distribution of E_γ for signal and background inside the predefined signal window [(a) $9.45 < M^{\rm recoil}_{\pi\pi} < 9.66$ GeV/c^2, (b) $\cos(\theta_{\pi\pi}) < 0.5$, (c) $p^{\tau}_{\rm vis} > 0.3$ GeV/c, (d) $N_\mu = 1$]. We try to optimize the E_γ between 0.2 to 1.2 GeV (Fig. 4.52). In absence of any proper optimization, we continue with $E_\gamma > 200$ MeV. Distribution of $M^{\rm recoil}_{\pi\pi\mu\gamma}$ inside the signal window is shown in Fig. 4.53.

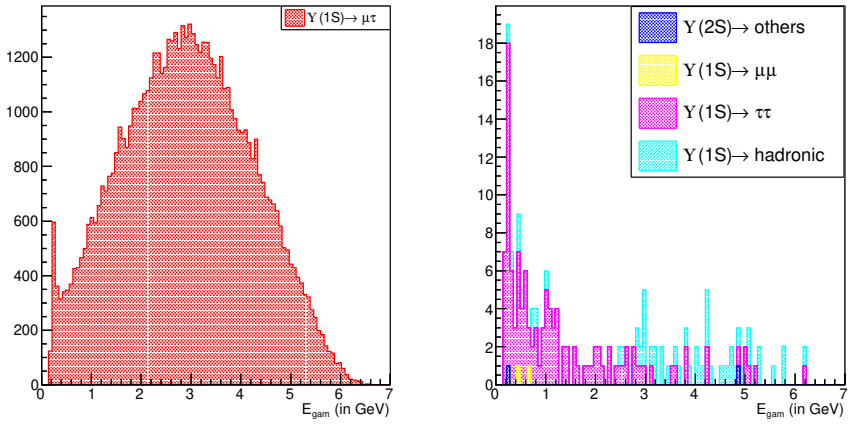

FIG. 4.51: E_γ (in GeV) distributions for $\Upsilon(1S) \to \gamma\mu^{\pm}\tau^{\mp}$ decays using signal MC sample (left) and using generic MC sample with scaled $\Upsilon(4S)$ off-resonance data (right).

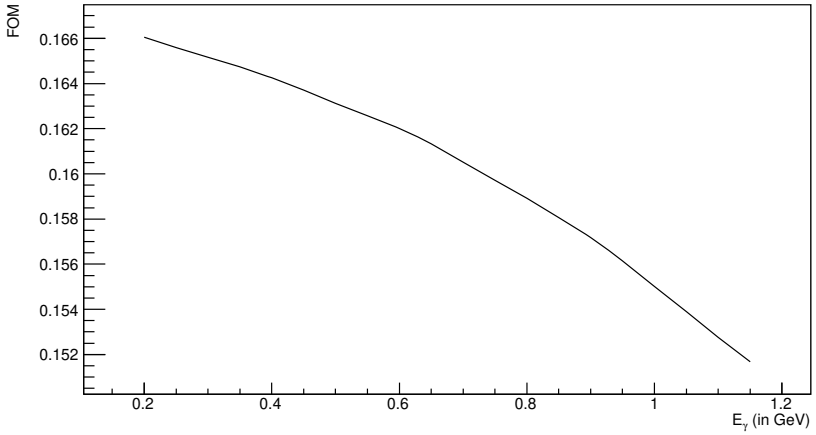

FIG. 4.52: Figure of merit for E_γ optimization for $\Upsilon(1S) \to \gamma\mu^{\pm}\tau^{\mp}$ decays.

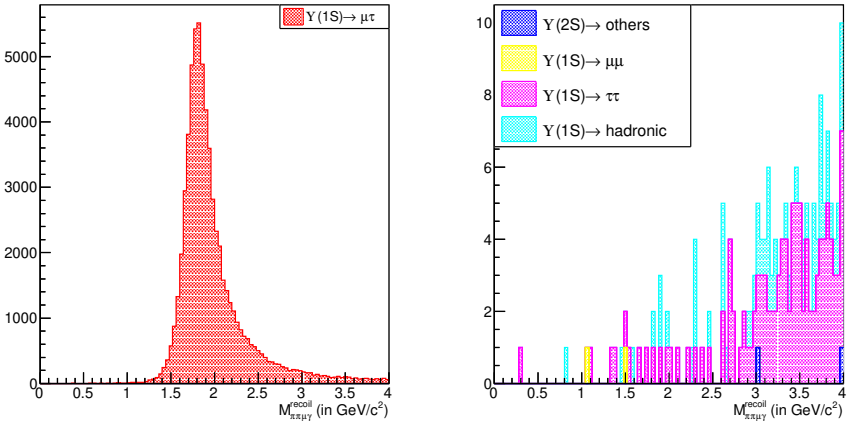

FIG. 4.53: $M^{\text{recoil}}_{\pi\pi\mu\gamma}$ (in GeV/c^2) distributions for $\Upsilon(1S) \to \gamma\mu^{\pm}\tau^{\mp}$ decays using signal MC sample (left) and using generic MC sample with scaled $\Upsilon(4S)$ off-resonance data (right).

4.8.6 Signal extraction

Here $\Upsilon(1S)$ decays to a 3-body final state. Further, τ decays through a 4-body final state for $\tau^- \to \pi^-\pi^+\pi^-\nu_\tau$ reconstruction mode. As a result the signal efficiency for $\tau^- \to \pi^-\pi^+\pi^-\nu_\tau$ mode is very less. We estimate the upper limit for two cases, with and without $\tau^- \to \pi^-\pi^+\pi^-\nu_\tau$ mode. We find that one could reach better sensitivity considering $\tau^- \to e^-\bar{\nu}_e\nu_\tau$ mode only. Therefore, we exclude the $\tau^- \to \pi^-\pi^+\pi^-\nu_\tau$ mode for further progress.

Signal MC fit: We perform 1D UML fit on $M^{\text{recoil}}_{\pi\pi\mu\gamma}$ with one Gaussian and one bifurcated Gaussian (Fig. 4.54). To estimate the signal efficiency and resolution, we use a MC sample with 0.5 million $\Upsilon(1S) \to \gamma\mu^{\pm}\tau^{\mp}$ decays, where tau decays generically. Fitted signal efficiency for $\Upsilon(1S) \to \gamma\mu^{\pm}\tau^{\mp}$ decay is estimated to be 6.1%.

Background estimation: More realistic background sample is prepared adding $\Upsilon(2S)$ generic MC data with scaled $\Upsilon(4S)$ off-resonance data. $\Upsilon(1S) \to \tau^+\tau^-$ is the dominant source of background here. To estimate the $\Upsilon(1S) \to \tau^+\tau^-$ background precisely, we use 40 million $\Upsilon(1S) \to \ell^{\pm}\ell^{\mp}$ MC sample. We use the exponential threshold like likelihood function in Eq. (4.4), to model the $\tau\tau$ background.

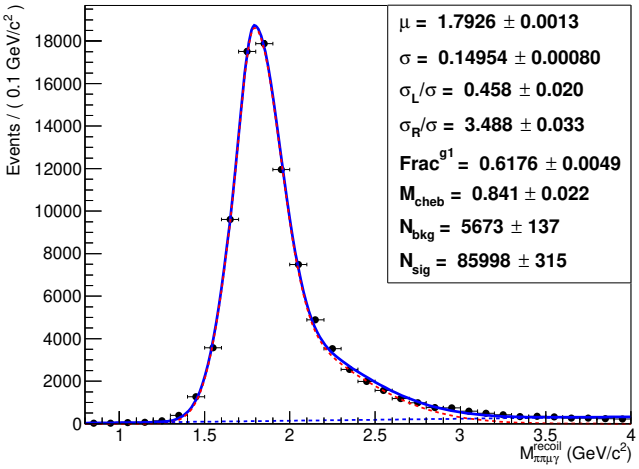

FIG. 4.54: UML fit to $M^{\text{recoil}}_{\pi\pi\mu\gamma}$ (in GeV/c^2) for $\Upsilon(1S) \to \gamma\mu^{\pm}\tau^{\mp}$ decays using signal MC sample.

All other background which mostly come from the hadronic decays of $\Upsilon(1S)$ are modeled with an exponential function. We perform $M^{\text{recoil}}_{\pi\pi\mu\gamma}$ fit to the generic MC background fixing the shape of two component background PDFs floating the fraction of two PDFs. Fig. 4.55 summarizes all the background fits.

Generic MC signal estimation: Finally, we fit the generic MC events fixing the shape of signal and background PDFs. We float the lower order coefficient of the $\tau\tau$ PDF to control the fit over any difference between data and MC. Also, as an alternative option, we fit the generic MC events considering a 2nd order polynomial as background. Both of the fits, shown in Fig. 4.56, look similar, and fitted χ^2 values also agree well. We are expecting 1.8 ± 5.1 and 2.5 ± 6.1 signal yields using nominal and polynomial background, respectively.

4.8.7 UL estimation with MC background

We estimate the sensitivity of $\Upsilon(1S) \to \gamma\mu^{\pm}\tau^{\mp}$ transition in a frequentist approach using nominal background. We plot the confidence level, percentage of the samples having signal yield greater than the expected signal yield, as a function of input yield. Considering 1.8 signal events with nominal background, the expected upper limit of the branching fraction for $\Upsilon(1S) \to \gamma\mu^{\pm}\tau^{\mp}$ decays at 90% CL is 4.6×10^{-6}.

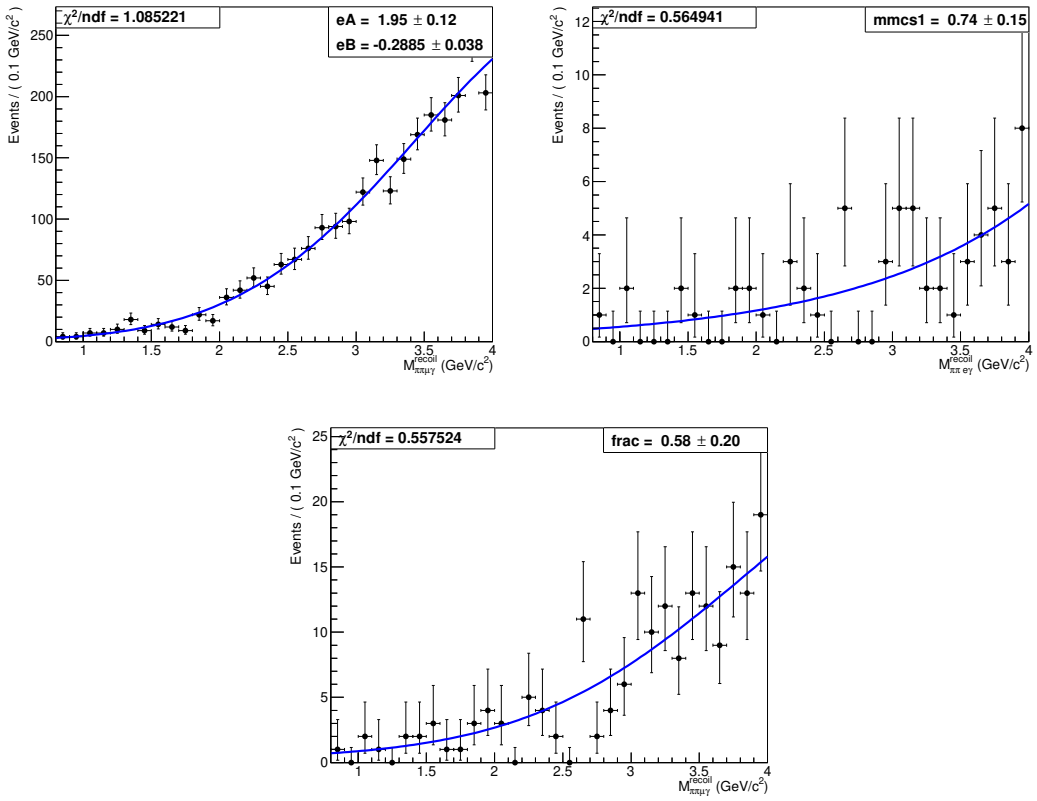

FIG. 4.55: UML fits to $M^{\text{recoil}}_{\pi\pi\mu\gamma}$ (in GeV/c^2) for $\Upsilon(1S) \to \tau^+\tau^-$ backgrounds using 40 million $\Upsilon(1S) \to \ell^\pm\ell^\mp$ MC sample (top left) and for all other backgrounds using generic MC sample (top right). Combined background fit using generic MC sample with scaled $\Upsilon(4S)$ off-resonance data (bottom).

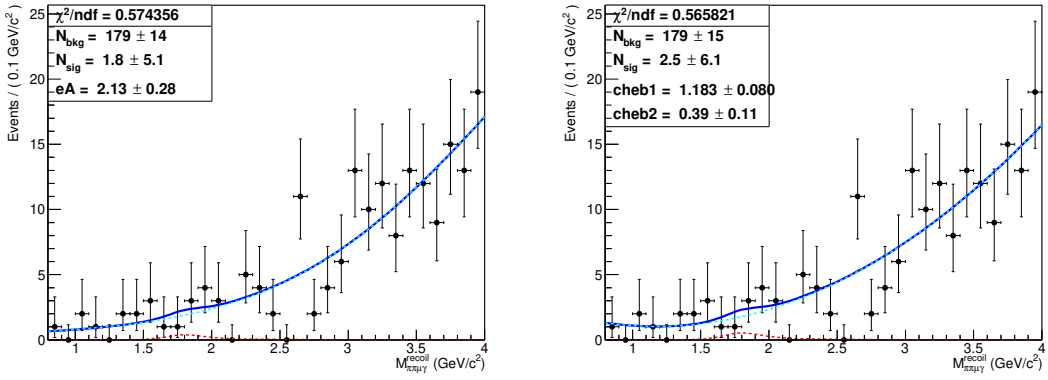

FIG. 4.56: UML fits to $M^{\text{recoil}}_{\pi\pi\mu\gamma}$ (in GeV/c^2) for combined signal and background with the nominal background PDF (left) and with the polynomial background PDF (right) using generic MC sample with scaled $\Upsilon(4S)$ off-resonance data.

4.9 Study of $\Upsilon(1S) \to \gamma e^{\pm}\tau^{\mp}$ decays

For $\Upsilon(1S) \to \gamma e^{\pm}\tau^{\mp}$ study, τ has been reconstructed in $\tau^- \to \mu^-\bar{\nu}_\mu\nu_\tau$ and $\tau^- \to \pi^-\pi^+\pi^-\nu_\tau$ decays. Analysis strategy and event selection are similar to the $\Upsilon(1S) \to e^{\pm}\tau^{\mp}$ decay (section 4.4). We extract the signal through recoil mass of $\pi\pi e\gamma$ ($M^{\rm recoil}_{\pi\pi e\gamma}$), which should peak at the τ mass. Photon from $\Upsilon(1S)$ has been selected with energy (E_γ) greater than 200 MeV.

4.9.1 Background study

We include all the selections which have been imposed on leptons and pion-pair systems for $\Upsilon(1S) \to \gamma e^{\pm}\tau^{\mp}$ study. In Fig. 4.57, we compare the distribution of E_γ for signal and background inside the predefined window [(a) $9.45 < M^{\rm recoil}_{\pi\pi} < 9.66$ GeV/c^2, (b) $\cos(\theta_{\pi\pi}) < 0.5$, (c) $p^{\tau}_{\rm vis} > 0.3$ GeV/c, (d) $N_{\rm e} = 1$]. Like $\Upsilon(1S) \to \gamma\mu^{\pm}\tau^{\mp}$ mode, we select the events with E_γ greater than 200 MeV. Distribution of $M^{\rm recoil}_{\pi\pi e\gamma}$ inside the signal window has been shown in Fig. 4.58.

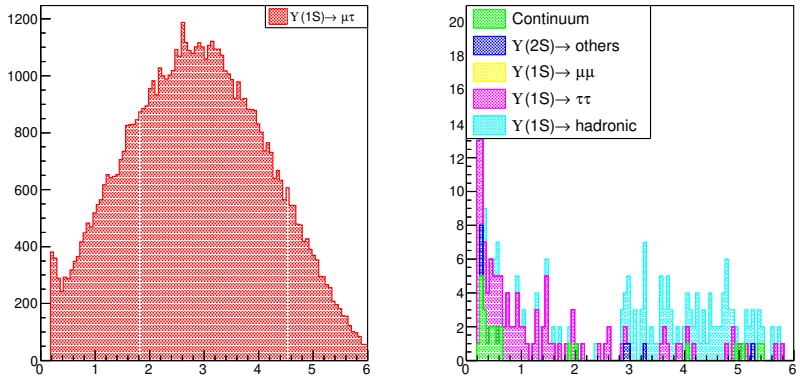

FIG. 4.57: E_γ (in GeV) distributions for $\Upsilon(1S) \to \gamma e^{\pm}\tau^{\mp}$ decays using signal MC sample (left) and using generic MC sample with scaled $\Upsilon(4S)$ off-resonance data (right).

4.9.2 Signal extraction

Like the $\Upsilon(1S) \to \gamma\mu^{\pm}\tau^{\mp}$ study, we exclude the $\tau^- \to \pi^-\pi^+\pi^-\nu_\tau$ mode for further progress due to low efficiency.

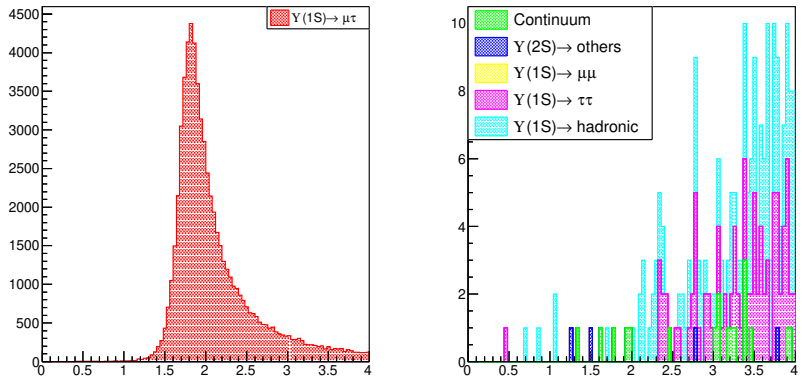

FIG. 4.58: $M^{\text{recoil}}_{\pi\pi e\gamma}$ (in GeV/c^2) distributions for $\Upsilon(1S) \to \gamma e^{\pm}\tau^{\mp}$ decays using signal MC sample (left) and using generic MC sample with scaled $\Upsilon(4S)$ off-resonance data (right).

Signal MC fit: We perform 1D UML fit on $M^{\text{recoil}}_{\pi\pi e\gamma}$ with sum of a Gaussian and a bifurcated Gaussian (Fig. 4.59). To estimate the signal efficiency and resolution, we use a MC sample with 0.5 million $\Upsilon(1S) \to \gamma e^{\pm}\tau^{\mp}$ decays, where tau decays generically. Fitted signal efficiency for $\Upsilon(1S) \to \gamma e^{\pm}\tau^{\mp}$ decay is estimated to be 5.2%.

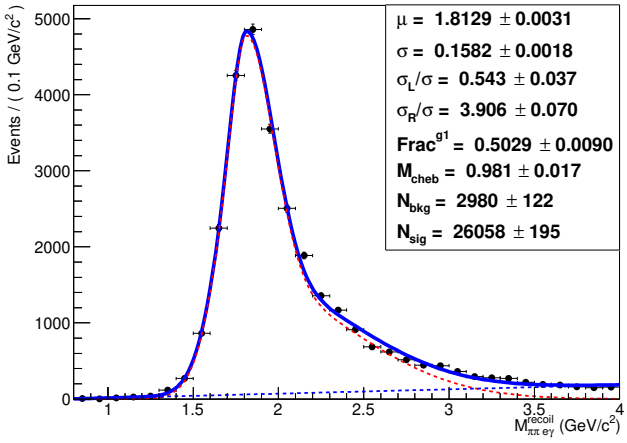

FIG. 4.59: UML fit to $M^{\text{recoil}}_{\pi\pi e\gamma}$ (in GeV/c^2) for $\Upsilon(1S) \to \gamma e^{\pm}\tau^{\mp}$ decays using signal MC sample.

Background estimation: To estimate the $\Upsilon(1S) \to \tau^+\tau^-$ background, we generate 40 million $\Upsilon(1S) \to \ell^{\pm}\ell^{\mp}$ MC sample. We use an exponential threshold like likelihood function in Eq. (4.4) to model the $\tau\tau$ background. All other backgrounds,

which mostly come from the hadronic decays of $\Upsilon(1S)$, are modeled with an exponential function. We perform $M^{\text{recoil}}_{\pi\pi e\gamma}$ fit to the generic MC background fixing the shape of two component background PDFs, and floating fraction of two PDFs. Fig. 4.60 summarizes all the background fits.

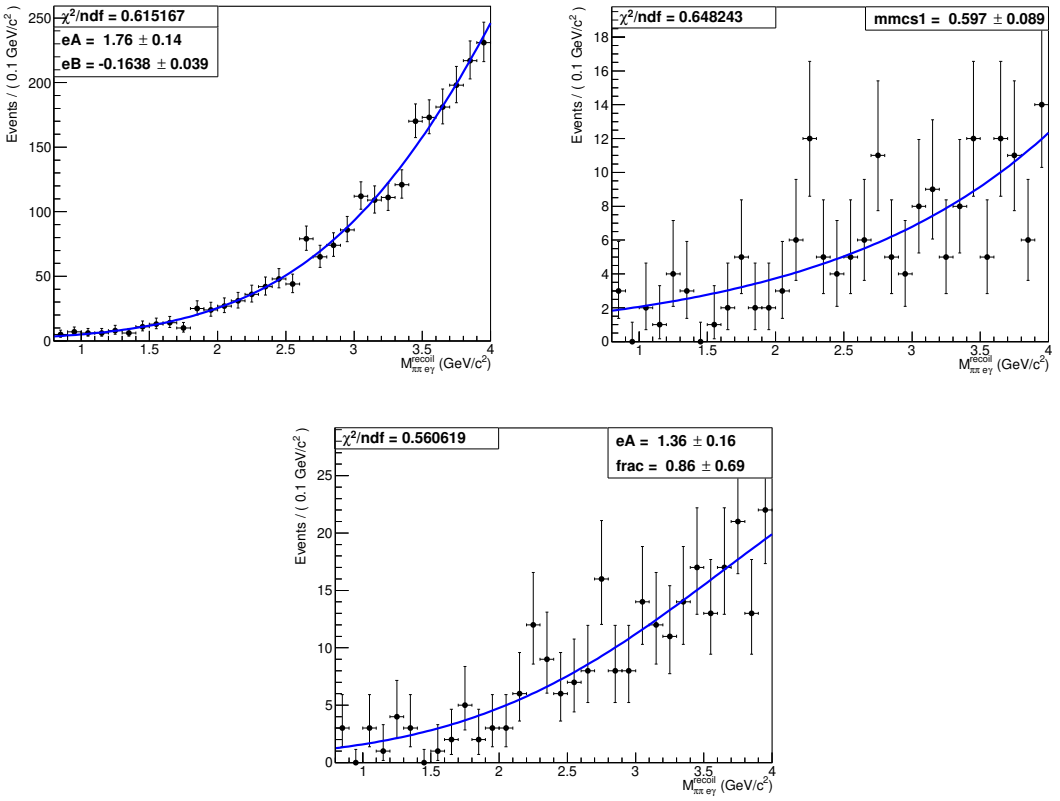

FIG. 4.60: UML fits to $M^{\text{recoil}}_{\pi\pi e\gamma}$ (in GeV/c^2) for $\Upsilon(1S) \to \tau^+\tau^-$ backgrounds using the 40 million $\Upsilon(1S) \to \ell^\pm\ell^\mp$ MC sample (top left) and for all other backgrounds using generic MC sample (top right). Total background fit using generic MC sample with scaled $\Upsilon(4S)$ off-resonance data (bottom).

Generic MC signal estimation: We fit the generic MC events fixing the shape of the signal and background PDFs. We float the lower order coefficient of threshold function (A) of the $\tau\tau$ PDF to get systematic effect. Also, as an alternative approach, we fit the generic MC events considering a 3rd order polynomial as background. Both of the fits (Fig. 4.61) look similar, and fitted χ^2 also agree well. We are expecting -7.9 ± 7.6 and -3.8 ± 9.0 signal yields with nominal and polynomial background, respectively.

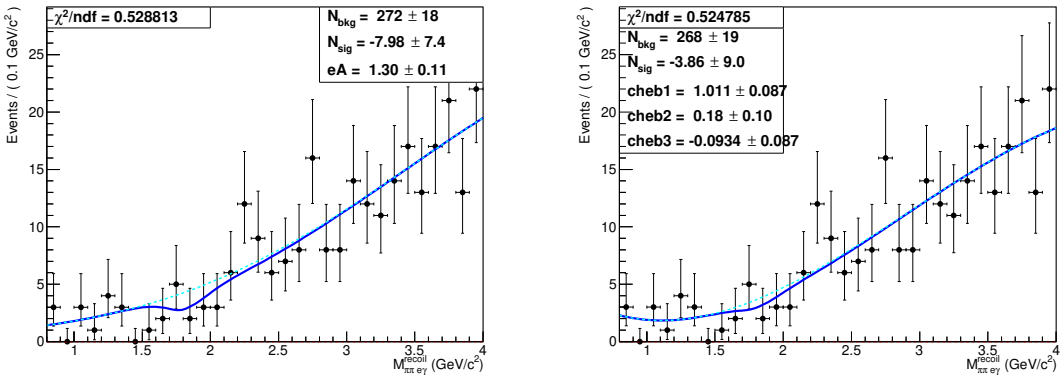

FIG. 4.61: UML fit to $M^{\text{recoil}}_{\pi\pi e\gamma}$ (in GeV/c^2) for combined signal and background with nominal background PDF (left) and with polynomial background PDF (right) using generic MC sample with scaled $\Upsilon(4S)$ off-resonance data.

4.9.3 UL estimation with MC background

We estimate the sensitivity of $\Upsilon(1S) \to \gamma e^{\pm}\tau^{\mp}$ transition using the nominal background PDF in a similar approach to $\Upsilon(1S) \to e^{\pm}\tau^{\mp}$ study. We plot the confidence level, percentage of the samples having positive signal yield, as a function of input yield. Considering nominal background, expected upper limit of the branching fraction for $\Upsilon(1S) \to \gamma e^{\pm}\tau^{\mp}$ at 90% CL is 4.9×10^{-6}.

4.10 RLFV study with data

Fits using $\Upsilon(2S)$ data: We perform the 1D UML fit with $\Upsilon(2S)$ on resonance data for each of the RLFV modes. $\Upsilon(1S) \to \gamma e^{\pm}\mu^{\mp}$ signal resolution in data is fixed from the signal MC corrected the average of data and MC difference on ΔM for $\Upsilon(1S) \to e^+e^-$ and $\Upsilon(1S) \to \mu^+\mu^-$ events. For $\Upsilon(1S) \to \gamma\ell\tau$ fits, signal resolutions in data are fixed from the signal MC corrected by the obtained data and MC difference on $M^{\text{recoil}}_{\pi\pi\ell}$ using $\Upsilon(1S) \to \ell\ell$ events. Fits for the $\gamma e\mu$, $\gamma\mu\tau$, and $\gamma e\tau$ are given in Fig. 4.62, Fig. 4.63, and Fig. 4.64, respectively. Considering no significant peaking background contribution, fitted signal yields for $\Upsilon(1S) \to \gamma e^{\pm}\mu^{\mp}$, $\Upsilon(1S) \to \gamma\mu^{\pm}\tau^{\mp}$ and $\Upsilon(1S) \to \gamma e^{\pm}\tau^{\mp}$ decays are 0.8 ± 1.5, 2.1 ± 5.9 and -9.5 ± 6.3, respectively.

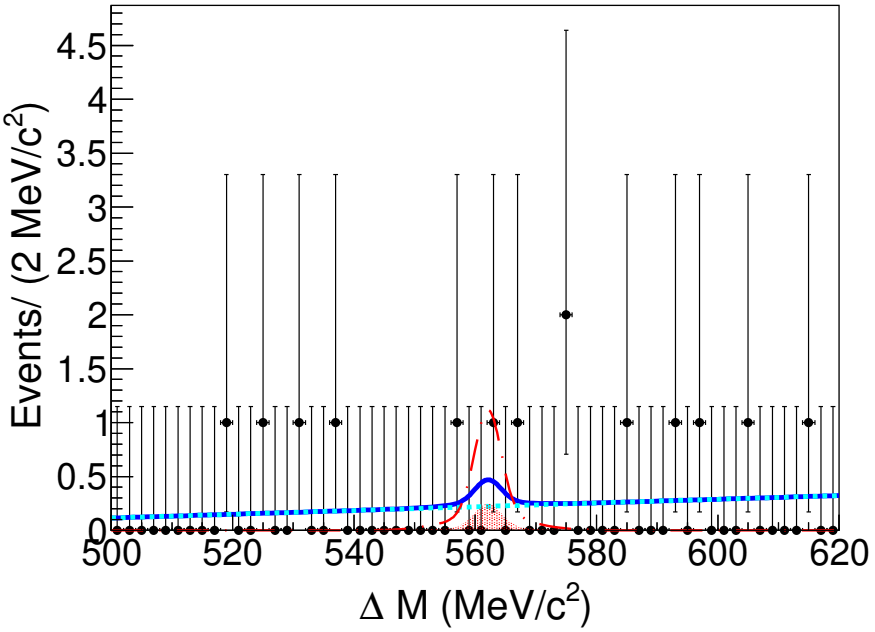

FIG. 4.62: ΔM fit with $\Upsilon(2S)$ data for $\Upsilon(1S) \to \gamma e^{\pm}\mu^{\mp}$ decay. Filled red region represents the fitted signal yield. The long-dashed red curve represent the signal PDFs corresponding to 5 hypothetical signal events.

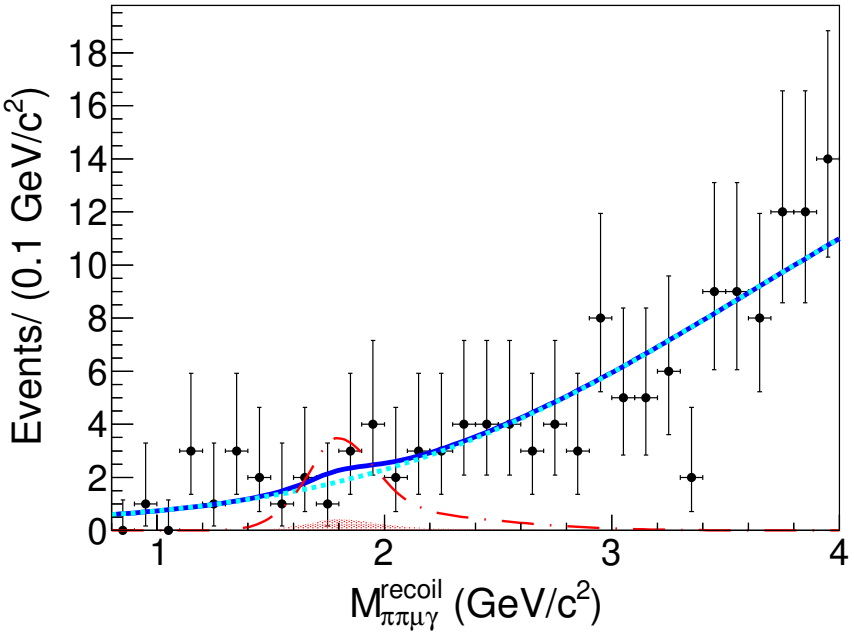

FIG. 4.63: $M^{\text{recoil}}_{\pi\pi\mu\gamma}$ fit with $\Upsilon(2S)$ data for $\Upsilon(1S) \to \gamma\mu^{\pm}\tau^{\mp}$ decay. The long-dashed red curve represent the signal PDFs corresponding to 20 hypothetical signal events.

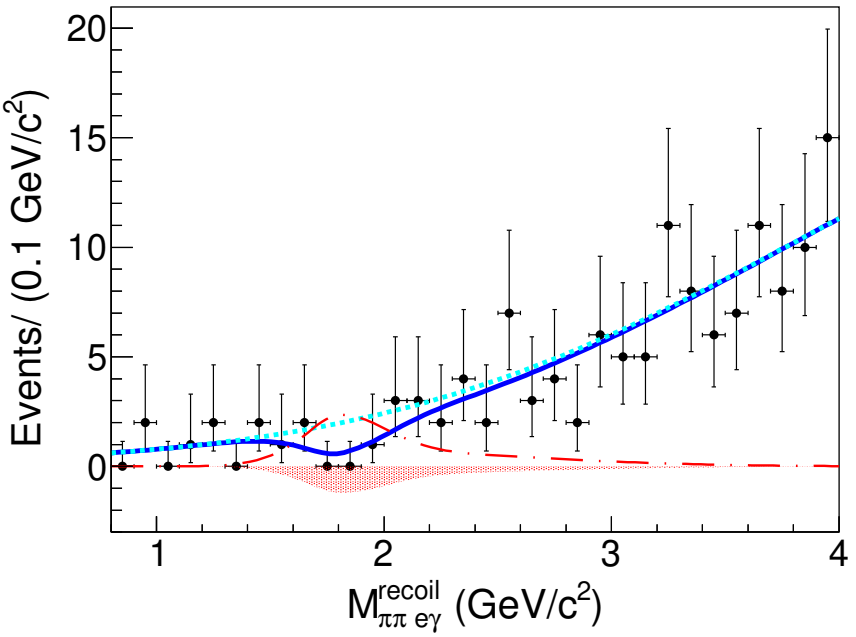

FIG. 4.64: $M^{\rm recoil}_{\pi\pi e\gamma}$ fit with $\Upsilon(2S)$ data for $\Upsilon(1S) \to \gamma e^{\pm}\tau^{\mp}$ decay. The long-dashed red curve represent the signal PDFs corresponding to 20 hypothetical signal events.

Result for RLFV: One can calculate the branching fractions using the following relation,

$$\mathcal{B}[\Upsilon(1S) \to \gamma\ell^{\pm}\ell'^{\mp}] = \frac{N_{\rm sig}}{N_{\Upsilon(2S)} \times \mathcal{B}[\Upsilon(2S) \to \pi^+\pi^-\Upsilon(1S)] \times \epsilon_{\rm cor}} \tag{4.8}$$

Where $N_{\rm sig}$ and $\epsilon_{\rm cor}$ are the signal yield and the corrected efficiency of the signal respectively. All the results for the branching fractions of RLFV modes are statistically dominated. For $\gamma e\mu$, $\gamma\mu\tau$, and $\gamma e\tau$ decays, the yield of signal events ($N_{\rm sig}$) is expected to be 0.8, 2.1, and 0.0, respectively. In absence of significant signal, we estimate the UL of branching with the frequentist method using an ensemble of 500 pseudo experiments. We calculate the CL as percentage of the pseudo experiments with fitted yield greater than expected signal yield in data. Systematic of the RLFV modes have been included by smearing the yield of the pseudo experiments within the fluctuations. In Fig. 4.65, we show the CL distribution as a function of input signal yield for different RLFV modes.

Considering number of $\Upsilon(2S)$ as 157.8 million [86], and $\mathcal{B}[\Upsilon(2S) \to \pi^+\pi^-\Upsilon(1S)]$ as 0.1785, we estimate the ULs using Eq. (4.8). We summarize those upper limits

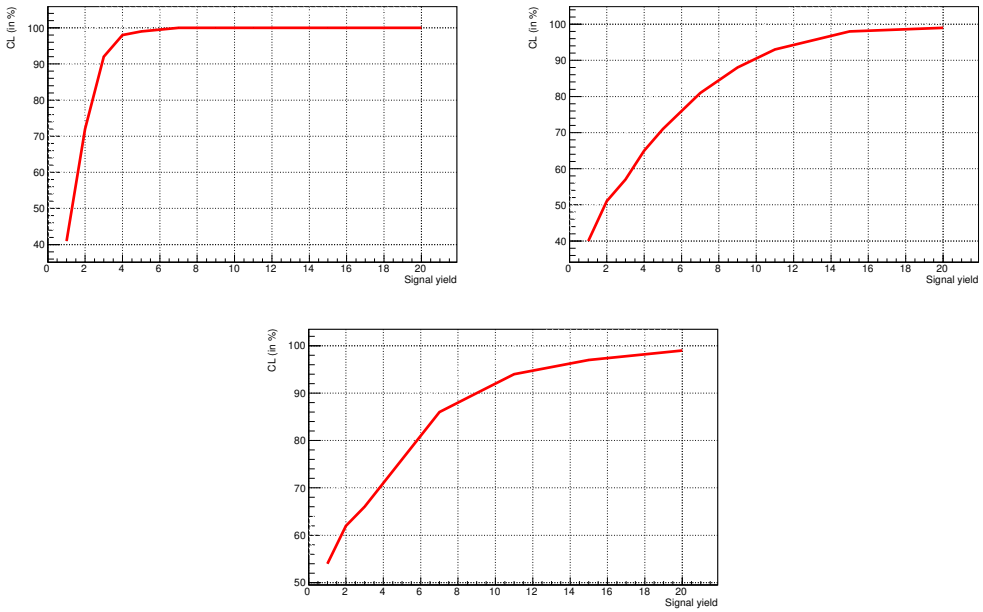

FIG. 4.65: Confidence level distributions for $\Upsilon(1S) \to \gamma e^{\pm}\mu^{\mp}$ (top left), $\Upsilon(1S) \to \gamma\mu^{\pm}\tau^{\mp}$ (top right), and $\Upsilon(1S) \to \gamma e^{\pm}\tau^{\mp}$ (bottom) decays.

Decay	ϵ_{cor} (%)	N^{UL} (90% CL)	UL @ 90% CL
$\Upsilon(1S) \to \gamma e^{\pm}\mu^{\mp}$	24.6	2.9	4.2×10^{-7}
$\Upsilon(1S) \to \gamma\mu^{\pm}\tau^{\mp}$	5.8	10.0	6.1×10^{-6}
$\Upsilon(1S) \to \gamma e^{\pm}\tau^{\mp}$	5.0	9.1	6.5×10^{-6}

TAB. 4.7: Results of RLFV searches in $\Upsilon(1S) \to \gamma\ell^{\pm}\ell'^{\mp}$ decays.

in Tab. 4.7. Estimated ULs for $\Upsilon(1S) \to \gamma e^{\pm}\mu^{\mp}$, $\Upsilon(1S) \to \gamma\mu^{\pm}\tau^{\mp}$, and $\Upsilon(1S) \to \gamma e^{\pm}\tau^{\mp}$ at 90% CL are 4.2×10^{-7}, 6.1×10^{-6}, and 6.5×10^{-6}, respectively.

4.11 Systematic uncertainty

Estimating the systematic uncertainty is crucial for any physics measurement. We evaluate the systematic uncertainty from various sources. Those have been discussed in this section.

4.11.1 Systematic from the number of $\Upsilon(2S)$

In order to calculate the systematic from the number of $\Upsilon(2S)$, we use a previous Belle measurement [86]. The expected number of $\Upsilon(2S)$ in 24.7 fb^{-1} on resonance data is estimated to be 157.8 ± 3.6 million. This result indicates the uncertainty from $N_{\Upsilon(2S)}$ is 2.3%.

4.11.2 Track reconstruction

Reconstruction of charged particle tracks are studied using partially reconstructed $D^{*+} \to D^0[K^0_S(\pi^+\pi^-)\pi^+\pi^-]\pi^+$ decay sample with $p^T > 200$ MeV/c [87]. Systematic uncertainty per charged track is estimated to be 0.35%. Due to correlation, errors are added linearly. Systematic from charged track reconstruction efficiency for various decays modes can be found in Tab. 4.8.

Decay		Tracking systematic (%)
$\Upsilon(1S) \to e^\pm\mu^\mp$		1.4
$\Upsilon(1S) \to \mu^\pm\tau^\mp$	$\tau^- \to e^-\bar{\nu}_e\nu_\tau$	1.4
	$\tau^- \to \pi^-\pi^+\pi^-\nu_\tau$	2.1
$\Upsilon(1S) \to e^\pm\tau^\mp$	$\tau^- \to \mu^-\bar{\nu}_\mu\nu_\tau$	1.4
	$\tau^- \to \pi^-\pi^+\pi^-\nu_\tau$	2.1
Control mode	$\Upsilon(1S) \to e^+e^-$	1.4
	$\Upsilon(1S) \to \mu^+\mu^-$	1.4

TAB. 4.8: Systematic from the charged track reconstruction.

4.11.3 Pion from $\Upsilon(2S)$

Uncertainty from the pion identification in $\Upsilon(2S) \to \pi^+\pi^-\Upsilon(1S)$ reconstruction may effect our results. In order to estimate it, we use standard results obtained by particle identification working group based on the $D^{*+} \to D^0(K^+\pi^-)\pi^+_{\rm slow}$ decays [88]. A correction for the difference in efficiency (between data and signal MC) is reported here. This correction is used to correct the efficiency, and the error on it is added as systematic error coming from pion identification. For all the decays, the efficiency correction factor and systematic from the identification of pion-pair are estimated to be 0.9998 and 1.9%, respectively.

4.11.4 Lepton identification

For lepton identification, systematic errors are calculated from the comparison between data and MC for two-photon mediated process $e^+e^- \to e^+e^-(e^+e^-/\mu^+\mu^-)$. We are using $L_e > 0.6$ for electron identification and $L_\mu > 0.95$ for muon identification. Those lepton selections are already studied before. In the case where tau has been identified in leptonic decays, we calculate the systematic in the same way. For $\tau^- \to \pi^-\pi^+\pi^-\nu_\tau$ decays, we calculate the systematic using the procedure mentioned in section 4.11.3. The systematic from lepton identification is summarized in Tab. 4.9.

Decay		Efficiency correction		Systematic (%)	
$(\Upsilon(1S) \to \ell_1\ell_2)$		ℓ_1	ℓ_2	ℓ_1	ℓ_2
$\Upsilon(1S) \to e^\pm\mu^\mp$		0.9994	0.9941	1.56	1.13
$\Upsilon(1S) \to \mu^\pm\tau^\mp$	$\tau^- \to e^-\bar{\nu}_e\nu_\tau$	0.9907	0.9973	1.11	1.79
	$\tau^- \to \pi^-\pi^+\pi^-\nu_\tau$	0.9963	0.8915	0.81	1.34
$\Upsilon(1S) \to e^\pm\tau^\mp$	$\tau^- \to \mu^-\bar{\nu}_\mu\nu_\tau$	1.0000	0.9790	1.52	1.66
	$\tau^- \to \pi^-\pi^+\pi^-\nu_\tau$	1.0000	0.8914	1.46	1.36
Control mode	$\Upsilon(1S) \to e^+e^-$	0.9992	0.9992	1.72	1.72
	$\Upsilon(1S) \to \mu^+\mu^-$	0.9957	0.9957	1.24	1.22

TAB. 4.9: Systematic from lepton reconstructions.

4.11.5 Uncertainty in the signal efficiency

Due to finite number of generated signal events, we have certain uncertainty in the fitted yield of signal events. As a result there is some uncertainty in the signal efficiency (ϵ), which can act as a source of systematic uncertainty. To estimate that, we take the ratio of uncertainty to the fitted events ($\frac{\delta\epsilon}{\epsilon}$). Tab. 4.10 summarizes the systematic uncertainty from signal efficiency.

4.11.6 Secondary branching fraction

We used some previously measured branching fractions to draw the final results. These fractions have some uncertainty, which should be taken as a source of systematic uncertainty. Tab. 4.11 summarizes the systematic errors coming from the secondary branching fractions.

Decay		Efficiency systematic (%)
$\Upsilon(1S) \to e^{\pm}\mu^{\mp}$		0.24
$\Upsilon(1S) \to \mu^{\pm}\tau^{\mp}$	$\tau^- \to e^-\bar{\nu}_e\nu_\tau$	0.33
	$\tau^- \to \pi^-\pi^+\pi^-\nu_\tau$	0.63
$\Upsilon(1S) \to e^{\pm}\tau^{\mp}$	$\tau^- \to \mu^-\bar{\nu}_\mu\nu_\tau$	0.47
	$\tau^- \to \pi^-\pi^+\pi^-\nu_\tau$	0.79
Control mode	$\Upsilon(1S) \to e^+e^-$	0.44
	$\Upsilon(1S) \to \mu^+\mu^-$	0.32

Tab. 4.10: Systematic from the signal efficiency.

Decay		Secondary BF systematic (%)
$\Upsilon(1S) \to e^{\pm}\mu^{\mp}$		1.45
$\Upsilon(1S) \to \mu^{\pm}\tau^{\mp}$	$\tau^- \to e^-\bar{\nu}_e\nu_\tau$	1.47
	$\tau^- \to \pi^-\pi^+\pi^-\nu_\tau$	1.55
$\Upsilon(1S) \to e^{\pm}\tau^{\mp}$	$\tau^- \to \mu^-\bar{\nu}_\mu\nu_\tau$	1.47
	$\tau^- \to \pi^-\pi^+\pi^-\nu_\tau$	1.55
Control mode	$\Upsilon(1S) \to e^+e^-$	1.45
	$\Upsilon(1S) \to \mu^+\mu^-$	1.45

Tab. 4.11: Systematic from the signal efficiency.

4.11.7 Signal extraction PDF

Signal yield is extracted by fitting the experimental data. To obtain the fits, we fix some parameters of the signal and background PDFs. Those parameters are always associated with some uncertainty, which may affect extracted signal yield. We estimate that systematic uncertainties varying all the fixed parameters by $\pm 1\sigma$ from its central values. For $\Upsilon(1S) \to \mu^+\mu^-$ and $\Upsilon(1S) \to e^+e^-$ decays, systematic uncertainties from signal PDFs are estimated to be 0.04% and 0.08%, respectively. In absence of significant signal events for CLFV modes, we take the average value of control modes (0.06%) as the systematic from signal PDF. Also, we fixed some parameters of the background PDF for $\Upsilon(1S) \to \ell^{\pm}\tau^{\mp}$ and $\Upsilon(1S) \to \gamma\ell^{\pm}\tau^{\mp}$ modes. The systematic from background PDFs of $\Upsilon(1S) \to \mu^{\pm}\tau^{\mp}$, $\Upsilon(1S) \to e^{\pm}\tau^{\mp}$, $\Upsilon(1S) \to \gamma\mu^{\pm}\tau^{\mp}$, and $\Upsilon(1S) \to \gamma e^{\pm}\tau^{\mp}$ decays are estimated to be 1.4%, 0.8%, 0.7%, and 1.4%, respectively. To obtain the combined systematic uncertainty from fitting model, we take a sum of the individual systematic of signal and background PDFs.

4.11.8 Total systematic

Systematic from $N_{\Upsilon(2S)}$, track reconstruction, particle identification, signal efficiency, secondary branching fractions, and fit PDF have been calculated. For $\Upsilon(1S) \to \mu^{\pm}\tau^{\mp}$ and $\Upsilon(1S) \to e^{\pm}\tau^{\mp}$ decays, there have been involved two τ modes. We derive a normalization factor with respect to the efficiencies of the respective τ modes. Finally, respective tau mode systematics are multiplied by those normalization factors, and added up to get the final values of the systematic uncertainties for the $\Upsilon(1S) \to \mu^{\pm}\tau^{\mp}$ and $\Upsilon(1S) \to e^{\pm}\tau^{\mp}$ decays. Finally, the systematic uncertainties from various sources have been added in a quadrature to get the total systematic uncertainty. We summarize the systematic uncertainties for different $\Upsilon(1S)$ decays in Tab. 4.12, and efficiency correction factors for different $\Upsilon(1S)$ modes in Tab. 4.13.

Source	Systematic uncertainty(%)							
	$\mathcal{S}_{e\mu}$	$\mathcal{S}_{\mu\tau}$	$\mathcal{S}_{e\tau}$	$\mathcal{S}_{\gamma e\mu}$	$\mathcal{S}_{\gamma\mu\tau}$	$\mathcal{S}_{\gamma e\tau}$	$\mathcal{S}_{ee}$	$\mathcal{S}_{\mu\mu}$
Number of $\Upsilon(2S)$	2.3	2.3	2.3	2.3	2.3	2.3	2.3	2.3
Track reconstruction	1.4	1.5	1.5	1.4	1.4	1.4	1.4	1.4
Photon reconstruction	-	-	-	2.0	2.0	2.0	-	-
Reconstruction of $\pi^+\pi^-$ from $\Upsilon(2S)$	1.9	1.9	1.9	1.9	1.9	1.9	1.9	1.9
1st lepton identification	1.6	1.1	1.5	1.7	2.0	1.7	1.7	1.2
2nd lepton identification	1.1	1.8	1.7	2.0	1.9	1.8	1.7	1.2
MC statistics	0.2	0.3	0.6	0.3	0.4	0.4	0.4	0.3
Secondary branching fractions	1.5	1.5	1.5	1.5	1.5	1.5	1.5	1.5
Fit PDF	0.1	1.5	0.9	0.1	0.8	1.5	0.1	0.0
Total	4.1	4.5	4.4	4.9	5.1	5.1	5.0	4.4

TAB. 4.12: Summary of the systematic uncertainties for the measurement of branching fractions of the $\Upsilon(1S) \to e^{\pm}\mu^{\mp}$ ($\mathcal{S}_{e\mu}$), $\Upsilon(1S) \to \mu^{\pm}\tau^{\mp}$ ($\mathcal{S}_{\mu\tau}$), $\Upsilon(1S) \to e^{\pm}\tau^{\mp}$ ($\mathcal{S}_{e\tau}$), $\Upsilon(1S) \to \gamma e^{\pm}\mu^{\mp}$ ($\mathcal{S}_{\gamma e\mu}$), $\Upsilon(1S) \to \gamma\mu^{\pm}\tau^{\mp}$ ($\mathcal{S}_{\gamma\mu\tau}$), $\Upsilon(1S) \to \gamma e^{\pm}\tau^{\mp}$ ($\mathcal{S}_{\gamma e\tau}$), $\Upsilon(1S) \to e^+e^-$ ($\mathcal{S}_{ee}$), and $\Upsilon(1S) \to \mu^+\mu^-$ ($\mathcal{S}_{\mu\mu}$) decays.

4.12 Summary

In this study, we report the searches for charged lepton-flavor-violation in $\Upsilon(1S) \to \ell^{\pm}\ell'^{\mp}$ decays and radiative lepton-flavor-violation in $\Upsilon(1S) \to \gamma\ell^{\pm}\ell'^{\mp}$ decays conducted at the Belle experiment, where $\ell, \ell' = e, \mu, \tau$. The searches are based on the 28 million $\pi^+\pi^-\Upsilon(1S)$ decays produced in 25 fb^{-1} (world largest) of e^+e^- collisions collected at the $\Upsilon(2S)$ resonance. We study the sources of possible background using a

Decay		Correction factor	Corrected efficiency (%)
$\Upsilon(1S) \to e^{\pm}\mu^{\mp}$		0.9933	35.2
$\Upsilon(1S) \to \mu^{\pm}\tau^{\mp}$	$\tau^- \to e^-\bar{\nu}_e\nu_\tau$	0.9689	8.6
	$\tau^- \to \pi^-\pi^+\pi^-\nu_\tau$	0.8916	0.8
$\Upsilon(1S) \to e^{\pm}\tau^{\mp}$	$\tau^- \to \mu^-\bar{\nu}_\mu\nu_\tau$	0.9795	7.0
	$\tau^- \to \pi^-\pi^+\pi^-\nu_\tau$	0.8948	0.7
$\Upsilon(1S) \to \gamma e^{\pm}\mu^{\mp}$		0.9538	24.6
$\Upsilon(1S) \to \gamma\mu^{\pm}\tau^{\mp}$		0.9438	5.8
$\Upsilon(1S) \to \gamma e^{\pm}\tau^{\mp}$		0.9643	5.0
Control mode	$\Upsilon(1S) \to e^+e^-$	0.9983	28.3
	$\Upsilon(1S) \to \mu^+\mu^-$	0.9914	35.6

TAB. 4.13: Effective efficiency correction factors for different modes.

large $\Upsilon(2S)$ MC sample. To validate the signal extraction procedure we measure the branching fractions for $\Upsilon(1S) \to e^+e^-$ and $\Upsilon(1S) \to \mu^+\mu^-$ modes and find $\mathcal{B}[\Upsilon(1S) \to e^+e^-] = (2.40 \pm 0.01(\text{stat}) \pm 0.12(\text{syst})) \times 10^{-2}$ and $\mathcal{B}[\Upsilon(1S) \to \mu^+\mu^-] = (2.46 \pm 0.01(\text{stat}) \pm 0.11(\text{syst})) \times 10^{-2}$, respectively. These results agree well with the PDG values. In the absence of signal, we set upper limits on the branching fractions of the CLFV decays at the 90% CL. The result for the $\Upsilon(1S) \to \mu^{\pm}\tau^{\mp}$ decay is 2.3 times more stringent than the previous result from the CLEO collaboration [48], while the remaining modes are searched for the first time.

Chapter 5

Search for CLFV decays of $\chi_{bJ}(1P)$

Belle has the world largest $\Upsilon(2S)$ on resonance data sample (24.7 fb^{-1}) in the world, which corresponds to 158 million $\Upsilon(2S)$ mesons. The branching fractions correspond to $\Upsilon(2S) \to \gamma\chi_{bJ}(1P)$ decays are 3.8%, 6.9%, and 7.2% for spin values 0, 1, and 2, respectively. One expects number of $\chi_{bJ}(1P)$ produced in $\Upsilon(2S)$ decays to be around 6.0, 10.8, and 11.3 million, respectively. The statistics for $\chi_{bJ}(1P)$ samples is good enough to study radiative transition and CLFV transitions in $\chi_{b[0,1,2]}(1P)$ decays. In this section we describe analysis procedure, Monte-Carlo simulations, and expected results on the search for CLFV in $\chi_{bJ}(1P)$ decays.

5.1 Signal Monte Carlo generation

Decay mode	Calibration modes
$\chi_{b[0,1,2]}(1P) \to e^{\pm}\mu^{\mp}$	$\chi_{b[0,1,2]}(1P) \to \gamma\Upsilon(1S)[\to e^+e^-]$
$\chi_{b[0,1,2]}(1P) \to \mu^{\pm}\tau^{\mp}$	$\chi_{b[0,1,2]}(1P) \to \gamma\Upsilon(1S)[\to \mu^+\mu^-]$
$\chi_{b[0,1,2]}(1P) \to e^{\pm}\tau^{\mp}$	

Tab. 5.1: Generated MC samples and corresponding control modes.

We have generated 0.25 million signal events for each of the samples and corresponding control samples using the EvtGen package [93], as mentioned in Tab. 5.1. For $\chi_{b2}(1P) \to \gamma\Upsilon(1S)$ decay, we use the PHSP model, and all other radiative decays have been generated using the HELAMP model. The VLL model has been used to generate $\Upsilon(1S) \to e^+e^-/\mu\mu$ transitions. In absence of any proper model for CLFV

transitions, we use the PHSP model with the PHOTOS [94] to generate the events for $\chi_{b[0,1,2]}(1P) \to \ell^{\mp}\ell'^{\mp}$ decays.

5.2 $\chi_{bJ}(1P) \to \gamma\Upsilon(1S)$ study

As $\chi_{bJ}(1P) \to ee/\mu\mu$ decays are forbidden, we consider double radiative $\Upsilon(2S) \to \gamma\chi_{b[0,1,2]}(1P)[\to \gamma\Upsilon(1S)]$ decays as calibration modes. There are only two charged tracks in the final states with one or two photons in the final state, which makes this analysis difficult. First, we validate the signal experimental setup and analysis strategy by measuring the branching fraction for $\chi_{bJ}(1P) \to \gamma\Upsilon(1S)$ for different spin values (J=0, 1, 2), where $\Upsilon(1S)$ has been reconstructed in $\Upsilon(1S) \to e^+e^-$ and $\Upsilon(1S) \to \mu^+\mu^-$ decays.

5.2.1 Analysis strategy

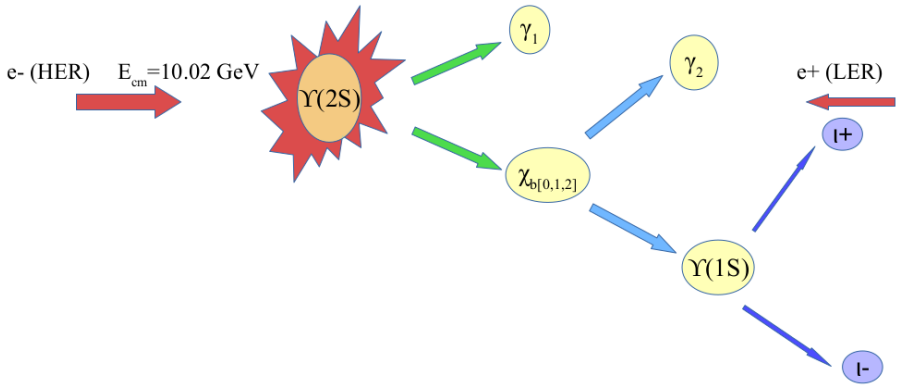

FIG. 5.1: Schematic diagram for $\Upsilon(2S) \to \gamma\chi_{b[0,1,2]}(1P)[\to \gamma\Upsilon(1S)]$ decay.

Decay mode	E_{γ_1} (MeV)	E_{γ_2} (MeV)
$\Upsilon(2S) \to \gamma_1\chi_{b0}(1P)[\to \gamma_2\Upsilon(1S)]$	163.8	391.1
$\Upsilon(2S) \to \gamma_1\chi_{b1}(1P)[\to \gamma_2\Upsilon(1S)]$	130.5	423.0
$\Upsilon(2S) \to \gamma_1\chi_{b2}(1P)[\to \gamma_2\Upsilon(1S)]$	111.1	441.6

TAB. 5.2: Energies of the radiative photons involved in different $\chi_{bJ}(1P)$ modes.

Schematic diagram of $\Upsilon(2S) \to \gamma\chi_{b[0,1,2]}(1P)[\to \gamma\Upsilon(1S)]$ decay is represented in Fig. 5.1. All the photons involved in the $\chi_{b[0,1,2]}(1P)$ decays have the energy ranging from 100 to 450 MeV (Tab. 5.2), which makes them difficult to separate from each

other. The energies of the γ_1 are in the order of 100 MeV. Beam background photons and soft photons cause lots of potential background in this energy range. We look at the recoil mass of two photons ($M_{\gamma\gamma}^{\rm recoil}$), which can be derived using the following relation.

$$M_{\gamma\gamma}^{\rm recoil} = \sqrt{E_{\rm cm}^2 + M_{\gamma\gamma}^2 - 2E_{\rm cm}E_{\gamma\gamma}} \tag{5.1}$$

Where $E_{\rm cm}$, $M_{\gamma\gamma}$, and $E_{\gamma\gamma}$ are the energy of colliding e^+e^-, invariant mass of the photon pair, and energy of the photon pair in the center of mass frame, respectively. We apply cut on $M_{\gamma\gamma}^{\rm recoil}$ to remove the background in two photon reconstruction. In the rest-frame of $\Upsilon(2S)$, γ_1 and $\chi_{bJ}(1P)$ should be back to back. In order to remove the background in the γ_1 reconstruction, one can apply a cut on $\cos(\theta_{\gamma\chi})$, where $\theta_{\gamma\chi}$ is the angle between γ_1 and $\chi_{bJ}(1P)$ in $\Upsilon(2S)$ rest-frame. Finally we extract the signal through the recoil mass distribution of γ_1 ($M_{\gamma}^{\rm recoil}$), which can be written as the following equation.

$$M_{\gamma}^{\rm recoil} = \sqrt{E_{\rm cm}^2 - 2E_{\rm cm}E_{\gamma}} \tag{5.2}$$

Where E_γ is the energy of the γ_1. $M_{\gamma}^{\rm recoil}$ should peak at the corresponding $\chi_{b[0,1,2]}(1P)$ mass.

5.2.2 Event selection

We have two photons and two leptons in the final state. We apply the following selection to select the charged particle states.

- The distances of closest approach from the IP for all the charged particles in horizontal (vertical) direction has to be less than 4.5 cm (1.5 cm).
- Electron (muon) candidates with L_e (L_μ) greater than 0.1 are selected. Further these selections are to be optimized.

Following selections are applied to select the photon candidates.

- KEKB is an asymmetric energy accelerator with an high energetic electron moving along the +z direction. As a result, most of the beam background get encountered at the forward endcap of the ECL. We look at energy distribution of the photons as a function of its polar angle distribution (Fig. 5.2). For low energetic photon (γ_1), we set the energy threshold depending on the angular

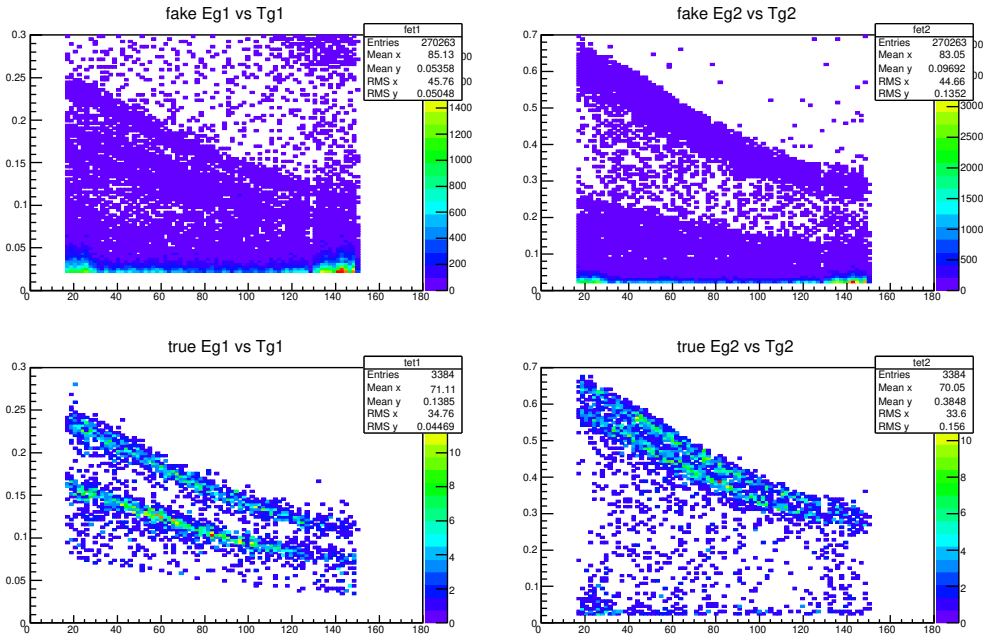

FIG. 5.2: Energy vs polar angle distribution of γ_1 (left) and γ_2 (right). Distribution for background events using generic MC sample (top) and truth matched signal events using $\chi_{bJ}(1P) \to \gamma\Upsilon(1S)$ signal MC sample (bottom).

distribution of them inside the ECL. For forward endcap, barrel region, and backward endcap photons (γ_1) are selected with the energy thresholds 70 MeV, 50 MeV, and 60 MeV, respectively.

- Energy threshold for high energetic photon (γ_2) is 250 MeV.
- Photons within 50 mrad of each $e^{\pm}$ track are selected as bremsstrahlung photons.

Further, we select the events with mass of the two leptons pairs $M_{\ell\ell}$ within in 9.1 to 9.8 GeV/c^2.

5.2.3 Four constraint fit

Mass of $\chi_{b1}(1P)[\to \gamma\Upsilon(1S)]$ and $\chi_{b2}(1P)[\to \gamma\Upsilon(1S)]$ are very close to each other. Due to the detector resolution, it is difficult to separate the $\chi_{b1}(1P)$, $\chi_{b2}(1P)$ peaks in $M_{\gamma}^{\text{recoil}}$ distribution especially for $\Upsilon(1S) \to e^+e^-$ events. In order to improve the resolution, we perform four constrained fit (4C-fit) with 4-momentum of reconstructed particles (as discussed in appendix C.1). In Fig. 5.3, we compare

the distributions of $M_{\gamma}^{\text{recoil}}$ before and after 4C-fit. One can see a clear improvement in the resolution after applying the 4C-fit. We use the predicted 4-momentum of the particles for the calculation purpose, and thus resolution is improved. Further we use the minimized χ^2 after 4C-fit (χ^2_{4C}) for background suppression and best candidate selection.

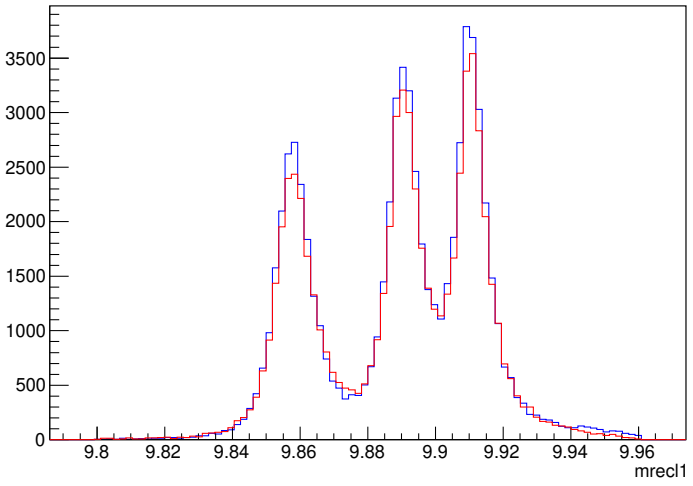

FIG. 5.3: Distribution of $M_{\gamma}^{\text{recoil}}$ (in GeV/c^2) before (red) and after (red) 4C-fit.

5.2.4 Best candidates selection

Photon coming from $\Upsilon(2S) \to \gamma\chi_{b[0,1,2]}(1P)$ decay have the energy in the order of 100 MeV. Many of the beam background photons create lot of fake candidates. As a result, fractions of events with multiple candidates for ee and $\mu\mu$ events are 21% and 20%, respectively. Minimized χ^2_{4C} after 4C-fit has been used to select the best candidate among the multiple $\Upsilon(2S)$ candidates. One can estimate the best candidate selection (BCS) efficiency using the following relation.

$$\text{BCS efficiency} = \frac{\text{Number of truth matched events with } \chi^2_{min}}{\text{Number of events with multiple}\Upsilon(2S)\text{ candidate}} \times 100\% \quad (5.3)$$

Inside signal search window (defined later), we estimate the BCS efficiency inside the signal window. Using Eq. (5.3), our BCS efficiency is 97.9% for both of the ee and $\mu\mu$ channels.

5.2.5 Bhabha veto using TSIM

We have only two charged tracks and two photons. So the appearance of our ee events is similar to Bhabha events. As cross-section for Bhabha scattering is much larger than $\Upsilon(2S)$ production cross-section, the Bhabha events dominate the signal events. Bhabha veto is already applied during $\Upsilon(2S)$ data recording to get a Bhabha rejection in the order of 99%. But some of the signal events also get rejected with the Bhabha veto. For calculating branching fraction for different $\chi_{bJ}(1P)$ mode, we need to know the correct efficiency for each $\chi_{bJ}(1P)$ mode after applying Bhabha veto. We simulate the trigger effect to apply Bhabha veto on the signal MC simulated events using TSIM (as mentioned in appendix C.2). The events passed through this anti-Bhabha trigger have been used to estimate the expected efficiency.

5.3 Study of $\chi_{b[0,1,2]}(1P) \to \gamma\Upsilon(1S)[\to \mu^+\mu^-]$ decays

5.3.1 Background study

We study the possible sources of background using 158 million $\Upsilon(2S)$ generic MC sample, and we study the $e^+e^- \to q\bar{q}$ backgrounds using 80 fb^{-1} $\Upsilon(4S)$ off-resonance data. As the luminosity ($\mathcal{L}$) and energy at the CM frame (E_{cm}) are higher for $\Upsilon(4S)$ off-resonance data, the number of $e^+e^- \to q\bar{q}$ events are scaled with a factor of $\frac{\mathcal{L}_{on}E^2_{off}}{\mathcal{L}_{off}E^2_{on}}$ [85], where $\mathcal{L}_{on}$ and $\mathcal{L}_{off}$ are the on resonance and off-resonance luminosities, respectively. For our study, that factor is estimated to be 0.3.

L_μ selection: Our goal is to study the CLFV decay modes. Therefore, we optimize lepton identification cuts using the $\chi_{bJ}(1P) \to e^{\pm}\mu^{\mp}$ samples. Muons with L_μ greater than 0.9 are selected for further study.

$M^{recoil}_{\gamma\gamma}$ window selection: As one can see in Fig. 5.4, most of the background come from the $\Upsilon(2S) \to \pi^0\pi^0\Upsilon(1S)$ decay mode, where photon from π^0 decay ($\pi^0 \to \gamma\gamma$) is misidentified as signal candidates. We optimize the $M^{recoil}_{\gamma\gamma}$ window using figure of merit (FOM). We draw the FOM distribution varying boundaries of $M^{recoil}_{\gamma\gamma}$ window

with a step of 0.01 GeV/c^2 using the following relation.

$$\text{FOM} = \frac{S_i}{\sqrt{S_i + B_i}} \tag{5.4}$$

Where S_i is the number of $\chi_{bJ}(1P) \to \gamma\mu^+\mu^-$ events, and B_i is the number of background in a particular interval. The distribution of FOM is shown in Fig 5.5. We select the optimize $M^{\text{recoil}}_{\gamma\gamma}$ region from 9.39 to 9.50 GeV/c^2. Using the $M^{\text{recoil}}_{\gamma\gamma}$ cut, 94% of the background is rejected with a signal loss of 9%.

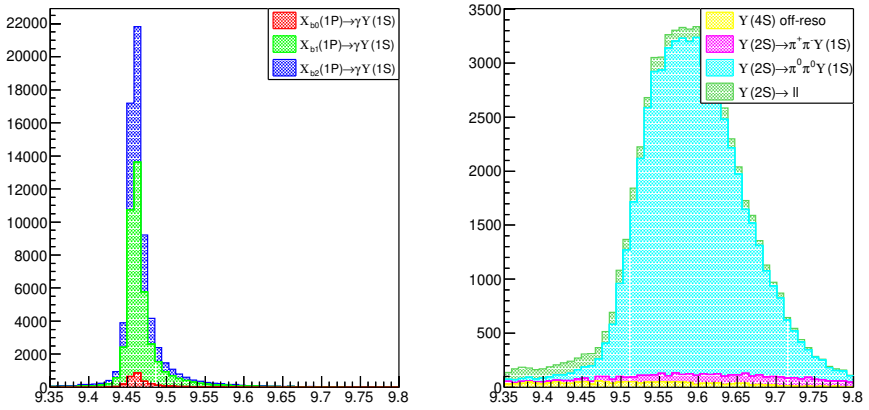

FIG. 5.4: $M^{\text{recoil}}_{\gamma\gamma}$ (in GeV/c^2) distributions for $\chi_{bJ}(1P) \to \gamma\mu^+\mu^-$ decays with tagged signal events (left) and background events (right) using generic MC sample with scaled $\Upsilon(4S)$ off-resonance data.

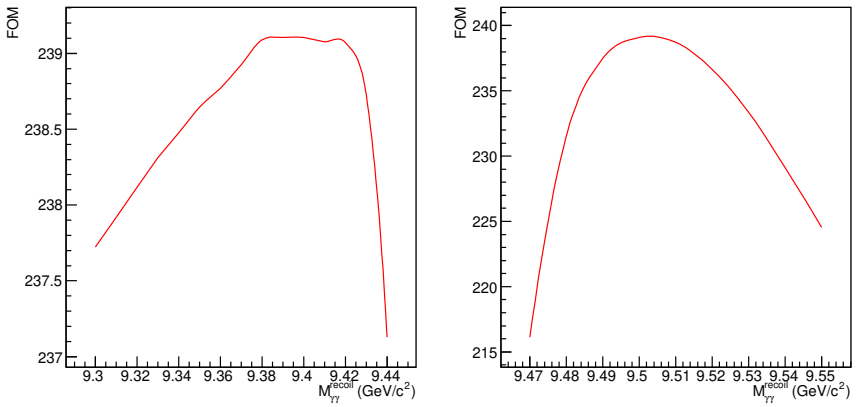

FIG. 5.5: Figure of merit for $M^{\text{recoil}}_{\gamma\gamma}$ optimization for $\chi_{bJ}(1P) \to \gamma\mu^+\mu^-$ decays.

$\cos(\theta_{\gamma\chi})$ **cut:** Fig. 5.6 shows the distribution of Cosine of angle between γ_1 and $\chi_{bJ}(1P)$ in the rest frame of $\Upsilon(2S)$. For ideal reconstruction $\cos(\theta_{\gamma\chi})$ should peak at -1. We apply a loose cut, $\cos(\theta_{\gamma\chi}) < 0$ to remove the background coming from γ_1 reconstruction. $\cos(\theta_{\gamma\chi})$ cut further remove 19% of background and 2% of the signal events.

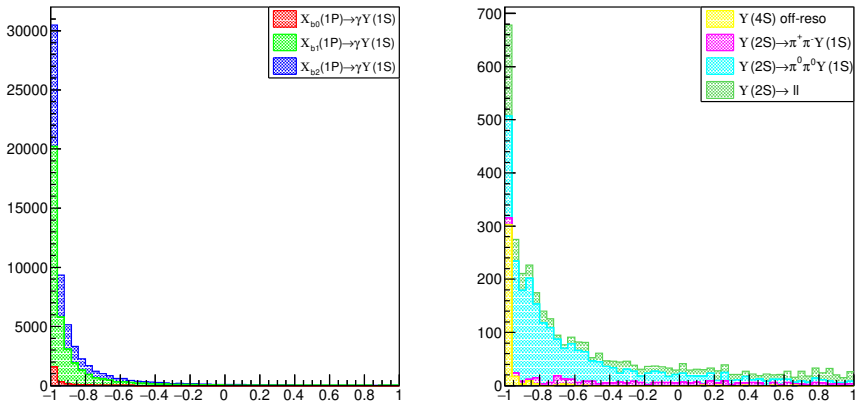

FIG. 5.6: $\cos(\theta_{\gamma\chi})$ distributions for $\chi_{bJ}(1P) \to \gamma\mu^+\mu^-$ decays with tagged signal events (left) and background events (right) using generic MC sample with scaled $\Upsilon(4S)$ off-resonance data.

χ^2_{4C} **cut:** We perform the 4C-fit with the 4-momentum of the reconstructed particles to improve the resolution, and the fitted χ^2_{4C} has been used to reduce the backgrounds. Events with $\chi^2_{4C} < 500$ are selected to remove the events which do not fit well (Fig. 5.7). It removes 7% of the signal events with reduction of background by 71%.

$M_{\gamma}^{\text{recoil}}$ **distribution:** Using all the selection criteria discussed in the event selection and background study, we plot the distribution of the signal and background events (Fig. 5.8). Number of backgrounds inside the signal window is very less as compared to signal events, and there are no peaking backgrounds.

5.3.2 Signal extraction

Signal MC fit: We perform 1D UML fit with sum of a Gaussian and a bifurcated Gaussian with common mean on $M_{\gamma}^{\text{recoil}}$ to get the resolution and efficiency of each $\chi_{bJ}(1P)$ separately. $M_{\gamma}^{\text{recoil}}$ fits are performed before and after applying Bhabha veto

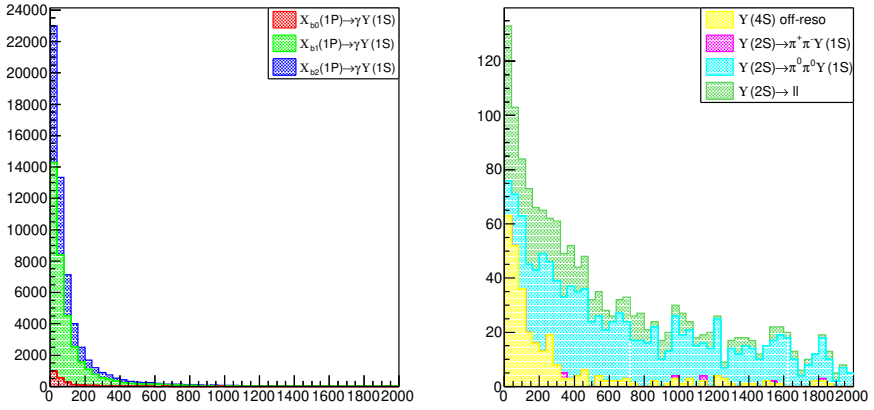

FIG. 5.7: χ^2_{4C} distributions for $\chi_{bJ}(1P) \to \gamma\mu^+\mu^-$ decays with tagged signal events (left) and background events (right) using generic MC sample with scaled $\Upsilon(4S)$ off-resonance data.

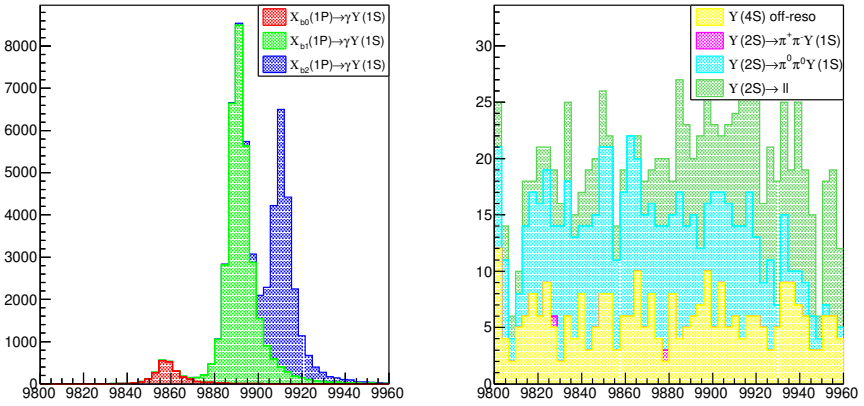

FIG. 5.8: $M_{\gamma}^{\text{recoil}}$ (in MeV/c^2) distributions for $\chi_{bJ}(1P) \to \gamma\mu^+\mu^-$ decays with tagged signal events (left) and background events (right) using generic MC sample with scaled $\Upsilon(4S)$ off-resonance data.

to check the effect of Bhabha veto. In Fig. 5.9, we show the fitted distribution for different $\chi_{b[0,1,2]}(1P)$ modes after applying the Bhabha veto. Tab. 5.3 summarizes the efficiency for different $\chi_{b[0,1,2]}(1P)$ modes. As the energy deposited on the lepton pair increases from $\chi_{b0}(1P)$ to $\chi_{b2}(1P)$, they behave more like a Bhabha event. Efficiency loss due to anti-Bhabha trigger increases from $\chi_{b0}(1P)$ to $\chi_{b2}(1P)$.

Generic MC fit: We prepare the background sample by adding scaled $\Upsilon(4S)$ off-resonance data with generic MC background. Three $\chi_{bJ}(1P)$ PDFs are combined by

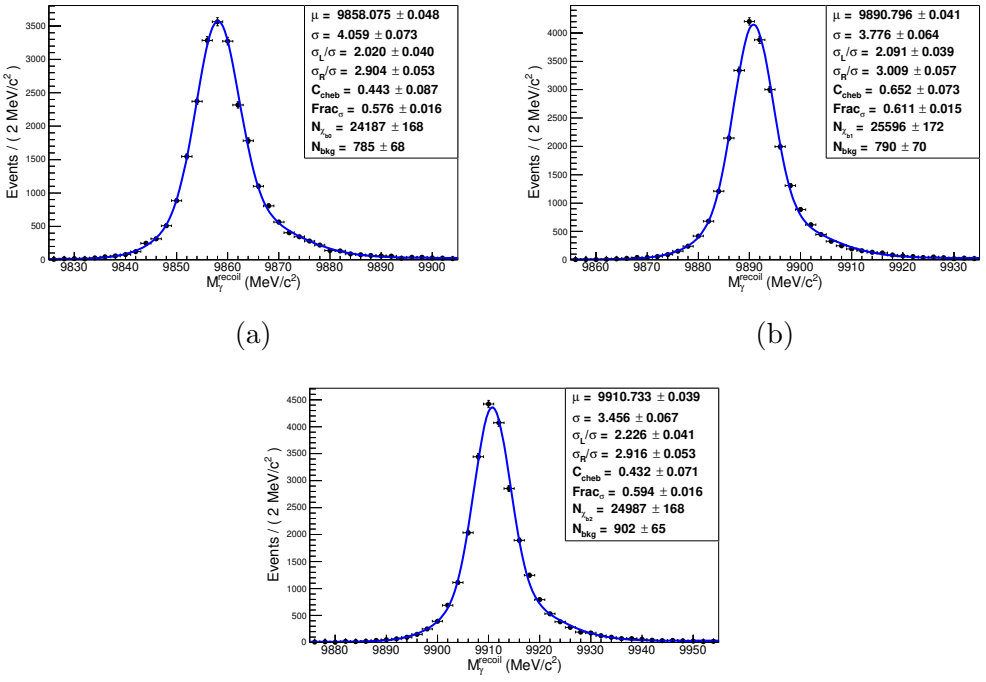

FIG. 5.9: UML fits to $M_{\gamma}^{\text{recoil}}$ (in MeV/c^2) for $\chi_{bJ}(1P) \to \gamma\mu^+\mu^-$ decays with $\chi_{b0}(1P)$ (a), $\chi_{b1}(1P)$ (b), and $\chi_{b2}(1P)$ (c) resonances using signal MC sample.

$\chi_{bJ}(1P)$	Before veto ϵ (in%)	After veto ϵ (in %)
J=0	30.1	29.0
J=1	33.3	30.7
J=2	32.7	30.0

TAB. 5.3: Expected efficiency (ϵ) before and after applying Bhabha veto for $\chi_{bJ}(1P) \to \gamma\mu^+\mu^-$ events.

fixing all the parameters from the MC signal PDFs (after applying Bhabha veto), except the mean and standard deviation of $\chi_{b1}(1P)$ PDF. Resolutions of $\chi_{b0}(1P)$ and $\chi_{b2}(1P)$ are fixed with respect to the resolution of $\chi_{b1}(1P)$. While fitting the generic MC events (Fig. 5.10), we fix the difference in the mean position of $\chi_{b0}(1P)$ ($\chi_{b2}(1P)$) and $\chi_{b1}(1P)$ according to the input mass difference.

$\Upsilon(2S)$ data fit: We model the $\Upsilon(2S)$ on-resonance data (Fig. 5.10) using the PDF that has been used for fitting the generic MC events. The separations of the $\chi_{b0}(1P)$ ($\chi_{b2}(1P)$) from $\chi_{b1}(1P)$ are fixed according to the mass difference in PDG [15]. The

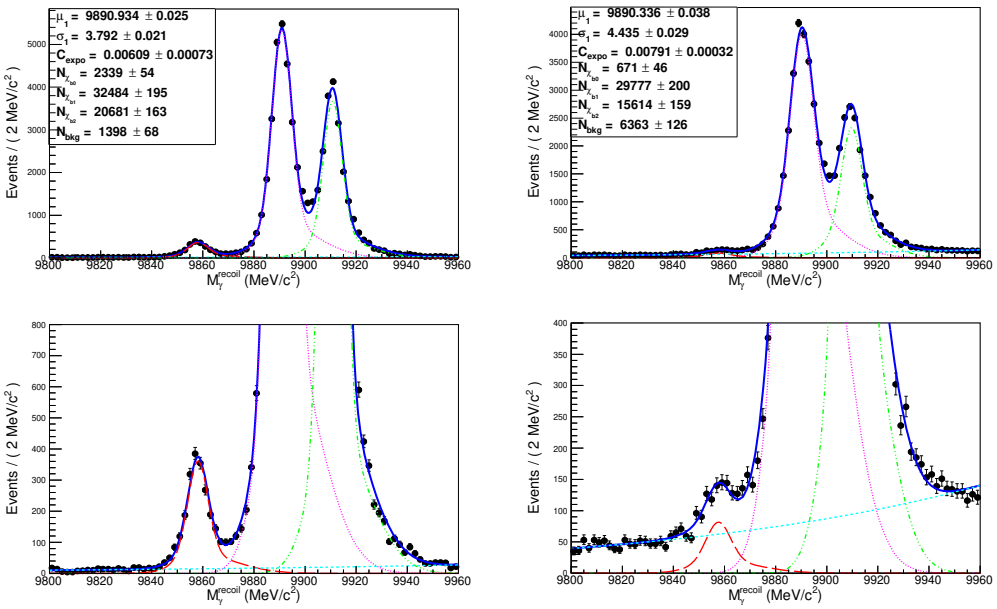

FIG. 5.10: UML fits to $M_{\gamma}^{\text{recoil}}$ (in MeV/c^2) for $\chi_{bJ}(1P) \to \gamma\mu^+\mu^-$ decays using generic MC sample with scaled $\Upsilon(4S)$ off-resonance data (left) and using $\Upsilon(2S)$ data (right). Bottom plots are zoomed view of the corresponding above plots to show the $\chi_{b0}(1P)$ events.

combined fitted distributions for MC and data have been used for calculating the branching fractions.

5.3.3 Result of $\chi_{bJ}(1P) \to \gamma\mu^+\mu^-$ decays

One can calculate the branching fraction corresponding to different $\chi_{bJ}(1P)$ modes using the following relation.

$$\mathcal{B}[\Upsilon(2S) \to \gamma\chi_{bJ}(1P)] \times \mathcal{B}[\chi_{bJ}(1P) \to \gamma\Upsilon(1S)] \times \mathcal{B}[\Upsilon(1S) \to \ell^{\pm}\ell^{\mp}] = \frac{N_{\text{sig}}^{J}}{N_{\Upsilon(2S)} \times \epsilon_J} \tag{5.5}$$

Where N_{sig}^{J} and ϵ_J are the signal yield and the efficiency of the signal for different J, respectively. Using Eq. (5.5), one can calculate the branching fractions for MC events, and can compare them with the input branching fractions to check the validity of the fitting model. Anti-Bhabha trigger can not be applied for generic MC events. Therefore, to validate the input branching fractions, we use the efficiency before applying the Bhabha veto. As one can see in Tab. 5.4, our fitted results agree with the input values. We compare the branching fractions, calculated using $\Upsilon(2S)$

data, with PDG values [15]. Result for $\chi_{b0}(1P)$ in data is slightly underestimated from the expectation (but consistent within 1 sigma).

$\Upsilon(2S) \to \gamma\gamma\mu\mu$	MC result		Data result	
	Input BF (10^{-4})	Fit result (10^{-4})	PDG value (10^{-4})	Our result (10^{-4})
J=0	0.486	0.492 $\pm$0.011	0.183 $\pm$0.032	0.147 $\pm$0.010
J=1	6.182	6.178 $\pm$0.037	6.023 $\pm$0.504	6.144 $\pm$0.041
J=2	4.027	4.003 $\pm$0.032	3.192 $\pm$0.245	3.300 $\pm$0.034

TAB. 5.4: Calculated composite branching fractions for $\Upsilon(2S) \to \gamma\gamma\mu\mu$ decays with different $\chi_{bJ}(1P)$ resonances.

5.4 Study of $\chi_{bJ}(1P) \to \gamma\Upsilon(1S)[\to e^+e^-]$ decays

5.4.1 Background study

We study the possible sources of background using 158 million $\Upsilon(2S)$ generic MC sample, and $e^+e^- \to q\bar{q}$ background using 80 fb^{-1} $\Upsilon(4S)$ off-resonance data. As in previous $\chi_{bJ}(1P) \to \gamma\mu^+\mu^-$ study, here also $e^+e^- \to q\bar{q}$ background has been scaled by a factor of 0.3.

L_e selection: Our aim is to study the CLFV decay modes. Therefore, we optimize the L_e cut using the $\chi_{bJ}(1P) \to e^{\pm}\mu^{\mp}$ samples (Fig. 5.19). Electron/positron with L_e greater than 0.5 are selected for further study.

$M^{\rm recoil}_{\gamma\gamma}$ window selection: Most of the background comes from the $\Upsilon(2S) \to \pi^0\pi^0\Upsilon(1S)$ decay mode (as one can see in Fig 5.11), where photon from π^0 decay ($\pi^0 \to \gamma\gamma$) is misidentified as signal candidates. We optimize the $M^{\rm recoil}_{\gamma\gamma}$ window using FOM in a similar approach to $\chi_{bJ}(1P) \to \gamma\mu^+\mu^-$ decay (using Eq. 5.4). The distribution of FOM is shown in Fig. 5.12. We select the optimized $M^{\rm recoil}_{\gamma\gamma}$ region from 9.39 to 9.50 GeV/c^2, which reduces 92% of background and 9% of signal events.

$\cos(\theta_{\gamma\chi})$ selection: For perfect reconstruction, $\cos(\theta_{\gamma\chi})$ should peak at -1. We apply a loose cut, $\cos(\theta_{\gamma\chi}) < 0$ to remove the background coming from γ_1 reconstruction

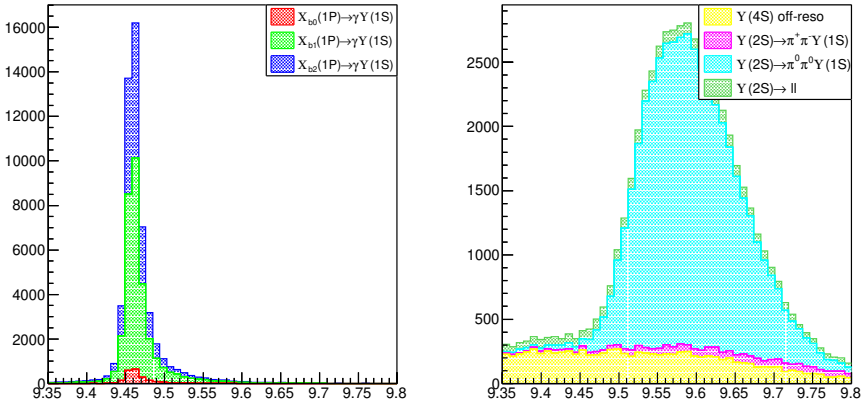

FIG. 5.11: $M^{\text{recoil}}_{\gamma\gamma}$ (in GeV/c^2) distributions for $\chi_{bJ}(1P) \to \gamma e^+e^-$ decays with tagged signal events (left) and background events (right) using generic MC sample with scaled $\Upsilon(4S)$ off-resonance data.

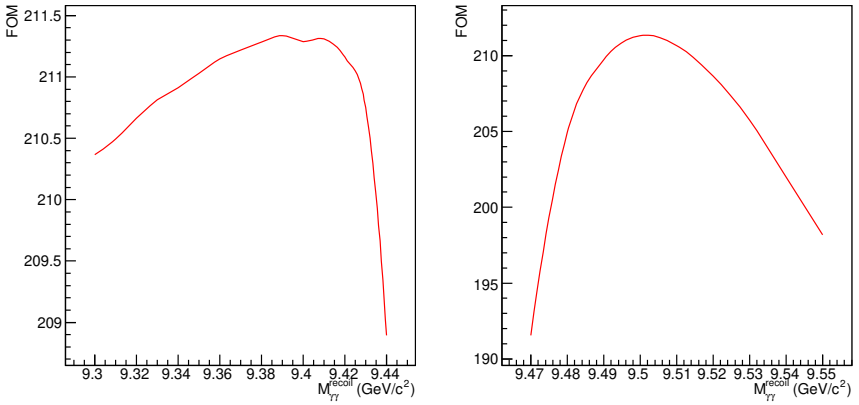

FIG. 5.12: Figure of merit for $M^{\text{recoil}}_{\gamma\gamma}$ optimization for $\chi_{bJ}(1P) \to \gamma e^+e^-$ decays.

(Fig. 5.13). $\cos(\theta_{\gamma\chi})$ selection further remove 13% of background and 5% of signal events.

χ^2_{4C} **selection:** Similar to the $\chi_{bJ}(1P) \to \gamma\mu^+\mu^-$ study, events with $\chi^2_{4C} > 500$ are rejected to reduce the events which do not fit well (Fig. 5.14). It removes further 11% of signal and 69% of background events.

$M^{\text{recoil}}_{\gamma}$ **distribution:** Inside the signal window, we show the distributions of the signal and background (Fig. 5.15) events. As one can see, all the backgrounds are

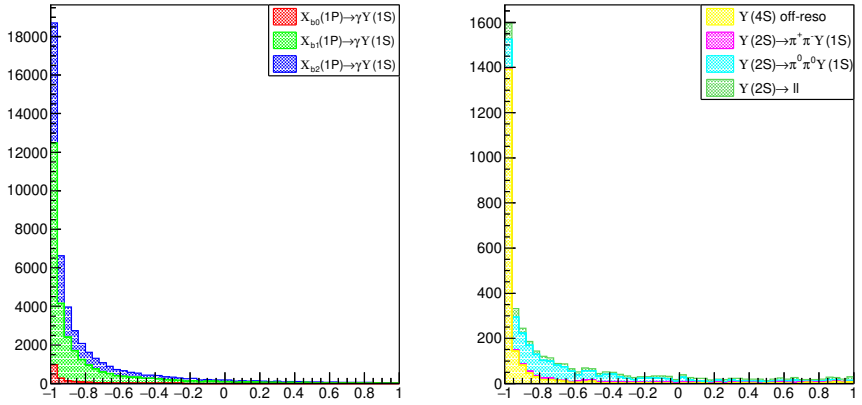

FIG. 5.13: $\cos(\theta_{\gamma\chi})$ distributions for $\chi_{bJ}(1P) \to \gamma e^+ e^-$ decays with tagged signal events (left) and background events (right) using generic MC sample with scaled $\Upsilon(4S)$ off-resonance data.

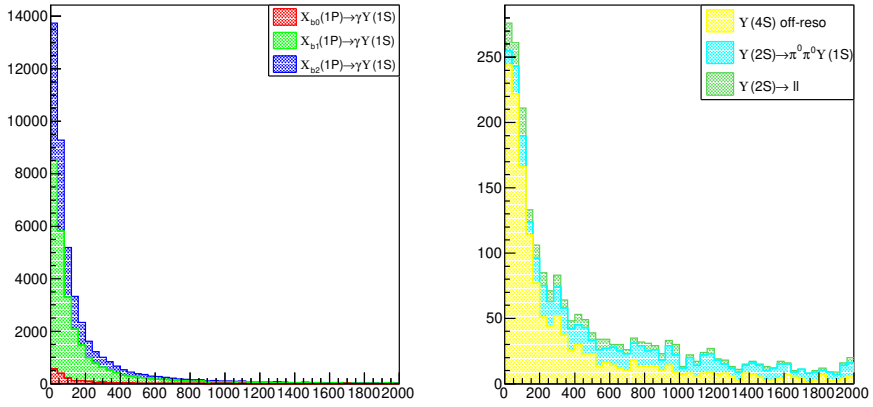

FIG. 5.14: χ^2_{4C} distributions for $\chi_{bJ}(1P) \to \gamma e^+ e^-$ decays with tagged signal events (left) and background events (right) using generic MC sample with scaled $\Upsilon(4S)$ off-resonance data.

flat inside the signal window.

5.4.2 Beam background rejection for $\chi_{bJ}(1P) \to \gamma e^+ e^-$ events

As KEKB is an asymmetric accelerator, most of the beam background is expected from the forward endcap of ECL. For *ee* mode, most of the backgrounds come from the Bhabha events and beam backgrounds. In Fig. 5.16, we compare the angular distribution of $e^{\pm}$ and $\gamma_{1,2}$ for data and MC. One can see some highly background

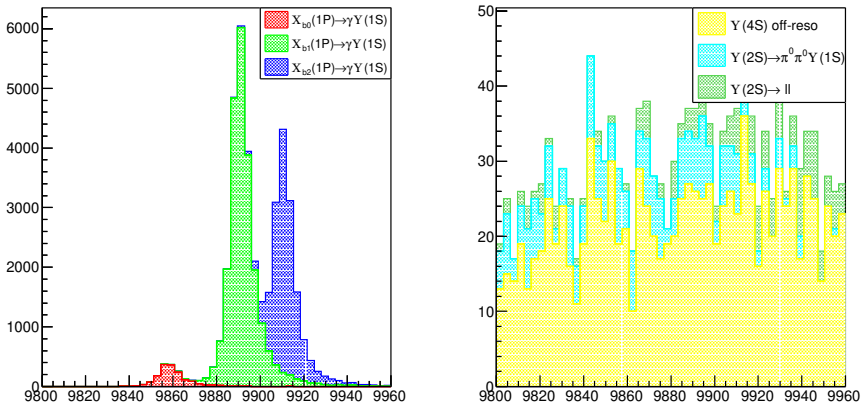

FIG. 5.15: $M_{\gamma}^{\text{recoil}}$ (in MeV/c^2) distributions for $\chi_{bJ}(1P) \to \gamma e^+ e^-$ decays with tagged signal events (left) and background events (right) using generic MC sample with scaled $\Upsilon(4S)$ off-resonance data.

dominated region for $\Upsilon(2S)$ data. Following vetoes are applied to remove such background.

- $\theta_{e^-} < 35^\circ$ and $\theta_{\gamma_1} < 30^\circ$
- $\theta_{e^-} < 35^\circ$ and $\theta_{\gamma_2} < 30^\circ$
- $100^\circ < \theta_{e^+} < 120^\circ$ and $\theta_{\gamma_1} < 30^\circ$

These kind of background dominated regions are not found for generic MC sample. The angular veto rejects 14% background with a signal loss of only 3%.

5.4.3 Signal extraction

Signal MC fit: We perform 1D UML fit to $M_{\gamma}^{\text{recoil}}$ with sum of a Gaussian and a bifurcated Gaussian sharing common mean to get the resolution and efficiency for each $\chi_{bJ}(1P)$ separately. Fig. 5.17 shows the fitted distributions for different $\chi_{b[0,1,2]}(1P)$ signal modes, after applying Bhabha veto. Tab. 5.5 summarizes the efficiencies of different $\chi_{b[0,1,2]}(1P)$ modes before and after applying Bhabha veto. The impact of Bhabha veto is higher for $\chi_{bJ}(1P) \to \gamma e^+ e^-$ events than that of $\chi_{bJ}(1P) \to \gamma \mu^+ \mu^-$ events. As seen in $\chi_{bJ}(1P) \to \gamma \mu^+ \mu^-$ study, signal loss due to Bhabha veto increases from $\chi_{b0}(1P)$ to $\chi_{b2}(1P)$.

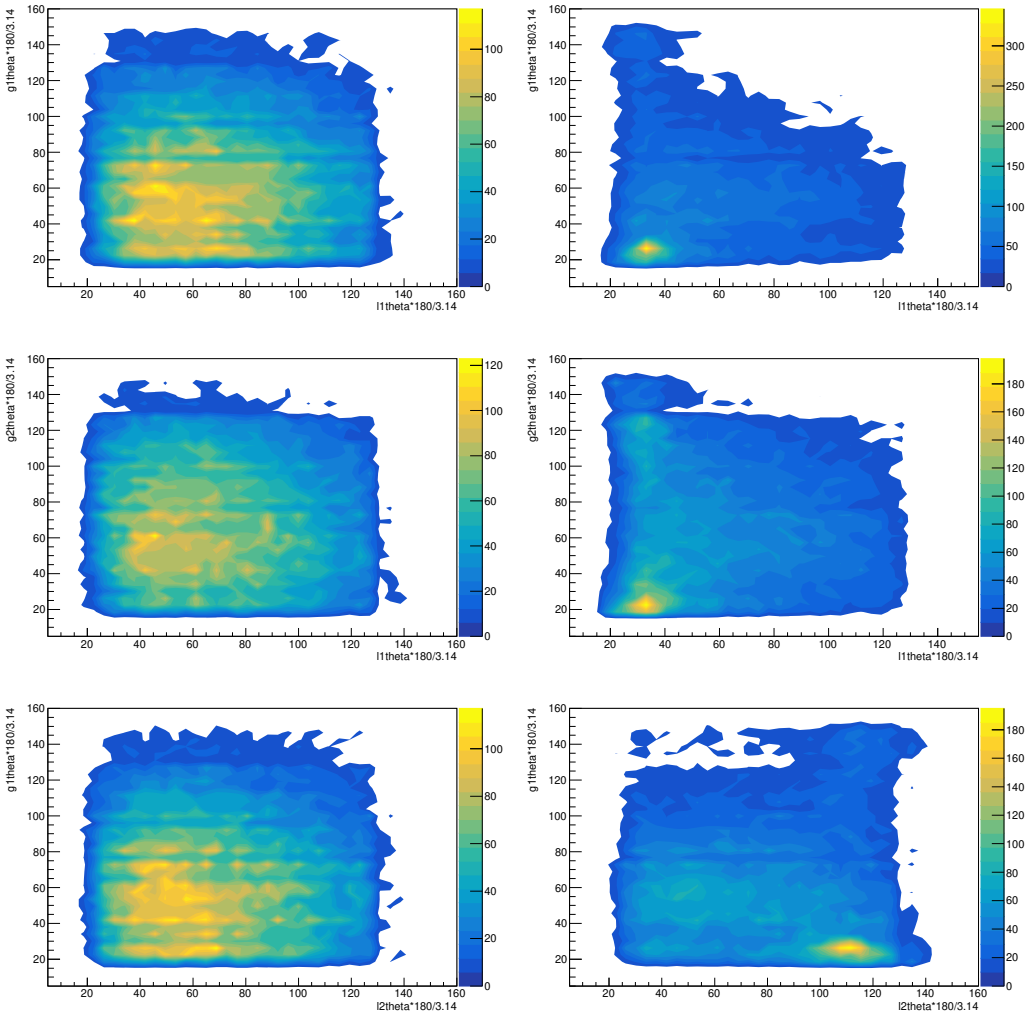

FIG. 5.16: Left (right) column represents generic MC ($\Upsilon(2S)$ data) distributions. Row[1, 2, 3] represent the 2D distribution in polar angle of [(γ_1,e^-), (γ_2,e^-), (γ_1,e^+)].

$\chi_{bJ}(1P)$	Before veto ϵ (in %)	After veto ϵ (in %)
J=0	21.2	17.0
J=1	23.3	16.4
J=2	22.7	13.3

TAB. 5.5: Expected efficiency (ϵ) before and after applying Bhabha veto for $\chi_{bJ}(1P) \to \gamma e^+ e^-$ events.

Generic MC fit: Three $\chi_{bJ}(1P)$ PDFs are combined by fixing all the parameters from the signal MC fits except the mean and resolution of $\chi_{b1}(1P)$. Resolutions of $\chi_{b0}(1P)$ and $\chi_{b2}(1P)$ are fixed with respect to the resolution of $\chi_{b1}(1P)$. Background

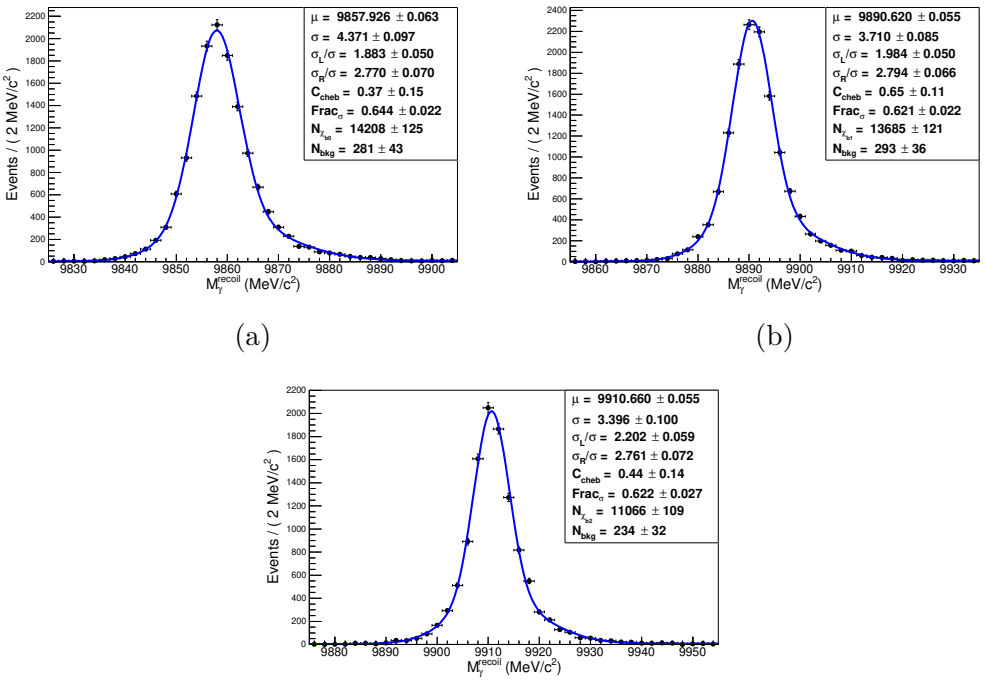

FIG. 5.17: UML fit to $M_{\gamma}^{\text{recoil}}$ (in MeV/c^2) for $\chi_{bJ}(1P) \to \gamma e^+ e^-$ decays with $\chi_{b0}(1P)$(a), $\chi_{b1}(1P)$(b), and $\chi_{b2}(1P)$(c) resonances using signal MC sample.

increases rapidly above $\chi_{b2}(1P)$ region on $M_{\gamma}^{\text{recoil}}$ distribution due to large number of soft photons. Therefore, we take an exponential function to represent the background PDF. To fit the Generic MC events (Fig. 5.18), we fix the separation of $\chi_{b0}(1P)$ ($\chi_{b2}(1P)$) from $\chi_{b1}(1P)$ according to the input mass difference.

$\Upsilon(2S)$ **data fit:** We model $\Upsilon(2S)$ on resonance data (Fig. 5.18) using the PDF that has been used in the generic MC fit. The separation of the $\chi_{b0}(1P)$ ($\chi_{b2}(1P)$) from $\chi_{b1}(1P)$ is fixed according to the PDG values [15].

5.4.4 Result of $\chi_{bJ}(1P) \to \gamma\Upsilon(1S)[\to e^+e^-]$ decays

Using Eq. (5.5), we calculate the branching fractions. In Tab. 5.6, we show the calculated branching fractions using MC and data. All the results from MC agree with the input branching fractions, and calculated results from $\Upsilon(2S)$ data agree with the PDG values [15] within one sigma.

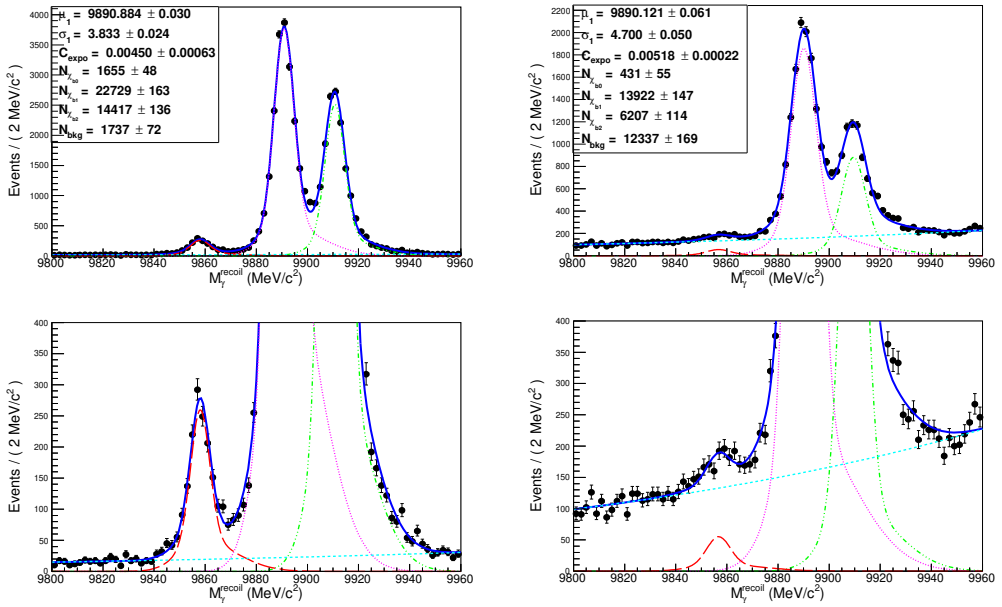

FIG. 5.18: UML fits to $M_{\gamma}^{\text{recoil}}$ (in MeV/c^2) for $\chi_{bJ}(1P) \to \gamma e^+ e^-$ decays using generic MC sample with scaled $\Upsilon(4S)$ off-resonance data (left) and using $\Upsilon(2S)$ data (right). Bottom plots are zoomed view of the corresponding above plots to show the $\chi_{b0}(1P)$ events.

$\Upsilon(2S) \to \gamma\gamma ee$	MC result		Data result	
	Input BF (10^{-4})	Fit result (10^{-4})	PDG value (10^{-4})	Our result (10^{-4})
J=0	0.486	0.494 $\pm$0.014	0.175 $\pm$0.032	0.160 $\pm$0.020
J=1	6.182	6.185 $\pm$0.044	5.781 $\pm$0.540	5.372 $\pm$0.057
J=2	4.027	4.012 $\pm$0.038	3.063 $\pm$0.267	2.962 $\pm$0.054

TAB. 5.6: Calculated composite branching fractions for $\Upsilon(2S) \to \gamma\gamma ee$ decays with different $\chi_{bJ}(1P)$ resonances. Efficiency correction and systematic uncertainties are not included yet.

5.5 Study of $\chi_{bJ}(1P) \to \ell^{\pm}\ell'^{\mp}$ decays

Our control samples have been established. Our environment is ready to search for CLFV transition in $\chi_{b[0,1,2]}(1P) \to \ell^{\mp}\ell'^{\mp}$ $[\ell, \ell' = e, \mu, \tau]$ decays. MC signal for $\Upsilon(2S) \to \gamma\chi_{b[0,1,2]}(1P)$ decay has been generated using the HELAMP model of EvtGen package [93], and the PHSP model with the PHOTOS [94] has been used to generate CLFV decays. Further, we generate τ decays using the TAUOLA package [96] of PYTHIA package [97]. For $\chi_{b[0,1,2]}(1P) \to \mu^{\pm}\tau^{\mp}$ ($\chi_{b[0,1,2]}(1P) \to$

$e^{\pm}\tau^{\mp}$) decays, tau has been reconstructed in $\tau^- \to e^-\bar{\nu}_e\nu_\tau$ ($\tau^- \to \mu^-\bar{\nu}_\mu\nu_\tau$) decays to avoid the huge background from $\Upsilon(2S) \to \gamma_{\rm ISR}\ell^+\ell^-$ decays.

5.5.1 Analysis strategy

There is no γ_2 and $\Upsilon(1S)$ for the CLFV decays of $\chi_{bJ}(1P)$. Therefore, $M^{\rm recoil}_{\gamma\gamma}$ variable does not exist anymore. For $\chi_{b[0,1,2]}(1P) \to e^{\pm}\mu^{\mp}$ decays, we use $\cos(\theta_{\gamma\chi})$, $\chi^2_{\rm 4C}$ to remove the background, and $M^{\rm recoil}_{\gamma}$ has been used to extract the signal. For $\chi_{b[0,1,2]}(1P) \to \ell^{\pm}\tau^{\mp}$ decays, 4C-fit does not work due to presence of undetected neutrinos from τ decays. We fit the $M^{\rm recoil}_{\gamma}$ and select $\pm 2\sigma$ region from the mean position of $M^{\rm recoil}_{\gamma}$. Then we extract the signal using recoil mass of $\gamma\ell$ ($M^{\rm recoil}_{\gamma\ell}$), which is defined in the following equation.

$$M^{\rm recoil}_{\gamma\ell} = \sqrt{E^2_{\rm cm} + M^2_{\gamma\ell} - 2E_{\rm cm}E_{\gamma\ell}} \tag{5.6}$$

Where $M_{\gamma\ell}$ and $E_{\gamma\ell}$ are the invariant mass and total energy of $\gamma\ell$ in the $\Upsilon(2S)$ rest-frame. For $\chi_{bJ}(1P) \to \ell^{\mp}\tau^{\pm}$ signals, $M^{\rm recoil}_{\gamma\ell}$ should peak at the nominal τ mass (1.78 GeV/c^2).

5.5.2 Event selection

All the basic cuts and event selection criteria are similar to the control sample study (discussed in section 5.2.2). Also, the angular vetoes on the polar angle those have been used for the $\chi_{bJ}(1P) \to \gamma e^+e^-$ study are applied here expecting the similar effect on CLFV modes.

5.5.3 Bhabha veto using TSIM

There are only two charged tracks (one muon and one electron) and one photon in the final state. Therefore, Bhabha trigger might have activated, which might have rejected some events in the $\Upsilon(2S)$ data. We keep all the Bhabha veto parameters unchanged to produce the similar effect on our MC simulated CLFV events to get the correct efficiency. As there is one muon in the final state, the effect of Bhabha veto is expected to be less than *ee* events.

5.6 Study of $\chi_{bJ}(1P) \to e^{\pm}\mu^{\mp}$ decays

Due to the presence of low energetic photon, the fraction of events with multiple $\Upsilon(2S)$ candidates is 18%. $\chi^2_{\rm 4C}$ has been used to select the best candidate among the multiple candidates. Using Eq. (5.3) our BCS efficiency is 98%.

5.6.1 Background study

We prepare a combined sample by adding scaled $\Upsilon(4S)$ off-resonance data with generic MC events, which has been used for the optimization purpose.

L_e and L_μ selections: Using figure of merit ($\rm F_{OM}$), we optimize L_μ and L_e cuts. These optimized lepton selections have already been used for calibration mode studies. As CLFV transitions of $\chi_{bJ}(1P)$ mesons have not been included in the generic MC sample, one can use the following relation in small signal approach for optimization.

$$\rm F_{OM} = \frac{\epsilon}{\eta/2 + \sqrt{N_{bkg}}} \tag{5.7}$$

Where ϵ, η, and $N_{\rm bkg}$ are the efficiency, significance, and number of background, respectively. Here η has been taken as 3. From Fig. 5.19, the optimized L_μ and L_e cut can be taken as 0.9 and 0.5, respectively.

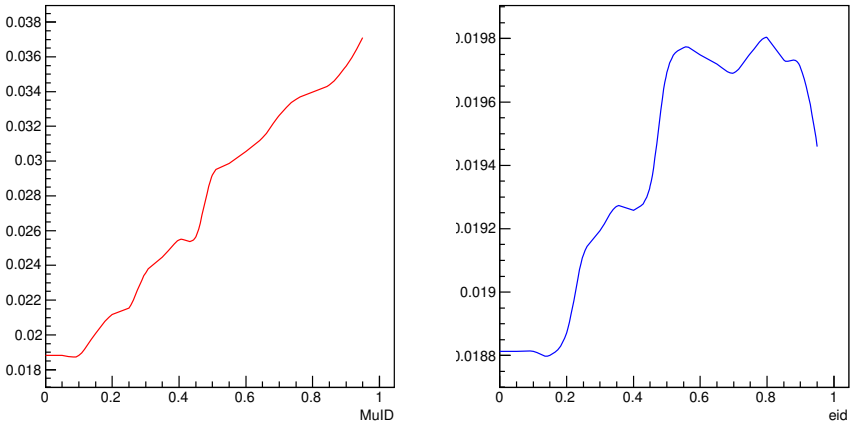

FIG. 5.19: Figure of merit for L_μ optimization (left) and L_e optimization (right) for $\chi_{bJ}(1P) \to e^{\pm}\mu^{\mp}$ decays.

Selection included from control modes:

- We select the candidates with $\cos(\theta_{\gamma\chi}) < 0$.
- We perform 4C-fit with reconstructed γ, e, and μ candidates. In order to remove backgrounds, events with $\chi^2_{\rm 4C}$ less than 500 are selected.

Prompt track selection: We count the number of electrons and muons with energy > 1 GeV as prompt electrons ($N_{\rm e}$) and prompt muons (N_μ), respectively. Here both leptons are high energetic, as they come from $\chi_{bJ}(1P)$ mesons. We select the events with $N_\mu = 1$ and $N_{\rm e} = 1$, which reject 25% of background events without any loss in signal events. Distribution of N_μ for signal and background are shown in Fig. 5.20.

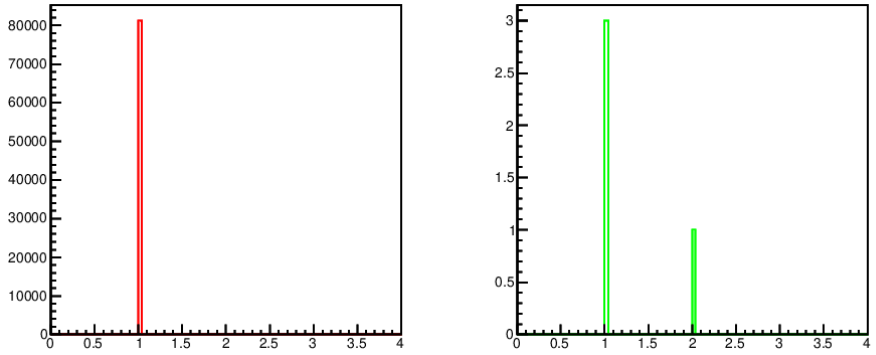

FIG. 5.20: N_μ distributions for $\chi_{bJ}(1P) \to e^{\pm}\mu^{\mp}$ decays using signal MC sample (left) and generic MC sample with scaled $\Upsilon(4S)$ off-resonance data (right).

Applying all these selection, 98% of background is removed with a signal loss of 20%. Inside the signal window, we did not find any event for generic MC data. We found only 3 events for $\Upsilon(4S)$ off-resonance data.

5.6.2 Signal extraction

Signal MC fit: 1D UML fit with sum of a Gaussian and a bifurcated Gaussian sharing common mean is performed on $M_\gamma^{\rm recoil}$ for each of the $\chi_{bJ}(1P) \to e^{\pm}\mu^{\mp}$ decays, using the events passed through the Bhabha veto. Using the fitted distributions in Fig. 5.21, we estimate the efficiencies and resolutions. The estimated efficiencies of different $\chi_{bJ}(1P) \to e^{\pm}\mu^{\mp}$ modes are shown in Tab. 5.7

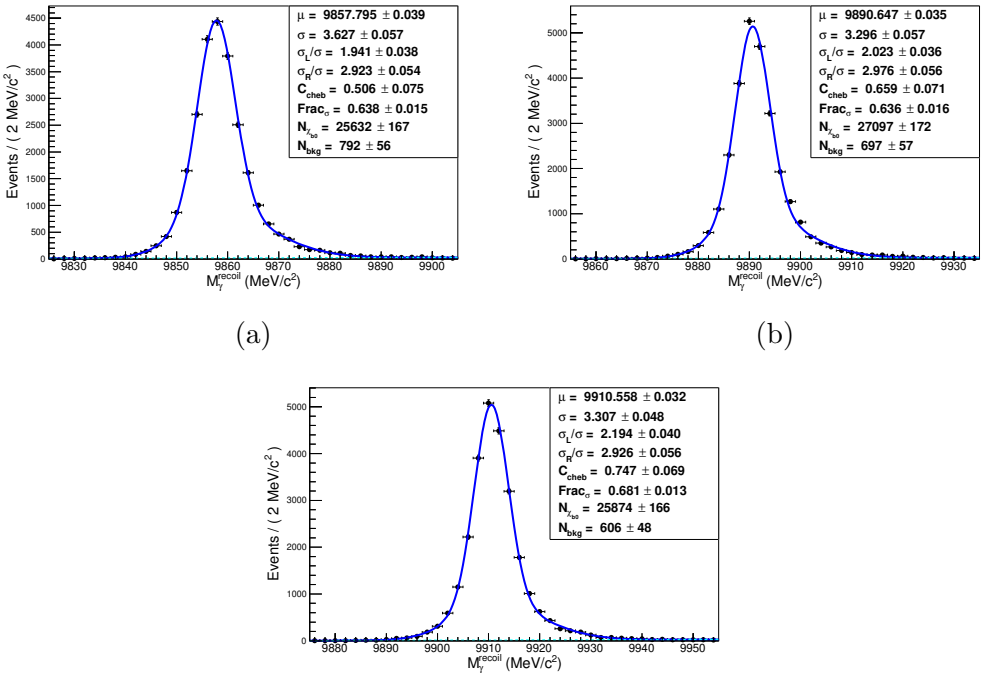

FIG. 5.21: UML fit to $M_{\gamma}^{\text{recoil}}$ (in MeV/c^2) for $\chi_{b0}(1P) \to e^{\pm}\mu^{\mp}$ (a), $\chi_{b1}(1P) \to e^{\pm}\mu^{\mp}$ (b), and $\chi_{b2}(1P) \to e^{\pm}\mu^{\mp}$ (c) decays using signal MC sample.

$\chi_{bJ}(1P) \to e\mu$	Efficiency (in %)
J=0	30.8
J=1	32.5
J=2	31.0

TAB. 5.7: Efficiency after Bhabha veto for $\chi_{bJ}(1P) \to e^{\pm}\mu^{\mp}$ events.

Background estimation: The background coming from $\Upsilon(2S)$ decays is expected to be 0, as we did not find any event inside the signal window for generic MC sample. We found 3 background events from $\Upsilon(4S)$ off-resonance data. We fit those background events fixing the mean and standard deviation of $\chi_{b0}(1P)$, $\chi_{b1}(1P)$, and $\chi_{b2}(1P)$ from MC signal fits. We consider an exponential function as the background PDF. As one can see in Fig. 5.22, background fit is unstable due to very less number of background.

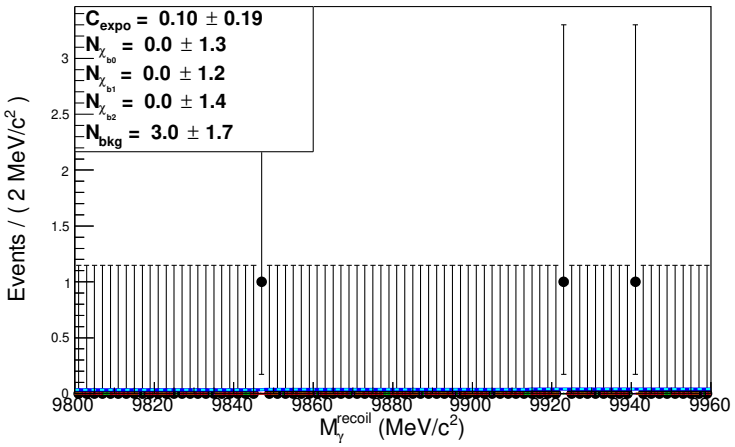

FIG. 5.22: UML fit $M_{\gamma}^{\text{recoil}}$ (in MeV/c^2) for combined signal and backgrounds using generic MC sample with scaled $\Upsilon(4S)$ off-resonance data.

5.6.3 Sensitivity test

Before studying the real data, we estimate the sensitivity of $\chi_{bJ}(1P) \to e^{\pm}\mu^{\mp}$ transitions. As the background fit is unstable, we plan to estimate the upper limit (UL) of branching fraction for different $\chi_{bJ}(1P)$ modes by counting the number of events inside the $\pm 2\sigma$ region of $M_{\gamma}^{\text{recoil}}$. One can calculate the UL of branching fraction using following relation.

$$\mathcal{B}[\chi_{bJ}(1P) \to \ell^{\pm}\ell'^{\mp}] < \frac{N_{\text{sig}}^{J}}{N_{\Upsilon(2S)} \times \mathcal{B}[\Upsilon(2S) \to \gamma\chi_{b[0,1,2]}(1P)] \times \epsilon_J} \tag{5.8}$$

Where ϵ_J and N_{sig}^{J} are efficiency and UL of signal yield for the corresponding J values, respectively. For the $\chi_{bJ}(1P)$ modes, no backgrounds have been found inside the $\pm 2\sigma$ regions. Considering 0 signal and 0 background case, N_{sig}^{J} at 90% CL for each of the $\chi_{bJ}(1P)$ modes has been estimated to be 2.4 [89]. Using Eq. (5.8), the expected UL of branching fractions for $\chi_{b0}(1P) \to e^{\pm}\mu^{\mp}$, $\chi_{b1}(1P) \to e^{\pm}\mu^{\mp}$, and $\chi_{b2}(1P) \to e^{\pm}\mu^{\mp}$ decays are estimated to be 1.3×10^{-6}, 6.9×10^{-7}, and 7.0×10^{-7}, respectively.

5.7 Study of $\chi_{bJ}(1P) \to \mu^{\pm}\tau^{\mp}$ decays

Due to the presence of low energetic photon and wide range of energy of $e^{\pm}$ from τ, fraction events with multiple $\Upsilon(2S)$ candidates has been increases to 24%. We perform a vertex fit with the charged lepton tracks, and fitted χ^2 value of vertex fit ($\chi^2_{\rm vtx}$) has been used to select the best candidate. Using Eq. (5.3) our BCS efficiency is 80%.

5.7.1 Background study

We use the optimized charged lepton selections, $L_\mu > 0.9$ and $L_e > 0.5$, as decided in $\chi_{bJ}(1P) \to e^{\pm}\mu^{\mp}$ study.

Prompt track selection: There are two charged leptons in the signal mode. The muon coming from $\chi_{bJ}(1P)$ mesons are always high energetic, and the electron coming from τ has a wide range of energy. Therefore, in this section, we select the events $N_\mu = 1$ and $N_{\rm e} \leq 1$, which rejects less than 1% of signal events and 82% of background events. Distributions of N_μ and $N_{\rm e}$ are shown in Fig. 5.23.

$p^{\tau}_{\rm vis}$ distribution: To clean up the τ reconstruction, we look at the visible momentum of τ decays ($p^{\tau}_{\rm vis}$). As one can see in Fig. 5.24, there is a sharp peak around 0.2 GeV/c on the $p^{\tau}_{\rm vis}$ distribution. Electron from a converted beam background photon has been misidentified here. We remove those background by selecting the events with $p^{\tau}_{\rm vis} > 0.4$ GeV/c, which further rejects 13% of signal events and 52% of background events.

Angular distributions of lepton and photon: We look at the polar angle distribution of the leptons and photon. We find the enhancement of the background for muon and photon in the endcap regions. Based on two plots in Fig. 5.25, we select the muons within $35^o < \theta_\mu < 120^o$ and photon with $\theta_\gamma < 130^o$, which further rejects 15% of signal events and 45% of background events.

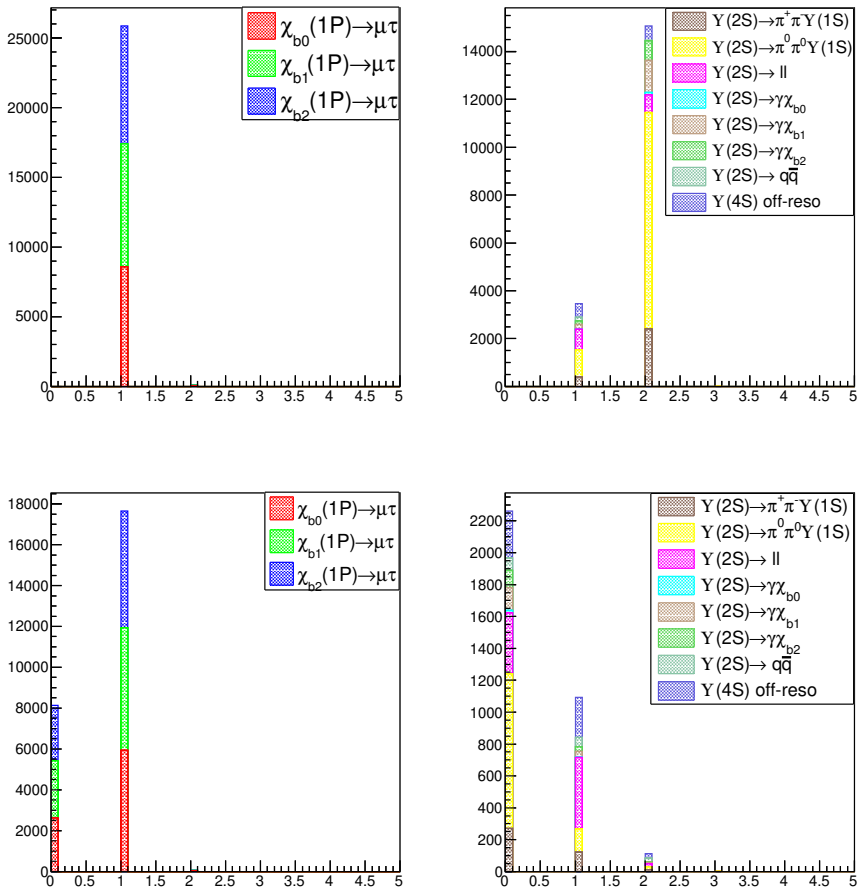

FIG. 5.23: N_μ (top) and $N_{\rm e}$ (bottom) distributions for $\chi_{bJ}(1P) \to \mu^{\pm}\tau^{\mp}$ decays using signal MC sample (left) and generic MC sample with scaled $\Upsilon(4S)$ off-resonance data (right).

Distribution of $M_{\gamma}^{\rm recoil}$ and $M_{\gamma\mu}^{\rm recoil}$: Inside the signal window, we check the distributions of $M_{\gamma}^{\rm recoil}$ and $M_{\gamma\mu}^{\rm recoil}$. As one can see in Fig. 5.26, there is no peaking background for $M_{\gamma\mu}^{\rm recoil}$ distribution, and the background increases exponentially due to increase in the number of soft photons as we approach to the low energy region.

5.7.2 Signal extraction

Signal MC fit: 1D UML fit with sum of a Gaussian and a bifurcated Gaussian sharing common mean is performed on $M_{\gamma}^{\rm recoil}$ for each of the $\chi_{bJ}(1P) \to \mu^{\pm}\tau^{\mp}$ decays. In Fig. 5.27, we show the fitted $M_{\gamma}^{\rm recoil}$ distributions with the events passing through anti-Bhabha trigger. From the $M_{\gamma}^{\rm recoil}$ fits, we calculate the $\pm 2\sigma$ regions

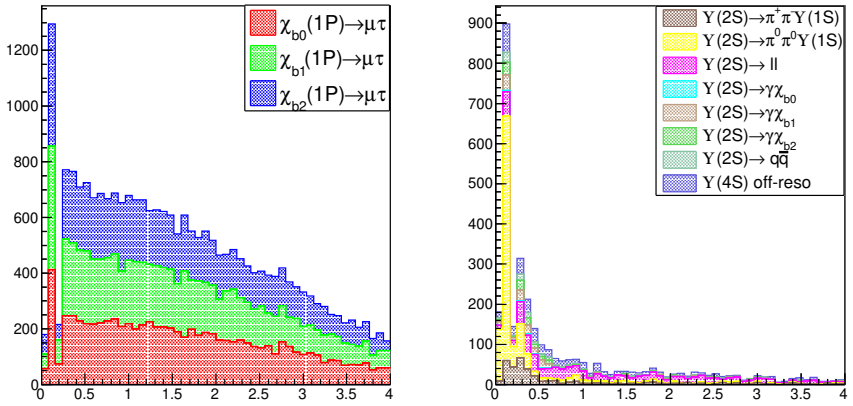

FIG. 5.24: $p^{\tau}_{\rm vis}$ (in GeV/c) distributions for $\chi_{bJ}(1P) \to \mu^{\pm}\tau^{\mp}$ decays using signal MC sample (left) and generic MC sample with scaled $\Upsilon(4S)$ off-resonance data (right).

from the mean position for each of the $\chi_{bJ}(1P)$ mesons. $M^{\rm recoil}_{\gamma}$ signal regions for $\chi_{b0}(1P)$, $\chi_{b1}(1P)$, and $\chi_{b2}(1P)$ are (9846 - 9874) MeV/c^2, (9880 - 9905) MeV/c^2, and (9900 - 9923) MeV/c^2, respectively. To extract the resolution and signal efficiency, we fit the $M^{\rm recoil}_{\gamma\mu}$ with sum of a Gaussian and bifurcated Gaussian within the respective $M^{\rm recoil}_{\gamma}$ window. In Fig. 5.27, we show the fitted distributions of $M^{\rm recoil}_{\gamma\mu}$ for different $\chi_{bJ}(1P)$ modes. Tab. 5.3 summarizes the expected signal efficiencies for different $\chi_{bJ}(1P)$ modes estimated from the $M^{\rm recoil}_{\gamma\mu}$ fits.

$\chi_{bJ}(1P) \to \mu^{\pm}\tau^{\mp}$	Efficiency (in %)
J=0	4.6
J=1	5.0
J=2	4.8

TAB. 5.8: Efficiency after applying Bhabha veto for $\chi_{bJ}(1P) \to \mu^{\pm}\tau^{\mp}$ decays.

Background estimation: To estimate the peaking background, we fit $M^{\rm recoil}_{\gamma\mu}$ distributions for different $\chi_{bJ}(1P) \to \mu^{\pm}\tau^{\mp}$ decay modes within respective $M^{\rm recoil}_{\gamma}$ windows. We fix the shape of the $M^{\rm recoil}_{\gamma\mu}$ signal PDFs for different $\chi_{bJ}(1P)$ modes to obtain the background fits. As background increases rapidly due increase of the number of low energetic soft photon and beam background, we model the backgrounds with an exponential PDF. Slope of the exponential PDF is allowed to float. Fitted $M^{\rm recoil}_{\gamma\mu}$ distribution for different $\chi_{bJ}(1P)$ modes are shown in Fig. 5.28.

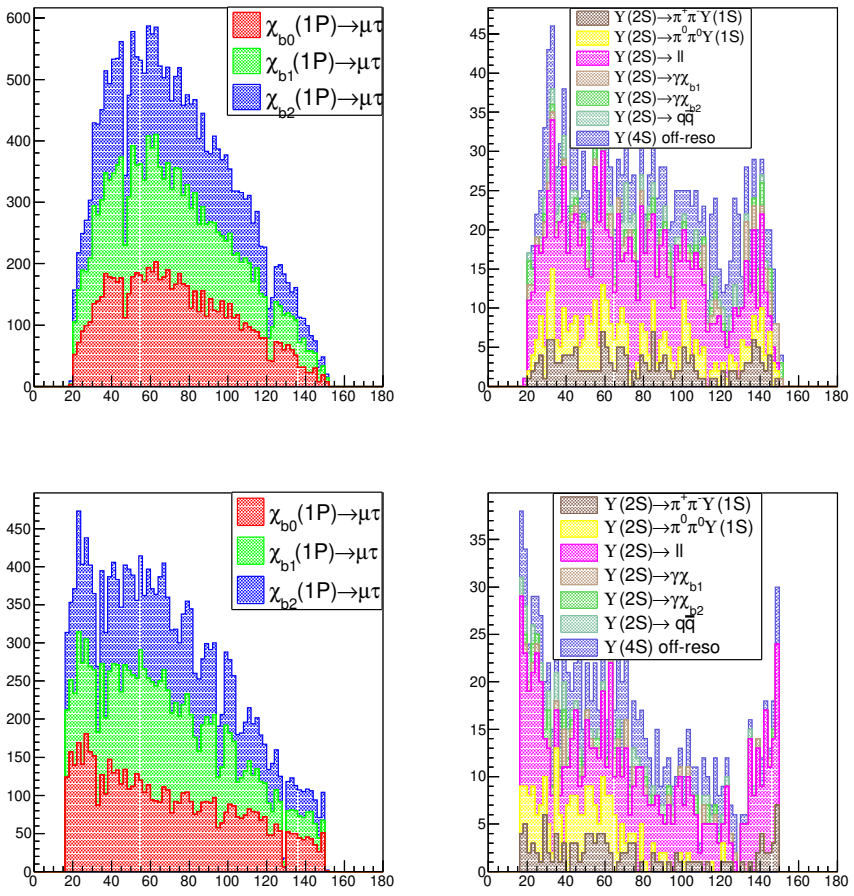

FIG. 5.25: θ_μ (top) and θ_γ (bottom) distributions for $\chi_{bJ}(1P) \to \mu^{\pm}\tau^{\mp}$ decays using signal MC sample (left) and generic MC sample with scaled $\Upsilon(4S)$ off-resonance data (right).

Expected signal yields for $\chi_{b0}(1P)$, $\chi_{b1}(1P)$, and $\chi_{b2}(1P)$ in $\Upsilon(2S)$ data are estimated to be -2.3 ± 2.8, 0.9 ± 5.5, and -1.0 ± 5.0 events, respectively.

5.7.3 Sensitivity test

We estimate the sensitivity of $\chi_{bJ}(1P) \to \mu^{\pm}\tau^{\mp}$ transitions using an ensemble of pseudo experiments. We generate the data sets for different $\chi_{bJ}(1P)$ modes fixing the shape of signal and background PDFs varying the yield of the signal from 1 to 20. In Fig. 5.29, the fitted distributions of CL as a function of input signal yield for different $\chi_{bJ}(1P)$ modes have been shown. The expected UL of signal yield at 90% CL for $\chi_{b0}(1P)$, $\chi_{b1}(1P)$, and $\chi_{b2}(1P)$ are 4.8, 8.4, and 7.7, respectively.

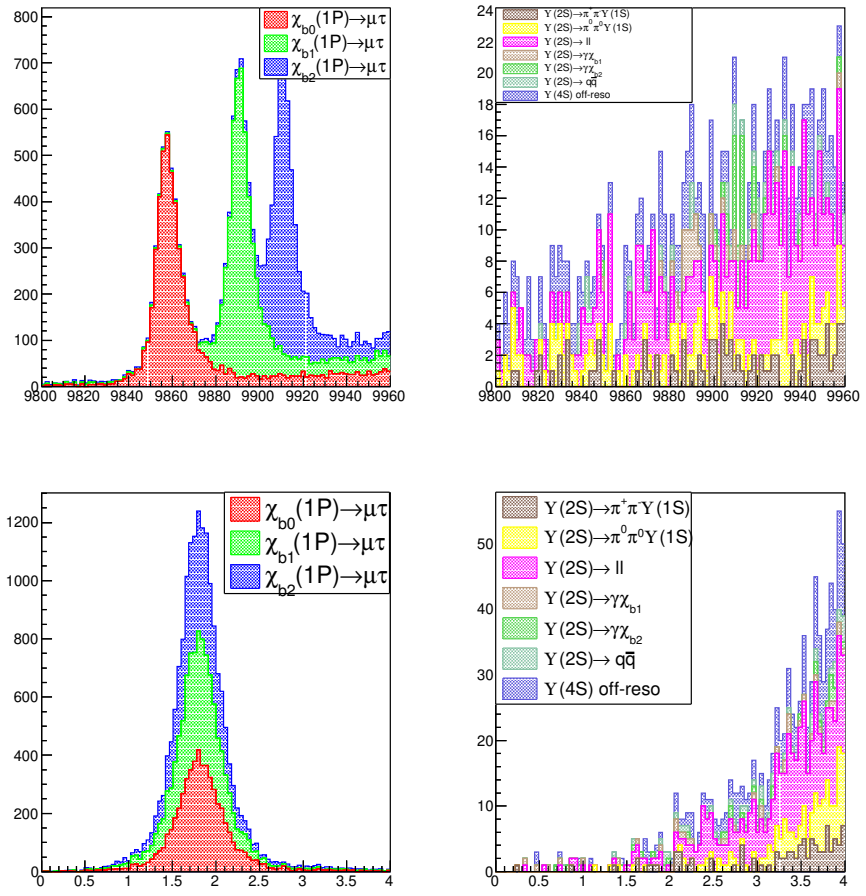

FIG. 5.26: $M_{\gamma}^{\text{recoil}}$ (in MeV/c^2) distributions (top) and $M_{\gamma\mu}^{\text{recoil}}$ (in GeV/c^2) distributions (bottom) for $\chi_{bJ}(1P) \to \mu^{\pm}\tau^{\mp}$ decays using signal MC sample (left) and generic MC sample with scaled $\Upsilon(4S)$ off-resonance data (right).

Using Eq. (5.8), expected UL of branching fraction at 90% CL for $\chi_{b0}(1P) \to \mu^{\pm}\tau^{\mp}$, $\chi_{b1}(1P) \to \mu^{\pm}\tau^{\mp}$, and $\chi_{b2}(1P) \to \mu^{\pm}\tau^{\mp}$ are estimated to be 1.7×10^{-5}, 1.5×10^{-5}, and 1.4×10^{-5}, respectively.

5.8 Study of $\chi_{bJ}(1P) \to e^{\pm}\tau^{\mp}$ decays

Due to the presence of low energetic photon and wide range of energy of $\mu^{\pm}$ from τ decays, the fraction events with multiple $\Upsilon(2S)$ candidates has been increases to 24%. We perform a vertex fit with the charged lepton tracks, and fitted χ^2 value from vertex fit (χ^2_{vtx}) has been used to select the best candidate. Using Eq. (5.3) our BCS efficiency is 80%.

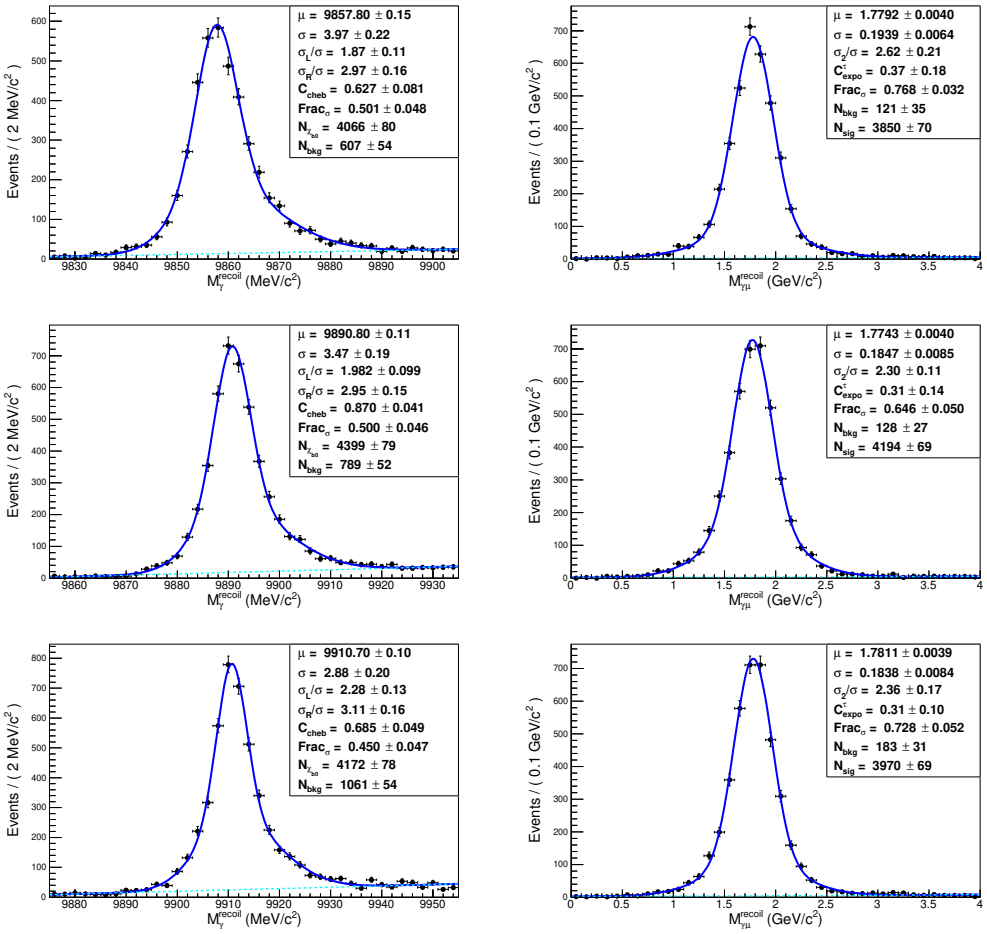

FIG. 5.27: UML fits to $M_{\gamma}^{\text{recoil}}$ in MeV/c^2 (left) and to $M_{\gamma\mu}^{\text{recoil}}$ in GeV/c^2 (right) for $\chi_{b0}(1P) \to \mu^{\pm}\tau^{\mp}$ (top row), $\chi_{b1}(1P) \to \mu^{\pm}\tau^{\mp}$ (middle row), and $\chi_{b2}(1P) \to \mu^{\pm}\tau^{\mp}$ (bottom row) decays using signal MC sample.

5.8.1 Background study

We use the optimized charged lepton selections, $L_{\mu} > 0.9$ and $L_e > 0.5$, as decided in $\chi_{bJ}(1P) \to e^{\pm}\mu^{\mp}$ study.

Prompt track selection: For $\chi_{bJ}(1P) \to e^{\pm}\tau^{\mp}$ decays, electrons coming from $\chi_{bJ}(1P)$ mesons are always high energetic, and muons coming from τ have a wide range of energy. Distributions of N_{e} and N_{μ} are shown in Fig. 5.30. We select the events $N_{\text{e}} = 1$ and $N_{\mu} \leq 1$, which rejects less than 1% of signal events and 13% of background events.

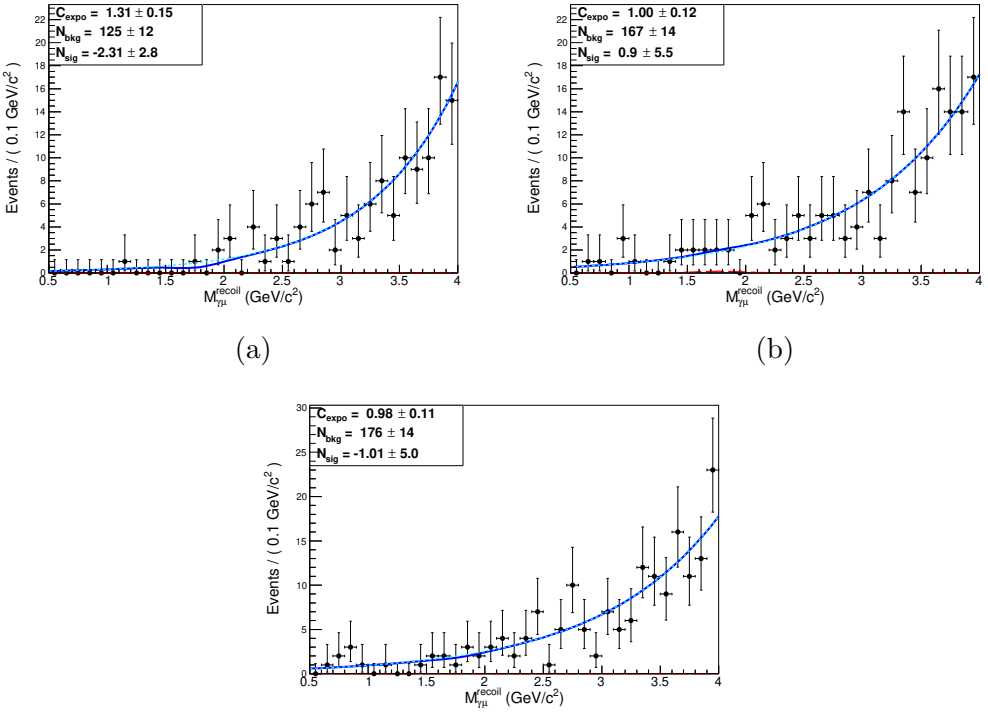

FIG. 5.28: UML fits to $M^{\text{recoil}}_{\gamma\mu}$ (in GeV/c^2) for combined signal and backgrounds for $\chi_{b0}(1P) \to \mu^{\pm}\tau^{\mp}$ (a), $\chi_{b1}(1P) \to \mu^{\pm}\tau^{\mp}$ (b), and $\chi_{b2}(1P) \to \mu^{\pm}\tau^{\mp}$ (c) decays using generic MC sample with scaled $\Upsilon(4S)$ off-resonances data.

p^{τ}_{vis} distribution: As one can see in Fig. 5.31, the p^{τ}_{vis} distribution for signal and background events are very similar. Therefore, we do not apply any selection on p^{τ}_{vis} for $\chi_{bJ}(1P) \to e^{\pm}\tau^{\mp}$ decays.

Angular distributions of lepton and photon: In the polar angle distribution of the leptons and photon, we find the enhancement of the background for electron and photon in the endcap regions. Looking at Fig. 5.32, we select the electrons within $30^o < \theta_e < 130^o$ and photons with $\theta_{\gamma} < 130^o$, which further rejects 13% of signal events and 41% of background events.

Distribution of $M^{\text{recoil}}_{\gamma}$ and $M^{\text{recoil}}_{\gamma\text{e}}$: Inside the signal window, we plot the distribution of $M^{\text{recoil}}_{\gamma}$ and $M^{\text{recoil}}_{\gamma\text{e}}$. As one can see in Fig. 5.33, there are no peaking backgrounds for $M^{\text{recoil}}_{\gamma\text{e}}$ distribution. The number background increases exponentially due to increase of the number of soft photons, as we approach to the low energy region.

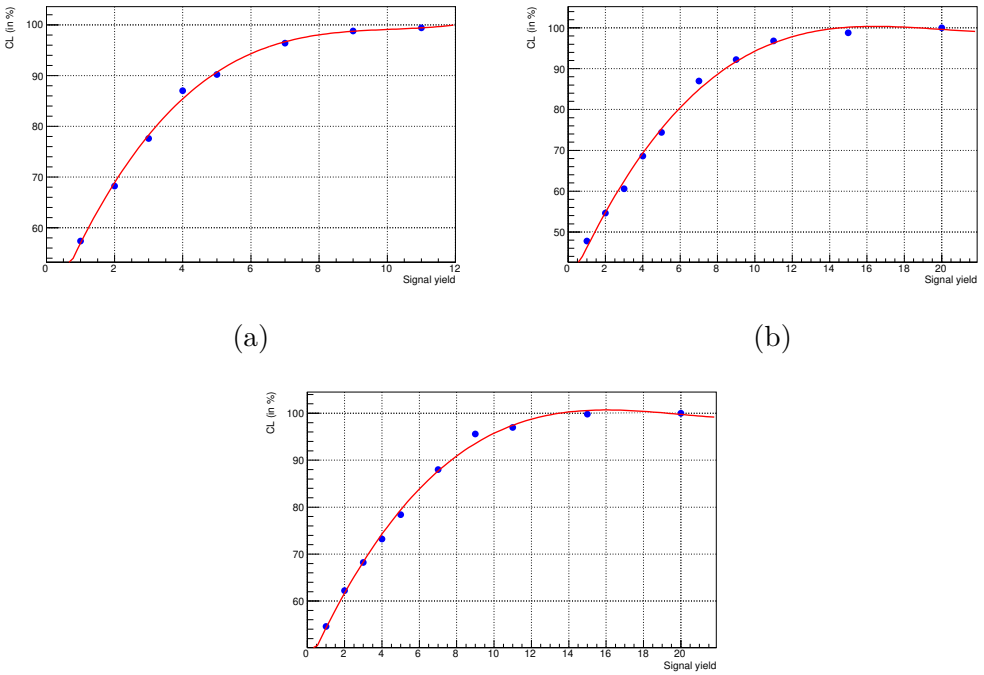

FIG. 5.29: Expected confidence level distributions as a function of input signal yield for $\chi_{b0}(1P) \to \mu^{\pm}\tau^{\mp}$ (a), $\chi_{b1}(1P) \to \mu^{\pm}\tau^{\mp}$ (b), and $\chi_{b2}(1P) \to \mu^{\pm}\tau^{\mp}$ (c) decays.

5.8.2 Signal extraction

Signal MC fit: We fit $M_{\gamma}^{\text{recoil}}$ distributions for different $\chi_{bJ}(1P)$ modes using a sum of a Gaussian and a bifurcated Gaussian sharing common mean. From different $M_{\gamma}^{\text{recoil}}$ fits, we calculate the $\pm 2\sigma$ regions for $\chi_{bJ}(1P)$ mesons. $M_{\gamma}^{\text{recoil}}$ signal regions for $\chi_{b0}(1P)$, $\chi_{b1}(1P)$, and $\chi_{b2}(1P)$ mesons are (9847 - 9873) MeV/c^2, (9881 - 9904) MeV/c^2, and (9901 - 9923) MeV/c^2, respectively. To extract the resolution and efficiency, we fit $M_{\gamma e}^{\text{recoil}}$ distributions with sum of a Gaussian and bifurcated Gaussian within the respective $\pm 2\sigma$ $M_{\gamma}^{\text{recoil}}$ regions. In Fig. 5.34, we show the fitted distributions of $M_{\gamma}^{\text{recoil}}$ and $M_{\gamma e}^{\text{recoil}}$ for different $\chi_{bJ}(1P)$ modes. Tab. 5.3 summarizes the expected signal efficiency for different $\chi_{bJ}(1P) \to e^{\pm}\tau^{\mp}$ modes.

Background estimation: We fit $M_{\gamma e}^{\text{recoil}}$ distributions (inside the respective $\pm 2\sigma$ $M_{\gamma}^{\text{recoil}}$ windows) using generic MC background fixing the shape of signal PDFs from signal MC. As the number backgrounds increases rapidly, we model background with an exponential function. Slope of the exponential PDF is allowed to float. Fitted

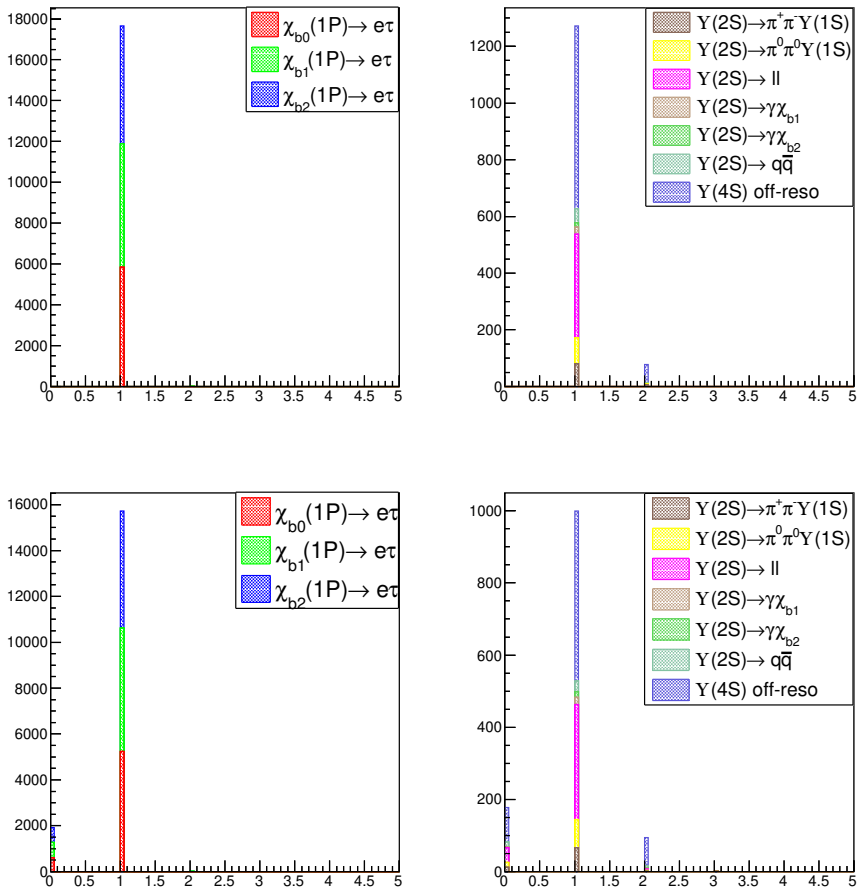

FIG. 5.30: $N_{\rm e}$ distributions (top) and N_{μ} distributions (bottom) for $\chi_{bJ}(1P) \to e^{\pm}\tau^{\mp}$ decays using signal MC sample (left) and generic MC sample with scaled $\Upsilon(4S)$ off-resonance data.

$\chi_{bJ}(1P) \to e^{\pm}\tau^{\mp}$	Efficiency (in %)
J=0	3.5
J=1	3.9
J=2	3.8

TAB. 5.9: Efficiency after applying Bhabha veto for $\chi_{bJ}(1P) \to e^{\pm}\tau^{\mp}$ decays.

$M_{\gamma e}^{\rm recoil}$ distribution for different $\chi_{bJ}(1P)$ modes are shown in Fig. 5.35. Expected signal yields of $\chi_{b0}(1P)$, $\chi_{b1}(1P)$, and $\chi_{b2}(1P)$ mesons in $\Upsilon(2S)$ data are estimated to be -2.1 ± 3.1, -2.3 ± 3.5, and -1.8 ± 2.6, respectively.

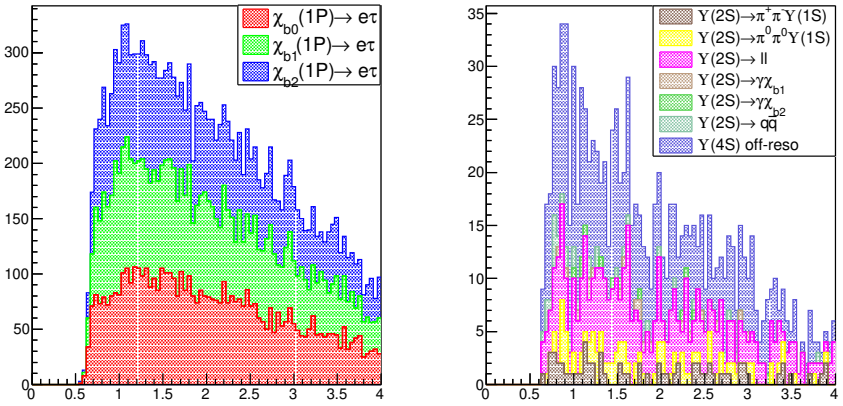

FIG. 5.31: $p^{\tau}_{\rm vis}$ (in GeV/c) distributions for $\chi_{bJ}(1P) \to e^{\pm}\tau^{\mp}$ decays using signal MC sample (left) and generic MC sample with scaled $\Upsilon(4S)$ off-resonance data.

5.8.3 Sensitivity test

We estimate the sensitivity of $\chi_{bJ}(1P) \to e^{\pm}\tau^{\mp}$ transitions using an ensemble of pseudo experiments, in a similar approach to $\chi_{bJ}(1P) \to \mu^{\pm}\tau^{\mp}$ transition. Fitted distributions of CL as a function of input signal for different $\chi_{bJ}(1P)$ modes are shown in Fig. 5.36. The expected UL of signal yields at 90% CL for $\chi_{b0}(1P)$, $\chi_{b1}(1P)$, and $\chi_{b2}(1P)$ are 6.5, 5.6, and 5.5, respectively. Using Eq. (5.8), expected UL of branching fractions at 90% CL for $\chi_{b0}(1P) \to e^{\pm}\tau^{\mp}$, $\chi_{b1}(1P) \to e^{\pm}\tau^{\mp}$, and $\chi_{b2}(1P) \to e^{\pm}\tau^{\mp}$ decays are estimated to be 3.1×10^{-5}, 1.3×10^{-5}, and 1.3×10^{-5}, respectively.

5.9 Summary

We present a preliminary search on the CLFV transitions in $\chi_{bJ}(1P) \to \ell^{\pm}\ell'^{\mp}$ decays based on the MC simulated events. We study the sources of possible backgrounds using $\Upsilon(2S)$ generic MC sample and $\Upsilon(4S)$ off-resonance data collected by the Belle detector. Signal extraction procedure has been validated by measuring the branching fractions for $\Upsilon(2S) \to \gamma\chi_{bJ}(1P)$ and $\chi_{bJ}(1P) \to \gamma\Upsilon(1S)$ decays.

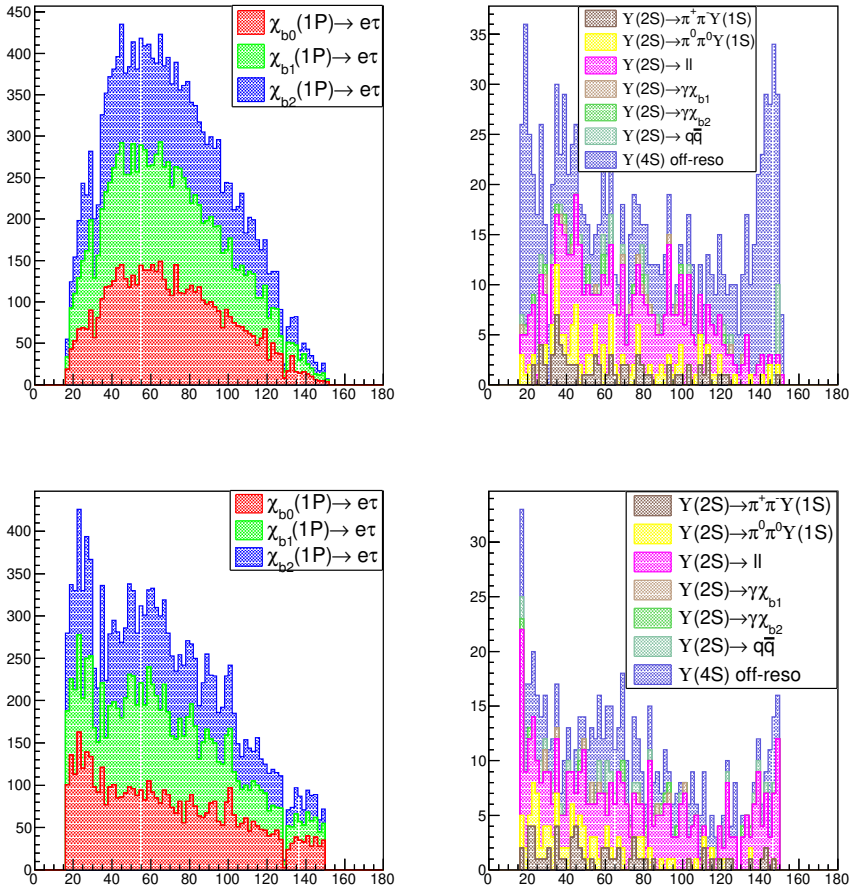

FIG. 5.32: θ_e distributions (top) and θ_γ distributions (bottom) for $\chi_{bJ}(1P) \to e^{\pm}\tau^{\mp}$ decays using signal MC sample (left) and generic MC sample with scaled $\Upsilon(4S)$ off-resonance data.

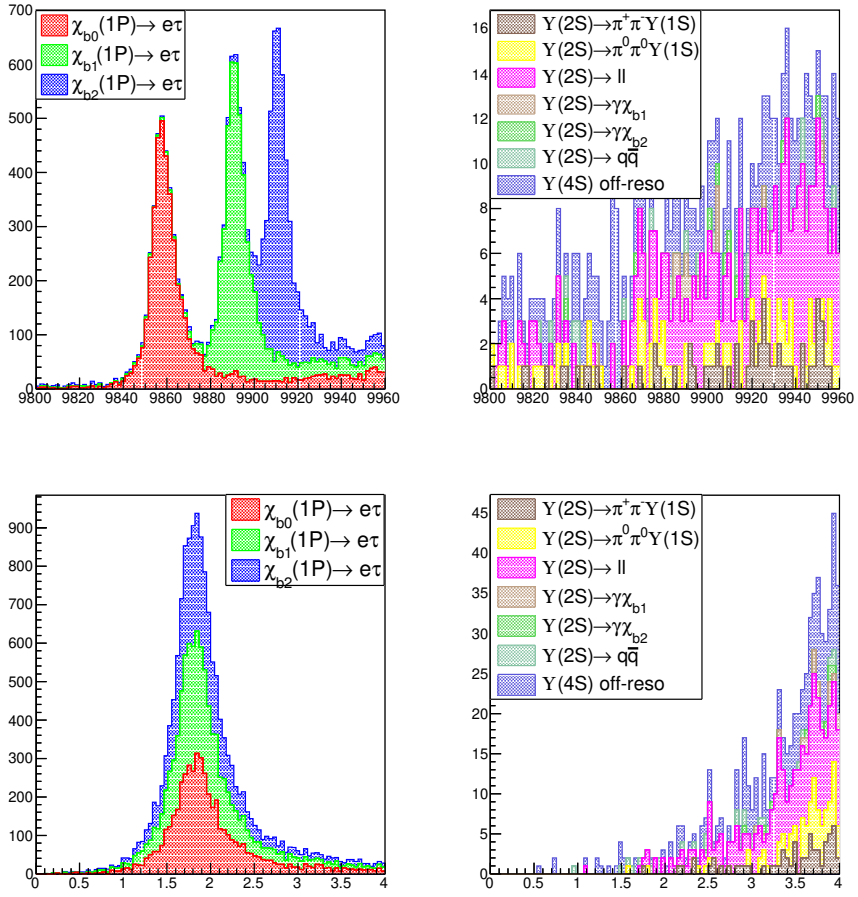

FIG. 5.33: $M_{\gamma}^{\text{recoil}}$ (in MeV/c^2) distributions (top) and $M_{\gamma e}^{\text{recoil}}$ (in GeV/c^2) distributions (bottom) for $\chi_{bJ}(1P) \to e^{\pm}\tau^{\mp}$ decays using signal MC sample (left) and generic MC sample with scaled $\Upsilon(4S)$ off-resonance data.

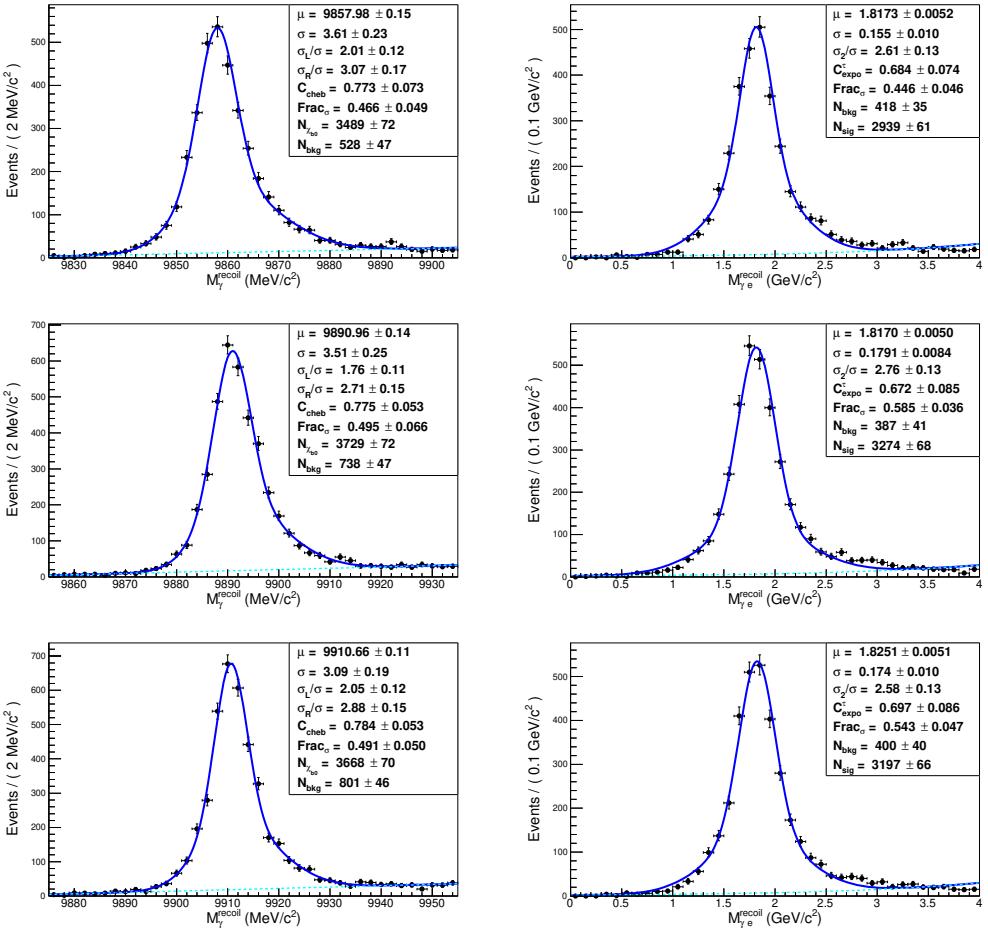

FIG. 5.34: UML fits to $M_{\gamma}^{\text{recoil}}$ in MeV/c^2 (left) and to $M_{\gamma\text{e}}^{\text{recoil}}$ in GeV/c^2 (right) for $\chi_{b0}(1P) \to e^{\pm}\tau^{\mp}$ (top row), $\chi_{b1}(1P) \to e^{\pm}\tau^{\mp}$ (middle row), and $\chi_{b2}(1P) \to e^{\pm}\tau^{\mp}$ (bottom row) decays using signal MC sample.

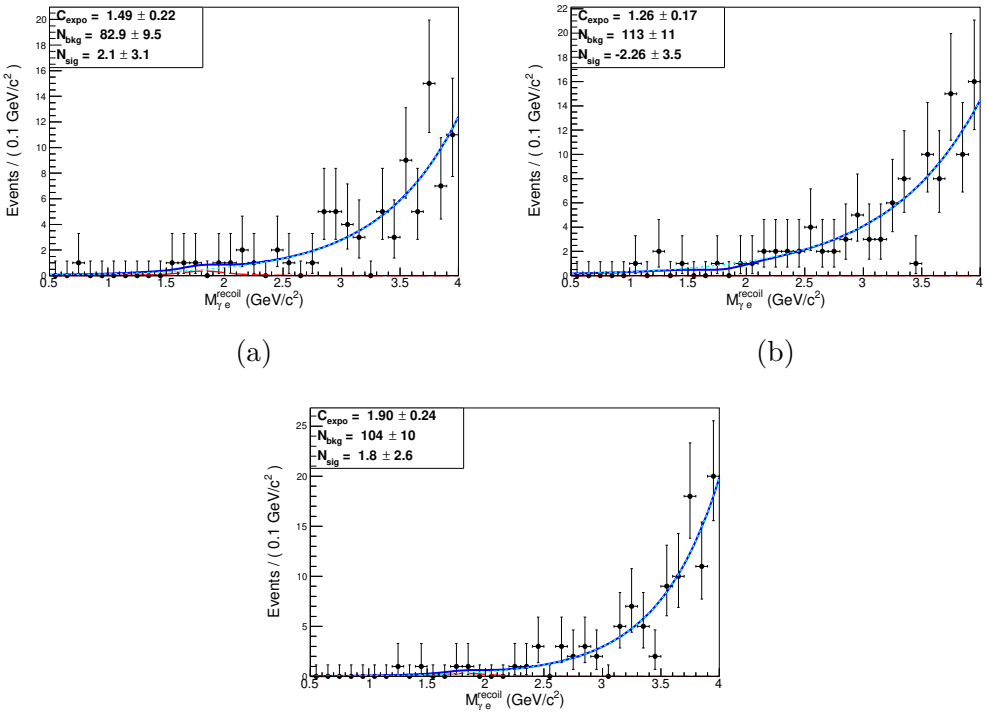

FIG. 5.35: UML fits to $M_{\gamma e}^{\rm recoil}$ (in GeV/c^2) for combined signal and backgrounds for $\chi_{b0}(1P) \to e^{\pm}\tau^{\mp}$ (a), $\chi_{b1}(1P) \to e^{\pm}\tau^{\mp}$ (b), and $\chi_{b2}(1P) \to e^{\pm}\tau^{\mp}$ (c) decays using generic MC sample with scaled $\Upsilon(4S)$ off-resonances data.

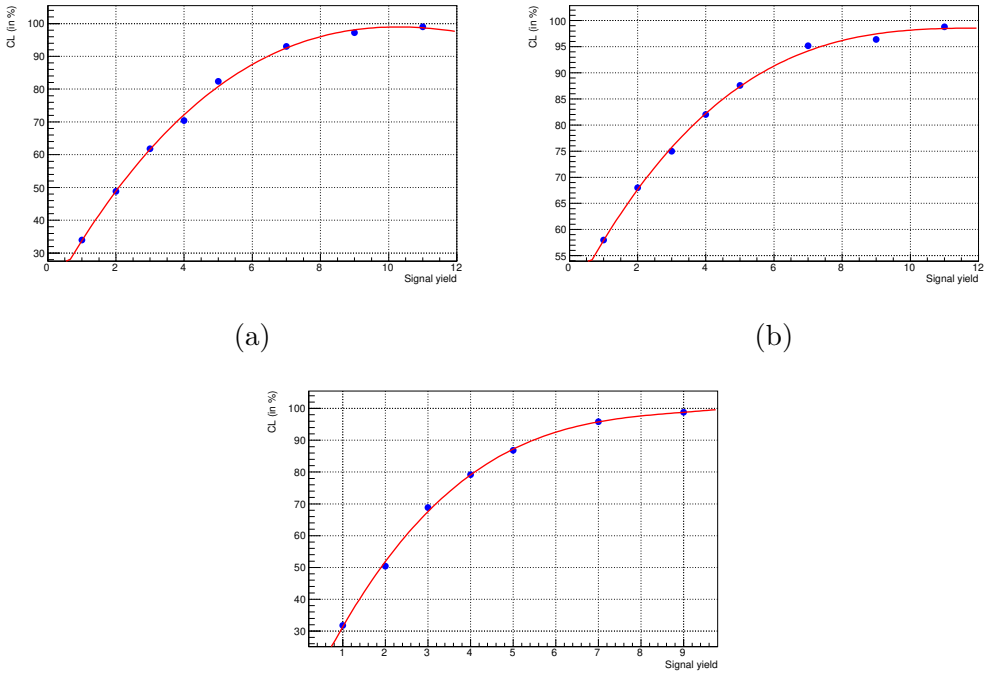

FIG. 5.36: Expected confidence level distributions as a function of input signal yield for $\chi_{b0}(1P) \to e^{\pm}\tau^{\mp}$ (a), $\chi_{b1}(1P) \to e^{\pm}\tau^{\mp}$ (b), and $\chi_{b2}(1P) \to e^{\pm}\tau^{\mp}$ (c) decays.

Chapter 6

GenMCTag Tool: A Background Tagging Utility

In this chapter, we discuss about a generic background tagging tool named "GenMCTag Tool", that we have developed for Monte-Carlo background tagging.

6.1 Introduction

Identifying the possible sources of background is crucial for any analysis in high energy physics. In almost all of the analyses, a generic MC sample is used to estimate the expected backgrounds. To guess or identify the possible sources background, one need to gain or have some experience. One can look at the mother and grand mother IDs of reconstructed MC particles to identify the background decay chain. But, tagging with reconstructed level information may fail for partially mis-reconstructed decays, where we reconstruct a fraction of background particles as signal event. Therefore, we try to identify a decay chain using the generator level information. If we know the generated decay chain associated with a reconstructed mode, we can easily understand the nature of background.

6.2 Tools used

The following tools have been used to extract the information, and plot the shape of the different background in any physical variables.

- Python, C++
- ROOT
- LaTeX

6.3 Purpose and philosophy

In the BASF2 framework, `isSignal` module is already present, which can identify the truth-matched signal events. But, it has some limitations. If the link between reconstructed and generated level information is broken, we can not use it properly. There are two available packages: TopoAna and Taudecay tagger, which can be used to understand the background.

TopoAna: One needs to store the whole generator level information, and then perform offline study to understand background. One need some level of expertise to use it. Further, dumping the whole generator level information may lead to increase the size of the output files. Therefore, managing disk space may be a serious issue in future. Also, it may not work properly for a decay linked with neutrino.

Tau decay tagger: There is also an another tool dedicated to tag the tau decays based on the generator level information (without storing the whole generator level information in the output root file). GenMCTag does the similar jobs generically for any particle with automated scripts.

No generic utility is available to separate the decays based on the generator level information. If one can tag the generic MC events, one can easily make sense of which background to expect. Philosophy of this utility is similar to the tagging procedure used by "Belle Charmonium Group". Our aim is to have less variables in

output root files with maximum information. We wrote a python script that picks up all the decays corresponding to a particle, and generates the module itself. In the present situation, we consider all the B meson, D meson, and τ lepton decays. Further, one can extend our project for other particles. We also provide a plotting utility, which can plot the distributions of different background for any physical variable.

6.4 Implementation in the BASF2

GenMCTag tool has been developed in the Belle II analysis software framework (BASF2). It consists of different levels of codes, which are discussed in this section.

Preparing tagging modules: We provide a python script, which run on the official Belle II decays tables, and can identify all the generated decay modes of the particle of interest. Further, one can easily extend to other particles. Our python script generates C++ module for a desired particle, which can now be directly plugged into the BASF2. The mentioned python script has to be run only once, when new decay modes are added MC decay tables.

Main module: The modules, generated for extracting information for different particles, are placed in the <analysis/utility> and compiled with the BASF2. We placed a script (`MCParticleTag.cc`) in <analysis/variables> to store the tagging information in the BASF2 variables. Tab. 6.1 summarizes all the scripts placed in the BASF2 framework.

Directory	Scripts included	Purpose
<analysis/utility>	GenBplusTag.cc	To tag B^+, B^-
	GenB0Tag.cc	To tag B^0, $\bar{B}^0$
	GenBsTag.cc	To tag B_s^0, $\bar{B}_s^0$
	GenDTag.cc	To tag D^{*+}, D^{*-}, D_s^+, D_s^-, D^+, D^-, D^0, $\bar{D}^0$
	GenTauTag.cc	To tag τ^+, τ^-
<analysis/variables>	MCParticleTag.cc	Registering variables to extract the tagging information

TAB. 6.1: Included scripts in the Belle II software framework.

Usage: For an existing module, one simply need to add the variables to the ntuple. Tab. 6.2 summarizes the registered variables for the listed particles.

Particle mode		Anti-particle mode	
Particle	Variable	Anti-particle	Variable
B^+	`BplusMode`	B^-	`BminusMode`
B^0	`B0Mode`	$\bar{B}^0$	`Bbar0Mode`
B_s^0	`Bs0Mode`	$\bar{B}_s^0$	`Bsbar0Mode`
D^{*+}	`DstplusMode`	D^{*-}	`DstminusMode`
D_s^+	`DsplusMode`	D_s^-	`DsminusMode`
D^+	`DplusMode`	D^-	`DminusMode`
D^0	`D0Mode`	D^0	`Dbar0Mode`
τ^+	`TauplusMode`	τ^-	`TauminusMode`

Tab. 6.2: Registered variables in the Belle II software framework.

6.5 Demonstration of GenMCTag output

Now we already have a number that reflects the information about the corresponding particle. Here we represent all the particle modes (in Tab. 6.2) with positive numbers greater or equal to +1001, and the anti particle modes with numbers less or equal to -1001. If desired particle does not exist in the MC particle list, it reflects -99. For some of the hadronic decays (generated using the PYTHIA [97]), daughter particles may not be properly defined. If a particle decay does not match with any of the defined decays (including the above mentioned hadronic decays), it reflects the number of daughters. Tab. 6.3 summarizes the representation of the returned values.

	Particle mode	Anti-particle mode
Particle not found	-99	-99
Decay not found	+(Number of daughters)	-(Number of daughters)
Decay found	+1001 to $+dddd$	-1001 to $-dddd$

Tab. 6.3: Representation of particle decays.

6.5.1 Neutral B meson mixing

Neutral B meson (B^0) and its antiparticle ($\bar{B}^0$) oscillate between each other. There is a chance to have two B^0 or two $\bar{B}^0$ at any instant. If a situation occurs with two

B^0, then both of the `B0Mode` and `Bbar0Mode` variables will be filled with positive numbers ($\geq$1001) depending on the two B^0 decays. For a situation with two $\bar{B}^0$, both of the `B0Mode` and `Bbar0Mode` variables will be filled with negative numbers ($\leq$-1001).

For example:

- Let us consider, there are two B^0 decays in an event instead of $B^0 - \bar{B}^0$.
- One B^0 decays to $D^-\eta\mu^+\nu_\mu$ (tag no +1035), and another decays to $J/\psi K^0_S$ (tag no +1729) state.
- In that case, B^0 mode variable `B0Mode` will be filled with +1035, and $\bar{B}^0$ mode variable `Bbar0Mode` will be filled with +1729.

6.5.2 Inclusion of final state radiation

Kinematics of the daughter particles may change, when there is any final state radiation (FSR) linked with a particular decay vertex. It is important to know the number of FSR photons especially for the events with π^0 in the final state, less charged track multiplicity, missing energy analysis, etc. We consider those photons into account for all the decays. If there are FSR photons, the original decay tag number $\pm(dddd)$ will be reflected as $\pm(N0dddd)$, where N implies the number of FSR photons linked with a decay vertex.

For example:

- If there is any $B^- \to D^+\pi^-\pi^-$ decay, `BminusMode` will be represented at **-1735**.
- With 2 FSR photons from the B^- decay vertex, that decay mode will reflected at **-201735**.
- With 3 FSR photons from the B^- decay vertex, that decay mode will reflected at **-301735**.

6.6 Understanding of background using plotting utility

We also provide a ROOT based utility (`plotMCTag.C`) as an example to plot all the sources of tagged background. Using this plotting utility, one can easily plot the background by plugging the information stored in a output root file. It can also be used outside the BASF2. One has to modify the inputs in the following lines.

```
input_rootfile « "example_input.root";

ntuple_name « "dpi";

plot_variable « "deltaE";

Particle_variable « "BplusMode";

antiParticle_variable « "BminusMode";

double lower_cut = -0.15, upper_cut = 0.15;

int Particle_sigTag = 1730, antiParticle_sigTag = -1730;

get_Particle_decay = B_plus[j]; get_antiParticle_decay = B_minus[j];
```

One has to provide the location of the root file (`input_rootfile`), name of the ntuple (`ntuple_name`), variable to be plotted (`plot_variable`), stored BASF2 tagging variables (`Particle_variable, antiParticle_variable`), range of the plots (`lower_cut, upper_cut`), etc. Signal tag numbers (`Particle_sigTag, antiParticle_sigTag`) should be chosen accordingly [107]. In the case where signal mode is not included in generic sample (like searches for new physics), one should choose 999 and -999, respectively. Further, one can include or exclude the charge conjugate mode. The possible background components are to be plotted in a postscript file with signal components in green histograms. All the component histograms will also be stored in an output root file. As GenMCTag tags both of the B, D, and τ particles produced in pairs, effective number of tagged particles seems to be doubled for such cases.

6.7 Case study using GenMCTag

We studied the backgrounds for several analyses using this tool. In this section, we discuss some of those background studies.

6.7.1 For $B^- \to D^0\pi^-$ decay

GenMCTag has been used to understand the background for $B^- \to D^0\pi^-$ decay by Manish Kumar. Here we check the background components for $B^- \to D^0\pi^-$ decay using a $B^\pm$ meson MC sample. As one can see in Fig. 6.1, signal components have been appeared in green histograms on ΔE variable. This tool easily identifies the possible peaking backgrounds.

6.7.2 For $D^0 \to K^0_S\pi^+\pi^-$ decay

We check the background components for $D^0 \to K^0_S\pi^+\pi^-$ decay using a $c\bar{c}$ MC sample. As one can see in Fig. 6.2, signal components have been appeared on ΔM variable in green histograms. Here K^0_S has been reconstructed from the $\pi^+\pi^-$ instead of using the standard K^0_S functions. Most of background components are expected to be flat near the signal region. For $D^0 \to \pi^+\pi^-\pi^+\pi^-$ decays, one of the $\pi^+\pi^-$ pairs has been misidentified, and hence this mode is peaking in the signal region.

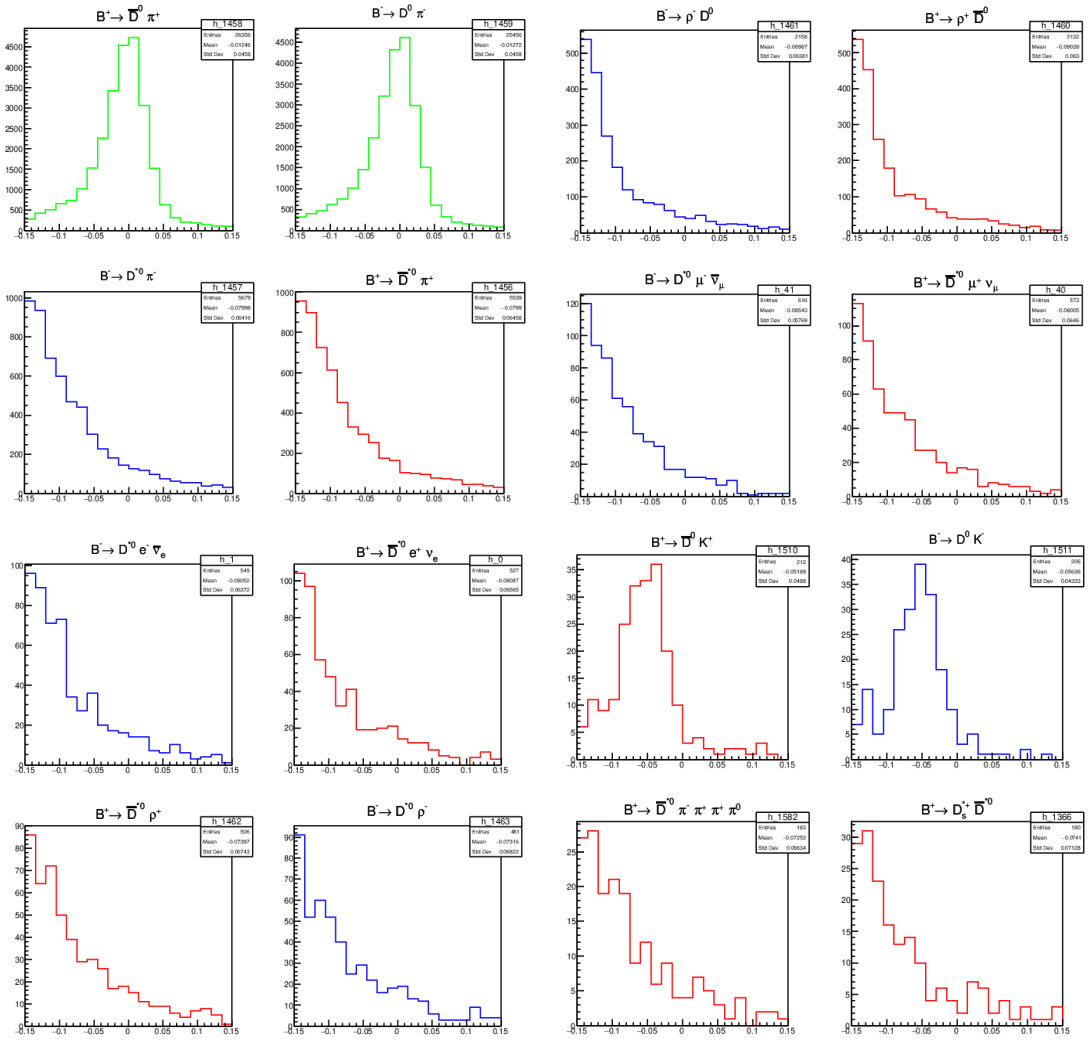

FIG. 6.1: Tagged $B^{\pm}$ background components for $B^- \to D^0\pi^-$ decay using GenMCTag tool.

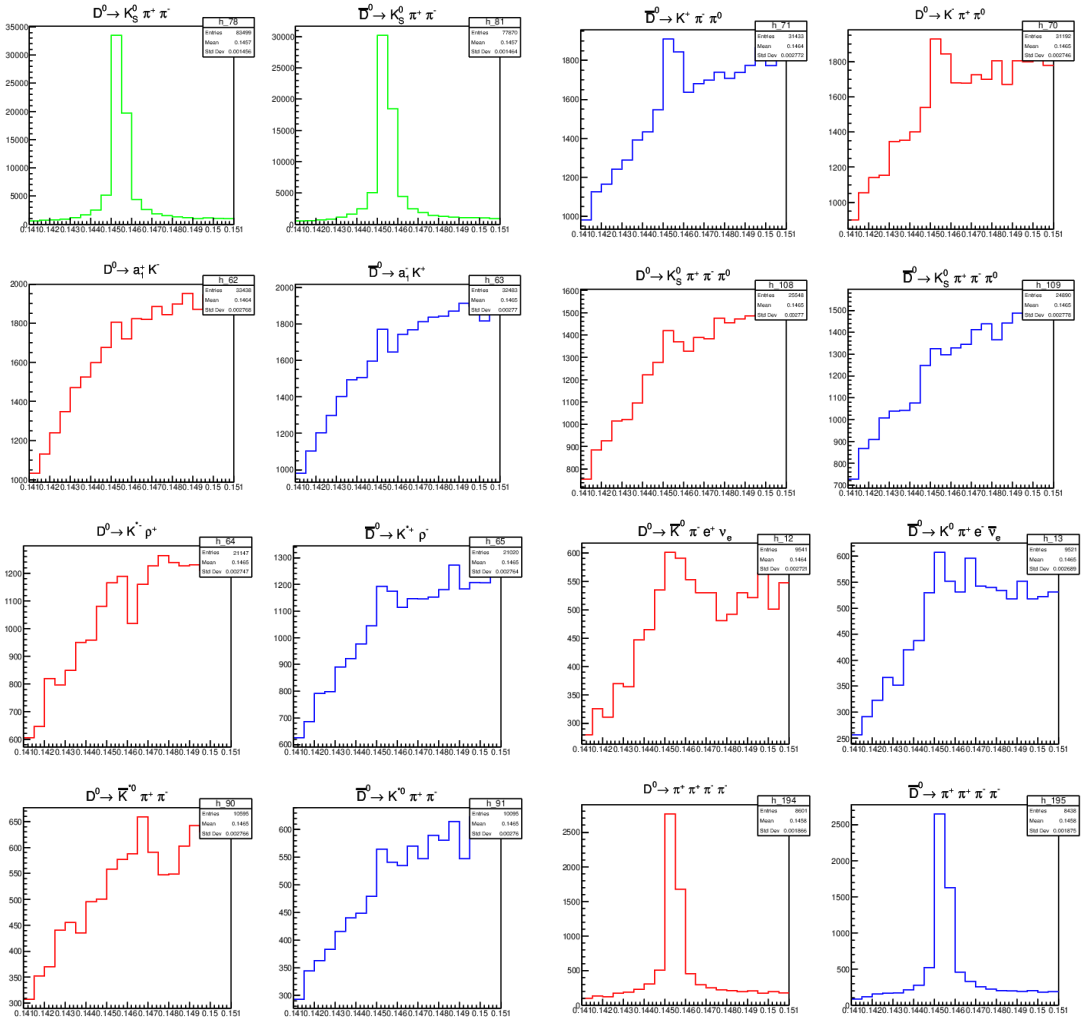

FIG. 6.2: Tagged D^0 background components for $D^0 \to K^0_S \pi^+ \pi^-$ decay using GenMCTag tool.

6.8 Summary

We develop a utility for background tagging using the generator level information. It also comes with a plotting utility for quick and better understanding of the potential sources of background. We studied the outcomes for different decays, and find it to be easy and safe all the time. Now GenMCTag tool is an official package of the Belle II software framework.

Chapter 7

Discussion on Results

In this chapter, we discuss the outlook of our studies.

7.1 Measure of isospin violation in $X(3872) \to J/\psi\omega$ decays

We generate the MC samples and optimize the selection criteria for the $B \to X(3872)K$, $X(3872) \to J/\psi\omega$. The fitting strategy is fixed and currently we are waiting for collaboration permission for the box opening. Once we obtain the result for $\mathcal{B}[B \to X(3872)K] \times \mathcal{B}[X(3872) \to J/\psi\omega]$ using $\Upsilon(4S)$ data collected by the Belle detector, we will obtain the $R_{3\pi/2\pi}$ using the previously obtained result for $\mathcal{B}[B \to X(3872)K] \times \mathcal{B}[X(3872) \to J/\psi\pi^+\pi^-]$.

7.2 Obtaining Wilson coefficients of CLFV operators

We obtained the results two-body and three-body CLFV decays of $\Upsilon(1S)$. Previously, $\Upsilon(1S) \to \mu^\pm\tau^\mp$ decay was studied by the CLEO collaboration. Our result for $\Upsilon(1S) \to \mu^\pm\tau^\mp$ mode is 2.3 times more stringent as compared to the CLEO result. For rest of the CLFV modes, we searched for the first time. CLFV dielectric operators are strictly constrained by the $\tau^\pm \to \ell^\pm\gamma$ searches [108, 109, 110]. Therefore, we calculate the upper bounds on the Wilson coefficients of vector and tensor

operators using the results obtained for $\Upsilon(1S) \to \ell_1\ell_2$ $[\ell_1, \ell_2 = e, \mu, \tau]$ searches. One can find the following relations for the Wilson coefficients of vector and tensor operators modifying Eq. (1.26).

$$\left|\frac{C_V^{b\ell_1\ell_2}}{\Lambda^2}\right| = \frac{4\pi\alpha Q_b}{M^2_{\Upsilon(1S)}}\sqrt{\frac{\mathcal{B}[\Upsilon(1S) \to \ell_1\ell_2]}{\mathcal{B}[\Upsilon(1S) \to e^+e^-]}} \tag{7.1}$$

$$\left|\frac{C_T^{b\ell_1\ell_2}}{\Lambda^2}\right| = \frac{\sqrt{2}\pi\alpha Q_q}{G_F\kappa_{\Upsilon(1S)}M^2_{\Upsilon(1S)}m_b m_{\ell_2}}\sqrt{\frac{\mathcal{B}[\Upsilon(1S) \to \ell_1\ell_2]}{\mathcal{B}[\Upsilon(1S) \to e^+e^-]}} \tag{7.2}$$

Here, we consider that there is no parity violation for the new physics operators. Using Eq. (7.1) and Eq. (7.2), we calculate the Wilson coefficients for vector and tensor operators, respectively. Obtained constrains are listed in Tab. 7.1. In Fig. 7.1, we compare $C_V^{b\mu\tau}$ from Belle and CLEO results for $\Upsilon(1S) \to \mu^\pm\tau^\mp$ decays. Region above the curve lines for two different experiments are excluded.

Wilson coefficient	Used result	Upper bound [in $(\mathrm{GeV}/c^2)^{-2}$]
$\lvert C_V^{be\mu}/\Lambda^2\rvert$	$\Upsilon(1S) \to e^\pm\mu^\mp$	1.4×10^{-6}
$\lvert C_V^{b\mu\tau}/\Lambda^2\rvert$	$\Upsilon(1S) \to \mu^\pm\tau^\mp$	3.8×10^{-6}
$\lvert C_V^{be\tau}/\Lambda^2\rvert$	$\Upsilon(1S) \to e^\pm\tau^\mp$	3.8×10^{-6}
$\lvert C_T^{be\mu}/\Lambda^2\rvert$	$\Upsilon(1S) \to e^\pm\mu^\mp$	1.9×10^{-1}
$\lvert C_T^{b\mu\tau}/\Lambda^2\rvert$	$\Upsilon(1S) \to \mu^\pm\tau^\mp$	3.0×10^{-2}
$\lvert C_T^{be\tau}/\Lambda^2\rvert$	$\Upsilon(1S) \to e^\pm\tau^\mp$	3.0×10^{-2}

TAB. 7.1: Constraints on the Wilson coefficients of vector and tensor operators using the results of two-body CLFV decays of $\Upsilon(1S)$.

To obtain the Wilson coefficients for axial vector operators, we use the experimental bounds obtained for $\Upsilon(1S) \to \gamma\ell_1\ell_2$ $[\ell_1, \ell_2 = e, \mu, \tau]$ decays. One can find the following relation for the Wilson coefficients for axial vector operators modifying Eq. (1.28).

$$\left|\frac{C_A^{b\ell_1\ell_2}}{\Lambda^2}\right| = \frac{12\pi}{Q_b f_{\Upsilon(1S)}}\sqrt{\frac{\Gamma_{\Upsilon(1S)}\mathcal{B}[\Upsilon(1S) \to \gamma\ell_1\ell_2]}{\alpha M^3_{\Upsilon(1S)}}} \tag{7.3}$$

Using the above equation, obtained constrains on Wilson coefficients for different axial vector operators are listed in Tab. 7.2. These are the first ever constrains for the corresponding operators.

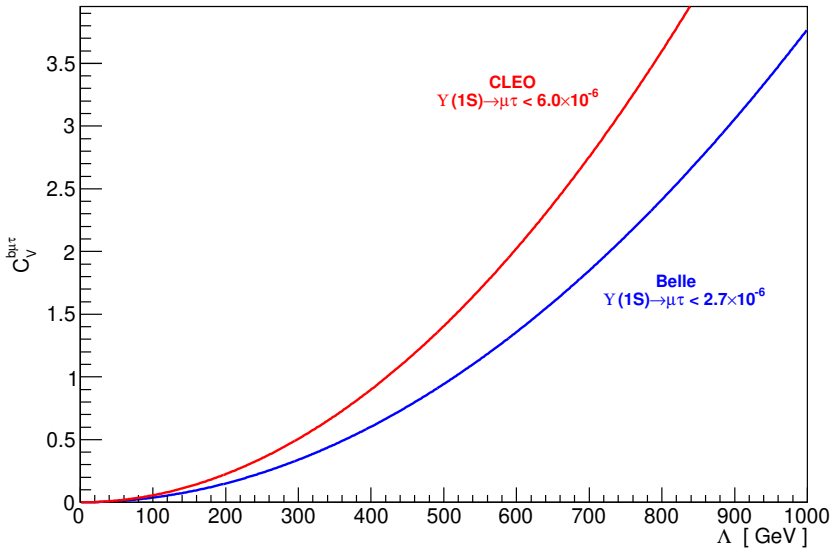

FIG. 7.1: We compare our result with the previously available result for $\Upsilon(1S) \to \mu^{\pm}\tau^{\mp}$ decays.

Wilson coefficient	Used result	Upper bound [in $(\mathrm{GeV}/c^2)^{-2}$]
$\lvert C_A^{be\mu}/\Lambda^2\rvert$	$\Upsilon(1S) \to \gamma e^{\pm}\mu^{\mp}$	3.3×10^{-4}
$\lvert C_A^{b\mu\tau}/\Lambda^2\rvert$	$\Upsilon(1S) \to \gamma \mu^{\pm}\tau^{\mp}$	1.3×10^{-3}
$\lvert C_A^{be\tau}/\Lambda^2\rvert$	$\Upsilon(1S) \to \gamma e^{\pm}\tau^{\mp}$	1.3×10^{-3}

TAB. 7.2: Constraints on the Wilson coefficients of axial vector operator using the results of three-body CLFV decays of $\Upsilon(1S)$.

Appendix A

Study of X(3872) & X(3915) in B meson decays

A.1 Correlation of $M_{\mathrm{J}/\psi\omega}$ with J/ψ momentum

In Fig. A.1, we compare the $|\vec{p}^{\,\mathrm{CM}}_{J/\psi}|$ distribution of signal and background events. On $|\vec{p}^{\,\mathrm{CM}}_{J/\psi}|$ distribution, the background dominates after above 1.2 GeV/c. In Fig. A.2, we compare the distribution of background on $M_{\mathrm{J}/\psi\omega}$ distribution before and after tight $|\vec{p}^{\,\mathrm{CM}}_{J/\psi}|$ selection, $|\vec{p}^{\,\mathrm{CM}}_{J/\psi}| < 1.2$ GeV/c. As one can see, the background events are peaking around 3.925 GeV/c^2 after the tight $|\vec{p}^{\,\mathrm{CM}}_{J/\psi}|$ selection. Therefore, we do not apply any further selection on $|\vec{p}^{\,\mathrm{CM}}_{J/\psi}|$ to avoid sculpting the of the background shape on $J/\psi\omega$ invariant mass distribution.

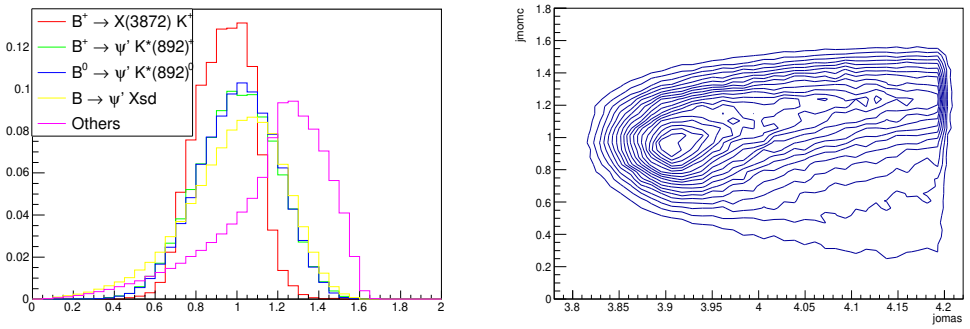

FIG. A.1: Distribution of $|\vec{p}^{\,\mathrm{CM}}_{J/\psi}|$ in GeV/c (left) and 2D distribution of $|\vec{p}^{\,\mathrm{CM}}_{J/\psi}|$ in GeV/c vs $M_{\mathrm{J}/\psi\omega}$ in GeV/c^2 (right) for $B^+ \to J/\psi\omega K^+$ decays using $B \to J/\psi X$ inclusive MC sample.

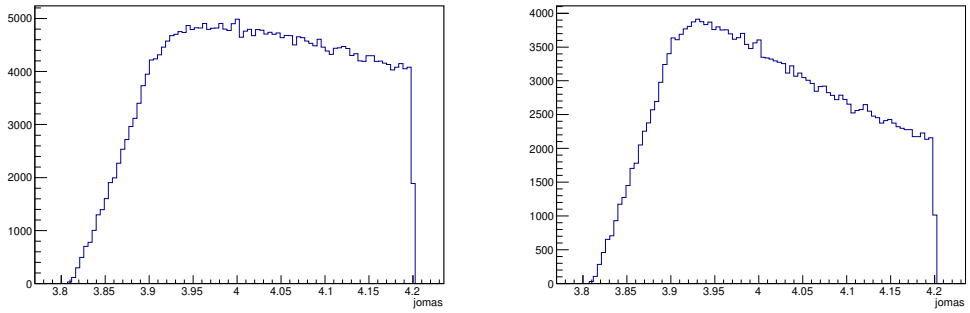

FIG. A.2: Comparison background for $B^+ \to J/\psi\omega K^+$ events before (left) and after (right) applying tight $|\vec{p}^{\,\mathrm{CM}}_{J/\psi}|$ (in GeV/c) selection.

A.2 Omega mass dependency on resonances

Probably $X(3872)$ mass is near the threshold to produce $J/\psi\omega$. Therefore, in Fig. A.3, mean of $M_{\pi^+\pi^-\pi^0}$ distributions for $X(3872)$ and $X(3915)$ are separated from each other. To understand that we generate the $J/\psi\omega$ events with a hypothetical particle $X(3877)$ having mass 3877 MeV/c^2. As one can see, the M_ω mass peak associated with $X(3877)$ resonance is somewhere in between $X(3872)$ and $X(3915)$ peaks on M_ω distribution.

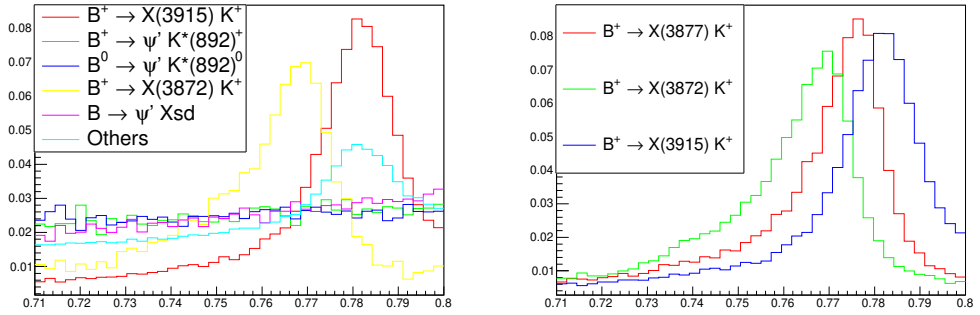

FIG. A.3: Distribution of M_ω (in GeV/c^2) (left). Right figure comparing the M_ω (in GeV/c^2) distributions from different resonances.

A.3 A set of background fits

We try several threshold functions to fit the shape of the background. Some of the fits are shown in Fig. A.4. Fig. (a), (b), (c), and (d) corresponding to Eq. (A.1), (A.2), (A.3), and (A.4), respectively. Fig. (b) has the minimum χ^2 value, but uncertainty

corresponding to threshold parameter C is very high. χ^2 value of Fig. (a) little higher than Fig. (b), but in the signal region (below 3.95 GeV/c^2) Fig. (a) shows better agreement with data points. Therefore, we choose Eq. (A.1) to model the background events.

$$\mathcal{L}(x; A, B, M_{th}) = \frac{e^{-N}}{N!} \prod_{i=1}^{N} (x - M_{th})^3 \exp\left[A(x - M_{th}) + B(x - M_{th})^2\right] \quad \text{(A.1)}$$

$$\mathcal{L}(x; A, B, M_{th}) = \frac{e^{-N}}{N!} \prod_{i=1}^{N} (x - M_{th})^3 \exp\left[A(x - M_{th}) + B(x - M_{th})^2 + C(x - M_{th})^3\right] \quad \text{(A.2)}$$

$$\mathcal{L}(x; A, B, M_{th}) = \frac{e^{-N}}{N!} \prod_{i=1}^{N} (x - M_{th})^2 \exp\left[A(x - M_{th}) + B(x - M_{th})^2 + C(x - M_{th})^3\right] \quad \text{(A.3)}$$

$$\mathcal{L}(x; A, B, M_{th}) = \frac{e^{-N}}{N!} \prod_{i=1}^{N} (x - M_{th})^4 \exp\left[A(x - M_{th}) + B(x - M_{th})^2\right] \quad \text{(A.4)}$$

A.4 Corrected efficiency for $X(3872)$ in data

In absence of an appropriate model for $X(3872) \to J/\psi\omega$ ($J = 1 \to 1 + 1$), we generate the signal events using the PHSP model. Also, in $B \to J/\psi X$ inclusive sample, $X(3872) \to J/\psi\omega$ decays is generated using the PHSP model. We estimate more realistic efficiency in data using the amplitude for $J = 1 \to 1{+}1$ interaction [106]. To estimate the corrected efficiency, we generate the signal events using the PARTWAVE model of EvtGen [93]. The fitted efficiency of the charged and neutral modes are estimated to be 5.18% and 3.12%, respectively. The corrected efficiencies (using PARTWAVE model) agree with the efficiencies estimated by using the PHSP model. In Tab. A.1, we compare the fitted efficiencies using two different models.

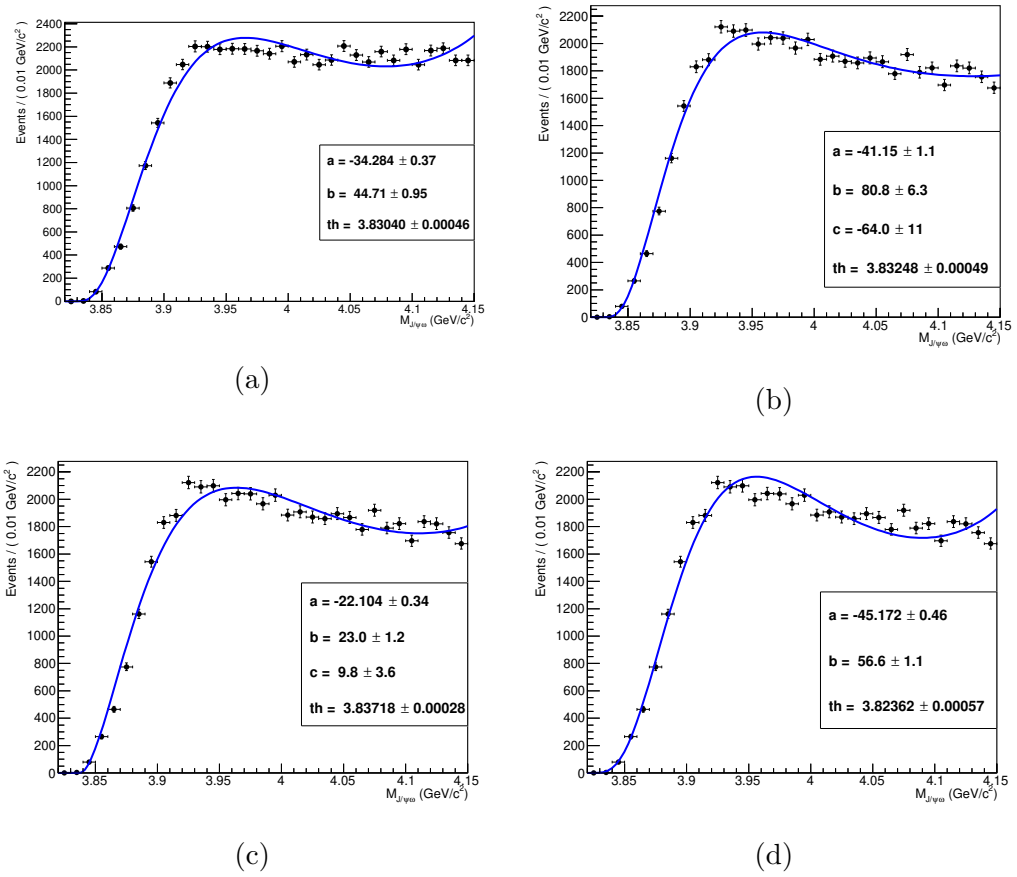

FIG. A.4: UML fits to $M_{\mathrm{J}/\psi\omega}$ (in GeV/c^2) corresponding to different threshold functions for $B^+ \to J/\psi\omega K^+$ decays using background events from $B \to J/\psi X$ inclusive MC sample.

Decay mode	Fitted efficiency using	
	PARTWAVE model (%)	PHSP model (%)
Charged	5.18	5.21
Neutral	3.12	3.15

TAB. A.1: Comparison of signal efficiencies using different models for generating $X(3872) \to J/\psi\omega$ decays.

Appendix B

Search for CLFV decays of $\Upsilon(1S)$

B.1 Lepton vs pion misidentification in $\tau^- \to \pi^- \nu_\tau$ decays

For $\Upsilon(1S) \to \mu^\pm\tau^\mp$ and $\Upsilon(1S) \to e^\pm\tau^\mp$ studies, we reconstruct tau in three decay modes. Most of the backgrounds come from the $\tau^- \to \pi^-\nu_\tau$ decays. Dominating background for $\tau^- \to \pi^-\nu_\tau$ reconstruction mode near signal region comes from the $\Upsilon(1S) \to \mu^+\mu^-$ ($\Upsilon(1S) \to e^+e^-$) for $\Upsilon(1S) \to \mu^\pm\tau^\mp$ ($\Upsilon(1S) \to e^\pm\tau^\mp$) decays, where one of the muon (electron) misident ified as pion. Polar angle distribution of those pions (Fig. B.1) shows two peaks near the junctions of the barrel and endcaps of the KLM (ECL) for $\Upsilon(1S) \to \mu^\pm\tau^\mp$ ($\Upsilon(1S) \to e^\pm\tau^\mp$) decays. It seems, muons and electrons remain undetected at the junctions have been misidentified as pions. We apply the following vetos to remove the fake pion peaks.

- Electron veto - 1) $31^o < \theta_\pi < 33^o$ and 2) $128^o < \theta_\pi < 131^o$
- Muon veto - 1) $\theta_\pi < 22^o$ and 2) $116^o < \theta_\pi < 121^o$

As the misidentified pions are distributed over the whole angular region, those vetos are very helpful. Finally we apply δM cut as described in section 4.3.3 and section 4.4.3, in order to remove those background. One can see the polar angle distributions of pions after applying the δM cut in Fig. B.1.

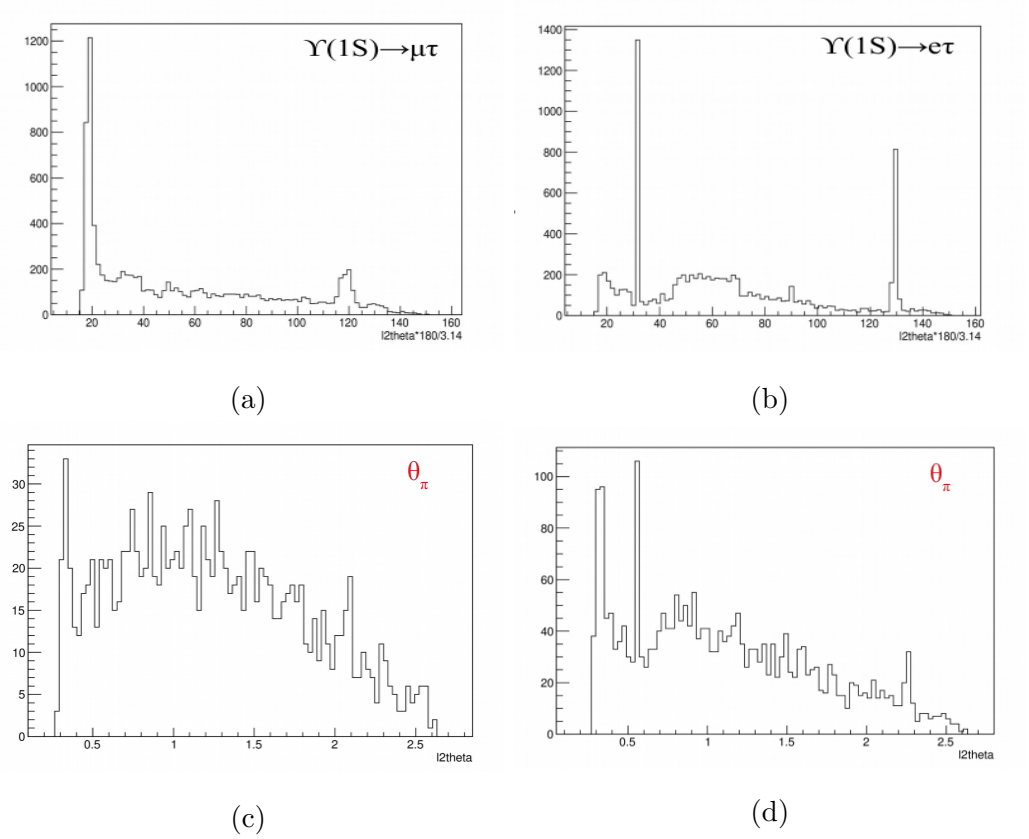

FIG. B.1: Polar angle distribution for misidentified pions for $\Upsilon(1S) \to \mu^{\pm}\tau^{\mp}$ decay (a) and for $\Upsilon(1S) \to e^{\pm}\tau^{\mp}$ decays (b). Polar angle distribution after δM cut for $\Upsilon(1S) \to \mu^{\pm}\tau^{\mp}$ decay (c) and $\Upsilon(1S) \to e^{\pm}\tau^{\mp}$ decay (d).

B.2 Lepton identification performance study

We also study lepton identification performance by comparing the yield in the MC and data. We plot the distributions of the signal yield as a function of L_{μ} and L_e (Fig. B.2). There is a discrepancy in the yield between MC and data due to the use of different branching fractions for generating $\Upsilon(1S) \to \ell^{\pm}\ell^{\mp}$ decays. In Fig. B.3, we show the ratio of yield from data to MC. Here one can see the good agreement for different L_{μ} and L_e selections.

B.3 Estimation of $\mu^{\pm}$ to $e^{\pm}$ misidentification

Electron vs muon misidentification plays a crucial role for $\Upsilon(1S) \to e^{\pm}\mu^{\mp}$ study. We estimated the lepton misidentification yield in MC using 40 million $\Upsilon(1S) \to$

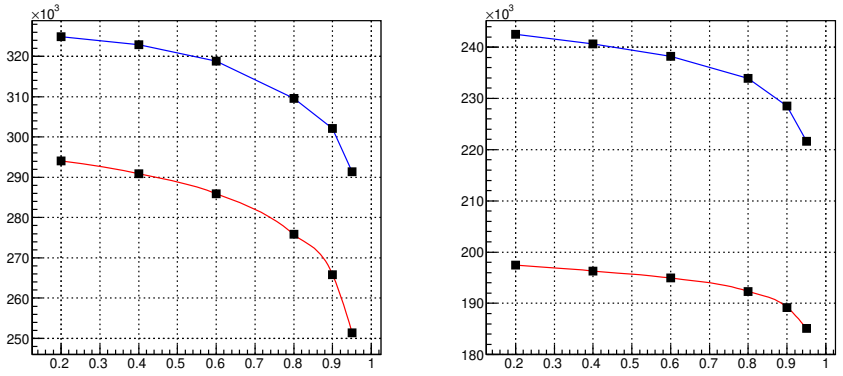

FIG. B.2: Signal yield comparison for different L_μ and L_e selections for generic MC (blue) and $\Upsilon(2S)$ data (red) for $\Upsilon(1S) \to \mu^+\mu^-$ events (left) and $\Upsilon(1S) \to e^+e^-$ events (right).

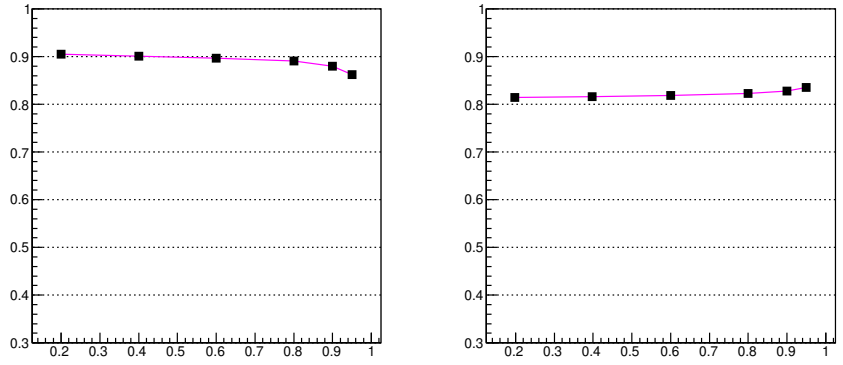

FIG. B.3: Ratio of data yield to MC yield for different L_μ and L_e selections for $\Upsilon(1S) \to \mu^+\mu^-$ events (left) and $\Upsilon(1S) \to e^+e^-$ events (right).

$\ell^{\pm}\ell^{\mp}$ sample. In this section, we draw a correction factor to estimate the $\mu^{\pm}$ to $e^{\pm}$ ($\mu\mu \to e\mu$) misidentified yield in $\Upsilon(2S)$ data. We measure the $e^{\pm}$ probing efficiency of $\mu^{\pm}$ using di-muon MC sample generated at 10.52 GeV and unskimmed $\Upsilon(4S)$ off-resonance data. As unskimmed $\Upsilon(4S)$ off-resonance data is available only for SVD II, we use the data from Exp 31 to Exp 73 data for this study. First, we check the polar angle distribution of probed electron and tagged muon track. As one can see in Fig. B.4, there is a sharp peak for tagged muon distribution at the junction of forward endcap and barrel of ECL, where electrons escape from the ECL and hit the KLM. To remove those background, we reject the tagged muons with theta less than 35^o. In Fig. B.5, we see the good agreement between data and MC for the probed $e^{\pm}$ after removing the tagged muons identified in the ECL forward endcap

region.

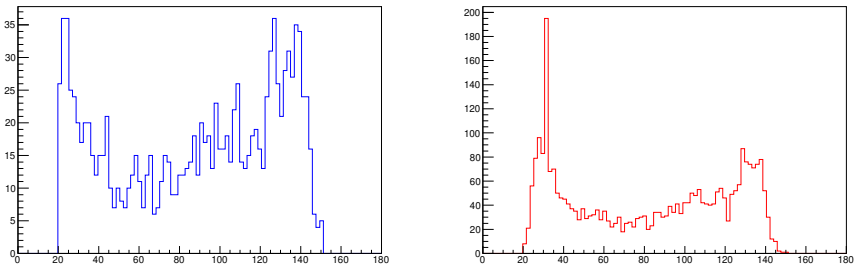

FIG. B.4: Polar angle distributions of tagged $\mu^{\pm}$ for $e^+e^- \to \mu^{\pm}\mathrm{x}^{\mp}$ events using di-muon MC sample (left) and $\Upsilon(4S)$ off-resonance data (right).

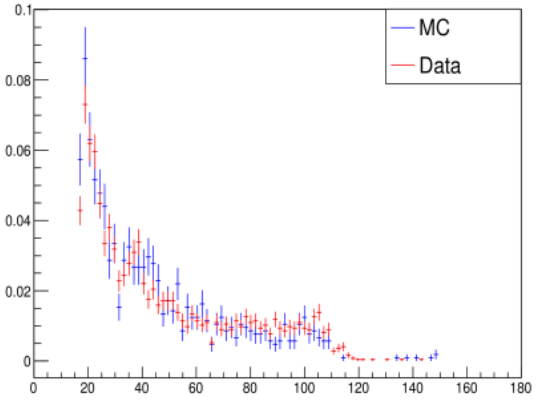

FIG. B.5: Polar angle distribution of probed $e^{\pm}$ for $e^+e^- \to \mu^{\pm}e^{\mp}$ events using using di-muon MC sample (blue) and $\Upsilon(4S)$ off-resonance data (red).

To get the yield of di-muon events, we fit the invariant mass of two charged tracks ($M_{\mathrm{x}\mu}$) with $L_\mu > 0.9$ for the tagged muon, and no particle identification selection for the other track (x). We perform a binned fit to $M_{\mathrm{x}\mu}$ (in Fig. B.6) distribution within 9 to 10.9 GeV/c^2 with sum of a Gaussian and a bifurcated Gaussian as signal PDF, and an Argus function terminated at 10.9 GeV/c^2 is used as background PDF. We fix the tail parameters of the signal PDF of data from the MC fit, while mean and sigma are floated.

In order to check the KLM health for the different experiments, we check the efficiencies of muon probing for different experiments. We fit the $M_{\mu\mu}$ for probed muon ($L_\mu > 0.9$) in a similar approach to tagged muon fit (Fig. B.7). We perform the same study for each of the experiment separately. Fig. B.8 summarizes the L_μ efficiencies and efficiency ratio (data/MC) for different experiments. We observe a sudden increase in the efficiency ratio from the Exp 51.

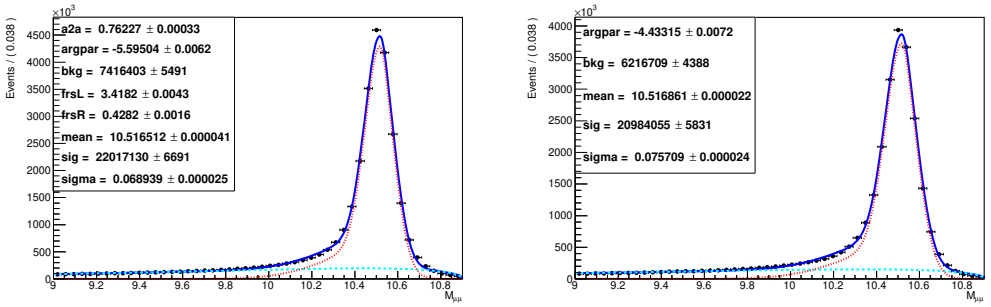

FIG. B.6: UML fit to $M_{x\mu}$ (in GeV/c^2) for $e^+e^- \to \mu^{\pm}x^{\mp}$ events using di-muon MC sample (left) and $\Upsilon(4S)$ off-resonance data (right).

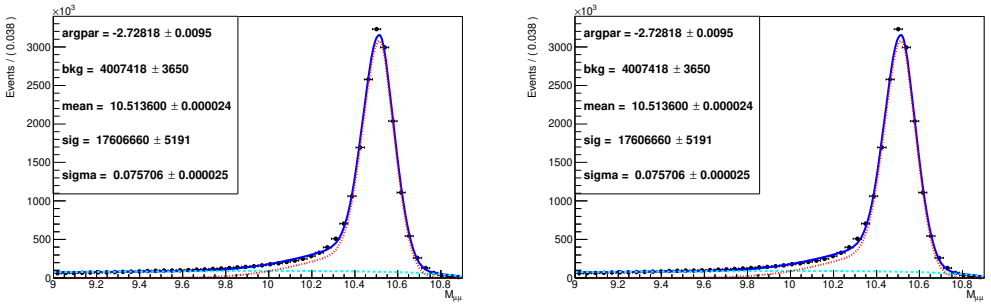

FIG. B.7: UML fit to $M_{\mu\mu}$ (in GeV/c^2) for $e^+e^- \to \mu^{\pm}\mu^{\mp}$ events using di-muon MC sample (left) and $\Upsilon(4S)$ off-resonance data (right)..

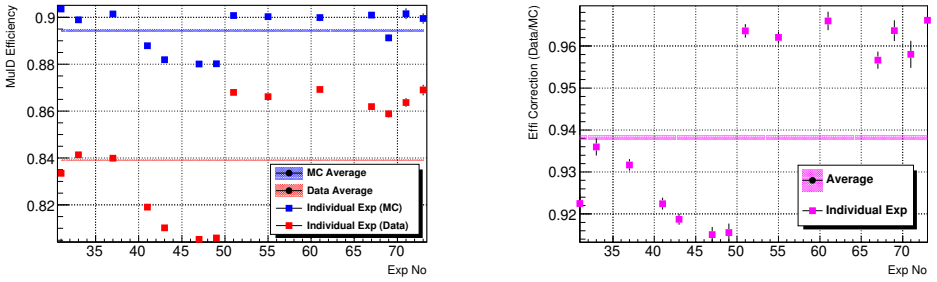

FIG. B.8: Muon probing efficiency (left) and efficiency ratio (right).

To get the yield of the misidentification events, we study the $e^{\pm}$ probed events with $L_e > 0.6$ (our desired L_e cut for $\Upsilon(1S) \to e^{\pm}\mu^{\mp}$ study). We fit the $M_{e\mu}$ with sum of a Gaussian and a bifurcated Gaussian as signal PDF, and an exponential function as background PDF (Fig. B.9). We divide all the experiments (31-73) into two sets, (a) Exp 31-49 and (b) Exp 51-73. To fit the data for a set of experiment, we fix the shape of the signal PDF from the overall fits. Tab. B.1 summarizes the misidentification efficiencies and correction factors for different set of experiments. From Fig. B.10, one can visualize the muon misidentification efficiencies and correction factors. Correction

factors for both of the set of experiments are found to be consistent with each other. $\Upsilon(2S)$ data has been taken in Exp 67 and Exp 71. As one can see in Fig. B.8, relative efficiency (effi ratio) of muon probing for Exp 51 and above is consistent Exp 67 and Exp 71, we use the 2.5 ± 0.5 as $\mu \to e$ misidentification correction factor in data.

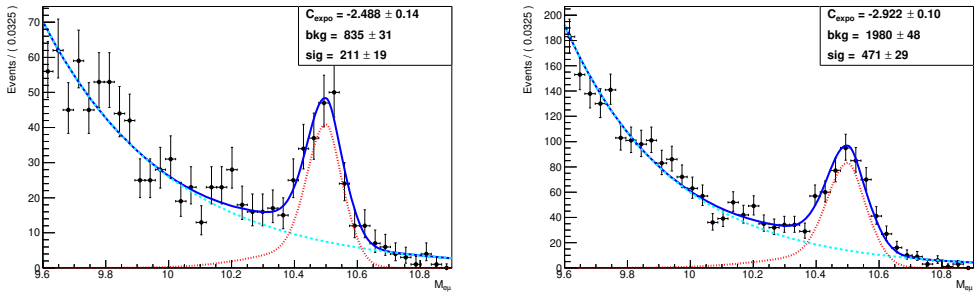

FIG. B.9: UML fit to $M_{\mu e}$ (in GeV/c^2) for $e^+e^- \to \mu^{\pm}e^{\mp}$ events using di-muon MC sample (left) and $\Upsilon(4S)$ off-resonance data (right).

Exp No	MC efficiency (10^{-6})	Data efficiency (10^{-6})	Correction factor(Data/MC)
31-49	10.3 ± 1.2	22.4 ± 1.7	2.2 ± 0.3
51-73	8.4 ± 1.2	21.0 ± 2.2	2.5 ± 0.5
All	9.6 ± 0.9	22.4 ± 1.4	2.3 ± 0.3

TAB. B.1: $\mu^{\pm} \to e^{\pm}$ misidentification efficiency and data to MC correction factor.

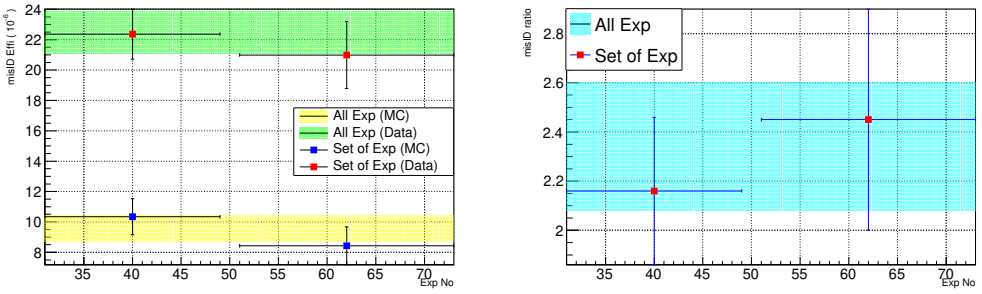

FIG. B.10: $\mu^{\pm} \to e^{\pm}$ misidentification efficiency (left) and data to MC correction factor (right).

Appendix C

Search for CLFV decays of $\chi_{bJ}(1P)$

C.1 4 constraint (4C) fit

Four constraint fitter is a kinematic fitter, which supports four-constraint simultaneous fit. The four constraints represents the conservation of four momentum, while the best fit is achieved by finding the smallest χ^2. Available code has been modified to get the maximum information. The χ^2_{4C} can be represented as a function of momentum covariance matrices and Lagrange undetermined multiplier [90].

$$\chi^2_{4C} = \sum_n \left(\vec{P}_n - \vec{P}^0_n\right)^T V_n^{-1} \left(\vec{P}_n - \vec{P}^0_n\right) + 2\lambda_x(p^x_f - p^x_i) + 2\lambda_y(p^y_f - p^y_i) + 2\lambda_z(p^z_f - p^z_i) + 2\lambda_e(E_f - E_i) \tag{C.1}$$

Here, n implies the number of final state particles. $\vec{P}^0_n$ and $\vec{P}_n$ represent reconstructed and predicted 3-momentum of n-th particle. V_n represents the error matrix corresponding to a particle, and λ indicates the Lagrange undetermined multiplier corresponding to a particular parameter. Indices (i, f) represent the (initial, final) state values corresponding to a particular parameter.

C.2 Simulating the ECL Bhabha triggers

In Fig. C.1, we show the ECL trigger flow for selecting a Bhabha event. There are 17 ϕ rings (5 in endcap regions and 12 in barrel region) in the ECL. Based on the simulations, Bhabha events are categorized into 11 types on the basis of angular

distributions and the energy of the e^+, e^- tracks. In addition to these categories, Bhabha veto is decided with the total number of the isolated clusters (ICN). We count the number of isolated cluster using cluster counting module coming from each trigger cell [91].

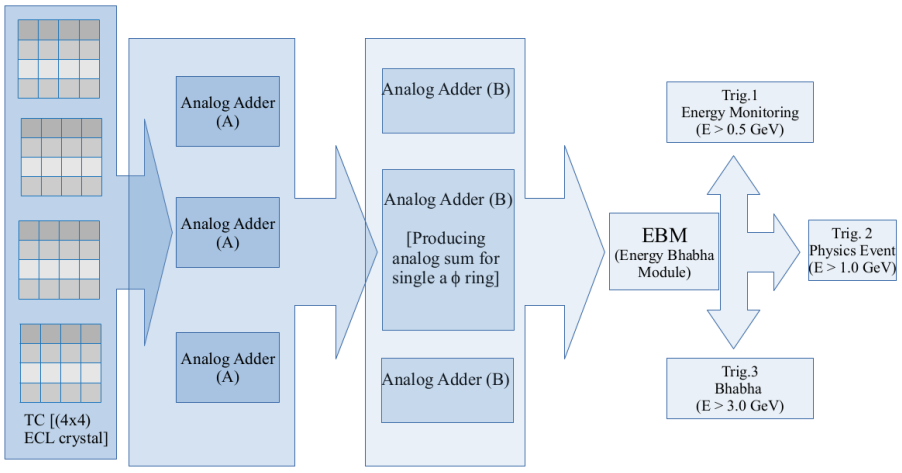

FIG. C.1: Schematic diagram of ECL trigger flow.

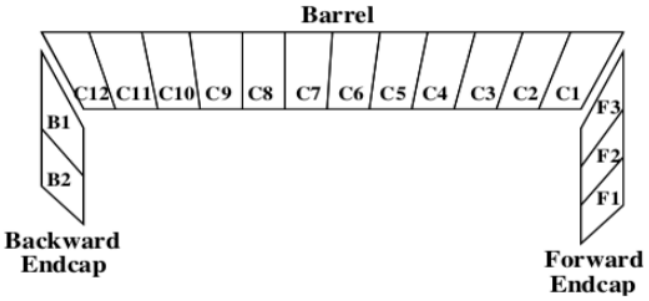

FIG. C.2: The distribution ϕ rings of ECL.

Depending on the distribution 17 ϕ rings, the threshold energies for 11 types of Bhabha events are summarized in Tab. C.1. Bhabha veto is applied on an event if that event fulfill any of these 11 threshold, along with if ICN is less than 4. There are two types of Physics trigger coming from the ECL trigger system.

- T1 $\Longrightarrow$ $(\mathrm{E_{tot}} > 1.0\mathrm{GeV})(\otimes\mathrm{Bhabha})(\otimes\mathrm{Cosmic})$
- T2 $\Longrightarrow$ $(\mathrm{ICN} > 3)(\otimes\mathrm{Cosmic})$

As we are interested to study the Bhabha like events in this section, we calculate the selection efficiencies for Bhabha trigger bits, which are linked with Bhbaha veto. As one can see in Fig. C.2, Bhabha veto is not applied if the ICN greater than 3.

Type	Logic	Threshold (in GeV)
1	F1+F2+B1+B2	5.3
2	F2+F3+B1+B2+C11+C12	5.6
3	F2	5.0
4	F3+C10+C11+C12	5.4
5	C1+C9+C10	5.4
6	C1+C2+C9	5.2
7	C2+C8+C9	5.5
8	C3+C7+C8	5.2
9	C4+C6+C7	5.2
10	C5+C6	5.2
11	C10	3.1

Tab. C.1: Threshold energies for Bhabha triggers.

Trigger	Bit	ee events		$\mu\mu$ events		$e\mu$ events	
		a	ϵ	a	ϵ	a	ϵ
ECL Bhabha veto trigger	21	93	59	< 1	81	54	87
ECL barrel Bhabha trigger	22	85	61	< 1	84	87	87
First bit of ICN counter	23	50	36	51	83	47	81
Second bit of ICN counter	24	56	32	59	85	81	91
Third bit of ICN counter	25	38	100	33	100	36	100
ECL cosmic veto trigger	27	7	8	8	30	5	25

Tab. C.2: Selection efficiencies for ECL Bhabha triggers and cosmic triggers. Here a and ϵ represent the percentage of events activated with and passed through the corresponding trigger bit, respectively.

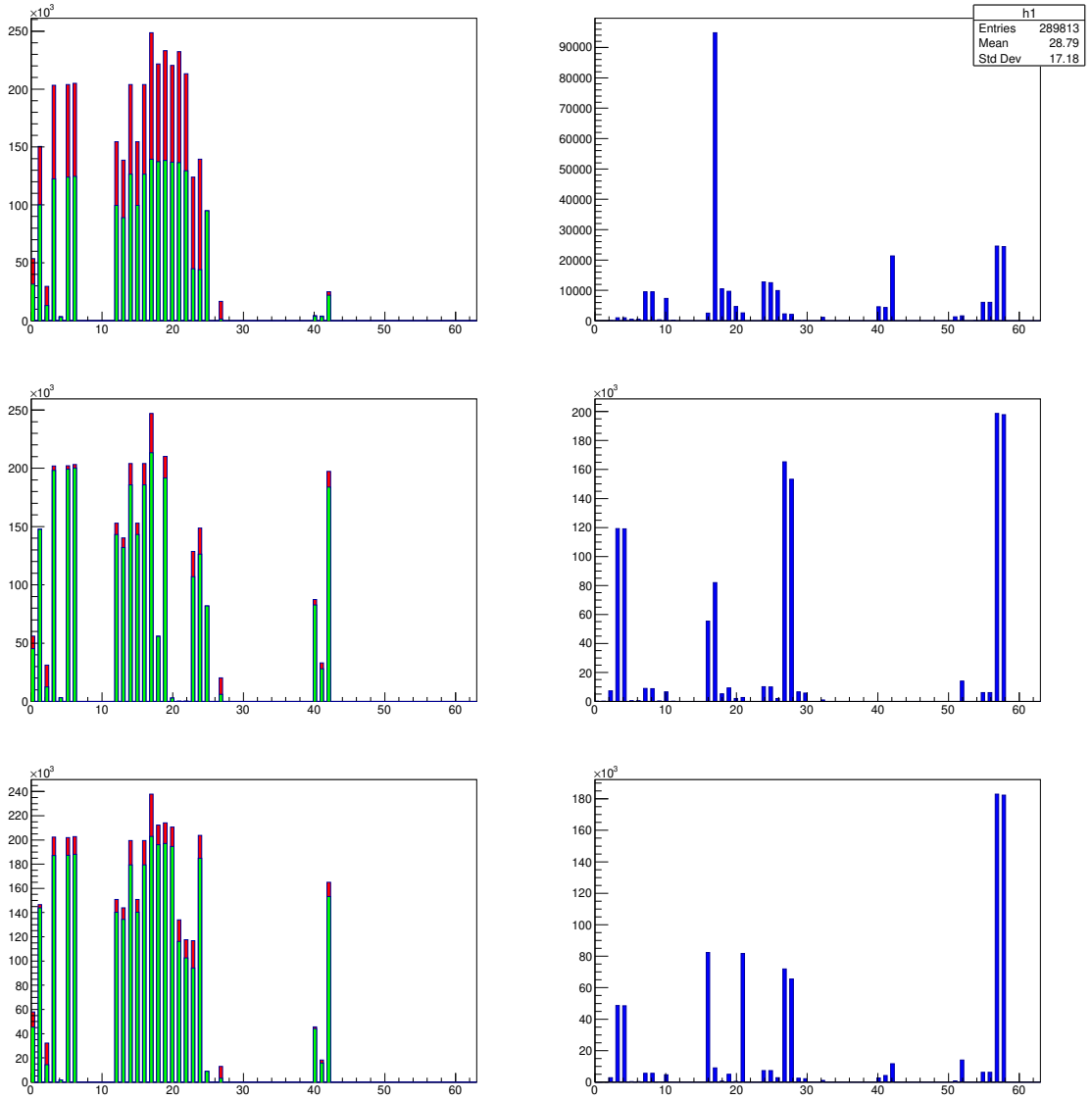

FIG. C.3: (Input, output) sub-triggers are represented in column(1,2). Row(1,2,3) representing the sub-triggers for $(ee, \mu\mu, e\mu)$ events. In the input trigger plots, the selected triggers (green) after Bhabha veto are projected on the total number of triggers (red) before Bhabha veto.

Bibliography

[1] G.L. Glashow, Nucl. Phys. **22** 579 (1961).

[2] A. Salam and J.C. Ward, Phys. Lett. **13** 168 (1964).

[3] S. Weinberg, Phys. Rev. Lett. **19** 1264 (1967).

[4] "Elementary particle", Wikipedia:en.wikipedia.org/wiki/Elementary_particle

[5] Standard Model. (2022, October 5). In Wikipedia. https://en.wikipedia.org/wiki/Standard_Model.

[6] D. Bjorken and E.A. Paschos, Phys. Rev. **185**, 1975 (1969).

[7] J.C. Pati and A. Salam, Phys. Rev. D **10**, 275 (1974).

[8] H. Georgi and S.L. Glashow, Phys. Rev. Lett. **32**, 438 (1974).

[9] P.W. Higgs, Phys. Letters **13** 508-509 (1964).

[10] G.S. Guralnik, C.R. Hagen and T.W. Kibble, Phys. Rev. Letters **13**, 585-587 (1964).

[11] G. Aad *et al.* (ATLAS Collaboration), Phys. Lett. B **716** 1 (2012).

[12] S. Chatrchyan *et al.* (CMS Collaboration), Phys. Lett. B **716** 30 (2012).

[13] J.H. Christenson, J.W. Cronin, V.L. Fitch, and R. Turlay Phys. Rev. Lett. **13**, 138 (1964).

[14] M. Kobayashi, T. Maskawa, Progress of Theoretical Physics **49**, 652–657 (1973).

[15] M. Tanabashi *et al.*, (Particle Data Group), Phys. Rev. D **98**, 030001 (2018).

[16] Y. Grossman and P. Tanedo, Just a Taste: Lectures on Flavor Physics, TASI **2016**, 109-295 (2018)

[17] S. Descotes-Genon, L. Hofer, J. Matias, and J. Virto, J. High. Energy Phys. **06**, 092 (2016).

[18] C. Bobeth, G. Hiller, and G. Piranishvili, J. High. Energy Phys. **12**, 040 (2007).

[19] LHCb Collaboration, Nat. Phys. **18**, 277–282 (2022).

[20] M. Gell-Mann, Phys. Lett. **8**, 214 (1964).

[21] G. Zweig, CERN Report No.8419/TH.412

[22] B. Ketzer, B. Grube, D. Ryabchikov, Prog. Part. Nucl. Phys. **113** 103755 (2020).

[23] N. Brambilla, A. Pineda, J. Soto, and A. Vairo, Nucl. Phys. B **566** 275-310 (2000).

[24] H.S. Chung, J. Lee, D. Kang, J. Korean Phys. Soc. **52** 1151-1154 (2008)

[25] G.T. Bodwin, D. Kang, and J. Lee, Phys. Rev. D **74** 014014 (2006).

[26] J.J. Aubert *et al.*, Phys. Rev. Lett. **33**, 1404 (1974).

[27] J.-E. Augustin *et al.*, Phys. Rev. Lett. **33**, 1406 (1974).

[28] S.W. Herb *et al.*, Phys. Rev. Lett. **39**, 252 (1977).

[29] E. Eichten, S. Godfrey, H. Mahlke, and J.L. Rosner, Rev. Mod. Phys. **80**, 1161 (2008).

[30] Y. Fukuda *et al.* (Super-Kamiokande Collaboration), Phys. Rev. Lett. **81**, 1562 (1998).

[31] Q.R. Ahmad *et al.* (SNO Collaboration), Phys. Rev. Lett. **89**, 011301 (2002).

[32] T. Faber, M. Hudec, M. Malinský, P. Meinzinger, W. Porod, and F. Staub, Physics Letters B, **787**, (2018).

[33] S. Dwivedi, A. Falkowski, D.K. Ghosh, and N. Ghosh, Eur. Phys. J. C **80**, 263 (2020).

[34] S.L. Glashow, D. Guadagnoli, and K. Lane, Phys. Rev. Lett. **114**, 091801 (2015).

[35] A. Crivellin, D. Mueller, A. Signer, and Y. Ulrich, Phys. Rev. D **97**, 015019 (2018).

[36] M. Raidal *et al.*, Eur. Phys. J. C **57**, 13 (2008).

[37] A.M. Teixeira, J. Phys. Conf. Ser. **888**, 012029 (2016).

[38] C. Han, M.L. López-Ibáñez, A. Melis, O. Vives, L. Wu, and J.M. Yang, J. High Energy Phys. **05**, 102 (2020).

[39] T. Kobayashi, T. Shimomura, and M. Tanimoto, Phys. Lett. B **819**, 136452 (2021).

[40] T. Faber, Y. Liu, W. Porod, M. Hudec, M. Malinský, F. Staub, H. Kolešová, Rev. D **101**, 095024 (2020).

[41] J. Heeck, Phys. Lett. B **758**, 101 (2016).

[42] G. Cvetič, C. Dib, C.S. Kim, and J.D. Kim, Phys. Rev. D **66**, 034008 (2002).

[43] C. Yue, Y. Zhang, and L. Liu, Phys. Lett. B, **547**, 252-256 (2002).

[44] T. Fukuyama, T. Kikuchi, and N. Okada,Phys. Rev. D **68**, 033012 (2003).

[45] J. Ellis, J. Hisano, M. Raidal, and Y. Shimizu, Phys. Rev. D **66**, 115013 (2002).

[46] M. Raidal *et al.*, Eur. Phys. J. C **57**, 13 (2008).

[47] D.E. Hazard and A.A. Petrov, Phys. Rev. D **94**, 074023 (2016).

[48] W. Love *et al.*, Phys. Rev. Lett. **101**, 201601 (2008).

[49] J.P. Lees et al., Phys. Rev. Lett. **104** 151802 (2010).

[50] M. Ablikim *et al.* (BESIII Collaboration), Phys. Lett. B **598**, 172-177 (2004).

[51] M. Ablikim *et al.* (BESIII Collaboration), Phys. Rev. D **87**, 112007 (2013).

[52] S.-K. Choi *et al.* (Belle Collaboration), Phys. Rev. Lett. **91**, 262001 (2003).

[53] T. Aushev *et al.* (Belle Collaboration), Phys. Rev. D **81**, 031103(R) (2010).

[54] B. Aubert *et al.* (BABAR Collaboration), Phys. Rev. Lett. **102**, 132001 (2009).

[55] V. Bhardwaj *et al.* (Belle Collaboration), Phys. Rev. Lett. **107**, 091803 (2011).

[56] R. Aaij *et al.* (LHCb Collaboration), Nucl. Phys. B **886**, 665 (2014).

[57] P. del Amo Sanchez *et al.* (BABAR Collaboration), Phys. Rev. D **82**, 011101(R) (2010).

[58] M. Ablikim *et al.* (BESIII Collaboration), Phys. Rev. Lett. **122**, 202001 (2019).

[59] T. Iwashita *et al.* (Belle Collaboration), Prog. Theo. and Exp. Phys., **043** C01 (2014).

[60] A. Vinokurova *et al.* (Belle Collaboration), J. High Energy Phys. **2015**, 132 (2015).

[61] S.K. Choi. arXiv:1101.5691 (2011).

[62] K. Terasaki, arXiv:1411.7483 (2014).

[63] L. Meng, G.-J. Wang, B. Wang, and S.-L. Zhu, Phys. Rev. D **104**, 094003 (2021).

[64] K. Abe *et al.* (Belle Collaboration), arXiv:hep-ex/0505037 (2005).

[65] P. del Amo Sanchez *et al.* (BABAR Collaboration), Phys. Rev. D **82**, 011101(R) (2010).

[66] M. Ablikim *et al.* (BESIII Collaboration), Phys. Rev. Lett. **122**, 232002 (2019).

[67] K. Akai, *et al.*, Nucl. Instrum. and Meth. A **907**, 188-199 (2018).

[68] T. Abe, *et al.*, Belle II Technical Design Report, arXiv:1011.0352.

[69] N. Toge, *et al.* KEKB *B*-factory design report KEK Report 9 5-7 (1995); S. Kurokawa and E. Kikutanu, Nucl. Instrum. and Meth. A **499**, 1 (2003).

[70] G. Alimonti *et al.*, Nucl. Instr. Meth. A **453**, 71 (2000).

[71] Y. Ushiroda, Nucl. Intr. Meth. A **511**, 6 (2003).

[72] S. Uno *et al.*, Nucl. Instr. Meth. A **330**, 55 (1993).

[73] R. Fruwirth, Nucl. Instr. Meth. A **262**, 444 (1987); R. Harr, IEEE Trans. Nucl. Sci. **42**, 134 (1995).

[74] T. Iijima *et al.*, Nucl. Instr. Meth. A **453**, 321 (2000).

[75] H. Kichimi *et al.*, Nucl. Instr. Meth. A **453**, 315 (2000).

[76] H. Ikeda *et al.*, Nucl. Instr. Meth. A **441**, 401 (2000).

[77] K. Hanagaki *et al.*, Nucl. Instr. Meth. A **485**, 490 (2002).

[78] V. Zhilich *et al.*, Online luminosity measurements with CsI calorimeter at the Belle detector, Internal Belle Note **465**.

[79] A. Abashian *et al.*, Nucl. Instr. Meth. A **449**, 112 (2000).

[80] Y. Ushiroda *et al.*, Nucl. Instr. Meth. A **438**, 460 (1999).

[81] M. Nakao *et al.*, IEEE Trans. Nucl. Sci. **47**, 61 (2000).

[82] E. Nakano, Nucl. Instrum. Methods Phys. Res. Sect. A **494**, 402 (2002).

[83] A. Abashian *et al.*, Nucl. Instrum. Meth. Phys. Res., Sect. A **491**, 69 (2002).

[84] Gary J. Feldman and Robert D. Cousins, Phys. Rev. D57, 3873 (1998)

[85] Ilsoo Seong, Search for $\Upsilon(1S)$ decays to invisible particles and a single photon, Internal Belle Note **1427**.

[86] X. L. Wang, *et al.*, Determination of the number of $\Upsilon(2S)$ events, Internal Belle Note **1185**.

[87] B. Bhuyan, High p^T tracking efficiency using partially reconstructed D^* decays, Internal Belle Note **1165**.

[88] S. Nishida, Study of kaon and pion identification using Inclusive D^* sample, Internal Belle Note **779**.

[89] Gary J. Feldman and Robert D. Cousins, Phys. Rev. D **57**, 3873 (1998).

[90] Ruei-Jhu Li, Search for a light higgs boson in $\Upsilon(2S)$ decay, Internal Belle Note **1238**.

[91] B.G. Cheon *et al.*, Nucl. Instrum. and Meth. A **494** 548 (2002).

[92] Charge-conjugate modes are included throughout the analysis unless stated otherwise.

[93] D.J. Lange, Nucl. Instrum. Methods Phys. Res. A **462**, 152 (2001).

[94] E. Barberio and Z. Wąs, Comput. Phys. Commun. **79**, 291 (1994).

[95] R. Brun *et al.,* GEANT3.21, CERN Report No. DD/EE/84-1, 1984.

[96] S. Jadach, Z. Was, R. Decker, and J.H. Kuhn, Comp. Phys. Commun. **76**, 361 (1993).

[97] T. Sjostrand, S. Mrenna, and P. Skands, JHEP **0605**, 026 (2006).

[98] Charmonium Group "Event Selection of $B \to J/\psi K_S$", Internal Belle Note **318**.

[99] Inclusive J/ψ sample with charged B-meson decays can be found at `/group/belle/bdata_b/mcprod/specialmc2010/chargedjpsi/` and neutral B-meson decays can be found at `/group/belle/bdata_b/mcprod/specialmc2010/mixedjpsi/`.

[100] G.C. Fox and S. Wolfram, Phys. Rev. Lett. **41**, 1581 (1978).

[101] R. Garg, Search for $B \to Y(4260)K$ decay mode in Belle, Internal Belle Note **1454**.

[102] S. Ryu, Study of π^0 efficiency using $\tau^- \to \pi^-\pi^0\nu_\tau$, Internal Belle Note **1224**.

[103] N. Dash, Systematic uncertainty for the K^0_S reconstruction efficiency, Internal Belle Note **1472**.

[104] V. Chobanova, Measurement of the $B^0 \to \psi(2S)\pi^0$ branching fraction [Belle note 1323]

[105] S.-K. Choi *et al.* (The Belle Collaboration), Phys. Rev. D **84**, 052004 (2011).

[106] N. Mangiafave, J. Dickens, and V. Gibson, A Study of the Angular Properties of the $X(3872) \to J/\psi\pi^+\pi^-$ Decay, LHCb-PUB-2010-003, (2010).

[107] S. Patra, V. Bhardwaj, MC decay tagging using generated level information with GenMCTagTool, Internal BELLE II Note **2021-002**.

[108] K. Hayasaka *et al.* (Belle Collaboration), Phys. Lett. B **666** 16 (2008).

[109] B. Aubert *et al.* (BABAR Collaboration), Phys. Rev. Lett. **104**, 021802 (2010).

[110] K. Uno *et al.* (Belle Collaboration), J. High Energ. Phys. **2021**, 19 (2021).